This work is protected by copyright and other intellectual property rights and duplication or sale of all or part is not permitted, except that material may be duplicated by you for research, private study, criticism/review or educational purposes. Electronic or print copies are for your own personal, non-commercial use and shall not be passed to any other individual. No quotation may be published without proper acknowledgement. For any other use, or to quote extensively from the work, permission must be obtained from the copyright holder/s.

Preparation and Evaluation of Polymer Coated Magnetic Nanoparticles for Applications in Gene Delivery

Kaarjel Kauslya Narayanasamy

Doctor of Philosophy
in Biomedical Engineering

June 2018
Keele University

Abstract

With the advent of powerful gene editing tools such as CRISPR/Cas9, advances in gene therapy have gained a second wind. Despite this, disease therapy still has not progressed beyond clinical trials due to limitations in current delivery methods. The work presented in this thesis studies the development of a non-viral gene delivery method which is the nanomagnetic transfection method, which is the delivery of genes to cells using magnetic nanoparticles (MNPs) with a cationic surface charge and an external magnetic field. The advantage of nanomagnetic transfection over other non-viral chemical methods is the low dosage required to transfect cells coupled with a short transfection time. The presence of an external magnet provides targeting functionality, whereby the MNPs carrying the gene of interest are pulled towards the cells, thus increasing the efficiency of cell to MNP contact.

The research looks at the synthesis of MNPs using thermal decomposition to obtain particles with a narrow size distribution and exhibiting a combination of Brownian and Néel relaxation. The MNPs were coated with polyethyleneimine (PEI), which binds and condenses DNA to deliver into cells for protein expression. PEI is known to be toxic to cells at high concentrations, hence PEI not bound to MNPs were removed using dialysis. A unique study observing the gradual loading of PEI coating on MNPs using AC susceptometry (ACS) is described. ACS provided information on the MNP coating and aggregation process that was not accessible through dynamic light scattering (DLS) due to the additional presence of non-magnetic polymer particulates in the suspensions. In combination with complementary structural characterization techniques, a simple method was derived to obtain dense, uniform PEI coatings affording high-stability suspensions without excessive quantities of unbound PEI to reduce cytotoxic effects. This method can be used for improving coating and functionalization therefore advancing MNP-drug/gene delivery studies.

The PEI-coated MNPs were subsequently studied for their transfection capabilities in HeLa cells and compared to commercial MNP transfection agents. It was found that nanomagnetic transfection had higher GFP reporter expression compared to Lipofectamine and PEI. The parameters affecting transfection activity were determined in order to improve transfection rates of synthesized MNPs. A trade-off between transfection efficiency and cytotoxicity was observed, where the presence of unbound PEI improved transfection but affected cell viability. To overcome this, polymers and block-copolymers with a lower charge density should be developed.

The proton-sponge effect, which is the mechanism of MNP-PEI escape from the endolysosome was studied by measuring the AC susceptibility of MNP-PEI in live cells. However, the low transfection efficiency of MNP-PEI and low sensitivity of the AC susceptometer made it difficult to obtain conclusive evidence. A novel study using Raman spectroscopy to obtain fingerprint spectra of the MNP-PEI complexes and to determine their localization in cells is reported. Individual spectra of MNP and PEI were obtained, as well as the area map of the cell, however the localization of MNPs within the cell was not possible due to the limited sensitivity of the Raman spectrometer. Finally, the effect of the MNP-PEI transfection agents on cells were identified. It was observed that MG-63 and HeLa cells expressed increased cell stress with the formation of actin stress fibres and increased cell adhesion. Between the two transfection components, PEI antagonized the cell adhesion effect compared to MNPs. In addition, the genes associated with actin fibres and cell adhesion were identified, which were ACTA2, ACTN1, MVCL, VCL, P4HA2, PCDHB12, SVIL, and TGFBI, which showed increased expression to MNP-PEI treatment. Collectively, the study conducted reports the development of an MNP transfection agent, from synthesis to application.

Contents

List of Figures

List of Tables

List of abbreviations

ACS – AC susceptometry
BSA – Bovine serum albumin
CM – Complete supplemented media
CMV – Cytomegalovirus CoP MNP – Co-precipitated MNP
CRISPR/Cas9 – Clustered regularly interspaced short palindromic repeats associated nuclease 9
DF – Dilution factor DLS – Dynamic light scattering
DMEM – Dulbecos Modified Eagle Medium
DMSO – Dimethyl sulfoxide
ECM – Extracellular matrix
FA – Focal adhesion
FBS – Fetal bovine serum
FS-MNP – Flame synthesized MNP
GFP – Green fluorescent protein
ICC – Immunocytochemistry
IMS – Industrial methylated spirits
MagSep – Magnetic separation
MCA – Multivariate curve analysis
MICA – Magnetic Ion Channel Activation
MNP – Magnetic nanoparticle
MWCO – Molecular weight cut-off
NLS – Nuclear localization sequence
PBS – Phosphate buffered saline
PEG – Polyethylene glycol
PEI – Polyethyleneimine
qPCR – Quantitative polymerase chain reaction
ROS – Reactive oxygen species
SERS – Surface enhanced Raman spectroscopy
SPION – Superparamagnetic iron oxide nanoparticle
tdMNP – Thermal decomposition MNP
TEM – Transmission electron microscopy
TGA – Thermogravimetric analysis
UV – Ultraviolet

Acknowledgements

This PhD fellowship is funded by the Marie Curie Intra-European Fellowship within the 7th European Community Framework: Functionalized Magnetic Nanoparticles and Their Application on Chemistry and Biomedicine (MAGNETICFUN), Grant Number 290248.

Firstly, I would like to express my sincere gratitude to my supervisor Dr. Neil Telling for the continuous support of my PhD research. This work would not be possible without your whole-hearted guidance and advice. Thank you for allowing me to formulate and expand upon my ideas, which has made this project fulfilling and (hopefully) made me a better researcher. I am also grateful to my co-supervisor Prof. Jon Dobson, who believed that I could undertake this PhD project when I thought I was way in over my head! Thank you very much for the opportunity to work on this cool project and at the Dobson lab. I have learnt so much from you, and you always had my back whenever I messed up (which was quite often). Thank you for the wonderful experience. Prof. Carlos Rinaldi, I am glad to have known and worked with you. Thank you for your guidance and advice during my time in Florida. Your help with the particle synthesis made this project much more than it would have been.

To my fellow lab-mates Dali, James, and Sandhya, it was wonderful working with all of you. Daliborcék, you are my bestest buddy here (even now), and I cherish the good times we had together, in and out of work. Life here became a bit less colourful since you left. I would also like to thank my fellow PhD and postdoc colleagues at the ISTM, who were always ready to lend a helping hand. To my friends in Florida; Melissa, Adam, Matt, Ming, Sheri, Dan, Lorena, Isaac and more, I had one of the best times of my life in Florida thanks to all of you. It was an awesome working environment on that floor and we were always goofing around and having great laughs, especially when that bloody flow cytometer kept breaking down! I miss all of you very much.

As Isaac Newton said, *" If I have seen further, it is by standing on the shoulders of giants".* When I think of how far I've come in academia, it is thanks to my previous supervisors who instilled in me a passion for science and who have always encouraged me, even to this day! Thank you for your support and guidance, Prof. Shafinaz Shahir, Prof. Shahir Shamsir, Dr. Johan Kotze, and Prof. Heikki Setälä. You are an inspiration to me.

To my friends Shrikanth and Erika, you guys have always looked out for me, from those cold days in Finland until now! To my dear friends in Malaysia, it has been 7 long years since I left and I am starting to feel it. I am very grateful that you guys still take time out of your busy schedules to "Assemble!" whenever I make my annual visits home. Hanging out with all of you, it feels like I never left. KlangTop!

To that special creature in my life, Joshua Price. You have been the driving force behind completing this PhD and a constant source of encouragement especially when I was at my worst. Thank you for seeing me as more than I really am, I think I'm starting to believe it! I love you very much. To Josh's family, Ma, Pa and brothers, thank you for welcoming me into your loving family. Ike, Beauty, and Mango (my cats), I carry you always in my heart.

I have no words to describe my gratitude to my extended family in Malaysia. All of you are our safety net, and we were able to leave home and pursue our dreams because you are there to keep everything under control.

Finally, to my darling family; Papa, Amma, Shaman anna, and Sai. You are the reason I carry on. Life is meaningless without you.

Thank you all.

Chapter 1

Introduction

1.1 Overview

The key to understanding how biological and chemical processes in living organisms work is to first elucidate the role of genetic material and the flow of genes to proteins, which govern all biochemical processes in an organism. The central dogma theory of biology was proposed in 1957 by Francis H. C. Crick (Crick, 1958) which states:

"In more detail, the transfer of information from nucleic acid to nucleic acid, or from nucleic acid to protein may be possible, but transfer from protein to protein, or from protein to nucleic acid is impossible. Information means here the precise determination of sequence, either bases in nucleic acid or of amino acid residues in protein."

Cricks' theory describes the role of replication, transcription and translation, as well as that the transfer of information from nucleic acids to peptides and protein can only occur in one direction. The study by Marshall Nirenberg in 1968 had also provided essential information on how codons in genetic material code for certain amino acids and short lengths of nucleotides called genes can be transcribed into mRNA and translated to form a functional polypeptide (LeVine, 2006).

This knowledge in molecular biology was the foundation for the scientific discipline of genetic engineering. This field of study involves the manipulation of genetic material through various methods. A foreign gene can be inserted into an organism, or genes in an organism can be silenced or down-regulated using small-interfering RNA (siRNA) or various oligonucleotides involved in the RNA interference (RNAi) mechanism (Resnier et al., 2013). The ability to modify genes is important in order to gain an understanding of the behaviour of cells, biochemical processes in an organism, how biological systems interact, and ultimately to extrapolate these information into applications in clinical settings, such as for drug discovery and treatment of diseases.

This introduction examines a section of the field of genetic engineering, which is, improving gene delivery into mammalian cells using magnets and magnetic material. This study integrates the different disciplines of biotechnology where gene delivery is a crucial aspect, chemical engineering which explains the synthesis of magnetic nanoparticles, and the physics behind the behaviour of magnets and magnetic materials. The inter-disciplinary approach to improve and expand the rather stagnant technique of gene delivery using contemporary methods currently available seems promising.

1.2 Transfection

Transfection is a method of delivering nucleic acids into a cell. It is a fundamental technique in the field of cell biology as transfection can be used to understand the function and structure of genes and proteins, and the biochemical regulation of cells. This technique involves the insertion

of a foreign gene into a cell or tissue to study the effect of expressing exogenous genes, or the silencing of a gene in the cell by means of endogenous or exogenous inhibitory RNAs whereby the resulting protein is knocked-down or downregulated. The changes in cellular behaviour and metabolism for both these methods can be observed to gain an understanding of the biochemical processes in an organism (Davidson and McCray, 2011; Kim and Eberwine, 2010; Luo and Saltzman, 2000).

Clinical applications of gene transfection are also being developed to treat various genetic and acquired diseases in a process known as gene therapy. During cell division and DNA replication, errors such as basepair mismatch may occur where the wrong nucleotide is inserted in a genetic sequence and some errors may change the structural conformation of the DNA itself by forming loops and other nonduplex structures. Cells have a regulatory mechanism where various repair proteins are usually able to repair damaged DNA, otherwise the cells undergo apoptosis to eliminate mutated cells that could potentially be cancerous (Sancar et al., 2004). Although cells have this repair mechanism to restore DNA to its original form, incidences happen where this mechanism fails to work, hence genetic defects arise. There are two types of genetic defects; a mutation which occurs in somatic cells is non-heritable and so is not passed down to the next generation of offspring, but mutations in the germ line can cause heritable genetic diseases.

The concept of gene therapy is to deliver foreign genes into cells containing the defective DNA, either a plasmid DNA that has the correct sequence of codons to produce a protein normally, or a silencing oligonucleotide that knocks down the production of defective proteins that could potentially be harmful. The method of gene silencing was discovered by Fire and Mello in 1998 (Fire et al., 1998) and is known as RNA interference (RNAi). A commonly used gene therapy approach is the delivery of double-stranded siRNA. Once cells uptake siRNA, it forms an RNA-induced silencing complex (RISC) with proteins such as argonaute, and this complex inhibits translation of mRNA into polypeptide chains by binding to it or cleaving the mRNA. The RISC is recyclable, whereby having cleaved the target mRNA, it moves on to the next mRNA target. Therefore only a small concentration of siRNA is required to produce a high silencing effect, which can last for days (Jinek and Doudna, 2009). The silencing of unwanted genes have been demonstrated numerous times, with diseases such as cystic fibrosis (Clark et al., 2013; Gianotti et al., 2013), cancer (Deng et al., 2013; Nishimura et al., 2013; Yonenaga et al., 2012), and HIV infections (Fu et al., 2014; Wheeler et al., 2013).

Another application of oligonucleotides for gene therapy is the use of splice-correcting oligonucleotides (SCOs) or splice-swithing oligonucleotides (SSO). These oligonucleotides act on the pre-mRNA in the nucleus to correct defects, largely related to Duchenne muscular dystrophy (DMD), spinal muscular atrophy, and other myotonic dystrophies (Langel, 2011; Scholz and Wagner, 2012; Wood et al., 2010). More recently, the clustered regularly interspaced short palindromic repeats (CRISPR) associated nuclease 9 (CRISPR-Cas9) complex has been hailed as one of the biggest scientific breakthroughs in gene therapy. The CRISPR/Cas9 gene editing tool has been used extensively in gene therapy studies due to its high fidelity in replacing deleterious genes or adding new genes and its flexibility for creating breaks and nicks at any location in the genome *in vivo* (Xue et al., 2016; Cai et al., 2016).

Factors that determine a good transfection method are the ability to achieve high transfection efficiency, which is the delivery of genes through the cytoplasm of cells into the nucleus and the translation of the gene into its corresponding protein (Luo and Saltzman, 2000). Furthermore, the viability, proliferation, and differentiation of transfected cells are important determinants of a good transfection method (Kim and Eberwine, 2010; Luo and Saltzman, 2000; Mahmoudi et al., 2012; Reddy et al., 2012).

Once cells take up exogenous DNA, the gene can be expressed in the cell in either a stable or transient expression. The former incorporates foreign nucleic acids into the genome of the cell and is replicated when the cell divides; whereas the latter does not integrate into the genome, so that protein expression is diluted during cell division, and the gene eventually

disappears (Kim and Eberwine, 2010). Ultimately, a transfection method should be able to be translated from *in vitro* to *in vivo* for clinical studies in gene therapy (Luo and Saltzman, 2000).

The delivery of genes into cells mainly requires the use of a vector or carrier. Carriers have to be designed so that they can condense the plasmid onto their surface, and avoid plasmid degradation by endonuclases (Wattiaux et al., 2000). The use of viral vectors for gene delivery is known as transduction. Different viruses are used in gene delivery as the type of virus chosen for transduction depends on the size of nucleic acid to be delivered, the targeting efficiency of the virus, the requirements for stable versus transient transfections, and the cell type to be transduced.

The types of virus used are retroviruses such as Moloney murine leukemia virus (MMLV) and human immunodeficiency virus (HIV), adenoviruses, and adeno-associated viruses (Robbins and Ghivizzani, 1998). Virus-mediated transductions are very efficient in delivering genes to different cell types, in producing stably transfected cells and have potential for applications *in vivo*. However, this method is not very popular in clinical studies as it is immunogenic which can cause inflammatory responses in the target tissue, and due to its random insertion sites can cause mutations in the genome (Naldini, 2015). It also has limited nucleic acid carrying capacity and is expensive to produce (Kim and Eberwine, 2010; Luo and Saltzman, 2000).

Owing to the many complications of virus-mediated gene delivery, nonviral delivery methods are preferred. Physical methods of transfection involve the mechanical delivery of DNA into the cell using physical forces like pressure, electricity, or sound to create pores in the cell membrane, or by puncturing the cell to deliver DNA into the cytoplasm or nucleus. Such methods include microinjection, biolistic particle bombardment, electroporation, and ultrasonication, to name a few. The drawback of these methods is the cells undergo physical damage and therefore have a high mortality rate. Most of the equipment for these methods are also expensive, and the skill required to operate them is high (Kim and Eberwine, 2010; Luo and Saltzman, 2000). Chemical methods such as cationic liposomes and polyplexes, lipids, calcium phosphates, DEAE-dextran and activated dendrimers are preferred methods for delivering genes into eukaryotic cells *in vitro* as the DNA complex is fairly easy to form, is cheap and does not require expensive instruments for delivery, and works well for high-throughput systems. A popular method of non-viral transfection is the use of cationic chemicals as a vector to carry genes into the cell. This is preferred because of its relatively low immunogenicity and because entry into the cell is induced by the natural mechanism of cellular endocytosis. Cationic lipids or polymers, for example, form a complex with the anionic phosphate backbone of nucleic acids to form a lipoplex or polyplex. This complex is internalized into cells by endocytosis or perforation (Kim and Eberwine, 2010).

An obstacle with transfection of mammalian cells is the limited size of a plasmid that can be delivered into the cell. Investigations have been conducted to determine how the sizes of plasmids affect transfection efficiency. It was found that small plasmids had better transfection and expression compared to larger plasmids coding the same reporter gene. This has led to the commercial production of the Minicircle DNA, which significantly reduces the plasmid size by removing the antibiotic resistance gene and the origin of replication (ori) sequence (Chabot et al., 2013; Magin-Lachmann et al., 2004; Yin et al., 2005).

The intracellular delivery of genes for gene therapy require DNA vectors that contain sections of the human genome for promoter and regulator sequences. The bacterial artificial chromosomes (BAC) or the P1 based artificial chromosomes (PAC) are commonly used DNA vectors that can be stably cloned to carry large sequences of human genes, sometimes of more than 100 kbp, and are able to efficiently express the gene of interest (Cheung et al., 2012; Laner et al., 2005). Although a stable large gene is able to be produced, problems arise with the delivery of large genes into mammalian cells. Viral vectors, although a popular method for gene delivery, are only able to package small DNA. For example, lentiviral viruses can package DNA of up to 7.5 kb, whereas Adeno-associated viruses could carry a maximum length of approximately 5 Kbp DNA (Wu et al., 2010; al Yacoub et al., 2007). Inserting large fragments of genes into viral carriers that have limited carrying capacity can result in recombination of genes by deletion and insertion,

and may be deleterious if used in gene therapy (Chatterjee et al., 2013; Cheung et al., 2012).

Although the method seems promising, gene therapy is still in its clinical trial stages because the only vectors that are able to target cells and tissues with high efficiency are viral vectors, which is a potential risk as it can elicit an immunogenic response from the body. On the other hand, chemical methods such as cationic liposomes and polymers are inefficient, especially *in vivo* (Davidson and McCray, 2011; Peer and Lieberman, 2011). Hence, although many transfection methods are commercially available, there are clear advantages and limitations of each method. For this reason new strategies for delivering genes into cells are still actively being pursued. One method that has been heavily researched in recent years is magnetically-assisted gene delivery. In order to understand the technique of nanomagnetic transfection and the materials used it is first necessary to review the basics of magnetism and magnetic materials.

1.3 Magnetism and Magnetic Materials

There are two ways magnetic fields can be generated; one is by the flow of an electrical current which is known as an electromagnetic field, and the other is from intrinsic and orbital electron spins of atoms which relates to properties of a permanent magnet (Feynman et al., 1963; Jiles, 1991).

The magnetization $\mathbf{M}$ is the sum of magnetic moments (μ) divided by the volume of material, shown in the equation below:

$$\mathbf{M} = \frac{\Sigma\mu}{V} \tag{1.1}$$

The magnetic susceptibility, χ is denoted by the equation:

$$\chi = \frac{|\,\mathbf{M}\,|}{|\,\mathbf{H}\,|}, \tag{1.2}$$

which is the magnetization divided by the magnetic field. The magnetic susceptibility of MNPs is discussed in detail in Chapter 1.8.

The magnetic flux density, $\mathbf{B}$ is defined in the equation below, where μ is the magnetic permeability, $\mathbf{H}$ is the magnetic field intensity and $\mathbf{M}$ is the magnetization:

$$\mathbf{B} = \mu_0(H + M) \tag{1.3}$$

To understand magnetism in matter, it is important to know that all matter is magnetic. The difference is the type of magnetism of materials, which can be grouped into three main classes which are diamagnetism, paramagnetism, and ferromagnetism (Figure 1.1). Subclasses branching off from ferromagnetism are materials having ferrimagnetic, antiferromagnetic, helimagnetic, and superparamagnetic properties. The last-mentioned is a size-dependent property that is exhibited when synthesizing particles on a nanometer scale (Jiles, 1991). Unlike diamagnets and paramagnets, ferromagnets, and the subclasses ferrimagnets and antiferromagnets exhibit strong magnetic characteristics. Ferromagnets can also be permanently magnetized without the influence of an external field. This is due to the magnetic spins that lie along the easy axis of magnetization based on its crystal structure, shape, and texture. Another characteristic of ferromagnets is that they can have microscopic domains, where each domain has its spins pointing along its easy axis which is the energetically favourable direction of spontaneous magnetization.

Superparamagnetism is a term coined by Néel, and applies to ferromagnetic particles with a volume so small that they only possess a single domain magnetic structure. When these single domain particles are below a size limit, the direction of the single domain axis is unstable and can flip randomly. A collection of such particles will therefore have no overall net magnetization and they are termed superparamagnetic (Coey, 2010). Properties of superparamagnetism are that they show no hysteresis on a magnetization versus magnetic field (M-H) curve (Figure 1.3), but

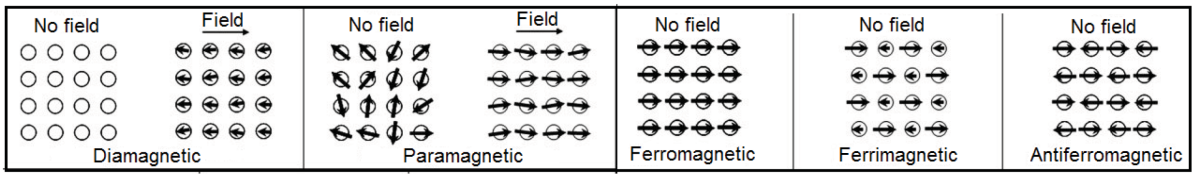

Figure 1.1 Magnetic-spin orientation with and without a magnetic field, for 5 types of magnetic material (Jeong et al., 2007). Reprinted with permission from John Wiley and Sons publishing group [license number: 4155410478711]

have large magnetic susceptibility due to a large moment of each particle. Magnetic susceptibility is also dependent on particle size and crystal deformation, where larger superparamagnetic particles have higher susceptibility, whereas smaller and deformed particles achieve magnetic saturation quickly (Bean and Livingston, 1959).

1.4 Magnetic Nanoparticles

Nanoparticles are defined as particles in the scale of 1 – 100 nm (Boholm and Arvidsson, 2016). Nanoparticles can be classified into 'soft' and 'hard'. The former is formed by weak interactions between the molecules and are fragile, such as micelles and vesicles. 'Hard' nanoparticles are more rigid, such as metallic or mineral nanoparticles and carbon nanotubes (Canton and Battaglia, 2012). In this study, 'hard' nanoparticles are the focus, specifically magnetic nanoparticles. Magnetic materials in the nanoscale domain have different properties compared to their macroscopic counterparts, as discussed in Section 1.3 above. The magnetic coercivity and susceptibility of magnetic particles are thus dependent on their size, shape and chemical structure (Jun et al., 2008).

In many applications of MNPs, the particles are required to exhibit certain magnetic characteristics. To achieve this, the size, shape, magnetic anisotropy, or chemical composition of the MNPs is tuned using different synthesis methods. MNPs exhibit either ferromagnetic, ferrimagnetic or superparamagnetic behaviour, where particles having single- and multi- domains are usually ferri- and ferromagnetic, but below a critical size, single domain particles exhibit superparamagnetic behaviour (Figure 1.2).

The magnetic properties of superparamagnetic iron oxide nanoparticles (SPIONs) are highly favourable for magnetic manipulation as their superparamagnetic property allows the particle magnetic moments to align parallel to the external magnetic field (Dobson, 2006), whilst removal of the external magnetic field allows the SPIONs magnetic moments to scatter in random directions so that the ensemble of particles are demagnetized, whereby remnant magnetization is zero due to thermal randomization of the nanoparticle magnetic moments. This eliminates aggregation of MNPs once the external field is removed and the particles return to a colloid state. With increase in size, particles still retain single domain magnetic moments but have coercive fields where the particles retain their magnetism with the absence of a magnetic field and require an external field in order to be demagnetized (Figure 1.3). In nanomagnetic transfection applications, the sedimentation of MNP vectors onto cells due to an external magnetic gradient is an important factor for transfection efficiency, which is achieved more efficiently by a larger particle size due to stronger magnetization. (Furlani and Xue, 2012). However transfection with ferromagnetic particles would be difficult as they would tend to aggregare into large clumps and therefore affect cellular internalization of MNPs.

1.4.1 Synthesis of MNPs

Magnetic particles can be engineered using different starting materials to suit an application or to provide certain magnetic properties. Particles that are commonly synthesised for biomedical and clinical applications are iron oxide derivatives such as magnetite, maghemite, and the lesser

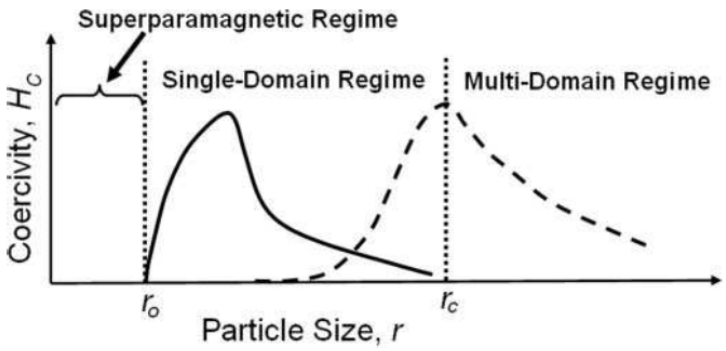

Figure 1.2 Schematic of particle size versus coercivity, with superparamagnetic particles showing no coercivity below size ro, and ferri- or ferromagnetic particles in the single- or multi-domain region (Jeong et al., 2007). Reprinted with permission from John Wiley and Sons publishing group [license number: 4155430735055].

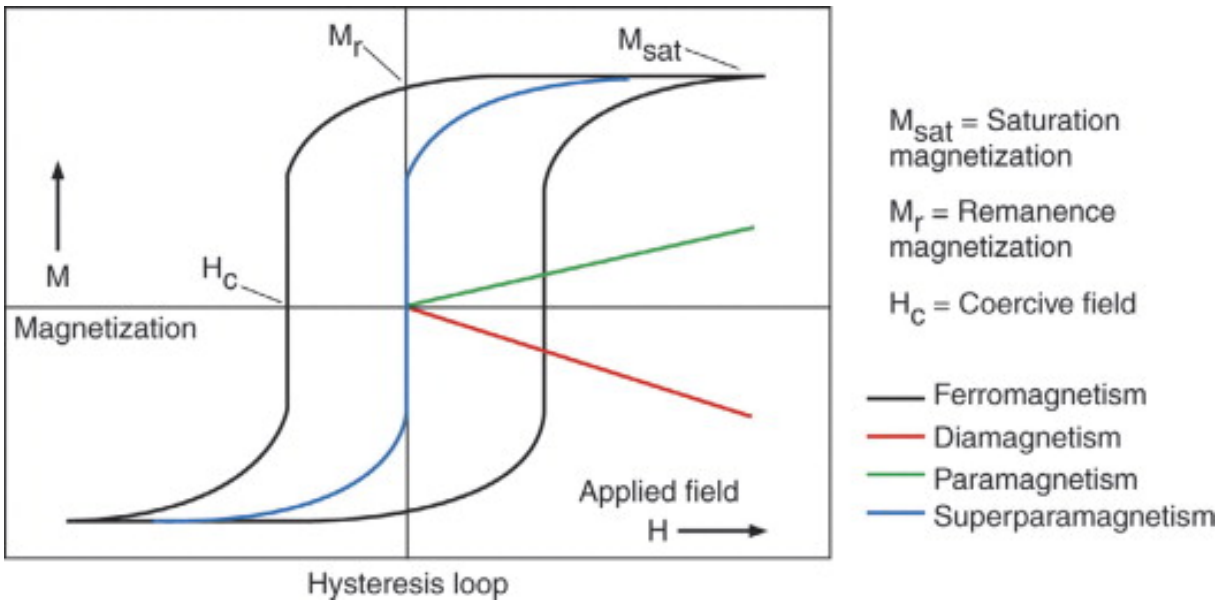

Figure 1.3 A magnetization curve of four types of magnetic material (Arruebo et al., 2007). Reprinted with permission from Elsevier publishing group [license number: 4155470662199].

synthesised hematite (Mahmoudi et al., 2011). Iron oxide particles are favoured for biomedical applications because they are FDA approved, are biocompatible, and non-toxic to cells. Other ferromagnetic metals being researched for potential applications are 3d transition metals (which are elements in the periodic table have an incompletely filled d sub-shell containing at least one electron) to form iron oxide doped manganese, cobalt, or nickel, as well as some rare earth metals.

Iron oxide nanoparticles can be produced using three general methods – the physical, chemical, and microbial method. Synthesis of MNPs is usually followed by a stabilization procedure to prevent the aggregation of the nanoparticles during *in vitro* and *in vivo* applications. The coating is also to prevent oxidation or solubilization of the iron oxide nanoparticles and can be used for further functionalizing the particles with biological molecules for functional applications (Reddy et al., 2012). For use in nanomagnetic transfection, nanoparticles with metal oxide cores are usually coated with cationic polymers or lipid that interact with the phosphate backbone of nucleic acids through electrostatic interactions (Cruz-Acuna et al., 2016; Plank et al., 2011).

With the various applications and potential of magnetic nanoparticles in medicine and technology, the need to develop methods to produce highly controlled characteristics of MNPs to suit each application has become paramount. Characteristics of MNPs such as the size, yield, material composition, size polydispersity, magnetic characteristics, and shape need to be controlled by investigating various synthesis methods and parameters.

A simple and widely used method to obtain particles with high yield is by co-precipitation (Laurent et al., 2008). In this method, iron salts of Fe^{3+} and Fe^{2+} are combined in the presence of a base such as NaOH or NH_4OH in anoxic conditions (Gupta and Gupta, 2005).
To create an oxygen-free environment during the synthesis, nitrogen gas or other inert gasses are passed through the reaction mixture to prevent the oxidation of magnetite to ferric hydroxide $Fe(OH)_3$(Gupta and Gupta, 2005; Karaagac et al., 2010; Mahmoudi et al., 2011). The disadvantage of this method is that it creates particles with large size distribution.

Alternatively, synthesis methods that are being investigated to control particle size include the reverse micelle or emulsion method which creates nanodroplets in which the metal oxide grows. Growth of the MNP is limited by the size of the micelle and therefore a uniform size distribution of particles can be achieved. To vary the size of particles using the reverse micelle method, the amount and concentration of metal salts, surfactant and solvent can be adjusted. The emulsion method is similar, where it uses water and oil emulsions to achieve the same effect of a constrained shell to limit nanoparticle growth. Other similar methods include the sol-gel preparation and polymer-matrix mediated synthesis (Gupta and Gupta, 2005; Laurent et al., 2008). Therefore the size of particle size be controlled by varying the two parameters; cation concentration in the reaction and vesicle diameter, in accordance to their linear relationship to particle diameter.

A biological method employed to synthesise MNPs is by biomineralization to form magnetosomes in these magnetotactic bacteria. These bacteria was discovered and described by Salvatore Bellini in 1963 and Richard P. Blakemore in 1975, respectively (Blakemore, 1975; Yan et al., 2012). These bacteria produce magnetite or greigite Fe_3S_4 crystals surrounded by a membrane containing proteins specific to these bacteria. Formation of these magnetosome chains in magnetotactic bacteria involves a multistep process. Although the exact mechanism of magnetosome formation is not known, the general mechanism is formation of empty vesicles along the axis of bacteria, transport of iron from the external environment into the bacteria and mineralization of the iron oxides in the vesicles (Yan et al., 2012).

Synthesis of MNPs takes place in two parts: the nucleation phase and the growth phase. LaMer and Dinegar proposed the theory explaining the mechanism of nucleation in a supersaturated solution to produce a colloidal suspension (LaMer and Dinegar, 1950). To obtain particles with a narrow size distribution, methods to separate the two phases are employed, where nucleation stops occurring during the growth phase. The spontaneous nucleation phase occurs

when the mixture reaches supersaturation at critical concentrations of metal oxide clusters. Once nucleation occurs, the solution concentration decreases below supersaturation and nucleation stops. The growth phase occurs immediately and the nuclei grow at the same rate to achieve uniform sizes (Schladt et al., 2009). Another method to create uniform sized particles is to use the Ostwald ripening method which has nucleation and growth occurring at the same time, although this creates larger particles (Mahmoudi et al., 2011; Park et al., 2004).

By synthesizing different sizes of superparamagnetic particles, their magnetic properties are affected. With the decrease of particle size to the 'nano' domain, the magnetic susceptibility is lowered as well. This is attributed to noncollinear spins and crystalline defects on the surface of magnetite particles. With increasing surface area to volume ratio, the sphere curvature of particles increase, creating more defects which reduces its magnetic susceptibility (Gupta and Gupta, 2005).

1.4.2 Functionalization of MNPs

MNPs have the tendency to aggregate in suspension as they are hydrophobic and this minimizes their surface energy. MNPs which exhibit ferromagnetism tend to form clusters, and the magnetization of those clusters attracts more particles to them to form larger aggregates. This property is not favourable in functional cellular studies as the aggregates lose their superparamagnetic property. Therefore the surface of MNPs has to be modified to improve their colloidal stability to form homogeneous ferrofluids. Ferrofluids are defined as colloidal suspensions of magnetic nanoparticles that can be magnetically manipulated under strong magnetic fields without losing its fluidity (Gupta and Gupta, 2005). To prevent aggregation, the MNP coating has to overcome hydrophobic interactions, magnetic forces between particles, and Van der Waals forces (Mahmoudi et al., 2011). To promote stability of a colloidal MNP suspension, particles can be surface-modified with surfactants, natural and synthetic polymers or even biomolecules. Besides stability, surface functionalization is used to facilitate binding and internalization of MNPs into cells, or for gene and drug delivery (McBain et al., 2008b). Therefore, choosing a material for coating MNPs is crucial in carrying out their function effectively. Furhtermore, previous studies have shown that uncoated superparamagentic iron oxide nanoparticles (SPIONs) have a detrimental effect on cells (Mahmoudi et al., 2012). Therefore the MNPs have to be coated to improve compatibility with cells and to induce natural uptake of nanoparticles through endocytosis.

A polymeric stabilizer that specialized in carrying out a specific function is polyethylenimine (PEI). PEI has been used as a reagent for the delivery of DNA into cells since 1995 (Boussif et al., 1995). This polymer is preferred because it exhibits properties suitable for carrying DNA into cells. PEI comes in a branched and linear form and contains numerous primary, secondary, and tertiary amines on its surface which gives it its cationic property. The high density of terminal amine groups on the PEI contributes to DNA attachment as they interact with the negatively charged phosphate backbone of the nucleic acid to form ionic bonds (Park et al., 2006; Reddy et al., 2012).

DNA attached to PEI also condenses onto the polyplex, therefore the DNA takes up little space, allowing for an increased amount of DNA that can be bound onto PEI. The condensation effect also does not increase the size of the PEI carrier, therefore the uptake of DNA-PEI complex into cells is not affected by a change in size. Besides that, the unprotonated amines in a cell create a proton sponge effect(Boussif et al., 1995; Behr, 1997), which is useful in delivering exogenic material as this effect helps the DNA-PEI carrier escape endosomal entrapment. This mechanism works by the strong buffering capacity of the amine groups on PEI which recruits H^+ ions to protonate the amines and subsequently the influx of Cl^- counter ions into the vesicle. The high osmotic pressure in the endosome causes an influx of water which eventually causes swelling and endosomal lysis (Fig. 1.4). These properties of PEI make it a suitable polymer for coating onto MNPs and for delivering nucleic acids into cells.

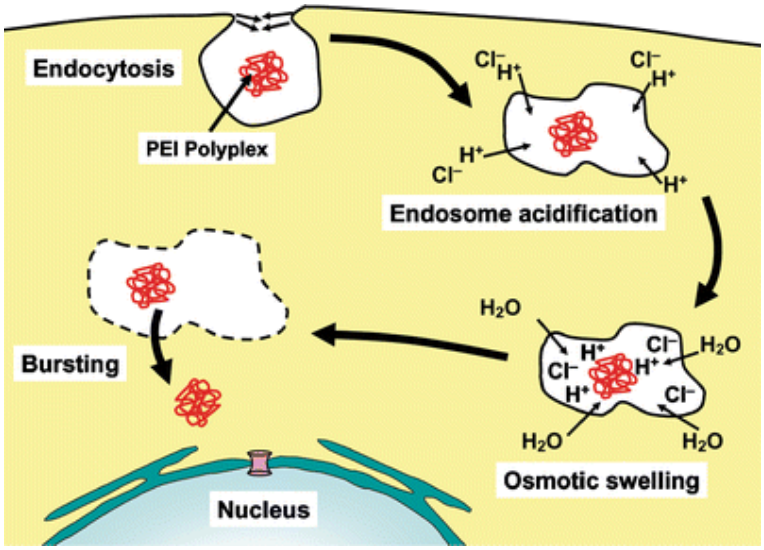

Figure 1.4 Illustration of the proton sponge effect by the buffering capacity of PEI to cause endosomal lysis (El-sayed et al., 2009). Reprinted with permission from Springer publishing group [license number: 4175951318193].

The disadvantage of using PEI is that it confers a toxic effect on cells at high density and with increased branching (Park et al., 2006). The effect of increased toxicity to cells can be seen with increasing concentrations of DNA-MNP complexes used for transfection, which shows a dose-dependent effect (Lim et al., 2012). Other widely used polymeric stabilizers for MNP coating are poly(ethyleneglycol) (PEG), poly(vinyl alcohol) (PVA), chitosan, and dextran, to name a few.

Organic molecules and surfactants such as alkyl phosphonates and phosphates containing a double bond kink are useful for stabilizing MNPs in non-aqueous solvents such as hexane and toluene. Another advantage of having surfactants on MNPs is that the double bond on the tail can be oxidized to form carboxylic functional groups. This configuration will render MNPs unstable in organic solvents but stable in aqueous solutions which is suitable for biomedical applications. Coating iron oxide magnetic particles with a metallic material such as gold or inorganic material like silica are also being investigated especially for applications *in vivo* (Zhang et al., 2017; Mehravi et al., 2017; Chen et al., 2017).

When determining a suitable coating for MNPs for applications in cellular and biomedical studies, the cytotoxicity of surface-coated magnetic nanoparticles has to be assessed to determine its effect on cell and tissue morphology and mortality. For studies in gene delivery, ideally, a cell should retain good metabolic activity, proliferation, cellular phenotype, and viability after transfection (Mahmoudi et al., 2012; Reddy et al., 2012). With a suitable coating, the MNPs can be biocompatible and thus cell viability is not severely reduced after transfection.

Although PEI exhibits excellent properties for gene delivery and has higher transfection efficiency compared to other cationic polymers, it has been shown to be toxic to cells in high concentrations (Ang et al., 2011). Therefore, PEI alone as a nucleic acid carrier is not suitable as it confers high cytotoxicity in cells. With the use of magnetic nanoparticles coated with PEI, the carrier dosage can be lowered as magnetically-targeted delivery increases interaction between the cells and DNA-MNP complex whereby MNPs carrying the gene of interest are pulled towards the cells by external magnets, thus improving chances for internalizaiton into cells. PEI-coated MNPs have the added advantage of PEI to improve transfection efficiency by improving internalization into the cell due to its positive surface charge and the ability to escape endolysosomal degradation in the endocytic pathway.

1.5 Application of MNPs in biomedicine

There is an abundance of applications of magnetic material, especially in the biomedical discipline. The ease of manipulation of magnetic particles and fibres makes it an attractive material to work with, especially for *in vivo* applications, as researchers are seeking methods to improve diagnosis and treatment in a non-invasive fashion. Applications include the use of MNPs as contrast agents for magnetic resonance imaging (MRI), for drug and gene delivery, magnetic separation of cells, and local application of hyperthermia (Xing et al., 2014; Park et al., 2017b; Hsiao et al., 2017; Céspedes et al., 2014; Carrey et al., 2011; Pankhurst et al., 2003).

Iron oxide nanoparticles are made from oxidized iron, in the form of magnetite Fe_3O_4 or maghemite Fe_2O_3. Although there are other ferromagnets that can be used to synthesize magnetic nanoparticles, such as cobalt and nickel, iron is the preferred metal for use in mammalian tissue studies because iron exists naturally in the human body (Ke et al., 2015; Baynes et al., 1994; Weir et al., 1984). The human body has approximately 4 grams of iron and is present in haemoglobin and myoglobin for gaseous transport, as well as ferritin and transferrin for the storage and transport of iron in the body (Walczyk and von Blanckenburg, 2005). Therefore the breakdown of iron oxide nanoparticles in the body will result in the least toxicity and the incorporation of iron into the body for functional purposes (Zhang et al., 2017; Jain et al., 2008).

Application in biomedicine requires MNPs to have certain characteristics. Particles are usually required to exhibit superparamagnetic properties; therefore the particles are usually in the range of 3 – 20 nm. Their superparamagnetic property gives particles high magnetic susceptibility and they are able to be magnetized using a permanent magnet and electromagnet, as well as exhibit a loss in magnetization once the external magnetic field is removed (Reddy et al., 2012). Superparamagnetic behaviour is favoured as MNP aggregation is reduced once the external magnetic field is removed which prevents complications *in vivo* such as the formation of emboli in blood capillaries (Arruebo et al., 2007). Particle hydrodynamic diameters, that is, the diameter of the magnetite core and its surface coating, ranging from 10 – 100 nm is also favourable as they have longer circulation time in the blood and can prolong reticuloendothelial system (RES) clearance from the body (Decuzzi et al., 2006).

Aside from application in transfection, MNPs in biomedicine have been extensively investigated for cancer diagnosis and therapy. The development of functionalized MNPs for photothermal cancer therapy using a low-density laser were used to ablate cancer cells and tumour tissues, as well as act as a contrast agent for MRI and thermal imaging (Du et al., 2017). Du et al. also developed a novel imaging technique, where the synthesis of zinc oxide and iron oxide MNPs in cancer cells occurred when mice were injected with Zn^{2+} and Fe^{3+} metal ions, which were used for imaging (Du et al., 2017). The tuning of MNP properties were studied for appllications in MRI and hyperthermia (Byrne et al., 2014; Céspedes et al., 2014). Other MNP-induced cancer theranostics include microwave therapy (Peng et al., 2017) and cancer-targeting MNPs for imaging and drug delivery (Hsiao et al., 2017). Raju et al. prepared MNPs for biosensing to detect and scavenge aluminium ions *in vivo* (Raju et al., 2017) and Park et al. delivered genes to stem cells using MNPs and directed cellular migration by application of an external magnetic field (Park et al., 2017b). With the current emergence of antibiotic-resistant superbugs, functionalized MNPs were studied as a non-antibiotic treatment to induce bacterial death at infected tissue sites using hyperthermia (Raval et al., 2017). Nanomagnetic transfection is also being explored for future use in *in vivo* clinical trials in spinal injuries (Delaney et al., 2017).

The successful breakthrough of MNPs in biomedicine mainly stems from their high functionality and multi-modality for gene and drug delivery, hyperthermia, biosensing, molecule and nucleic acid scavenging, and imaging, to name a few. The various characteristics of MNPs have been explored to perform a wide scope of applications for diagnosis and therapy. Most MNP applications in diagnostics and therapy fail to reach the clinical trials stage due to a lack of understanding of MNP biodistribution, fate, and toxicity in the body. However this gap in knowledge is being filled by current studies in this field.

1.6 Nanomagnetic Transfection

The term magnetofection was coined by Scherer et al., who developed the method for magnetically-enhanced gene delivery into cells (Scherer et al., 2002). Prior to that study, the first paper published on magnet-assisted gene delivery was by Hughes and colleagues who studied streptavidin-coated paramagnetic particles attached to retroviral vectors to improve viral infection in cells (Hughes et al., 2001).

The principle of nanomagnetic transfection is the non-viral delivery of genes into a cell using magnetic particles complexed with DNA and a magnetic field to attract the magnetic particle complex onto the surface of the cell (Ang et al., 2011; Plank et al., 2011). The MNPs are pulled down towards cells which increases cell surface-to-particle interaction, unlike non-specific interaction of contemporary chemical transfection methods. As a consequence, active targeting improves transfection parameters such as reducing transfection time by a few hours and lowering the dosage of transfection reagent (Scherer et al., 2002) which improves cell viability while increasing the efficiency of gene delivery. External magnetic fields from permanent magnets are being studied for nanomagnetic transfection. An important factor for increasing sedimentation of the particles/DNA onto adherent cells are magnetic gradients. A high magnetic gradient exerts a vector force (in magnitude and direction) on MNPs towards the permanent magnets and increases the rate of transfection (Dobson, 2006).

One reason for good cell viability achieved using nanomagnetic transfection is because cells take up the DNA-MNP complex via endocytosis, which is a natural cellular process. Transfection using MNPs and other non-viral methods follow an energy dependent pathway and therefore use the natural entry mechanism into cells (Lim et al., 2012). After internalization into the cell, MNP complexes that are able to escape endosomal lysis and cytoplasmic nucleases are then able to travel to the nucleus of the cell. The DNA is either dissociated from the MNP in the cytoplasm or the MNP complex travels into the nucleus through the nuclear pore before the DNA is released. Another method of entry into the nucleus is during cell division, when there is absence of a nuclear membrane (Luo and Saltzman, 2000).

1.6.1 Endocytosis

Endocytosis is a process which allows the interaction of a cell with its external environment. Endocytosis describes the production of cellular vesicles from the plasma membrane lipid bilayer, whereby extracellular fluid and matter become encapsulated and internalized into the cell (Doherty and McMahon, 2009). Conversely, the expulsion of material from the cell into the extracellular environment is the process of exocytosis, with the reverse mechanism of fusing vesicles to the lipid bilayer, also contributing to the expansion of the cell membrane. Internalization of material into the cell can occur passively, which is fluid phase endocytosis, or it can occur by the interaction of a material with the cell membrane receptors which activates internalization (Vercauteren et al., 2012). Endocytosis can be classified into two distinct groups, that is, phagocytosis and pinocytosis. The latter is sub-classified into macropinocytosis, clathrin-dependent endocytosis (CDE) and clathrin-independent endocytosis (CIE) (Mayor and Pagano, 2007; Vercauteren et al., 2012) based on certain characteristics, such as vesicle formation, cargo size, interaction with proteins and receptors, and endosome trafficking in the cell (Lerch et al., 2013).

The most extensively studied endocytic process is the clathrin-dependent pathway. Clathrin-mediated vesicles with an average size of 100 to 150 nm are identified by the formation of a lattice-like structures made of clathrin proteins around the vesicle. The presence of dynamin, a large GTPase which functions in the pinching-off of the clathrin invagination to form a vesicle, is also characteristic of this pathway (Gillard et al., 2014; Lerch et al., 2013; Mayor and Pagano,

2007; McMahon and Boucrot, 2011).

Caveolae-mediated pathways are characterized by the formation of 50 – 80 nm flask-like invaginations, and the vesicles are lined with caveolin, glycosphingolipids, and cholesterol, known as lipid rafts. This pathway is reported to be dependent on dynamin, actin, Rab5 and Src kinases. (Gillard et al., 2014; Mayor and Pagano, 2007; Vercauteren et al., 2012). Macropinosomes can be identified by the formation of actin-ruffles and protrusions of the membrane to engulf matter into the cell, where the actin cytoskeleton is regulated by the p21-activated kinase (PAK1). Vesicles that form are typically 1 μm, but not exceeding 10 μm. (Gillard et al., 2014; Lerch et al., 2013; Vercauteren et al., 2012).

Other, clathrin-independent pathways are the flotillin- mediated endocytosis, clathrin-independent carriers (CLIC) and glycosylphosphatidylinositol (GPI)-enriched compartments (GEEC) endocytosis which are mediated by small G-proteins CDC42, Arf6, and RhoA- dependent endocytosis (Doherty and McMahon, 2009; Mayor and Pagano, 2007). A new mechanism has also been proposed recently, describing an excavator shovel mechanism, which is similar to macropinocytosis as it is formed in the presence of actin and dynamin (Lerch et al., 2013).

Uptake of MNPs for transfection occurs as an endocytic process. This was shown by Lim et al. (2012) whereby the transfection efficiency was negatively affected in the presence of endocytic inhibitors. As cells could not carry out endocytosis, MNP-DNA complexes were unable to enter cells and gene delivery was prevented. Studies to elucidate the endocytic pathways of MNP complex internalization have shown two prevailing types; clathrin-mediated and caveolae-mediated endocytosis. To study this, the ligands folate and transferrin were complexed to the particles to target caveolar and clathrin mediated pathways, respectively. Drugs were also used to inhibit caveolar or clathrin pathways.

To improve efficiency of gene delivery, the transfection agent, since it is a non-viral delivery method, has to be able to escape endolysosomal degradation in the cytoplasm of the cell. It was shown that the pH of endosomes were dependent on the pathway that particles followed. Caveolar-mediated endocytosis had endosomes with the pH of 5.5 whereas clathrin-targeted and untargeted complexes had a lower pH value. The caveolar pathway suggests more efficient transfection of cells as the MNPs were trafficked to lysosomes at a slower rate (Gabrielson and Pack, 2009). Furthermore, the attachment of complexes onto the plasma membrane is not random. The particles interact with specific sites on the membrane before internalization (Godbey et al., 1999b). Sauer et al. studied the mechanism of internalizing and intracellular trafficking of magnetic lipoplexes and polyplexes (Sauer et al., 2009). They showed that the particles associate with heparan sulfate proteoglycans (HSPGs) on the cell membrane for internalization, and movement of the particles in the cell occurs through active transport using actin and microtubules.

One method to improve endosomal escape in cells is the use of polyamines in the synthesis of MNPs for transfection (Sonawane et al., 2003). PEI is one such polyplex that is able to escape lysis due to its terminal amines. The proposed mechanism for the escape of nanoparticle complex from being digested by lysosomes is the proton sponge effect. This involves unprotonated amine groups, as well as the primary, secondary, and tertiary amines with different pKa values which allow PEI to act as a buffer by absorbing protons into the endosome, thus increasing the protons being pumped into the vesicle. This causes an influx of Cl^- ions and osmolytic swelling from an influx of water to counter the osmotic pressure in the vesicle. Eventually the vesicle ruptures and the nanoparticle complex is released into the cytoplasm (Benjaminsen et al., 2013; Canton and Battaglia, 2012; Sonawane et al., 2003). Sonawane and colleagues (Sonawane et al., 2003) studied this effect using PEI and polyamidoamine (PAM), which have high proton buffering capacity, and polylysine (POL) as a polyamine with no buffering ability. They found that the endosomal escape of PEI and PAM polyplexes were due to the proton sponge effect, where at 30 – 75 minutes from transfection the endosomes were lysed or leaking from osmotic swelling of the proton-sponge effect. However, contrasting evidence to this proposed mechanism has also been reported where no change in lysososmal pH was detected (Benjaminsen et al., 2013; Godbey

et al., 2000).

1.6.2 Oscillating external magnets

The use of oscillating magnetic arrays has been studied extensively for enhancing gene delivery. This method has been an alternative to other non-viral transfection techniques because it has potential to increase transfection efficiency, reduce transfection time, improve cell viability, and deliver genes to cells that are difficult to transfect (Dobson, 2006; Subramanian et al., 2013). Nanomagnetic transfection using an oscillating system was developed by the Dobson group (McBain et al., 2008a), where the lateral movement of neodymium iron boron (NdFeB) magnets significantly improved transfection of cells *in vitro* at an oscillation frequency of 2 Hz and amplitude of 0.2 mm. The lateral oscillation coupled with magnetic fields has shown to not affect the viability of cells. This method not only improved transfection efficiencies compared to conventional methods, it also decreased transfection time to 6 times lower than with the Lipofectamine2000 reagent (Fouriki and Dobson, 2013; McBain et al., 2008a). This oscillating system, known as the magnefect-nano has been commercialized and sold by nanoTherics (Chapter 2.6) (www.nanotherics.com). A study by Lim et al. (2012) to determine nanomagentic transfection using oscillating systems for gene silencing showed that it was able to silence GFP at lower concentrations of siRNA as well as maintain good cell viability compared to nucleofection and lipofection methods. Similarly, Pickard and Chari observed increased transfection of astrocytes with the oscillating magnet compared to a static magnet, suggesting that the oscillating movement improves endocytosis and intracellular processing (Pickard and Chari, 2010b).

Other dynamic magnetic systems had also been developed to generate higher transfections efficiencies such as the orbiting magnetic array on one plane by Karpov et. al (Karpov et al., 2014). This system promotes the even distribution of magnetic particles on the surface of well plates and increased particle-cell contact. The magnetic force bioreactor developed by Dobson and El Haj uses a vertical oscillating magnetic array which produces a translational force along the magnetic gradient vector (Chapter 2.6) (Dobson et al., 2002). This bioreactor is mainly used for ion channel activation, where MNPs are attached to ion channels on the cell membrane and an oscillating magnetic force generates mechanical tension and movement which activates the membrane channels (Dobson et al., 2002; Dobson, 2006; Markides et al., 2012). This system had been commercialised and is sold through the company MICA.

Dynamic magnetic fields have also been developed, such as the Dynamic Marker from Stetter Elektronik which uses an alternating electromagnetic current generated by coils at the x- and y- plane to induce MNP oscillation which enhanced nanomagnetic transfection (Kamau et al., 2006). A similar AC dynamic magnetic field was developed to control the rotation of MNPs which increased cellular uptake of the particles (Zhang et al., 2014a).

1.7 Improving transfection efficiency

When a DNA-complex is introduced into a cell, it has to avoid many intracellular processes as it traverses the cytosol into the nucleus. In terms of nanomagnetic gene transfection, the first barrier that the MNP-DNA complex has to overcome is the cell membrane where it has to penetrate the membrane bilayer by enhancing internalization into cells through endocytosis. Cells which are terminally differentiated, stem cells, and primary cells are usually difficult to penetrate. Besides that, the DNA has to be protected from intracellular nucleases which may otherwise result in DNA degradation and failure in transcription (Luo and Saltzman, 2000). To reduce the activity of nucleases on DNA, endosomal trafficking is important as it shortens the distance that the complex has to travel to the nucleus, provided the complex is able to escape lysosomal degradation. Endosomal trafficking of the complex after internalization usually involves acidification and fusion to lysosomes to degrade the DNA. The DNA must also be able to decondense from the surface of the MNP to enter the nucleus (Li and Huang, 2006; Sauer et al., 2009).

The delivery of DNA from the cytoplasm to the nucleus is thought to occur by diffusion, and therefore is a relatively slow process (Luo and Saltzman, 2000). Therefore the amount of DNA delivered into the cell has to be sufficient to aid this process, taking into account the DNA-MNP complex that does not escape lysosomal degradation and nuclease activity. To increase the chances of DNA locating and moving towards the nucleus, nuclear localization sequences (NLSs) can be added into the plasmid (Luo and Saltzman, 2000).

Methods to further improve nanomagnetic gene transfection are being developed. Scherer and colleagues demonstrated that magnetic transfection using commercially available MNP-PEI, combined with the use of retroviral vectors, was able to generate a 20-fold transduction efficiency increase relative to only viral transduction (Scherer et al., 2002). Activity of peptides or aptamers for cell targeting and intracellular delivery can also be affected by steric hindrance due to limited exposure. The length of a cell-targeting biomolecule has to be long enough to be able to interact with cell membranes.

1.8 AC Susceptometry

Magnetic nanoparticles possess the advantage that they can be characterized magnetically in addition to conventional NP characterization techniques to obtain more information regarding the MNPs. Magnetometry is a technique used to measure the magnetic properties and behaviour of materials. Specifically, the technique employed in this study is AC susceptometry which measures the magnetic susceptibilty of magnetic material when an external oscillating magnetic field is applied. The AC susceptometer was built in-house and can measure from frequencies of 10 Hz up to 1 MHz. The output generated from sample measurement provides information about the real and imaginary susceptibility curves, as well as the volume susceptibility given by the real and imaginary components which corresponds to the amount of magnetic material in the system. ACS measurements can also detemine the relaxation properties of MNPs, which are either Brownian or Néel relaxation.

Analogous to AC electronics, the AC magnetic susceptibility (ACS) signal is measured as

$$\tilde{\chi} = \chi' - i\chi'' \tag{1.4}$$

where the real part, χ', represents the susceptibility component of the particles that is in-phase with the applied AC magnetic field, and the imaginary part, χ", is the corresponding out-of-phase component. The relative proportion of the two components thus reveals the phase lag between the magnetisation of the particles and the applied AC field, with the case where χ' and χ" are equal indicating a 45 degree phase angle.

ACS measurements are important for observing magnetisation relaxation in MNP suspensions. This is the process in which the initial magnetic alignment of the particles induced by the external magnetic field is lost over a corresponding *relaxation time*, τ. For particles which are magnetically blocked (i.e. remain magnetised during an AC field cycle) relaxation is caused by the physical re-orientation of the particles due to collisions with molecules in the suspension media (Brownian motion). Therefore the corresponding Brownian relaxation time is given by

$$\tau_B = \frac{\pi \eta {D_H}^3}{2\kappa_B T} \tag{1.5}$$

where η is the dynamic viscosity of the fluid, κ_B is the Boltzmann constant and T is the absolute temperature. Thus if all other parameters remain fixed, enlarging the hydrodynamic size D_H of the particles will increase the Brownian relaxation time.

Both the magnitude and the phase angle of the AC susceptibility depend on the product ($\omega\tau$) of the angular frequency of the AC field, ω, and the relaxation time, τ (Carrey et al., 2011).

However, whilst the phase angle gets larger as the frequency of the magnetic field increases, the corresponding magnitude of the susceptibility decreases. In fact it can be shown that a maximum value of the out-of-phase component (χ") is reached when $\omega\tau = 1$. For blocked particles this happens when the Brownian relaxation time is equal to the rotational cycle time of the applied field. This is shown as a peak in the χ" susceptibility component when the frequency is swept. For larger hydrodynamic sizes, the correspondingly longer Brownian relaxation time will shift this peak to lower field frequency, as shown schematically in Figure 1.5. Thus ACS measurements as a function of field frequency enable determination of the Brownian relaxation time and subsequently the hydrodynamic size of the particles using equation 1.5 above.

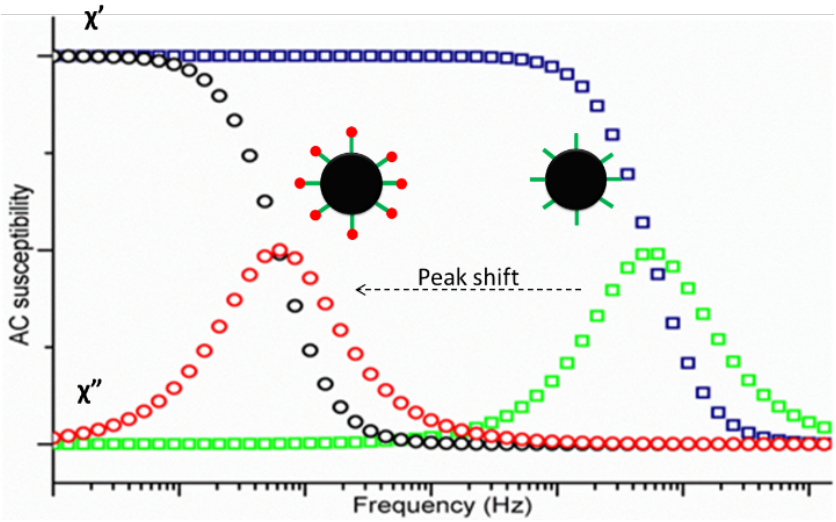

Figure 1.5 Schematic showing the AC susceptibility versus frequency curve expected for blocked magnetic nanoparticles displaying Brownian relaxation. Particles with small hydrodynamic sizes show a peak in the curve at high frequencies (green curve), whilst an increase in hydrodynamic size creates a shift of this peak to lower frequencies (red curve).

MNPs that exhibit Néel relaxation are caused by internal single magnetic domains that rotate and depends on the magnetic particle volume, the magnetic anisotropy property and the temperature of the system. However it does not depend on hydrodynamic properties as it does not exhibit physical rotation and so is insensitive to local environmental factors such as viscosity. The Néel relaxation time is given by the equation

$$\tau_N = \tau_0 e \frac{KV}{\kappa_B T} \tag{1.6}$$

1.9 Raman spectroscopy and SERS

The use of various analytical techniques in research are advantageous as they allow one to build a more complete description of chemical and biological processes, as each technique is sensitive to different parts of the process. In the biological sciences, optical microscopes are highly favoured as instruments to probe cell and tissue processes due to their high sensitivity and ability to visualize live processes in stained and unstained samples down to the nanometer scale. Recent breakthroughs in optical microscopy have produced microscopes that overcome the diffraction limit, such as dSTORM, PALM, SIM, and TIRF. Similarly Raman spectroscopy is one such technique that has been developed to improve sensitivity and multi-modality and has become a complementary technique to optical microscopy as it provides information about the sample on a molecular scale. Raman spectroscopy can provide vibrational spectra identifying functional groups, type of molecular bonds and conformations (Movasaghi et al., 2007).

The Raman effect was discovered by C.V. Raman in 1928 (American Chemical Society International Historic Chemical Landmarks, 1998). Raman spectroscopy is a vibrational spectroscopic

technique which measures the inelastic light scattering from molecules and uses a monochromatic light source. Photons from the light beam bombards the sample and two scattering types occur – Rayleigh and Raman scattering. Rayleigh scattering is an elastic scattering where the energy of the incident photon remains unchanged after sample interaction. Raman scattering however creates a lower or higher energy scattered photon to the incident photon after sample bombardment, referred to as the Stokes and anti-Stokes scattering respectively (Figure 1.6). The disadvantage of detecting Raman scattering in the presence of Rayleigh scattering is the very low intensity of the signal, of around 10^{-6} to 10^{-9} compared to Rayleigh scattering (Moreira et al., 2008). Therefore a sensitive detector is required for signal collection, as well as filters to absorb or deflect Rayleigh scattering (Figure 1.7).

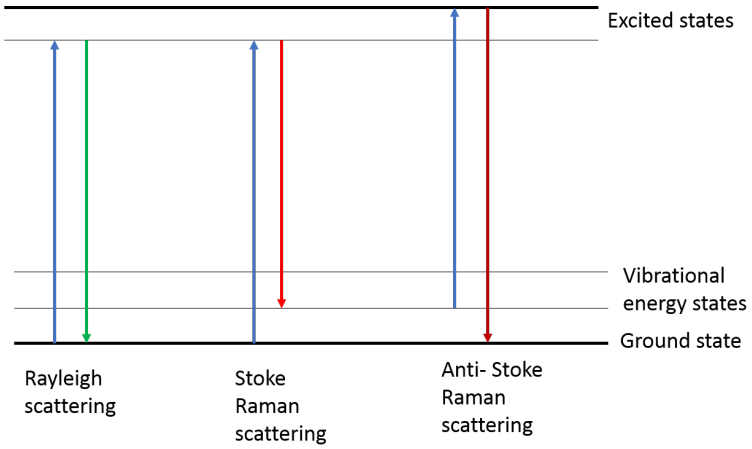

Figure 1.6 Jablonski diagram of light scattering which forms the basis of Raman spectroscopy. Incident photons interacting with molecules form either Rayleigh or Raman scattering. Rayleigh scattering has unchanged photon energy (left), whereas Raman scattering has loss or gain of photon energy (middle and right) (Yadav and Singh, 2015). Adapted with permission from Royal Society of Chemistry publishing group [license number: 4153111140021].

Raman spectroscopy has gained ground recently in the field of biological sciences due to its various advantages compared to diffraction limited optical and fluorescence microscopy, as well as biological assays that require sample processing and labelling. These advantages are that Raman spectroscopy is known to have high specificity in detecting biomolecules. Biological samples rarely require pre-processing and live cell spectrometry can even be performed without sample damage. More importantly, samples are analysed without the need for labelling or contrast-enhancing agents, which maintains biological samples in their native state.

The disadvantage of Raman spectroscopy is its low sensitivity due to the infrequent occurrence of Raman scattering compared to the common Rayleigh scattering (Butler et al., 2016). The development of Raman spectroscopy has led to better signal detection and generation of a stronger signal from molecules using surface-enhanced Raman spectroscopy (SERS), providing improved Raman analysis such as single-molecule Raman spectroscopy (Wang et al., 2013).

The Journal of Raman Spectroscopy saw around 370 papers published in 2 consecutive years alone in 2015 and 2016, suggesting it is a well-used characterization method. A review by W. Kiefer summarizing the applications of Raman spectroscopy in this journal, from art and archeology to biosciences and materials (Kiefer, 2007) which explains the versatility of this technique in various applications. The review defines the breadth of Raman spectroscopy applications and is development in the different sciences. Although Raman spectroscopy had been established for more than 70 years, it is only recently that this technique was utilized in biomedicine and cell biology. This development was mainly attributed to the advances in surface-enhanced Raman Spectroscopy (SERS).

SERS works to increase the intensity of the Raman scattering using surface plasmons. The

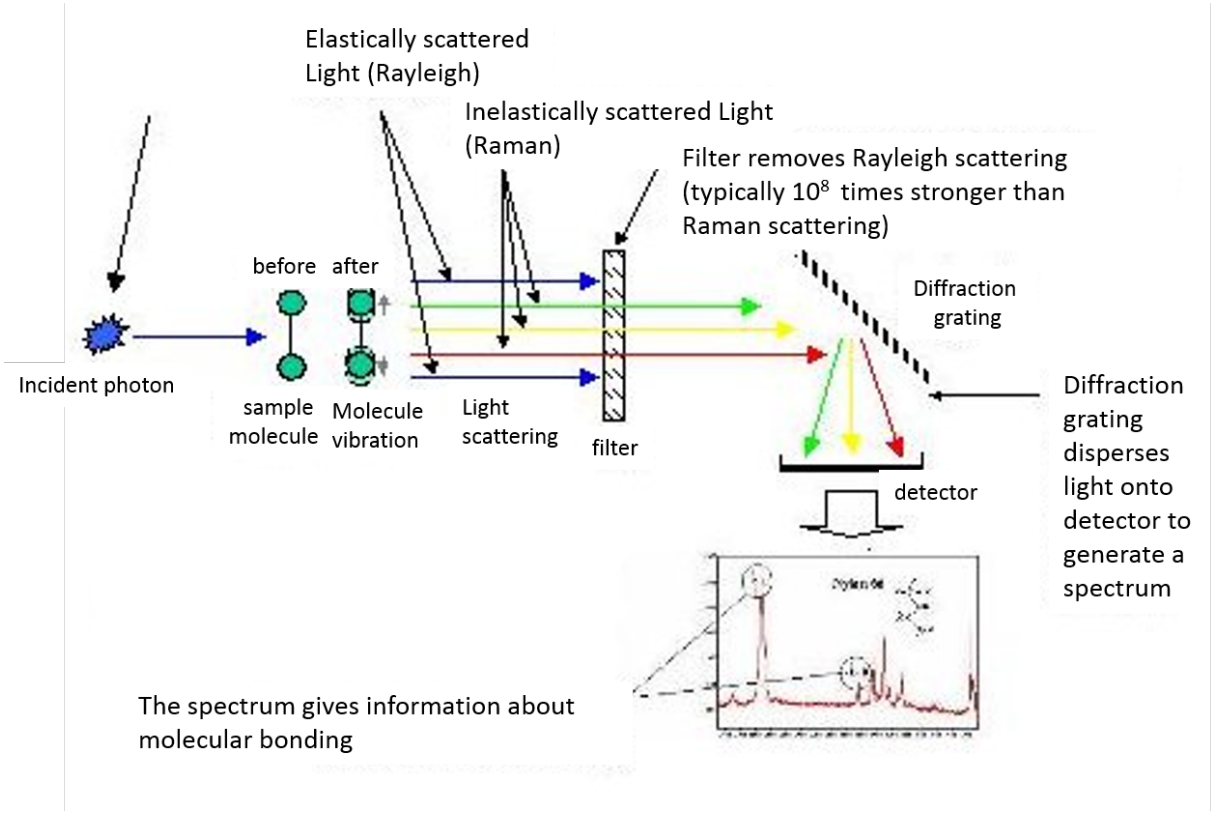

Figure 1.7 Principle of Raman spectrometer showing light scattering. Incident photons are bombarded at sample molecules which produce Rayleigh and Raman scattering. Rayleigh scattering is blocked by filters and Raman scattering is detected to form a Raman spectrum. Adapted from www.exeter.com (University of Exeter, 2017)

SERS effect can be produced using gold or silver nanoparticles, or the deposition of a sample on a rough gold or silver surface. Electromagnetic waves that interact with surface plasmons excite these plasmons which then amplifies the Raman signal to a million-fold or more, known as the electromagnetic enhancement (Browne and McGarvey, 2007; Stiles et al., 2008). The SERS technique has enhanced the use of Raman spectroscopy in biomedicine and in single-molecule spectroscopy.

Raman spectroscopy has been demonstrated in various biological applications, and due to their wide-spread interest in many research groups, protocols have been developed to guide users in the use of this technique for cell and tissue biology (Butler et al., 2016; Votteler et al., 2012). Base-level studies of the identification of biological molecules and organelles in cells and tissues have been evaluated to obtain a Raman spectra database of biological information (Moreira et al., 2008), used as reference in spectral identification. Basic methods to differentiate between live and dead cells have also been studied, which are useful for studying cell populations without the need for staining and sample destruction (Boyd et al., 2010). Single-molecule detection in cells, such as the cytochrome c has been observed during mitochondrial redox states and is associated with apoptosis (Okada et al., 2012).

Raman spectroscopy is also being used for the development of diagnostics, where molecular changes in diseased tissue can be identified. Recent advances in medical diagnostics involve cancer detection such as lung cancer detection using exosomes as a marker (Park et al., 2017a), detection of metastatic cancer in breast and colon cancer tissue (Shashni et al., 2017), and differentiating between cancer and healthy tissue using a nucleus-cytoplasm differential spectra (Liu et al., 2017) or fingerprint peaks (Holler et al., 2017). Besides cancer, SERS has been studied to detect bacterial infection in prosthetic joints (Fargašová et al., 2017). Due to its non-invasive technique, Raman spectroscopy is a promising tool for disease diagnosis and theranostics.

In Chapter 5, Raman spectroscopy is used to probe MNP localization in HeLa cells. Identification of characteristic spectra of MNP, PEI and MNP-PEI was determined, and cells with internalized MNP-PEI were measured using an area scan to locate the particles in the intracellular matrix. SERS was also studied to determine its effectiveness in refining the Raman spectra of MNP samples.

1.10 Conclusion

Magnetic nanoparticles remain a carrier that has potential in improving the limited gene delivery technique using nanomagnetic transfection. This area of research has room for significant improvement; by studying and modifying the types and synthesis of MNPs, the types of coating used on MNPs for DNA adsorption and internalization into the cell, elucidating and improving the methods to escape endosomal degradation, use of AC and DC fields, and functionalization of particles with cell targeting biomolecules. By developing this technology and overcoming limitations in transfection techniques such as adherent cell transfection, transient transfection and cytotoxicity, gene delivery techniques could be extrapolated to biomedical applications for diagnosis and treatment.

1.11 Objectives of the project

The main aim of this project is to develop magnetic nanoparticles as a non-viral gene delivery vector, in order to improve the efficiency of non-viral transfection vectors, thus providing a viable alternative to viral vectors. Firstly, a commercial nanomagnetic transfection reagent will be used, which is the nTMag from nanoTherics to transfect cells and compare their transfection efficiency to laboratory synthesized MNPs coated with PEI (tdMNP-PEI). The well characterized tdMNP-PEI will then be used to investigate the mechanism of nanomagnetic transfection by observing their movement and localization in the cell using various techniques. Finally, the effect of MNP-PEI internalization on cell responses and changes in cellular processes was explored with regard to cell adhesion.

1.11.1 Objective 1: Synthesis, preparation, and characterization of PEI-coated MNPs for transfection

To obtain stable, aqueous dispersed MNPs with a narrow size distribution, the thermal decomposition method will be used to synthesize magnetite iron oxide MNPs and oxidized. To obtain stably coated cationic MNPs for transfection, the particles will be coated with positively charged PEI for surface stabilization and to confer transfection functionality. To determine the ratio of tdMNP to PEI coating without excess PEI , the particles will be characterized with gradual low concentration loading of PEI into an MNP suspension. The coating mechanism of PEI on MNP and clustering behaviour of MNPs with PEI loading will be studied using AC susceptometry and other techniques. The techniques for size determination and changes in MNP clustering and coating will be compared between AC susceptometry and dynamic light scattering (DLS) to determine the reliability of AC susceptometry size measurements.

1.11.2 Objective 2: Optimization of transfection parameters using synthesized and commercial MNP

To determine the efficiencey of nanomagnetic transfection, commercial nTMag will be used to transfect HeLa cells and compared to the conventional lipofectamine method. Parameters that affect magnefect-nano transfection efficiency will be identified and nTMag transfection will be optimized to obtain highest transfection efficiency. Synthesized MNPs coated with PEI (tdMNP-PEI)

will also be optimized to obtain highest transfection efficiency without compromising cell viability.

1.11.3 Objective 3: Studying the mechanism of nanomagnetic transfection

To observe the movement of MNP transfection complex in cells from attachment until protein expression, the transfection components in cells will be studied using fluorescence confocal microscopy. To identify the endosomal escape mechanism, changes in the Brownian relaxation after MNPs are internalized in cells will be monitored using AC susceptometry. Finally, Raman spectroscopy will be used to study the localization and movement of MNP-PEI in cells.

1.11.4 Objective 4: Regulation of tdMNP-PEI induced cell focal adhesions and stress fibres

Changes in cellular processes in focal adhesions induced by tdMNP-PEI interaction with MG-63 cells will be determined. To determine the dose-dependency of tdMNP-PEI treatment on cell adhesion, the fluorescence intensity of vinculin expression will be quantified with different tdMNP-PEI doses. Reorientation of actin stress fibres and changes in adhesion-associated gene regulation with tdMNP-PEI interaction with cells will be determined.

Overall, this research has expanded from the main aim of the project to incorporate various other investigations. The studies undertaken in this PhD research has shown the overlap of different disciplines, from a materials chemistry and magnetics scope in the first aim, to the development of research methodology, techniques and instruments in the second and third aim, and finally a heavily cellular biology approach in the fourth aim. Overall, the research presented here is not only useful for future studies in nanomagnetic transfection, but can be translated across other applications involving MNPs and in biomedicine.

Chapter 2

Materials and Methods

2.1 Preparation of water dispersed iron oxide magnetite MNP by thermal decomposition

Iron oxide MNPs were prepared by the thermal decomposition technique, following a method previously described by Park et al. (2004). Synthesis of water dispersed iron oxide MNP takes place in 3 steps, with the preparation of an iron oleate precursor, synthesis by nucleation and growth of MNP, and oxidation of oleic acid.

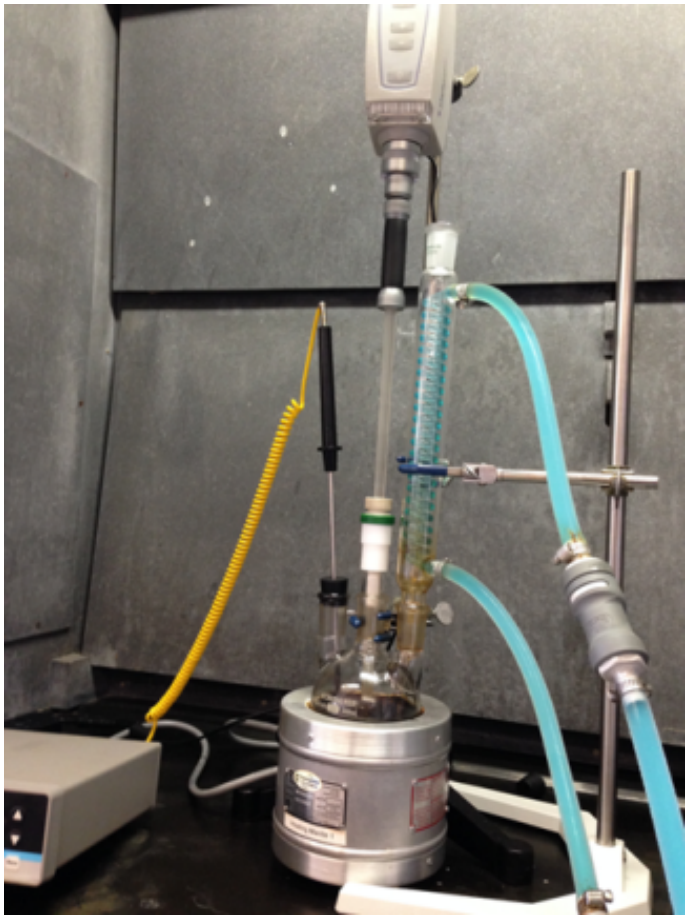

Figure 2.1 Equipment set-up for thermal decomposition.

Preparation of iron oleate precursor

7.5 g of ferrite (III) chloride hexahydrate was weighed and dissolved in 42 mL deionized water. The solution was sonicated until dissolved. The reactor was set up as in Figure 2.1, with a 3-hole glass balloon reactor for the synthesis to take place. 25.5 g of sodium oleate was weighed and

added into the glass balloon and mechanical mixing was turned on to medium intensity. The ferrite solution was decanted gradually into the reaction, along with 100 mL of hexane and 50 mL of ethanol. At this point, the solution turned black. When the mixture became homogenous, the temperature controller was turned on and set to 15 minutes ramp to 67 °C, 4 hours at 67 °C and 10 minutes at 30 °C. The cooler was turned on and the condenser was connected immediately to prevent loss of solvents. Once the procedure ended, two liquid phases were observed, which were the organic ferrite oleate phase (black) floating on top and the inorganic sodium chloride and water phase at the bottom. The organic phase was transferred into an extraction funnel and washed with water. The product was evaporated on a rotary evaporator for 30 minutes and transferred to a glass container. It was stored in an oven at 70 °C and aged for 3 days.

Preparation for MNP synthesis

In the MNP nucleation stage procedure, 130 mL of trioctylamine, 8.5 mg of oleic acid and 23.5 mg of the previously prepared iron oleate precursor were mixed together and sonicated in a 3-hole glass balloon with argon gas feeding into the balloon. The heating mantle procedure was set on the controller to 40 minutes ramp to 335 °C, held at 335 °C for 1 hour, a cooling cycle of 30 minutes at 30 °C and a cycle for 24 hours at 30 °C to allow the MNPs to be left overnight. After the procedure was inputted into the heating controller and the procedure started, the condenser was connected at 280 °C. The argon gas inlet was closed after 10 minutes and the reaction was left to proceed until completion. After the completion of the reaction, magnetic separation was performed to retain synthesized MNP and the product was washed with the same volume of chloroform and twice the volume of acetone. The supernatant was discarded and MNP product was dried at room temperature. The MNP was then suspended in toluene at 10 mg/mL. The MNPs were now oleic acid coated magnetite which were stable in an organic solvent but a final stage was required to obtain an aqueous suspension of MNPs.

Oxidation of MNPs for aqueous phase dispersion

In the third step, carboxylic acid functional groups were introduced to the oleic acid tails of the magnetic nanoparticles by oxidation to facilitate dispersion in water. 100 mg of MNPs were weighed into a 50 mL centrifuge tube and suspended in 10 mL of toluene. The suspension was vortexed to mix and centrifuged for 10 minutes at 1900 g at room temperature. The supernatant was retained and precipitate discarded. The MNP solution was then sonicated using an ultrasonicator for 20 minutes to disperse the particles. During sonication, 8 mL of prepared ethylacetate:acetonitrile (1:1 ratio) and 6 mL of 0.28 M sodium periodate dissolved in water was added into the suspension. At the end of the sonication, the reaction contained an organic and inorganic phase. The solution was centrifuged at 8000 g for 10 minutes. The supernatant was magnetically decanted and the remaining MNP in the tube was washed with hexane and subsequently ethanol. The precipitate was washed lightly with deionized water to remove traces of solvents and air dried at room temperature. The MNPs were dried and resuspended in 10 mL of deionized water with ultrasonication for 2 hours to disperse particle clusters. The resulting particles formed a stable aqueous suspension (Figure 2.2).

2.2 PEI coating of MNP suspension

Polyethyleneimine (PEI) purchased from Sigma Aldrich is a 25 kDa MW heterogenous branched cationic polymer with amine functional groups.

PEI was diluted in water at a concentration of 1 mg/mL and the pH was adjusted to 7 before storing at 4 °C. Two coating methods of PEI were performed on MNP, where one was the covalent binding of PEI on MNP using carboiimide crosslinkers, and the second method was the auto assembly of MNP and PEI by ionic interaction based on the negative and positive

Figure 2.2 Final product of MNP synthesized by thermal decomposition and suspended in water.

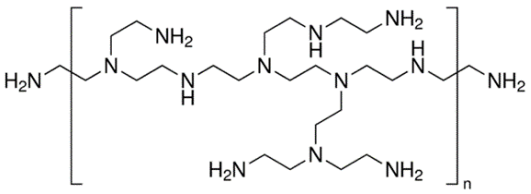

Figure 2.3 Chemical structure of PEI.

charges of MNP and PEI respectively. Detailed methods of PEI coating are described in Chapter 3.

2.3 Citric acid coating of MNP

25 mg maghemite or 20 mg magnetite dry powder was weighed and 1 mL distilled water added to form a suspension. The pH of the suspension was set to 2 and sonicated for 2 minutes. 15 mg citric acid per mL suspension was added and pH changed to 5.2. The suspension was heated to 70 °C for 10 minutes and sonicated in the water bath for 2 minutes for a total of 3 cycles. The unreacted citric acid was removed by magnetic decantation and washed with acetone 3 times. The citric acid coated MNPs were resuspended in distilled water >pH 9. Unstable MNPs were removed by placing a magnet under the tube which attracted the unstable MNPs to form a precipitate and the stable suspension was collected by decanting the suspension into a new tube.

2.4 Iron quantification assays

Prussian blue staining

Adherent cells were washed with PBS once and fixed with 95% methanol for 15 minutes at room temperature. The fixative was removed and cells washed with distilled water. Equal volumes of 20% aqueous hydrochloric acid (v/v) and 10% aqueous solution of potassium ferrocyanide (w/v) was prepared fresh and added to cells for 20 minutes at room temperature. The staining solution was removed and washed with distilled water. Cells were counterstained with Neutral Red solution for 5 minutes at room temperature and washed with distilled water. The samples were imaged under a brightfield microscope.

Ferrozine assay for iron quantification

200 μL of MNP suspension was prepared and 100 μL 6M nitric acid was added to it. The samples were incubated overnight at 70 °C. 150 μL of this digested sample was treated with equal amounts of 6.6 M hydroxylamine hydrochloride and incubated at room temperature for 2.5 hours. 100 μL of the reduced sample was treated with 700 μL of 2 mM Ferrozine reagent (0.1 g of 3-(2-pyridyl)-5,6-diphenyl-1,2,4-triazine-,p'-disulfonic acid monosodium salt hydrate + 5 mL HEPES buffer made up to a final volume of 100 mL with distilled water) and incubated for 1 hour. Absorbance was read at 562 nm in a plate reader.

Cell with MNP samples containing low iron content were pooled (3 wells of a 24 well plate) into a tube by digesting the cell samples in the wells with nitric acid overnight in the incubator and collecting the suspension into a tube. The digestion and reduction step was followed by evaporation to maintain detectable amounts of iron for the absorbance measurement.

2.5 Cell culture

Cell culture media

For all cell culture experiments, identical culture media was used. Dublecco's Modified Eagle Medium (DMEM)–high glucose with 4500 mg/L glucose, L-glutamine, sodium pyruvate, and sodium bicarbonate (Sigma) was supplemented with 10% fetal bovine serum (FBS; Lonza) and 1% penicillin-streptomycin (10 000 units/mL; Lonza).

Cell storage and expansion

HeLa or MG-63 cells were used in experiments, and cultured under the same conditions unless otherwise stated. HeLa and MG-63 cells were purchased from Sigma-Aldrich (Lot no 13B029 and 13B009 respectively). The cells were expanded and stored in 10% dimethyl sulfoxide (DMSO; Sigma) and 90% fetal bovine serum (FBS; Lonza) in liquid nitrogen until further use. Prior to experiments, the cells were seeded by thawing the cryovial in a 37 °C waterbath until some ice is left. 1 mL of pre-warmed supplemented DMEM and thawed cell suspension was centrifuged at 110 g for 5 minutes to pellet cells. The supernatant was discarded and the cell pellet was seeded in a T75 cell culture flask and kept in the incubator at 37 °C and 5% CO_2. During *in vitro* expansion, cells were passaged at approximately 90% confluency. Passages were performed by washing cells with phosphate buffered saline (PBS; Sigma) followed by a 5 minute incubation with Trypsin 1x (Lonza) at 37 °C. The reaction was quenched with 70% complete media (CM) and centrifuged at 110 g for 5 minutes. The cell pellet was resuspended in CM and seeded in a T75 flask at 10 000 cells/cm^2. Cells were used up to a passage number of 20.

2.6 Magnetic oscillating systems

Two magnetic oscillating systems were studied. The magnefect-nano system was used in all transfection and particle uptake in cell studies, whereas the MICA bioreactor was studied to compare transfection efficiency with the magnefect nano (Figure 2.4).

The magnefect-nano oscillating magnetic system was purchased from nanoTherics Ltd. This system fitted a 6-well, 24-well, or 96 well magnet array similar to a cell culture well plate. The magnet array on the magnefect-nano can be oscillated laterally at varying frequencies (0.5 to 5 Hz) and amplitudes (0.1 to 0.5 mm). During oscillation, the cell culture plate is placed on top of the magnet and the magnet array moves laterally at under the plate while the plate is static. The magnetic ion-channel activation (MICA) system is an external magnetic system that oscillates horizontally at large distances (up to 50 mm). This system also fitted a 6-well, 24-well, or 96 well magnet array. In this bioreactor, the cell culture plate is fitted on top of the magnet array and the magnet array moves down, away from the plate up to the specified distance before moving upwards towards the plate.

The difference between the magnetic field between the magnefect-nano and the MICA bioreactor is that the magnetic gradient on the magnefect-nano pulls the MNPs to the bottom of the plate. Therefore the MNPs maintain constant contact with adherent cells while moving on the x-plane. The MICA system however moves up and down on the y-axis which causes a strong magnetic field when the magnet is close to the plate but diminishes (at >10 mm) when the magnet array moves downwards away from the plate. Therefore stable suspensions of MNPs are pulled towards the cells when the magnet is close but are resuspended when the magnet moves

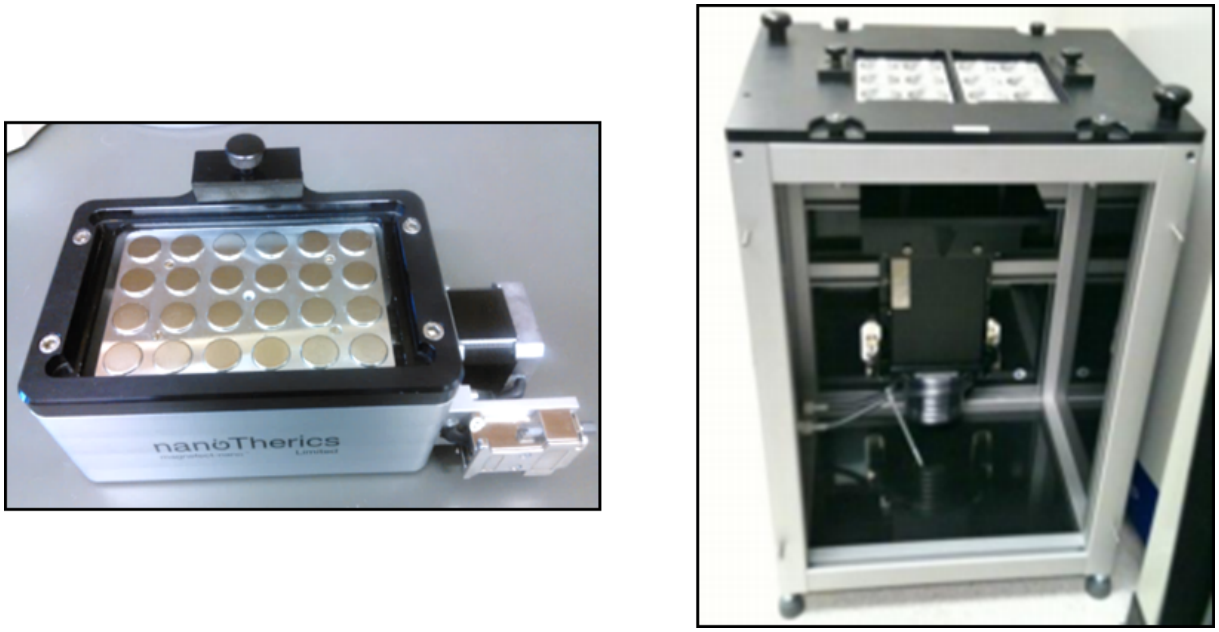

Figure 2.4 magnefect-nano lateral oscillating array for nanomagnetic transfection (left) and MICA vertical oscillating bioreactor (right).

away.

2.7 GFP plasmid for transfection studies

The plasmid containing genes for the expression of green fluorescent proteins (GFP) was used as a reporter plasmid. Successful delivery of the plasmid to the nucleus and translation into the protein will result in cells fluorescing green and can be observed under a fluorescence microscope. Therefore the efficiency of transfection was determined by the percentage of cells expressing GFP. The GFP plasmid used for transfection studies were a stock purchased from Clonetech. The plasmid was composed of 4733 base pairs and contained a human cytomegalovirus (CMV) promoter, depicted in Figure 2.5. The CMV promoter which drives the transcription of the gene of interest is used for strong gene expression in mammalian cells.

2.8 Nanomagnetic transfection - Transfection of adherent cells using MNPs and pGFP

The protocol of nanomagnetic transfection using the magnefect-nano system is depicted in Figure 2.6. In a 24 well plate, cells are seeded at a density of 35 000 cells/cm^2 and grown to a confluency of 70–80% in 24 hours. The transfection complex was prepared in a ratio of 1:1. For each well to be transfected, 0.6 μg DNA was pipetted into a tube and diluted with 20 μL of serum- and supplement-free DMEM. 0.6 μL of nTMag was added into the DNA solution and vortexed for 5 seconds. The nTMag-DNA complex was left to form for 15 minutes at room temperature. 500 μL/well complete media was then added to the complex and pipetted to mix. Media was aspirated from the wells and the media containing transfection complex was added. The plate was placed on the magnefect-nano oscillating system and set to a frequency of 2 Hz and 0.2 mm displacement for 30 minutes. The plate was removed immediately after the oscillating procedure, transfection complex was aspirated and fresh CM was added into wells. The cells were incubated for 48 hours, and protein expression was measured on the flow cytometer or confocal microscope.

MNPs synthesized by thermal decomposition (tdMNP) were also studied for transfection efficiency using the protocol described above, using different tdMNP-PEI to DNA ratios described in each experiment. The concentration of tdMNP-PEI used for each experiment was 0.3 mg/mL

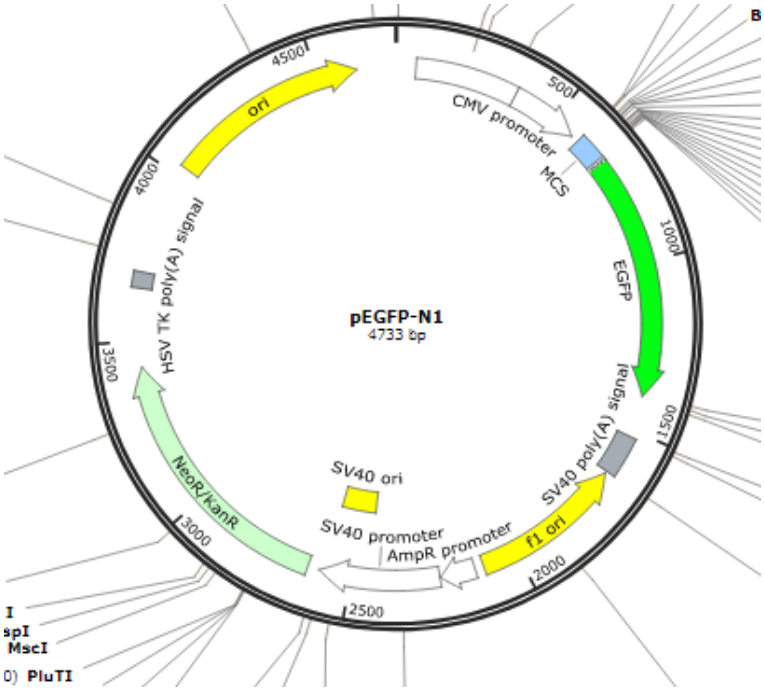

Figure 2.5 Plasmid map of pEGFP-N1 from Clonetech (www.snapgene.com).

Fe unless stated otherwise.

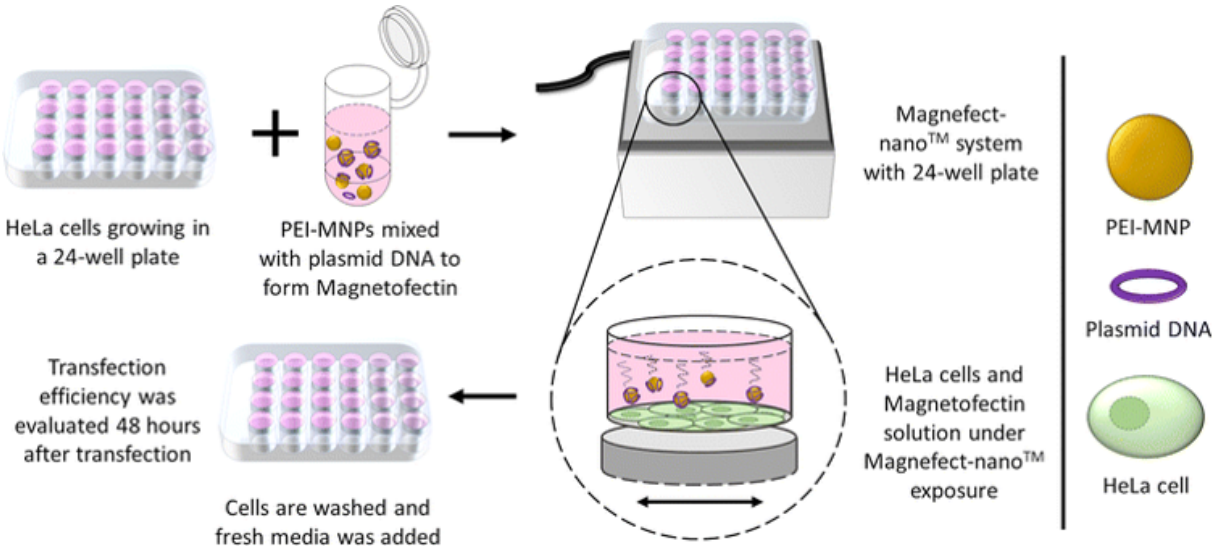

Figure 2.6 Protocol for nanomagnetic transfection using the magnefect-nano oscillating system (Cruz-Acuna et al., 2016). Reprinted with permission from Springer publishing group [license number: 4153010276693].

2.9 Flow cytometry measurements

Cells in a 24 well plate were trypsinized using 300 μL 1x trypsin for 5 minutes and neutralized with 300 μL CM. The cell suspension was transferred to Eppendorf tubes and centrifuged at 110 g for 5 minutes. The cell pellet is washed with flow cytometer buffer (PBS containing 2.5% FBS) twice and resuspended in 300 μL buffer and pipetted to remove cell clumps. The cell suspension is placed on ice until the start of the flow cytometer measurements. The flow rate of the flow cytometer (iCyt Eclipse Flow Cytometer Analyzer) was set at *medium* for high cell counts (100 000 cells/300 μL) and to *high* for low cell counts (35 000 cells/300 μL). Cell samples without GFP fluorescence were used as a control to set the FL1 threshold to measure GFP expression and to gate a population of single cells in a high density area using the polygon tool.

Propidium Iodide for flow cytometry

Propidium iodide (PI; 1 mg/mL in water, Thermo Fisher) was used to stain dead cells for flow cytometry analysis. PI cannot permeate across intact cell membranes, but can permeate into damaged cells where it can bind to double stranded DNA, which then emits a red fluorescence at 617 nm (FL2 channel). Therefore PI can be used in combination with transfected GFP cells (FL3 channel). Once cells were harvested and washed as per the flow cytometry protocol, the cells were then resuspended in 300 μL flow cytometer buffer. 10 μL of PI solution was added into the tube and immediately measured on the flow cytometer.

2.10 Fluorescence imaging

Confocal imaging

Fluorescence imaging was performed using a laser scanning confocal Olympus U-TBI 90 microscope. The microscope is able to image with three channel fluorescence. Image acquisition was obtained using Fluoview 10 software and image analysis by Fiji/ImageJ open access software.

DNA fluorescence labelling

The DNA labelling kit - Label IT Tracker Intracellular Nucleic Acid Localization Kit, Cy3 from Mirius was purchased to label pGFP for tracking studies. To label DNA, in an Eppendorf tube, 75 μL of sterile molecular biology grade water, 10 μL of 10x labelling buffer A, 10 μL of 1 mg/ml DNA, and 5 μL of Label IT reagent was added and pipetted to mix. The suspension was incubated for 30 minutes at 37 °C, then quickly centrifuged to bring down condensation from the cap and incubated again for 30 minutes at 37 °C. Then 100 μL of sterile water was added, along with 20 μL of 5M NaCl and 400 μL of 100% ethanol (Sigma-Aldrich) kept in the −20 °C freezer. The solution was vortexed and put in the −20 °C freezer for 1 hour. After incubation, the Eppendorf tube was centrifuged at 14 000 g at 4 °C for 15 minutes. The supernatant was removed and 500 μL of room temperature 70% ethanol was added. The tube was centrifuged again at 14 000 g for 10 minutes. The ethanol supernatant was removed and the DNA pellet was resuspended in 10 μL sterile water and stored at 4 °C.

MNP fluorescence labelling

MNPs were labelled with fluorescein sodium salt (Sigma Aldrich) to obtain green fluorescence. The fluorescein sodium salt powder was solubilized to 1 mg/mL stock solution. 5 mg of salt was weighed and 5 mL distilled water was added. The solution was stored at 4 °C.

0.1 M of HEPES buffer was prepared from 1 M HEPES stock solution. The pH of the HEPES buffer was adjusted to pH 8.5. To prepare a working solution of fluorescein sodium salt, the stock was diluted with the HEPES buffer at 1:100 000 dilution. For MNP labelling, 10 μL of MNP was mixed with 90 μL fluorescein in an Eppendorf tube and placed on a shaker overnight at room temperature in the dark. The suspension was then washed with distilled water using an Amicon centrifugal filter of 30k MWCO to remove excess fluorescein. The suspension was then used immediately for cell treatment.

2.11 Cell viability assays

Live/Dead cell viability assay

The Live/Dead cell viability assay (Thermo Fisher) works using two dyes: Calcein AM for live cells and ethidium homodimer-1 for dead cells. Calcein AM permeates live cells and is metabolized by viable cells into the green fluorescent dye calcein. The ethidium homodimer-1 permeated damaged membrane of dead or unhealthy cells and binds to double stranded DNA,

thus producing a red fluorescence. To prepare the assay, cells were seeded on 24-well plates and incubated for 24 hours. Cells were then treated according to the experiment. The Live/Dead assay was then performed by first washing the cell monolayer with PBS. In a centrifuge tube containing 10 mL PBS, 2 μL of ethidium homodimer-1 and 5 μL of Calcein AM was pipetted and vortexed. 300 μL of the solution was pipetted into 24 well plates to cover the bottom of the wells. The plate was incubated in the dark at room temperature for 30 minutes and images of the cells were taken on the confocal microscope using an excitation/emmision of 488/517 nm and 561/617 nm with a 20x objective.

XTT assay for cell viability

MNPs have been shown to quench fluorescence. Although the mechanism of fluorescence quenching has not been elucidated, hypotheses behind the quenching may be due to a nonradiative energy transfer between the dye and MNPs through electron couplings, collisions between the dye and MNPs, or the broad absorption of fluorescence by iron oxide (Zhang et al., 2017; Josephson et al., 2002). Therefore an XTT colorimetric assay (Sigma Aldrich) was used to determine cell viability. XTT is a yellow tetrazolium salt that is metabolized by viable cells into an orange formazan dye, which intensity can be measured colorimetrically. Cells were seeded at a density of 35 000 cells/cm^2 in 96 well plates and grown to a confluency of 70-80% in 24 hours. Following the cell uptake treatments described in Section 2.8, the CM was then replaced with 100 μL of fresh CM and 50 μL of XTT solution was pipetted into each well. The plate was incubated for 6 – 8 hours in the incubator and absorbance was measured on the plate reader at 450 – 500 nm.

CellTiter Blue (Resazurin) assay for cell viability

The CellTiter Blue assay (Promega) is used to determine cell viability using fluorescence. Similar to the XTT, viable cells convert the resazurin dye into the fluorescent end product resorufin. Cells were seeded at a density of 35 000 cells/cm^2 in 96 well plates and grown to a confluency of 70-80% in 24 hours. After treatment, CM was replaced with 100 μL of fresh CM and 20 μL of CellTiter Blue solution was pipetted into each well. The plate was placed on an orbital shaker for 10 seconds and incubated for 4 hours at 37 °C. After the incubation period, the plate was shaken again for 10 seconds and measured for fluorescence on the plate reader at an excitation/emission of 560/590 nm.

2.12 Statistical analysis

Statistical analyses were performed based on experiments and experimental groups, such as paired Students t-test, unpaired Students t-test, F-test, two sample t-test and two-way analysis of variance (ANOVA). Error bars shown in figures throughout the thesis are the calculated standard error of mean. The alpha value for statistical significance was set to 0.05. P values were denoted as *p<0.05, **p<0.005, ***p<0.0005.

Chapter 3

Investigation of optimised coating methods for PEI functionalised MNPs

3.1 Introduction

Magnetic nanoparticles (MNPs) are attractive for applications in biomedicine and bioengineering due to the ability to remotely direct their movement towards a target for cargo delivery, to harvest molecules, to act as contrast agent for diagnostics, or to induce localized heating (Pankhurst et al., 2003; Sensenig et al., 2012).

However, MNPs tend to aggregate in suspension as they are hydrophobic and clustering minimizes their surface energy. This property is not favourable in functional cellular studies as it can affect intrinsic magnetic properties as well as particle mobility. Therefore the surface of MNPs must be modified to improve colloidal stability and to form homogeneous bio-compatible aqueous suspensions. To prevent aggregation, the MNP coating should overcome hydrophobic interactions, magnetic forces between particles, and Van der Waals forces (Mahmoudi et al., 2011). To promote colloidal stability, particles can be surface-modified with surfactants (Ramimoghadam et al., 2014), natural and synthetic polymers (Shaterabadi et al., 2017), or biomolecules (Aires et al., 2017; Yu et al., 2014). In addition surface functionalization is used to facilitate binding and internalization of MNP into cells, or for gene or drug delivery for therapeutic purposes (Kang et al., 2017; McBain et al., 2008b).

As discussed earlier in Section 1.4.2, for nanomagnetic transfection applications polyethyleneimine (PEI) is often used to coat the surface of MNPs in order to optimise their functionality (Cruz-Acuna et al., 2016; Zhang et al., 2014b). The presence of unbound PEI in MNP suspensions used for these applications is problematic as the plasmids required for transfection can bind to unbound PEI rather than the intended MNP surface. This can have a dramatic effect on the efficacy of the application as MNPs are required for improved transfection efficiency using magnetic targeting and sedimentation onto cell monolayers. The presence of excess PEI causes unspecific binding with DNA, thus reducing the efficiency of nanomagnetic transfection (Arsianti et al., 2010). PEI also causes cell toxicity, therefore removing excess PEI improves cell viability (Godbey et al., 2001, 1999b).

Particle characterization is important in order to obtain physical and chemical information to understand the behaviour of MNPs in different systems and optimise performance for applications. In particular, particle size characterization is crucial for understanding particle-particle interaction, interaction within different matrices, and changes in size distribution and aggregation with different types of coatings. Common size characterization methods include dynamic light scattering (DLS), transmission electron microscopy (TEM), scanning electron microscopy (SEM), size exclusion chromatography (SEC), and nanoparticle tracking analysis (NTA) (Lim et al., 2013; Trekker et al., 2013). DLS and NTA are the most frequently used methods to obtain the

hydrodynamic diameter, D_H, which is a measure of the effective diffusive size of particles in liquid suspension. However these methods measure all particulate material in the suspension, including material not associated with the MNPs of interest such as coating fragments and buffer precipitates. It is however possible to use magnetic intruments to specifically characterize and isolate the size of MNPs only. In this chapter, measurements of AC magnetic susceptibility were exploited as a particle-specific probe to monitor the progression of PEI coating and aggregation of MNPs, where optimisation of these parameters is important for nanomagnetic transfection applications.

In Section 1.8, a simple method for determining hydrodynamic sizes when blocked particles are present was described. However more generally the suspensions will contain a distribution of particle sizes with both Brownian and Néel relaxation mechanisms. Therefore in this study, ACS results were compared to simulations using a computational model of polydisperse nanoparticle clusters in order to determine the size distribution of both particles and clusters, and how these responded to different coating treatments. The full details of the computational model is described in a study by Céspedes et al. (2014). These results were compared to equivalent measurements using dynamic light scattering. Complementary characterisation using structural and compositional analysis techniques was used to confirm the interpretation from the ACS measurements and to provide additional parameters for the model.

Objectives

1. **Synthesis and aqueous phase transfer of MNP.** To synthesize MNP by thermal decomposition and oxidize particles to obtain carboxylic functional groups for dispersion in aqueous suspension.

2. **Characterization of MNP and PEI-coated MNP.** To characterize MNPs and PEI-coated MNPs by TEM, zeta potential analysis, DLS, and TGA.

3. **ACS measurements and simulations of gradual PEI loading on MNP.** To compare changes in ACS measurements of MNP suspensions with different PEI loading, and assess the clustering/coating behaviour of PEI and MNP. ACS measurements were modelled for size determination and the point of PEI coating saturation on MNPs was determined.

3.2 Materials and Methods

3.2.1 Synthesis of magnetic nanoparticles and dispersion in aqueous suspension

Iron oxide magnetic nanoparticles were synthesized by the thermal decomposition method according to Cruz-Acuna et. al (Cruz-Acuna et al., 2016). The synthesis procedure is described in Section 2.1.

3.2.2 PEI coating of MNP using carboiimide chemistry

PEI solution in deionized water was prepared at 1% (w/w) containing 80 mg PEI (Sigma Aldrich). The pH of the PEI solution was adjusted to 4.5 – 5 using acetic acid and was sonicated for 1 hour using the ultrasonicator tip. During sonication, 4 mL of 10 mg/mL oxidized MNP was added into the PEI solution, followed by 38.3 mg of EDC and 6.95 mg of sulfo-NHS dissolved in 1 mL of deionized water. After sonication for 1 hour, the suspension was filtered using an Amicon centrifugal filter tube (MWCO 100 000) at 3500 rpm for 10 minutes by adding the same volume of water. The remaining particles were resuspended in deionized water.

3.2.3 PEI coating and dialysis of magnetic nanoparticles

Separate vials of 200 μL of the aqueous MNP suspensions at a concentration of 0.3 mg/ml Fe prepared by thermal decomposition were coated with different mass of PEI polymer (Sigma

Aldrich). To prepare the MNP-PEI coated suspensions, PEI of 25 kDa, branched at pH 7 (1 mg/mL) was added at volumes of 50, 500, 1000, and 2000 μL to the 200 μL MNP suspensions. These samples are hereafter referred to as *PEI 50, PEI 500, PEI 1000* and *PEI 2000* respectively. An uncoated suspension was also retained, referred to as *PEI 0*. All suspensions were sonicated with an ultrasonicator tip for 5 minutes prior to characterisation measurements.

In addition to the effect of PEI loading, the presence of free or loosely bound PEI in the suspensions was assessed using dialysis. For dialysis experiments, tdMNP-PEI suspensions were pipetted into separate dialysis tubes with a 50 kDa molecular weight cut off (MWCO; Sigma Aldrich) which were placed in a 2 L container filled with distilled water and magnetically stirred overnight (Fig. 3.1). The MNP suspensions were then concentrated using centrifugal concentrators of 30 kDa MWCO (Amicon) prior to post-dialysis characterisation.

During dialysis, the tubes containing samples of all PEI loading concentrations (including the uncoated PEI 0 sample) were placed in a shared dialysate to study the binding and redistribution of PEI between samples (Fig. 3.1). Dialysis was also used as a washing method to remove unbound or non-interacting PEI in MNP-PEI suspensions.

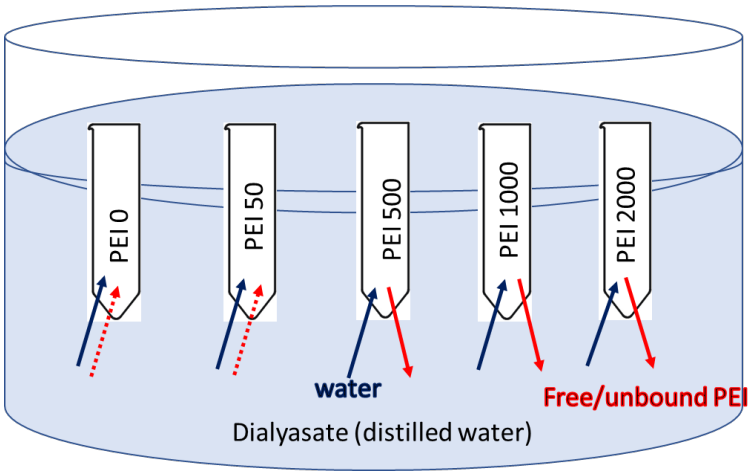

Figure 3.1 Schematic of the dialysis experimental set-up of an MNP-PEI sample set in the dialysate. Unbound PEI (red arrows) show outflux from samples containing high amount of PEI and PEI influx into samples with low concentration of PEI. Water influx is shown in blue.

3.2.4 Dynamic light scattering

Dynamic light scattering (DLS), also known as photon correlation spectroscopy (PCS) is a common intrument used to measure the size distribution of nanoparticles. A laser source illuminates the sample and the resulting scattering when the light hits the particles are detected. The particle motion is tracked and the DLS instrument uses the Stokes-Einstein equation to model particle hydrodynamic sizes based on their Brownian motion. This equation is given by

$$D_H = \frac{\kappa_B T}{3\pi\eta D_t} \tag{3.1}$$

where D_H is the hydrodynamic diameter, D_t is the translational diffusion coefficienct determined by DLS, κ_B is the Boltzmann constant, T is the temperature and η is the viscosity.

The zeta potential is measured using electrophoresis in a cell with electroedes at both ends and an alternating electric field is applied across the sample. The motion of particles when the electrodes are charged are detected and the zeta potential is determined.

DLS measurements were performed using a Malvern zetasizer model 3000 HSA. MNP samples were diluted 5x to a final volume of 2 mL using distilled water and pipetted into a glass cuvette for DLS measurements. Intensity-weighted size distributions were converted to number-weighted

distributions for analysis. MNP suspensions were measured before and after dialysis. Zeta potential measurements were performed by collecting 2 mL of the sample in a syringe and injecting it into the sample holder in the instrument. The zeta sizer measured the surface charge of the sample, before the sample was flushed off with distilled water.

3.2.5 AC susceptibility measurements and simulations

AC susceptibility measurements were performed at 37 °C on MNP suspensions both before and after dialysis, using an in-house built susceptometer capable of measuring at frequencies between 10 Hz and 1 MHz for concentrated ferrofluid samples (200 μL volume). For more dilute samples the upper frequency limit is reduced due to the weak sample signal dropping below background. The volume susceptibility was obtained following background subtraction and calibration using a known mass of Dy_2O_3 powder.

Simulated AC susceptibility curves were obtained using a computational model that considers nanoparticle clusters in suspension, by summing the susceptibility calculated for each cluster. The model, which is described in detail elsewhere (Céspedes et al., 2014) creates clusters by selecting nanoparticles at random from a log-normal size distribution derived from input parameters for the particles. The generation of a log-normal size distribution of clusters is attempted by the model, based on input parameters for the clusters. However the ability to form the intended cluster distribution depends on the match of the nanoparticle and cluster sizes and the computational limitations of the model. Thus a log-normal fit to the actual cluster distribution created by the model (which was subsequently used to calculate the susceptibility) is reported here as the simulation parameter rather than the original input cluster parameters.

3.2.6 Transmission electron microscopy

TEM samples were prepared on copper mesh grids with carbon film (Agar Scientific). MNP samples were diluted 50x in water and 5 μL of the suspension was dropped onto the grid. The grid was dried by touching filter paper to the tip of the grid to absorb water and allowing it to air dry for 5 minutes. Samples were imaged on a JEOL100CXII for low resolution and Tecnai F30 for high resolution images. Particle distribution size analysis was performed using the Image J image processing software.

3.2.7 Thermogravimetric analysis

Thermogravimetric analysis (TGA) is a technique which measures the change in mass when a sample is heated over a range of temperatures. The mass change can be used to determine the composition and percentage of materials within a sample based on their thermal stability.

Thermogravimetric analysis (TGA) was performed with a TA instrument SDTQ600. Samples were pipetted into a 70 μL alumina pan and dried in the oven at 70 °C and subsequently cooled before measuring on the TGA. Dried samples were heated at a rate of increase of 5 °C per minute under N_2 flow. The decrease in weight relative to temperature was analysed as organic PEI and moisture.

3.2.8 Viscosity measurements

A rheometer is used to measure the shear flow/strain of a liquid when an external force is applied, which can be used to obtain viscosity data of liquid samples.

Viscosity measurements were performed at 37 °C (to ensure consistency with ACS measurements) using a TA instrument AR-G2 Rheometer of 60 mm parallel plate geometry. Three PEI concentrations were prepared: 5 mg, 10 mg, and 20 mg PEI diluted in 22 mL distilled

water, corresponding to PEI concentrations in sample PEI 500, PEI 1000 and PEI 2000 before dialysis. Water, glycerol, and PEI at 1 mg/mL concentration were also measured as reference samples. The system was calibrated using a glycerol standard at the plateau region of the viscosity measurements at shear rate region 71–269 s^{-1}, corresponding to a known viscosity of 0.28 Pa.s at 40 °C (Segur & Oberstar, 1951). Absolute viscosity values were determined using the known viscosity of the glycerol reference sample. Viscosity was measured with increasing shear rate, and the mean viscosity determined using the average of values obtained in the plateau shear rate region 71–269 s^{-1}.

3.3 Results

3.3.1 Synthesis of MNPs by thermal decomposition

3.3.1.1 MNP synthesis using tris(2-ethylhexyl) amine

Magnetite iron oxide nanoparticles were synthesized using the thermal decomposition method, these particles are referred to as tdMNPs. In the initial batches, tris(2-ethylhexyl) amine (Fig. 3.2) was used as the solvent with a high boiling point of 334.8 °C (Sigma-Aldrich, 2017b) during the heating process. The particles suspended in toluene were measured on the ACS to obtain their magnetic behaviour, shown in Figure 3.3 A. The MNPs show superparamagnetic properties where the χ' and χ" show a stable Néel relaxation behaviour. DLS measurements (Figure 3.3) of the intensity-weighted derivation show 2 peaks at 25 and 200 nm. The volume and number distribution however show a predominantly small size population of ∼20 nm.

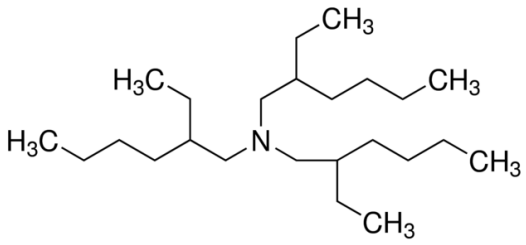

Figure 3.2 Chemical structure of tris(2-ethylhexyl)amine (Sigma-Aldrich, 2017b).

The particles were then oxidized following the procedure described in Section 2.1. The starting material of the magnetite tdMNP coated with oleic acid and suspended in an organic solvent toluene was observed to have a deep black colour and were well dispersed (Figure 3.3 C i). After oxidation of the oleic acid to form –COOH functional groups, the resulting magnetic suspension showed a change in colour to murky brown and was cloudy, contrary to a well dispersed colloid. The synthesis and oxidation procedure was performed several times but the nanoparticle suspension after oxidation resulted in a brown and unstable colloid (Figure 3.3 C ii). Since this method yielded an unstable MNP suspension, a different high boiling point solvent was used to replace tris(2-ethylhexyl) amine, described below.

3.3.1.2 MNP synthesis using trioctylamine

The thermal decomposition synthesis was repeated, however the high boiling point solvent used during the reaction was changed to trioctylamine (Figure 3.4) with a boiling point of 365 °C (Sigma-Aldrich, 2017). The oxidation procedure was carried out and the resulting nanoparticle solution was a brilliant black colour after sonication. Therefore the synthesis and oxidation procedure was successful and magnetite particles with oleic acid surface and carboxylic groups was prepared.

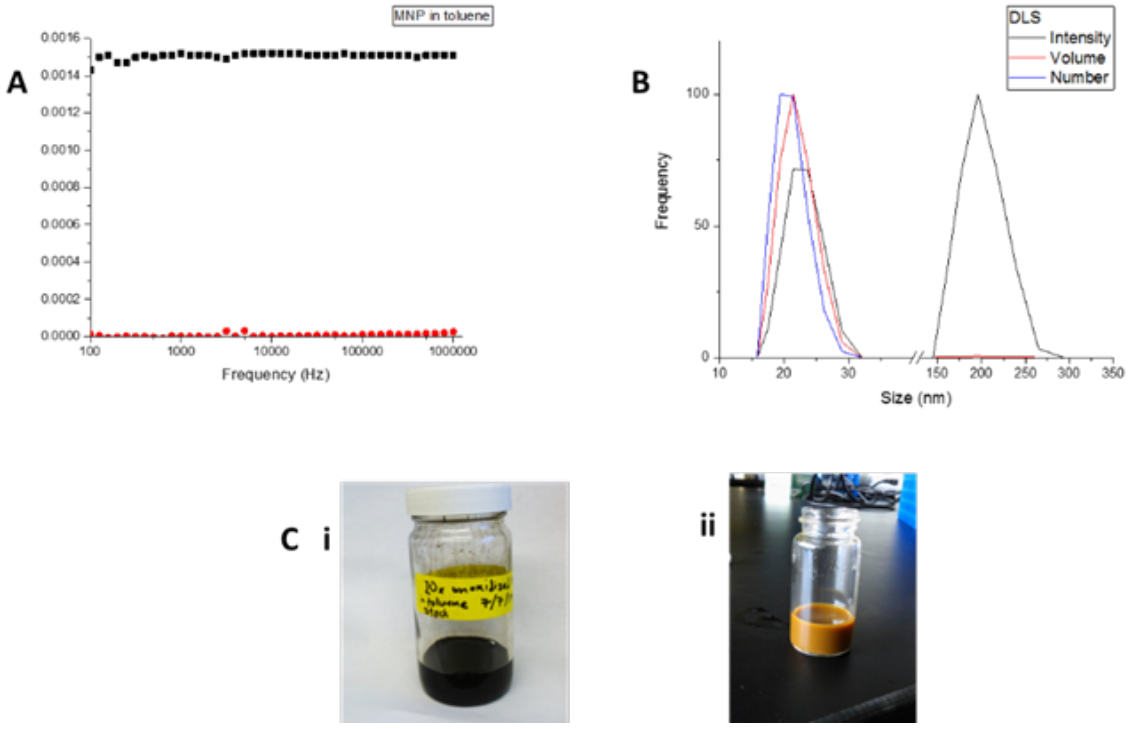

Figure 3.3 First batch of MNP synthesized by thermal decomposition. (A) ACS of MNP before oxidation in toluene. (B) DLS measurement of oxidized MNP. (C) Images of MNP after synthesis (i) in toluene before oxidation, (ii) in water after oxidation.

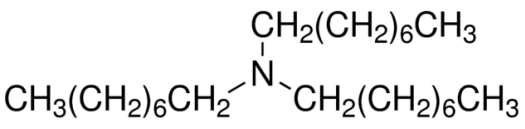

Figure 3.4 Chemical structure of trioctylamine (Sigma-Aldrich, 2017).

3.3.2 Size distribution of MNP by TEM

Once the second synthesis method was successful using trioctylamine (Section 3.3.1.2), the resulting tdMNPs were characterized and functionalized. Transmission electron microscope (TEM) images were obtained for tdMNPs (Figure 3.5a), showing them to be mainly spherical and relatively monodisperse, with a small proportion of smaller irregular shaped particles. Particle size distributions were obtained from TEM images by measuring the diameter of ~1000 particles using image processing software, and the histogram fitted with a lognormal distribution (Figure 3.5b). The average particle core diameter was found to be 17.4 nm with 15% polydispersity.

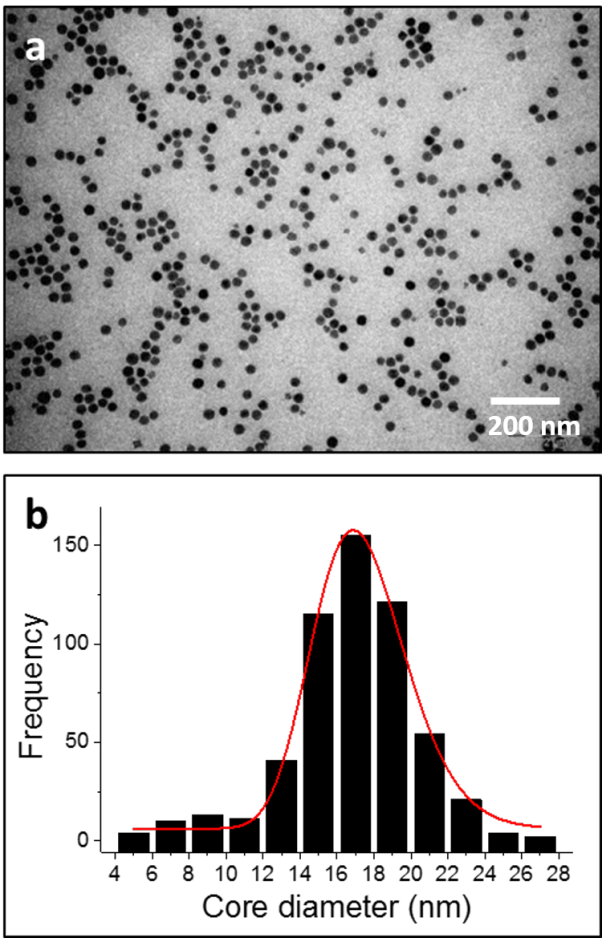

Figure 3.5 (a) TEM micrograph showing MNP core size distribution and shape and (b) histogram of MNP core diameter distribution fitted with a lognormal curve.

3.3.3 PEI functionalization of MNPs

tdMNPs were coated with PEI using two methods. The first method discussed below is by covalently binding the amine groups of PEI to the oxidized oleic acid on the surface of MNPs. This method prevents the dissociation of PEI from MNPs. The second method is the coating of PEI using ionic interaction where the cationic charge on amine groups attach to the anionic charge on carboxylic groups of the oxidized oleic acid. Both PEI-coated MNPs were characterized and studied for transfection efficiency in Chapter 4.

3.3.4 PEI coated onto MNP by covalent binding (MNP cPEI)

Oxidized MNP was coated with PEI using carboxiimide linkers to form covalent bonds. To ensure complete PEI coating on particle surface, the coating procedure was conducted twice and compared with MNP coated with PEI once. The PEI-coated MNP (MNP cPEI) were characterized for size and surface charge properties.

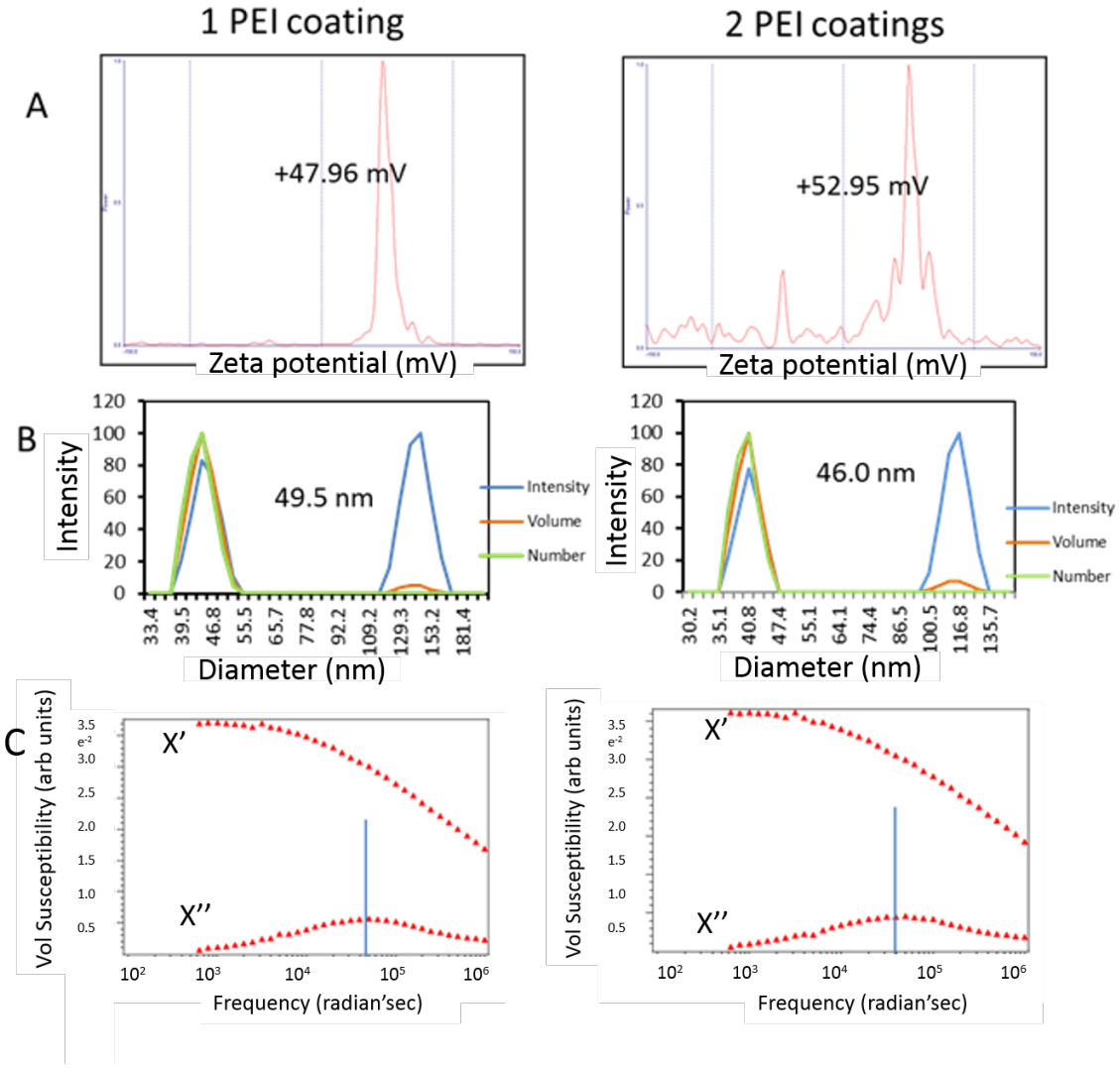

Figure 3.6 MNP particles with –COOH surface functionalization were covalently bound with PEI using carboxiimide linker chemistry. Column 1 is MNP with one PEI coating procedure and Column 2 is MNP which underwent 2 PEI coatings. MNP cPEI were characterized for (A) zeta potential (B) DLS hydrodynamic size and (C) ACS measurements.

Zeta potential measurements show that after the PEI coating procedure, tdMNP had a high positive charge density (Fig. 3.6 A). This result affirms the presence of bound PEI on MNP surface as MNPs with oxidized oleic acid has a negative surface charge, therefore the measured positive surface charge arises from the cationic PEI polymer coating. After the first PEI coating procedure, the zeta potential of tdMNP was +48 mV. A second coating on the same tdMNP cPEI suspension increased the zeta potential to +53 mV. DLS measurements in Figure 3.6 B show a reduction in hydrodynamic diameter from PEI coating 1 to 2, with only a small size decrease of 3.5 nm to 46 nm.

ACS measurements show the opposite size change compared to the DLS, where the Brownian peak of the MNP suspension with 1 PEI coating had a larger peak position at 49 kHz, and the second PEI coating shifted the peak to 45 kHz, signifying an increase in the hydrodynamic diameter from 23 nm to 24 nm with additional PEI coating. Since ACS measures the hydrodynamic change in size of tdMNP only, the size change is better reflected in the ACS measurements, as DLS measures tdMNP as well as other non-magnetic species such as unbound PEI. Since the size difference of tdMNP between the first and second coating is only 1 nm, and the zeta potential measurement of the second coating of PEI show noisy spectra which could be attributed to different charge density of unbound polyplexes, it was concluded that the first PEI coating on tdMNP is sufficient to completely coat MNP in the suspension.

3.3.5 PEI coated onto tdMNP by electrostatic interaction

Oxidized MNP in water is coated with PEI by electrostatic interaction, where PEI is added into an MNP suspension and the coating occurs spontaneously, where the cationic amine groups on PEI attaches to the negatively charged MNP surface with carboxylic functional groups. This reaction take place at neutral pH. Compared to MNP cPEI which is covalently bound, this electrostatic interaction is weak and PEI is able to dissociate from MNP surface.

Subsequent characterization methods described henceforth is based on tdMNP coated with PEI by ionic interaction (tdMNP-PEI).

3.3.6 Effect of sonication on particle size during coating

PEI can attach weakly onto the surface of carboxylic acid functionalised MNPs due to ionic interaction between the negative charges of the COO^- functional groups with the positively charged NH^{3+} groups of PEI. Figure 3.7 demonstrates the effect of sonication during MNP surface coating with PEI, measured before and after sonication with the addition of 500 μg of PEI to a 200 μL suspension of 1.3 mg/mL Fe of MNPs. There is an obvious χ" peak shift in all 3 samples, starting with sample PEI 0 (Figure 3.7, top) with a peak position at the far right ($\sim$45 kHz) followed by a large shift to 66 Hz with the addition of PEI (Figure 3.7, middle), and peak movement back to $>$10 kHz after sonication (Figure 3.7, bottom). The χ" curve of the MNP-PEI sample before sonication (Figure 3.7, middle) intercepts the y-axis above zero, indicating that a portion of the particle sample is highly clustered with a Brownian relaxation frequency below the measurement limit of 10 Hz. After sonication, the χ" peak shows a strong shift back towards higher frequencies.

From Fig. 3.7 it can be seen that each MNP treatment resulted in a Brownian frequency peak shift, indicating changes in the hydrodynamic size of the particles. The sample without PEI coating (referred to as PEI 0) was a stable colloid in water with negatively charged oleic acid surface coating which provided ionic and some stearic hindrance stability (Figure 3.7, top). The addition of positively charged PEI into the MNP suspension resulted in the formation of particulates with large hydrodynamic sizes, based on the low frequency χ" peak position (Fig. 3.7, middle). The large size could indicate particle aggregation and clustering due to uneven PEI coating around multi-core particles (Figure 3.7, middle). Another possibility is the assembly of multiple PEI layers forming a thick coating around individual MNPs.

Strong sonication of the MNP-PEI suspension appeared to induce MNP dispersion/declustering resulting in smaller particulates as revealed by the reduced hydrodynamic size (Figure 3.7, bottom). It is also possible that the PEI surrounding the particles could be redistributed at this stage. This hypothetical mechanism for the PEI coating process is illustrated schematically on the right-hand side of Fig. 3.7.

3.3.7 Evaluation of PEI coating and MNP clustering behaviour

To investigate these effects further, the changes in particle size and clustering with gradual loading of surface coating were considered. As described in Section 3.2.3, different volumes of 1 mg/mL PEI were added into 200 μL MNP suspensions of 0.3 mg/mL Fe to provide samples exposed to 50, 500, 100 and, 2000 μg PEI, as well as samples without any PEI added (PEI 0). These samples were then sonicated to disperse aggregates. These samples are referred to as PEI 50, PEI 500, PEI 1000, and PEI 2000.

As the Brownian relaxation depends on suspension viscosity (equation 1.5), it was necessary to measure the viscosity of PEI in water at concentrations corresponding to that present in the MNP samples. This was done using rheology (Figure 3.8) and the values obtained were used later in the AC susceptibility simulations. Using glycerol as reference viscosity, the viscosity of water was measured to be 0.0007 Pa.s and PEI suspensions of PEI 500, PEI 1000 and PEI 2000 had the same viscosity values of 0.0014 Pa.s at 37 °C. The similar viscosity values for the PEI

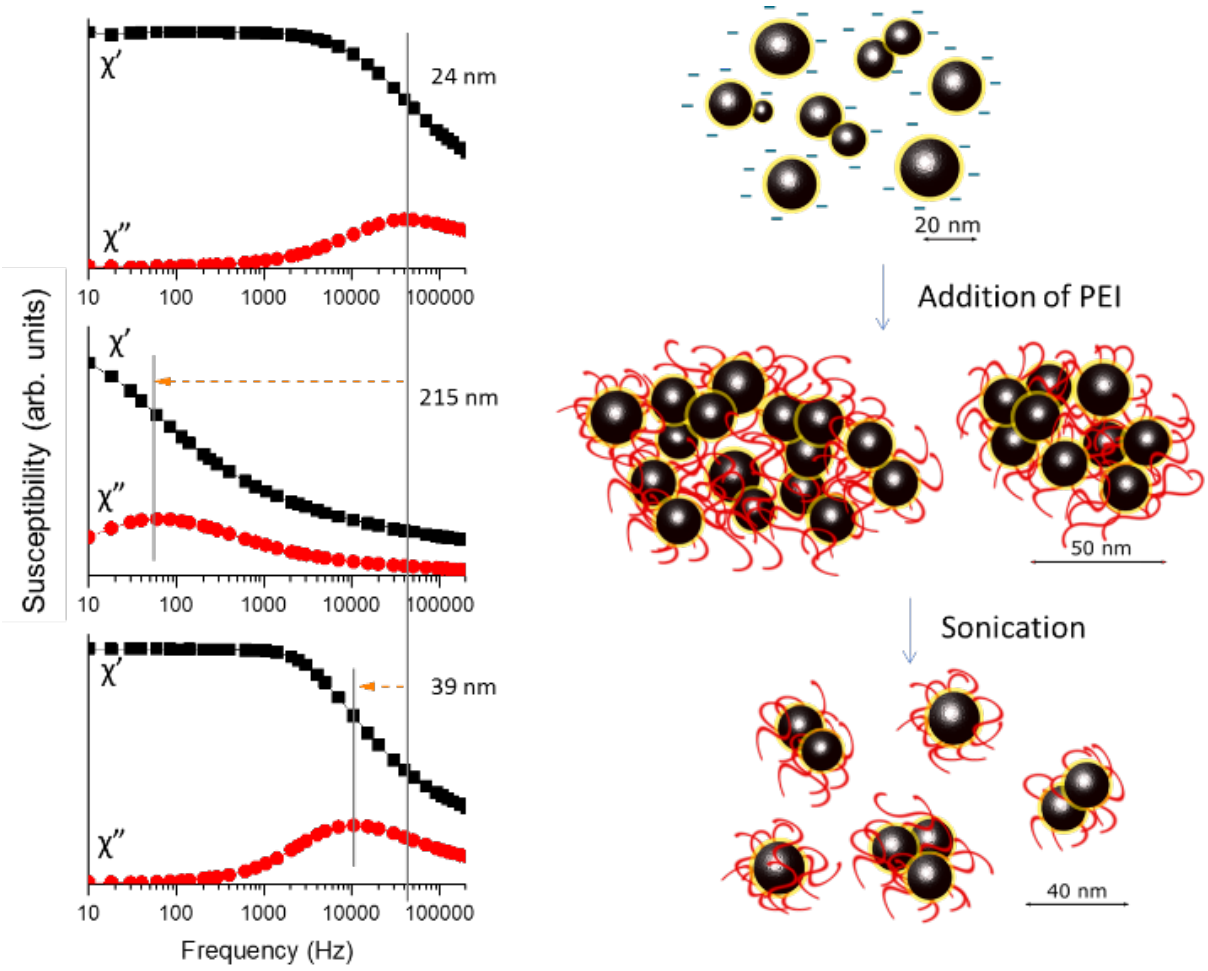

Figure 3.7 AC susceptibility measurements from: MNPs before PEI coating, sample PEI 0 (top), after PEI addition (middle), and after PEI addition and sonication (bottom). For each treatment, the hydrodynamic size of the particle or aggregate was estimated from the frequency position of the χ" peak using the Brownian relaxation time Equation 1.2 in Chapter 1.

samples may be due to the low sensitivity of the rheometer.

3.3.7.1 Determination of surface charge of MNP samples

The measured zeta potential of the samples before and after dialysis is shown in Table 3.1. The zeta potential of sample PEI 0 before dialysis was -38 mV, due to the contribution of the COOH– functional groups. PEI 0 after dialysis had a zeta potential close to zero, indicating that loosely or unbound PEI in the dialysate had permeated into the sample suspension and bound to the negatively charged PEI 0 MNPs. The positively charged amine group on the PEI thus neutralized the carboxylic charge, giving a net zeta potential of ∼0 mV. For the PEI-coated MNPs (PEI 50,500, 1000, and 2000) before dialysis, the surface charge was large and positive at around +30 to +40 mV indicating a degree of surface coverage of the PEI around the MNPs. After dialysis these values became more positive at around +50 to +60 mV, suggesting a denser packing of the PEI on the MNP surface probably due to the redistribution of loosely bound PEI.

3.3.7.2 PEI loading on MNP samples by weight-loss analysis

To confirm that the changes in zeta potential were indeed due to the presence of bound PEI on the MNP surfaces, thermo-gravimetric analysis (TGA) measurements were performed (Figure 3.9). Here the sample is burned continuously and the change in mass is monitored as a function of temperature. Oleic acid shows complete decomposition at 200 °C (Fig. 3.10), however sample PEI 0 before dialysis which only has oleic acid coating does not show a noticeable decrease in

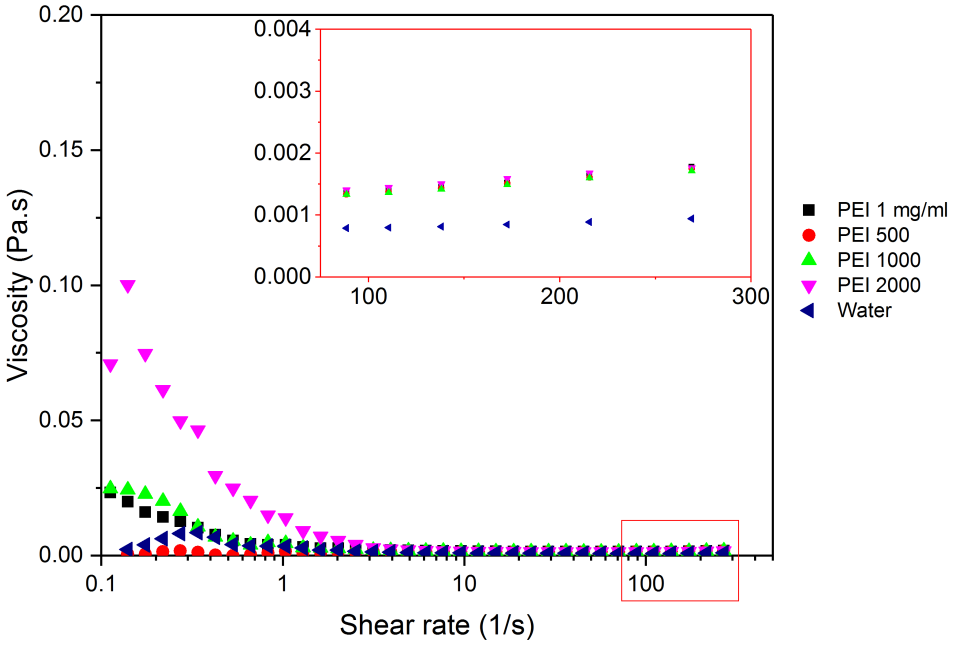

Figure 3.8 Viscosity measurements of PEI and reference samples (deionized water and PEI 1 mg/mL) with a box showing the plateau region. (Inset) Enlargement of viscosity data points at plateau region.

Table 3.1 Zeta potential measurements of the surface charge of MNP-PEI samples after sonication, before and after dialysis n=4, SEM ±4.

	Zeta Potential (mV) (±4)				
	PEI 0	PEI 50	PEI 500	PEI 1000	PEI 2000
Before dialysis	-38	+34	+36	+30	+40
After dialysis	-4	+56	+48	+59	+53

weight after burning, which could be attributed to the small amount of oleic acid relative to weight of the MNP core.

Figure 3.9 shows a consistent 3-step decay of all PEI-coated MNP samples. The first weight loss step plateaus at around 200 °C which corresponds to evaporation of sample moisture (Kapilov-Buchman et al., 2015). Since oleic acid also burns at the same temperature, the weight difference between moisture and oleic acid is indistinguishable. The second step decay is from 200 °C to 400 °C and contributes to the highest percentage of weight loss for samples PEI 1000 and above. This step is due to the decomposition of PEI and appears to scale with the gradual PEI loading, with PEI 2000 showing the largest step whilst PEI 50 shows only a change. It is also interesting to note that the steps seen in sample PEI 2000 measured after dialysis are sharp and plateau above 400 °C, whilst the equivalent sample measured prior to dialysis shows less defined step features, with the second step shifted to a lower temperature more consistent with that measured for a PEI reference sample (Fig. 3.10). This is indicative of the presence of loosely bound or free PEI in the sample before dialysis, and suggests dialysis is an effective washing method for removing excess PEI coating from particles.

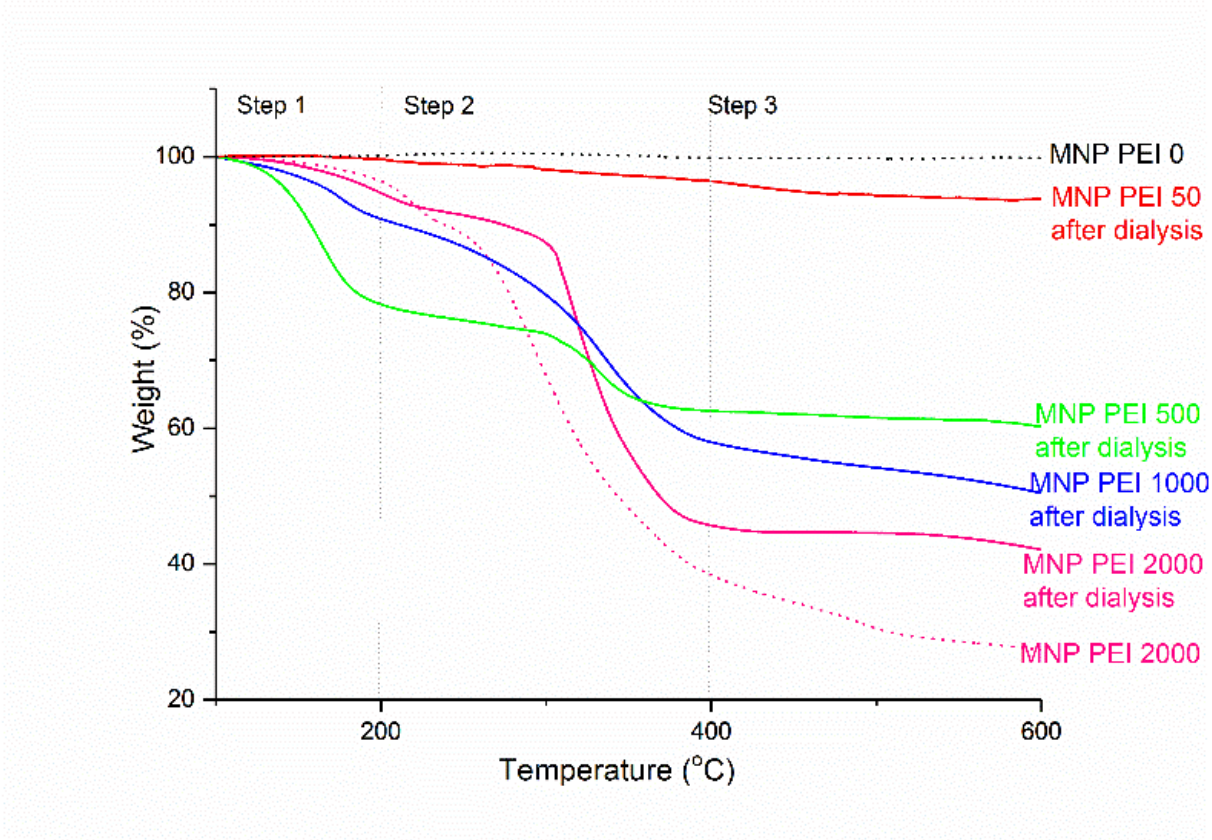

Figure 3.9 TGA analysis of samples PEI 0 (black dotted line) and PEI 2000 (pink dotted line) before dialysis, and samples PEI 50, PEI 500, PEI 1000, and PEI 2000 after dialysis (solid lines).

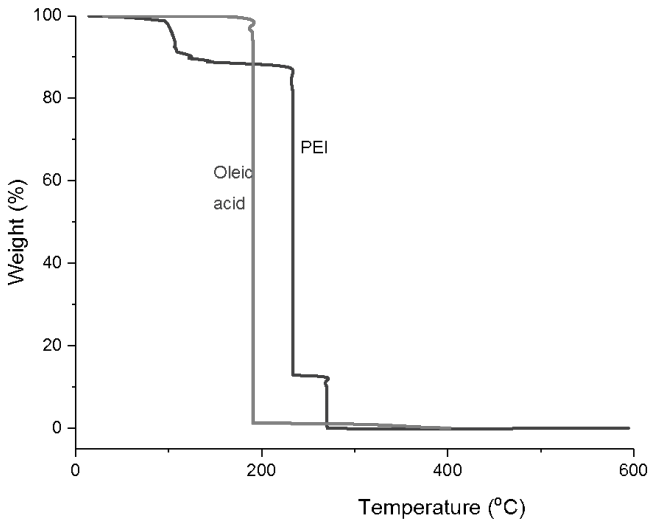

Figure 3.10 TGA analysis of oleic acid and PEI. Oleic acid and PEI decomposed at a temperature of 200 °C and 230 – 280 °C respectively.

3.3.7.3 Transmission electron microscopy of PEI coating on MNP samples

High-resolution TEM was also performed on the samples at each treatment stage. Figures 3.11 a&b show the distribution MNP cores of PEI 0 measured before dialysis which are spherical and have a relatively small size distribution compared to MNPs synthesized by the well-known co-precipitation method. The particles are also mainly singly distributed or paired with no significant aggregation, due to their stable oleic acid coating. In Fig. 3.11b, the high resolution TEM does not show coating around the MNPs, as the oleic acid is too small to observe, or the low electron density of oleic acid provided little contrast compared to the MNPs.

Figures 3.11c and 3.11d show sample PEI 50 measured before dialysis. Close observation reveals uneven layers of PEI polymer binding the particles (indicated by red arrows), resulting in the formation of large aggregates. This overall PEI coating may surround the aggregate leading to the measurement of positive zeta potential discussed earlier. In contrast a more uniform PEI coating can be seen in sample PEI 1000 measured before dialysis (Fig. 3.11e and 3.11f). Here the PEI coating surrounding each particle can be seen clearly, with space between the particles due to stearic hindrance of the polymer. The added polymer coating affords a higher level of stability to the particles in water compared to oleic acid coated particles, due to stronger stearic hindrance and electrostatic repulsion between particles, resulting in reduced aggregation.

Although the TEM results support the hypothetical mechanism for PEI coating of the MNPs, shown in Fig. 3.7, aggregation can also occur when the samples dry during TEM specimen preparation. To measure the MNP coating and aggregation effects in suspension, we compared the effectiveness of AC susceptibility measurements and dynamic light scattering (DLS) on all samples both before and after dialysis.

3.3.7.4 ACS simulations of mixed Brownian-Néel relaxation populations in an MNP suspension

As discussed earlier, polydisperse MNP suspensions can lead to a combination of Brownian and Néel relaxation mechanisms, complicating interpretation of the ACS curves. In order to analyse the changes occurring in the suspensions at each treatment stage, simulations were performed using the modelling parameters shown in Table 3.2. Parameters relating to the individual magnetic particle properties (e.g. mean size, anisotropy) were fixed for all treatments and were determined based on initial fitting to the ACS data from the PEI 0 sample, as well as from TEM measurements. The effects of combined Brownian and Néel relaxation mechanisms can be seen in Fig. 3.12, where the best-fit simulation curve is compared to the data from PEI 0 (middle plot). The effective magnetic anisotropy constant for the particles was determined to be 7200 Jm^{-3} which is consistent with oxidised magnetite nanoparticles.

Table 3.2 Parameters used for ACS simulations for Brownian and Néel fitting. Mean cluster diameter and polydispersity are outputs from simulations.

ACS simulations	K (Jm-3)	Ms (emu/cc)	Temperature (K)	Viscosity (mPa.s)	NP mean diameter	Polydispersity	Mean cluster diameter	Cluster polydispersity
Brownian only	**50000**	330	310	0.7	17.4	0.27	21.3	0.30
Brownian & Néel Best fit to data	**7200**	330	310	0.7	17.4	0.27	21.3	0.30
Predominantly Néel	**4000**	330	310	0.7	17.4	0.27	21.3	0.30

The results expected if the suspension contained either only blocked particles (Brownian relaxation), or predominately Néel relaxation behavoiur was simulated by increasing or decreasing the anisotropy constant respectively (see Table 3.2). These simulations are compared to the data in Figure 3.12 (top and bottom plots respectively) and show how both the apparent position as

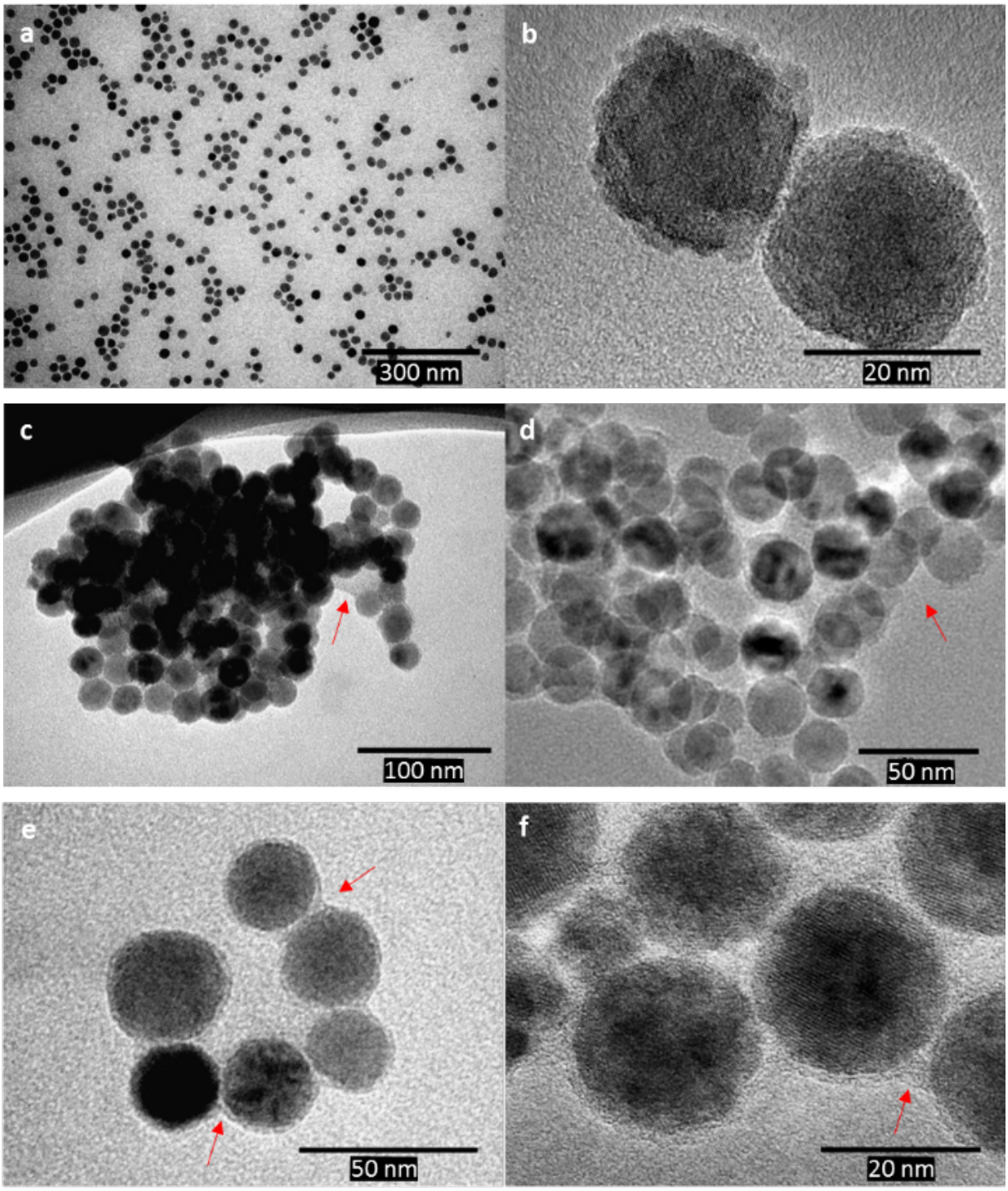

Figure 3.11 TEM micrographs of MNP samples of (a) and (b) PEI 0 without PEI coating, (c) and (d) PEI 50 showing MNP aggregation, and (e) and (f) PEI 1000 with even PEI coating around MNP. Red arrows indicate a layer of PEI coating around MNPs.

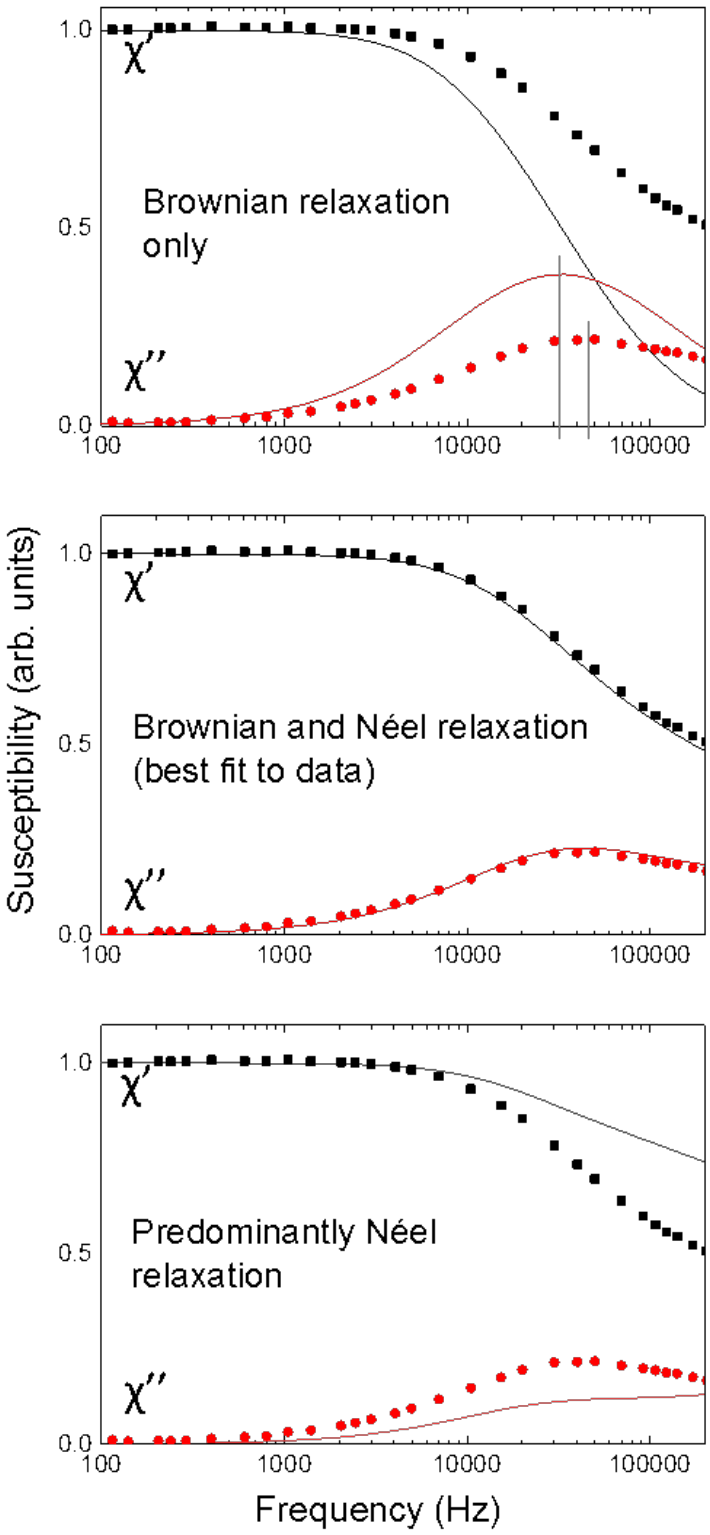

Figure 3.12 ACS measurements of sample PEI 0 before dialysis (symbols) compared to simulated data obtained by fitting the cluster size distribution and polydispersity. The middle plot shows the best-fit data whilst the magnetic anisotropy used in the simulations was varied to produce the expected result for particles undergoing purely Brownian relaxation (top) or predominantly Néel relaxation (bottom).

well as the intensity of the χ" peak is affected by the magnetic properties of the particles. The best-fit curve was obtained by modelling a log-normal distribution of nanoparticle clusters with a mean diameter of 20.4 nm. This value is only slightly larger than the mean nanoparticle diameter of 17.4 nm, which is consistent with the formation of small clusters in suspension containing one or occasionally two particles as suggested by the TEM images (Figure 3.11 a&b).

This analysis was extended to the PEI sample series where the change in viscosity of the suspensions with significant addition of PEI (i.e. samples PEI 500, PEI 1000 and PEI 2000) before dialysis, was included in the model (see Table 3.3). From equation 1.5 it can be seen that if the viscosity is assumed to be that of water, the calculated hydrodynamic diameter of the clusters will be ∼20% higher than that obtained using the viscosity values shown in Table 3.3.

Table 3.3 Parameters used for ACS simulations for each MNP sample. Mean cluster diameter and polydispersity are outputs from simulations.

Sample	Treatment	K (Jm-3)	Ms (emu/cc)	Temperature (K)	Viscosity (mPa.s)	NP mean diameter	Polydispersity	Mean cluster diameter	Cluster polydispersity
PEI 0	Before dialysis	7200	330	310	**0.7**	17.4	0.27	**20.4**	**0.30**
PEI 50	Before dialysis	7200	330	310	**0.7**	17.4	0.27	**31.7**	**0.44**
PEI 500	Before dialysis	7200	330	310	**1.4**	17.4	0.27	**22.2**	**0.32**
PEI 1000	Before dialysis	7200	330	310	**1.4**	17.4	0.27	**20.4**	**0.30**
PEI 2000	Before dialysis	7200	330	310	**1.4**	17.4	0.27	**20.6**	**0.30**
PEI 0	After dialysis	7200	330	310	**0.7**	17.4	0.27	**29.1**	**0.60**
PEI 50	After dialysis	7200	330	310	**0.7**	17.4	0.27	**42.7**	**0.33**
PEI 500	After dialysis	7200	330	310	**0.7**	17.4	0.27	**21.8**	**0.36**
PEI 1000	After dialysis	7200	330	310	**0.7**	17.4	0.27	**21.0**	**0.34**
PEI 2000	After dialysis	7200	330	310	**0.7**	17.4	0.27	**20.9**	**0.35**

3.3.7.5 Evaluation of PEI coating and MNP clustering behaviour

This study demonstrates the changes in MNP size and clustering with gradual loading of surface coating. PEI of different mass was added into an MNP suspension and sonicated to disperse aggregates. The starting material is MNP before addition of PEI (PEI 0 before dialysis). PEI of 1 mg/mL was then added into the MNP suspension at different mass (50, 500, 1000, 2000 μg) and sonicated to disperse particles. Based on Equation 1.5, ACS Brownian relaxation is affected by suspension viscosity. Therefore, the viscosity of PEI at concentrations corresponding to samples PEI 500, PEI 1000, and PEI 2000 before dialysis were measured using rheology and the values obtained were used for the corresponding samples to simulate average cluster sizes, assuming highest viscosity for the samples of 0.0014 Pa.s (Figure 3.8). After PEI coating, the MNP-PEI suspensions were subjected to dialysis to remove free PEI by passive diffusion.

ACS measurements were performed for all MNP-PEI samples before and after dialysis. Mean ACS plots with standard deviation (n=4) for all 10 samples are shown in Figure 3.13.

3.3.7.6 Simulations of ACS measurements to determine hydrodynamic sizes

The ACS data measured before and after dialysis, together with best-fit simulation curves are shown for the PEI 0, PEI 50 and PEI 2000 samples in Fig. 3.14a. In all cases a reasonably close fit was obtained. In particular, the simulations reproduce the changes to the peak positions and breadths for different treatments. The corresponding log-normal distribution of cluster sizes determined in each case are shown in Fig. 3.14b, whilst the results obtained for the full sample set are given in Table 3.4.

To determine particle clusters and hydrodynamic sizes, the primary MNP size (starting material) was set to 17.4 nm with polydispersity of 0.27 in the simulation software based on TEM size distribution. Particle cluster simulations were performed on all samples by inputting cluster particle size and polydispersity into the software to obtain the best simulated ACS fit

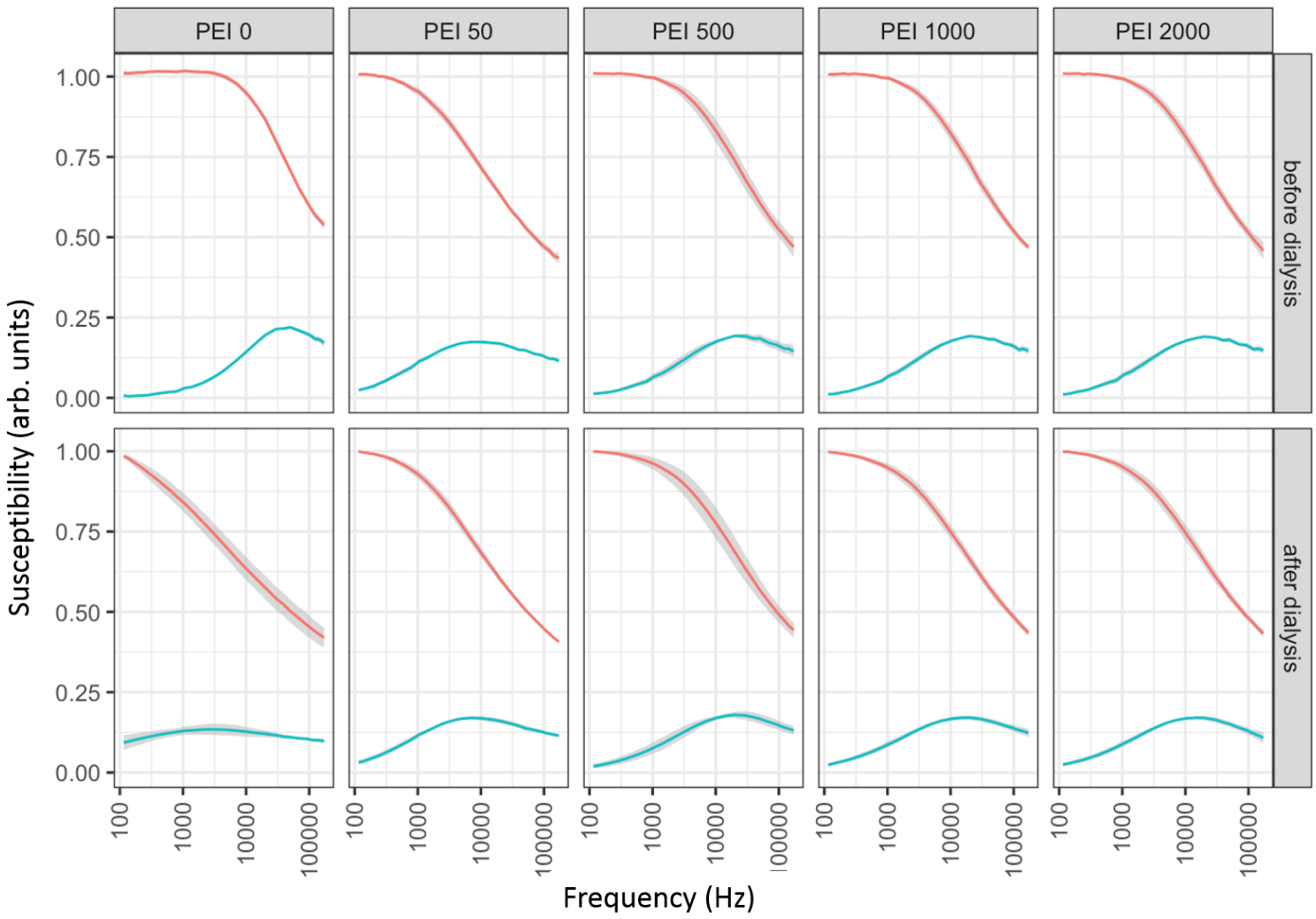

Figure 3.13 Mean of normalized AC susceptibility measurements of MNP loaded with different PEI concentrations, before and after dialysis with standard deviation (grey) (n=4).

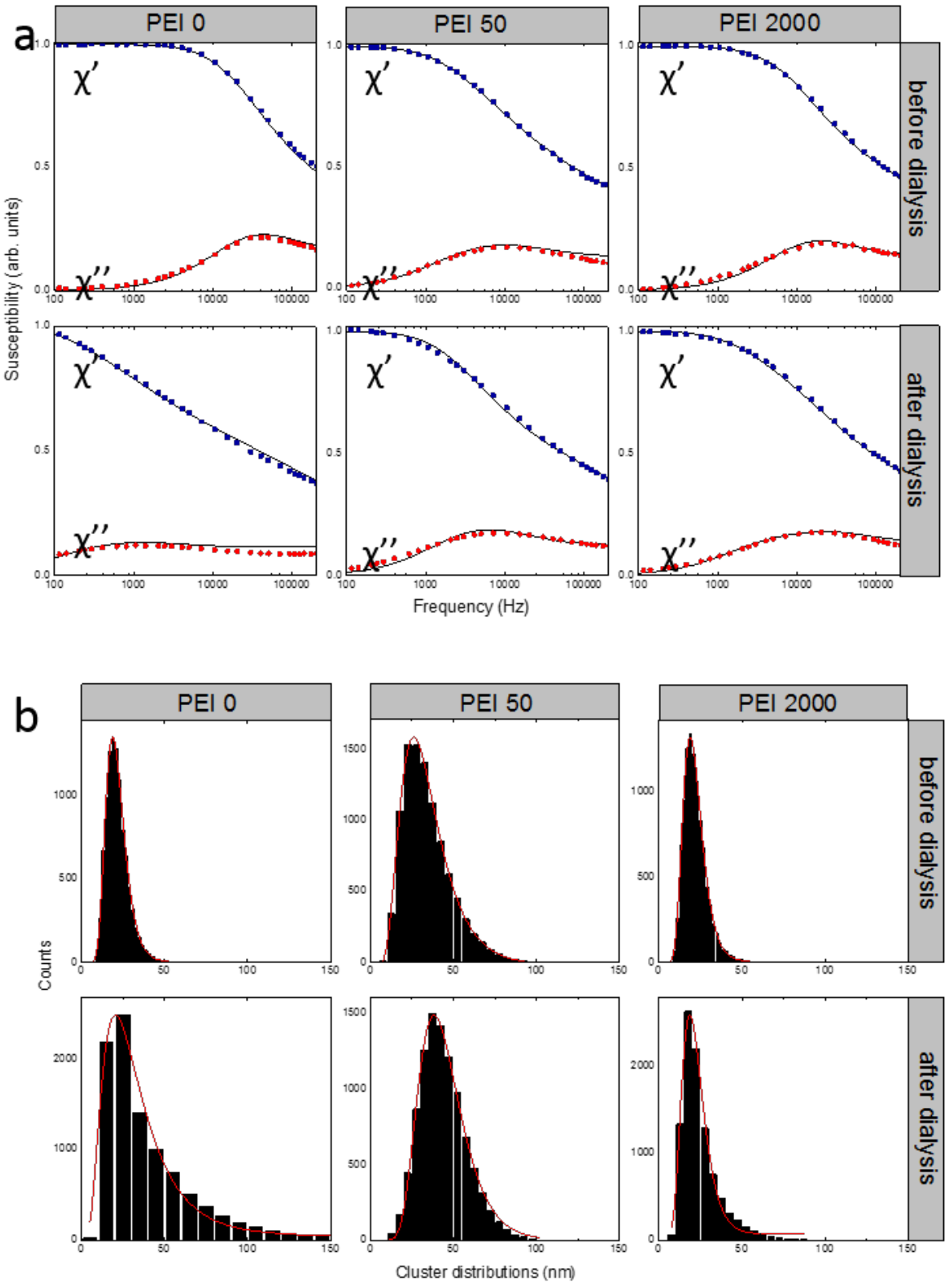

Figure 3.14 (a) ACS measurements from samples PEI 0, PEI 50, and PEI 2000 obtained both before and after dialysis (symbols), together with best-fit simulations. (b) Histograms showing the lognormal MNP cluster distributions used to obtain the best-fit ACS curves shown in Fig. 3.14a.

Table 3.4 Mean cluster diameter and polydispersity index determined from all MNP suspensions in as-prepared state and after dialysis, obtained from best-fit simulations to the measured AC susceptibility data. Errors shown represent the uncertainties estimated from the uniqueness of the simulation fits.

Sample		Mean cluster diameter (nm) ± 0.2	Polydispersity Index ± 0.01		Mean cluster diameter (nm) ± 0.2	Polydispersity Index ± 0.01
PEI 0	As prepared	20.4	0.30	After dialysis	29.1	0.60
PEI 50		31.7	0.44		42.7	0.33
PEI 500		22.2	0.32		21.8	0.36
PEI 1000		20.4	0.30		21.0	0.34
PEI 2000		20.6	0.30		20.9	0.35

to the real measurements. By monitoring gradual PEI coating using ACS, the concentration of coating required to uniformly coat MNPs can be determined.

Sample PEI 0 before dialysis shows a lognormal MNP distribution of 20.4 nm diameter and polydispersity of 0.30. Addition of 50 μg of PEI (PEI 50 before dialysis) shifts the χ" peak towards lower frequencies corresponding to a mean diameter of 31.7 nm, with a broad peak distribution attributed to a high polydispersity of 0.44. At PEI 500 before dialysis, the MNP diameter dropped to 22.2 nm with a low polydispersity of 0.32. At PEI 1000 before dialysis and PEI 2000 before dialysis, particle sizes begin to stabilize at around 20.4–20.6 nm, with the same polydispersity as the starting sample. The MNP size and Brownian peak stabilization at 19 800 Hz indicates saturation of PEI coating on the nanoparticles. PEI unattached to the MNPs in the system is not detected by the AC susceptometer, hence adding more PEI will not result in a significant change in MNP hydrodynamic size beyond coating saturation.

Samples after dialysis show higher polydispersity of MNP, which can be observed from the ACS plots showing broader peak distributions compared to samples before dialysis (Figure 3.14). Sample PEI 0 after dialysis served as an indicator to the dialysis process, in which all the samples from PEI 0 to PEI 2000 are dialyzed in the same water bath for each sample set. At high PEI concentration, samples containing free, unattached, or weakly bound PEI move into the dialysate through the semi-permeable membrane of 50 kDa molecular weight cut-off (MWCO). Similarly, PEI movement from the samples into the dialysate increases the concentration of PEI in the dialysate compared to sample PEI 0 before dialysis which contains no PEI. The resulting concentration gradient creates movement of free PEI into sample PEI 0 which then attaches to the negatively charged particles, forming highly aggregated particles due to electrostatic interactions and non-uniform coating (sample PEI 0 after dialysis). The χ" curve also intercepts above zero at the y-axis, indicating larger particle clusters with relaxation frequencies below the measurement limit of 10 Hz (Figure 3.14a, PEI 0 after dialysis). The clustering is largely due to insufficient amount of PEI to uniformly coat particles individually. PEI therefore wraps around clusters of particles creating multi-core aggregates and this results in instability and sample flocculation. The measured mean diameter is 29.1 nm, however the large polydispersity of 0.60 explains high MNP agglomeration.

After dialysis, the particles retain a similar average mean diameter. Sample PEI 50 after dialysis had a large mean cluster size of 42.7 nm, however in sample PEI 500 the particle sizes

dropped to 21.8 nm after dialysis. Mean particle sizes dropped further (∼1 nm) for samples PEI 1000 and PEI 2000 after dialysis. The polydispersity of samples PEI 500, PEI 1000, and PEI 2000 was higher compared to before dialysis. This effect could be due to the stripping of loosely bound PEI from the surface of MNPs, leaving only tightly bound MNPs which reduced stearic and ionic hindrance which caused incresed agglomeration.

3.3.7.7 Size determination by dynamic light scattering of MNP samples

PEI-coated MNP samples were measured on the zeta sizer to obtain a size distribution by DLS. The corresponding hydrodynamic sizes obtained by DLS are shown in Fig. 3.15. Sample PEI 0 before dialysis measured an average of 26 nm hydrodynamic size, which was larger compared to the AC susceptometer measurements. After dialysis, PEI 0 showed three large size distributions, from 160 to 3000 nm. Sample PEI 50 almost doubled in size with the introduction of PEI into the system, from 26 nm to 47 nm. After dialysis of PEI 50, the sample shows an increase in size to 62 nm, with 2 percent of the measured population posessing 194 nm size distribution. Similar to the ACS measurements, PEI 50 showed an increase in size after dialysis.

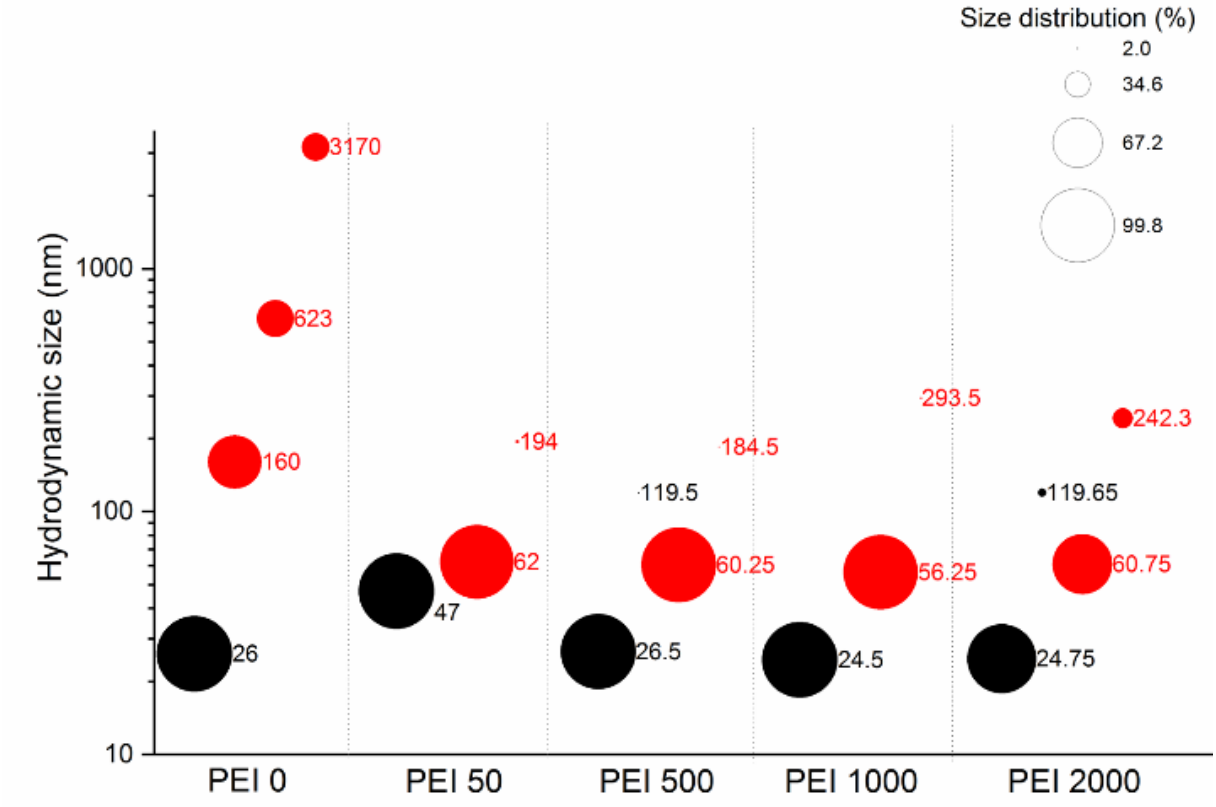

Figure 3.15 DLS hydrodynamic size measurements of MNP-PEI samples before dialysis (black) and after dialysis (red). The viscosity values are given in Table 3.3.

The addition of more PEI with sample PEI 500, the size distribution increased to 53 nm, with a small percentage of large aggregates. At PEI 1000 however, the particle size starts to decrease and remains constant at PEI 2000. Samples PEI 50, 500, 1000, and have a small distribution of particles above 150 nm. This can be attributed to excess PEI in the system which has a tendency to form large polyplexes, however the amount of large particles in the system are negligible. Samples after dialysis show a larger MNP size distribution, although the increase is much larger than calculated from ACS measurements.

3.4 Discussion

Synthesized MNP suspensions mostly consist of a mixture of Brownian and Néel relaxed particles. Maldonado-Camargo et al. derived simple equations to estimate the fractions of the two particle types within a suspension, on the condition that there was no overlap between both Brownian and Néel relaxation times (Maldonado-Camargo et al., 2016). However, often the synthesis of MNP suspensions leads to a combination of both Brownian and Néel particle behaviour that results in an overlap in the corresponding χ" peak positions. ACS simulations in Figure 3.12 show that in such MNP suspensions, the size of MNPs derived using the Brownian peak position using Equation 1.5 will be inaccurate as the overlap between the Brownian and Néel χ" peaks shifts the Brownian peak position to the right, making the calculated particle size smaller than its true value (top). Similarly, a predominantly Néel relaxation population diminishes the Brownian peak (bottom). Therefore the computational modelling of measured ACS samples improves the accuracy of size determination in this case, as the MNPs synthesized by thermal decomposition contains both Brownian and Néel relaxation populations.

Dialysis was performed as a washing step to remove unbound PEI from the tdMNP-PEI suspension. Dialysis is a relatively gentle process and so does no strip PEI attached to particles, nor subject the samples to harsh treatments such as strong forces with repetitive centrifugal filtration which may clump particles at the bottom of the filter, or magnetic separation columns which can strip the coating off by shear flow of washing solutions and which also requires a large amount of sample. During dialysis, passive diffusion occurs due to a concentration gradient, which generates movement of unbound PEI from high PEI concentration in the dialysis tube to low concentration in the dialysate (distilled water) until an equilibrium is reached. This allows unbound PEI to be removed from the MNP-PEI suspension, leaving only PEI attached to the particles.

Based on zeta potential measurements, the dialysis procedure was successful based on sample PEI 0 after dialysis, where due to the low concentration of PEI there was an influx of free PEI from the dialysate into sample PEI 0, which neutralized the anionic $-COO^-$ groups on the surface of tdMNPs. Besides that, zeta potential measurements provided evidence for the successful PEI coating on tdMNP surface, given the high positive charge density in samples containing PEI. The dialysis procedure was suitable for removing excess PEI in the suspensions without stripping PEI from the surface of MNP, as the ionic interaction between PEI and carboxylic groups was strong enough to withstand dialysis. Further studies of the presence of PEI coating on MNPs was performed using TGA, and the loss of weight from MNP samples with the addition of PEI (PEI 50, 500, 1000, and 2000) indicates the decomposition of PEI from the surface of MNP. The TGA measurement of PEI reference sample (Figure 3.10) decomposes at a lower temperature ($<300\,^{\circ}C$) than observed in MNP-PEI samples. Previous studies have also observed a higher PEI decomposition temperature when attached to NPs (Dinari and Ahmadizadegan, 2014). TEM micrographs confirms the presence of a coating on the surface of MNPs, where a thin layer of PEI can be observed for sample PEI 2000, showing a uniform coating around MNPs. TEM of sample PEI 50 reflects the large cluster size distributions modelled in Figure 3.14, where aggregates of MNP clusters can be observed.

From the results shown in Fig. 3.14b and Table 3.4 for fits to the measured ACS data, the addition of small amounts of PEI (as is the case for sample PEI 50) leads to a substantial increase in the mean cluster size from 20.4 nm to 31.7 nm, as well as an increase in the polydispersity of the clusters from 0.30 to 0.44. This is consistent with an insufficient amount of PEI to uniformly coat particles individually. PEI therefore wraps around clusters of particles creating multi-core aggregates and this results in instability and sample flocculation. This can be seen more dramatically for sample PEI 0 after dialysis, where a similar increase in mean cluster size was determined but with a very large polydispersivity index (0.60) suggesting a highly aggregated and destabilised sample. As this sample contains no PEI, the effect must be caused by free PEI diffusing along the concentration gradient from the dialysate into the dialysis tube of sample PEI 0, as suggested earlier by the neutralisation of the zeta potential. The PEI 0 sample thus acted

as an indicator of the dialysis process, confirming the removal of free and loosely bound PEI from the other samples. The PEI 50 sample also shows an increase in the mean cluster diameter after dialysis, again suggesting an influx of free PEI from the dialysate. This is not unexpected as there should be little free PEI in this sample, with a concentration gradient similar to PEI 0.

However, the higher loading PEI samples (PEI 500 and above) show no real change in mean cluster diameter after dialysis, and only a modest increase in polydispersivity. Interestingly, the mean cluster diameter is very similar to that determined for the stable uncoated particles (PEI 0). Although it is possible that some free PEI remains in the suspensions after dialysis, the viscosity was approximated as being the same as for water for these samples (Table 3.3). If a viscosity larger than water was used to determine the cluster sizes after dialysis, a value smaller than that measured for the original stable uncoated particles (PEI 0) would be obtained. As this result seems extremely unlikely, the assumptions made regarding the viscosity after dialysis would appear to be valid. Sample PEI 1000 reflects the amount of polymer sufficient to completely coat all MNPs individually with a layer of PEI, providing relative particle coating uniformity. At PEI 2000 and for subsequent addition of PEI into the MNP suspension will result in a high volume of unbound PEI with no change in MNP size or clustering due to saturation of PEI coating on MNP surface.

An advantage of using ACS measurements to study MNP coating for Brownian relaxed particles is that the AC susceptometer only detects the sample of interest without interference from other compounds in the system that do not interact with the particles. Using this technique, accurate measurements of the nanoparticles can be made, interactions with other magnetic and non-magnetic molecules can be studied, and saturation of particle coating can be quickly observed without additional characterization methods. By observing the changes in MNP hydrodynamic size, optimal coating with minimum free PEI in the system can be deduced and the amount of particle to coating ratio can be easily calculated. This information can help eliminate washing steps during MNP coating, as well as reducing the need for using excess coating material or surface ligands. Using ACS for characterization of MNP coating makes it a fast, efficient and cost effective process with no sample loss, minimal use of coating material, and exclusion of the washing step.

The hydrodynamic sizes obtained by DLS are shown in Fig. 3.15. It was observed that the trend in the values measured before dialysis is nearly identical to that found with the ACS measurements, but with hydrodynamic sizes $\sim$30% larger than the corresponding cluster diameters determined from ACS. However evidence of some much larger particles can also be seen (for example PEI 2000 before dialysis). As particles of such size are not seen in the ACS measurements, it is possible that these represent the formation of pure PEI polyplexes that are not detected by ACS.

The agreement with the ACS data is far worse for the samples measured after dialysis. A large proportion of very large particles (>160 nm) was observed for sample PEI 0 after dialysis. As evidence was found for free PEI diffusion into this sample, it is likely that DLS includes measurements of the resulting polydisperse tdMNP-PEI aggregates as well as a proportion of PEI polyplexes, thus making an assessment of MNP cluster sizes impossible. In a similar fashion the DLS measurement indicates much larger particle sizes than ACS for the PEI-coated MNPs after dialysis. Thus the different values determined by the two techniques could be due to the disproportionate response of DLS to large particles which can tend to skew the calculated hydrodynamic size distributions.

3.5 Conclusion

This study demonstrates that AC susceptibility is a sensitive and precise method to measure changes in aggregation and coating of MNPs in complex suspensions, even when both Brownian and Néel relaxation mechanisms are present. As the technique is sensitive to only the magnetic

signal in the suspension, it is possible to separate the behaviour of the MNPs from other particulates in the suspension. This enables insight into complex MNP suspensions where conventional techniques such as dynamic light scattering are compromised by the presence of other species such as PEI polyplexes.

By combining AC susceptibility with other characterisation techniques such as zeta potential measurements, TEM, and TGA, it was possible to determine the optimum PEI coating on tdMNPs to obtain small MNP clusters with dense PEI coatings. The results showed that the combination of PEI loading, sonication and dialysis results in the formation of clusters of similar size to the original uncoated MNP clusters, with stable high-density coating resulting in high zeta potential values of $\sim$+50 mV. Evidence from ACS and zeta potential measurements also suggested that free (unbound) PEI was removed from these particle suspensions after dialysis. The resulting uniform and highly stable PEI-coated MNPs are suitable for applications in nanomagnetic gene transfection applications.

Chapter 4

Uptake Efficiency and Optimization of MNP-PEI Transfection Complexes in Cells

4.1 Introduction

The principle of nanomagnetic transfection was discussed in Chapter 1, including the benefits of this method compared to conventional chemical transfection methods. Transient and stable transfection using MNPs have been shown to be successful across different cell types (Zhao et al., 2014). The usefulness of MNPs extends beyond transfection agents as they can perform secondary tasks such as MRI imaging, drug delivery, and cell separation (Sanchez-Antequera et al., 2011; Shah et al., 2013; Sun et al., 2008).

Biocompatibility of engineered biomaterials is important when used in applications for cell therapies. Many factors can affect cytotoxicity and cell-MNP interaction, such as the surface coating, size, surface charge, and core composition of MNP. Therefore, I will briefly discuss the effect of MNP size and core composition on their internalization into cells and the corresponding toxicity.

Commercial MNPs for transfection are readily available from companies such as nanoTherics, OZ Biosciences, and chemicell. These commercial MNPs are synthesized and designed for specific purposes such as protein expression and gene silencing, as well as for transfecting specialized cells such as neurons. nTMag is a popular nanomagnetic transfection agent from nanoTherics and has been shown to obtain high transfection efficiencies (Fouriki and Dobson, 2013; Lim et al., 2012). This study focuses on using nTMag as a transfection agent to study the parameters that affect nanomagnetic transfection efficiency such as MNP dosage, MNP to DNA binding ratio, cell density, and frequency and amplitude of magnefect-nano oscillation. nTMag will also be used as a benchmark to study the efficiency of the tdMNP transfection agent synthesized in the lab (described in Chapter 3). Using the same parameters that affect transfection rates of nTMag, the highest efficiency that tdMNP can achieve was studied while taking into account cytotoxity. PEI is widely used as a transfection agent for its availability, low cost, and ease of preparation. This polymer is, however, toxic to cells at high doses. Both nTMag and tdMNP were coated with PEI, and the toxicity of this PEI coating on cells was assessed. Finally, the commercial nTMag and lab-synthesized tdMNP-PEI will be compared for their transfection efficiency and cytotoxicity.

This chapter will be discussed in three parts; the first is the characterization of magnet arrays and localization of MNPs in cells, secondly the effect of coating and particle size on uptake into cells, and the third is assessment of transfection efficiency using nTMag and finally transfection using MNPs synthesized by thermal decomposition (tdMNP). Transfection complexes in this thesis referes to the transfection agent coupled with DNA.

Objectives

1. **Study the parameters that affect nanomagnetic transfection.** To obtain the highest transfection efficiency, the various parameters such as cell seeding density, effect of media change and ratio of MNP-PEI to DNA was determined for both nTMag commercial particles and synthesized tdMNP-PEI. nTMag was used to benchmark the transfection efficiency of tdMNP-PEI.

2. **Study the influence of PEI coating on MNP transfection efficiency.** The effect of excess PEI on transfection rates and cell viability was determined, as well as changes in PEI coating behaviour on MNP surface over time and the resulting transfection activity.

3. **Assess the effect of the horizontal magnefect-nano oscillating system on transfection efficiency.** To determine if an oscillating magnet array system improves transfection, and if oscillation in the horizontal or vertical planes with respect to the cell monolayer improves transfection efficiency. The optimal frequency and amplitude of oscillation on the horizontal magnefect-nano for both nTMag and tdMNP-PEI was also determined, and whether using different particles requires a change in oscillation dynamics.

4.2 Materials and Methods

4.2.1 MagScan and Hall probe measurements

The MagScan probe was placed at 1 mm from the surface to scan just above the surface of a magnet array for the 96-, 24-, and 6- well magnet arrays. The measured area and resolution of scans were set using the MagScan software. A field intensity distribution of the magnetic field was obtained from the scans.

Hall probe measurements were performed to measure magnetic strength. A single magnet from the magnet array was placed on a bench and the Hall probe was positioned at the centre or edge of the magnet, touching the surface (Figure 4.1). The magnetic strength was recorded from the gaussmeter. The probe was then moved upwards to a specific distance from the magnet and the magnet strength recorded. The procedure was repeated until the magnet strength dropped to 0 mT.

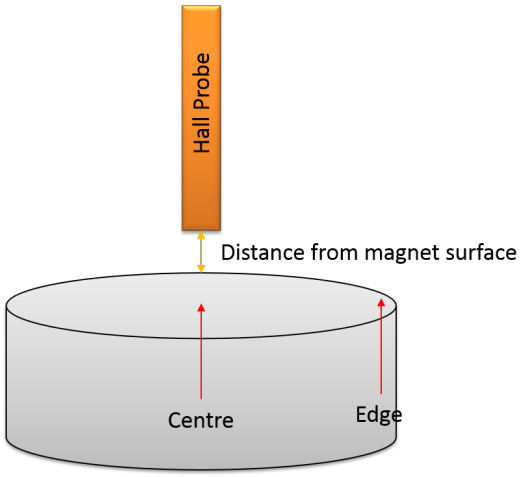

Figure 4.1 Schematic of Hall probe measurements on the surface of the magnet.

4.2.2 Micrograph evaluation of tdMNP-PEI uptake by HeLa cells in a 96- and 24- well plate

To determine the presence of tdMNP-PEI uptake hotspots/localization of uptake, HeLa cells were seeded into a 96- and 24- well plate at a seeding density of 35 000 cells/cm^2 and grown to a

confluency of 70-80% in 24 hours. 6 nL of tdMNP-PEI per 1 μL of CM with a concentration of 0.3 mg/mL Fe was added into the cell monolayer in 24- and 96- wells respectively and incubated for 24 hours. A Prussian Blue assay was performed on the wells and imaged on the confocal microscope from 4 edges of the well to the centre (Chapter 2.4). The images were stitched to obtain an overall view of the bottom of the well showing cells with MNP staining.

4.3 Magnetic separation to remove unbound PEI

The magnetic separation method was used to remove unbound PEI for the MNP cPEI suspension. The magnetic separation LS Column (MACS) was washed with distilled water and placed on the MidiMACS Separator attached to the Multistand. The MNP cPEI suspension was pipetted into the column and the magnetic material attaches to the column beads. The eluent from the column was collected in a waste container and the column was washed 3 times with 2 mL of distilled water to remove unbound PEI. To collect the MNPs, the column was removed from the MiDiMACS Separator and placed in a collection tube. 2 mL of distilled water was added to the column and the solution is flushed out using a column plunger.

4.4 DNA to MNP-PEI binding curve

The loading of DNA to MNP-PEI was studied with a binding curve assay for nTMag and polyMag. This assay was to determine the amount of MNP required to completely bind a fixed mass of 6 μg DNA. With gradual loading of MNP into the DNA solution, the amount of free or unbound DNA in the solution should decrease as the DNA binds and condenses to PEI. Therefore the ratio of MNP-PEI to completely bind 6 μg of DNA was determined.

In eppendorf tubes, 6 μg DNA was pipetted into each tube from a 1 $\mu g/\mu L$ stock solution. To study binding association with nTMag, each tube was pipetted with increasing volumes of the nTMag at 0, 0.1, 0.25, 0.5, 0.75, 1, 1.25, 1.5, 1.75, and 2 μL. Distilled water was added per tube to a final voume of 60 μL. The suspensions were vortexed to mix and left to stand for 15 minutes at room temperature for MNP-DNA complexation. The tubes were then centrifuged at 14 000 g for 5 minutes to pellet the MNP-DNA complexes, leaving unbound DNA in the supernatant. The absorbance of unbound DNA in the supernatant was measured on the Nanodrop 2000 at 260 nm. A graph was plotted for amount of MNP to unbound DNA to obtain the volume of MNP required to sufficiently bind 6 μg of DNA.

The DNA binding curve of polyMag was also studied using the same procedure above, with the same concentration of DNA and MNP transfection agent.

Similarly, the DNA binding curve of synthesized tdMNP-PEI was studied using 6 μg of DNA and with increasing volume of tdMNP-PEI of 0, 0.1, 0.25, 0.5, 0.75, 1.0, 1.25, 1.5, 1.75, 2.0, 2.4, 3.0, 4.5, 6.0, 12.0, 18.0, 24.0, 30.0, 36.0, and 48.0 μL. The assay was performed as detailed above.

4.4.1 Transfection using Lipofectamine 2000

Lipofectamine 2000 is a cationic lipid based transfection agent available commercially and used widely for lipofection gene delivery. This conventional method was used to compare transfection efficiency with the nanomagnetic transfection method.

Cells were seeded in 24 well plates at a density of 35 000 cells/cm^2 and grown to a confluency of 70-80% for transfection. 0.6 μg of DNA in 250 μL serum free DMEM was combined with Lipofectamine 2000 (Invitrogen) at a 1:1 ratio of DNA. The mixture was left to incubate for 5 minutes to form transfection complexes and added into each well containing cells and CM. Media

was changed to fresh CM after 6 hours. The cells were analysed for GFP expression on the flow cytometer 48 hours after transfection.

4.4.2 Transfection using PEI only

Since MNPs were coated with PEI to confer transfection functionality, the transfection efficiency of PEI alone without MNPs were studied.

Cells were seeded in 24 well plates at a density of 35 000 cells/cm^2 and grown to a confluency of 70-80% for transfection after 24 hours. PEI at 1 mg/mL was prepared in distilled water and the pH was adjusted to 7. The solution can be stored at 4 °C for up to 1 month. In 20% volume of serum-free media, PEI and DNA were pipetted and vortexed at a ratio of 4:1. The complex was incubated for 15 minutes and CM was added to make up to a volume of 500 μL per 24 well. The complex solution was added into cells and incubated for 24 hours, where the media containing PEI was replaced with fresh CM. Transfection of cells were measured at 48 hours from PEI-DNA addition.

Effect of pH of PEI on transfection (in Appendix)

PEI suspension of 1 mg/mL was prepared with distilled water and the initial pH was measured at ∼10. To study the effect of pH on PEI, the pH of the suspension was adjusted using HCl and NaOH. PEI was made up fresh and the pH was changed to pH 2, pH 7, pH 10.5, pH 2 and neutralized to pH 7, and aged PEI (>2 months) at pH 7.

Transfection was performed according to the protocol for PEI transfection.

4.4.3 Optimization of transfection – nTMag: DNA complex ratio and complex concentration

To optimize transfection rates using nTMag, the ratio of nTMag to DNA was studied, along with the concentration of the nTMag-DNA transfection complex at different nTMag to DNA ratios.

HeLa cells were seeded into 96-well plates. To make up the transfection complex (transfection agent complexed with DNA) with 1x dilution factor (DF), 6 eppendorf tubes were prepared. 2, 3, 4, 5, and 6 μg of DNA pGFP (1 mg/mL) was added into each tube, respectively. Then 200 μL serum-free media was added. In a 48-well plate, 2 μL of nTMag was pipetted into row A of the well plate, from A1 – A6. The DNA suspension was added into each well based on the transfection complex ratio with DF 1x in 4.1 Column 2. Each suspension was pipetted to mix and left for 15 minutes to form the nTMag-DNA transfection complex. After incubation, 300 μL of CM was added into the wells and mixed by pipetting. Then 250 μL of CM was added into wells B to F columns 1 to 6 in the 48-well plate. 250 μL of the transfection complex from well A1 was added into well B1 below, then 250 μL of the complex from well B1 was transferred into C1 and so on until well F1. The same procedure was performed for columns 2 – 6.

The 96-well plate with seeded HeLa cells were then obtained and 100 μL of each transfection complex was added in duplicate to a 96-well plate. For example, 100 μL of the complex from well A1 in the 48-well plate was transferred into well A1 and A2 of the 96-well plate. This procedure was repeated for all the wells in the 48-well plate. The 96-well plate was then placed on the magnefect-nano and the nanomagnetic transfection procedure was performed.

After GFP expression, the duplicate wells were pooled and transfection efficiency was measured using flow cytometry.

Table 4.1 Transfection complex formation for nTMag:DNA per 96-well.

nTMag : DNA ratio	Dilution factor (DF)					
	1x	2x	4x	8x	16x	32x
	nTMag (µl) : DNA (µg)					
1:1	0.4:0.4	0.2:0.2	0.1:0.1	0.05:0.05	0.025:0.025	0.013:0.013
1:1.5	0.4:0.6	0.2:0.3	0.1:0.15	0.05:0.075	0.025:0.038	0.013:0.019
1:4	0.4:1.6	0.2:0.8	0.1:0.4	0.05:0.2	0.025:0.1	0.013:0.05
1:6	0.4:2.4	0.2:1.2	0.1:0.6	0.05:0.3	0.025:0.15	0.013:0.075
1:8	0.4:3.2	0.2:1.6	0.1:0.8	0.05:0.4	0.025:0.2	0.013:0.1
1:10	0.4:4.0	0.2:2.0	0.1:1.0	0.05:0.5	0.025:0.25	0.013:0.125

4.4.4 Optimization of transfection – tdMNP-PEI: DNA complex ratio and complex concentration

To optimize transfection rates using tdMNP-PEI, the ratio of tdMNP-PEI to DNA was studied, along with the concentration of the tdMNP-PEI-DNA transfection complex at different tdMNP-PEI to DNA ratios.

The protocol for tdMNP-PEI to DNA is similar with nTMag to DNA and the concentration of tdMNP-PEI used was 0.3 Fe mg/mL. The transfection complex was prepared in 6 eppendorf tubes and 0.8, 1.2, 2.4, 4.8, 9.6 and 20 μg of DNA pGFP (1 mg/mL) was added into each tube, respectively. Then 200 μL serum-free media was added. In a 48-well plate, 4.8 μL of tdMNP-PEI was pipetted into row A of the well plate, from A1 – A6. For the samples containing free PEI, 10 μL PEI (1 mg/mL) was pipetted into well A1 – A6 without touching the MNP. The DNA suspension was added into each well based on the transfection complex ratio with DF 1x in Table 2 Column 2. Each suspension was pipetted to mix and left for 15 minutes to form the tdMNP-PEI-DNA transfection complex. After incubation, 300 μL of CM was added into the wells and mixed by pipetting. Then 250 μL of CM was added into wells B to F columns 1 to 6 in the 48-well plate. 250 μL of the transfection complex from well A1 was added into well B1 below, then 250 μL of the complex from well B1 was transferred into C1 and so on until well F1. The same procedure was performed for columns 2 – 6.

Table 4.2 Transfection complex formation for tdMNP-PEI:DNA in a 96-well.

tdMNP-PEI : DNA ratio	Dilution factor (DF)						free PEI (µg/96 well plate)
	1x	2x	4x	8x	16x	32x	
	tdMNP-PEI (µl) : DNA (µg)						
6:1	A1 0.96:0.16	B1 0.48:0.08	C1 0.24:0.04	D1 0.12:0.02	E1 0.06:0.01	F1 0.03:0.005	2
4:1	A2 0.96:0.24	B2 0.48:0.12	C2 0.24:0.06	D2 0.12:0.03	E2 0.06:0.015	F2 0.03:0.0075	1
2:1	A3 0.96:0.48	B3 0.48:0.24	C3 0.24:0.12	D3 0.12:0.06	E3 0.06:0.03	F3 0.03:0.015	0.5
1:1	A4 0.96:0.96	B4 0.48:0.48	C4 0.24:0.24	D4 0.12:0.12	E4 0.06:0.06	F4 0.03:0.03	0.25
1:0.5	A5 0.96:1.92	B5 0.48:0.96	C5 0.24:0.48	D5 0.12:0.24	E5 0.06:0.12	F5 0.03:0.06	0.125
1:0.24	A6 0.96:4.0	B6 0.48:2.0	C6 0.24:1.0	D6 0.12:0.5	E6 0.06:0.25	F6 0.03:0.125	0.0625

The 96-well plate with seeded HeLa cells were then obtained and 100 μL of each transfection

complex was added into each 96 well in duplicates. For example, 100 μL of the complex from well A1 in the 48-well plate was transferred into well A1 and A2 of the 96-well plate. This procedure was repeated for all the wells in the 48-well plate. The 96-well plate was then placed on the magnefect-nano and the nanomagnetic transfection procedure was performed.

After GFP expression, the duplicate wells were pooled and transfection efficiency was measured using flow cytometry.

4.4.5 Nanomagnetic transfection using the MICA vertical oscillating bioreactor

Cells were seeded in 24-well plates at a density of 35 000 cells/cm^2 and grown to a confluency of 70-80%. To prepare the transfection complex, DNA and nTMag at a 1:1 ratio was combined in 20 μL serum-free media per well, vortexed and incubated for 15 minutes in the cell culture hood. Complete media was then added to make up a total volume of 500 μL per well. CM in well plates were aspirated and the transfection complex was added. The plate was placed on the MICA magnet array and the oscillation was set to 1.4 Hz, 20 mm amplitude for 30 minutes. Media change was performed at the end of the MICA set and incubated for 48 hours until GFP expression analysis on the flow cytometer.

4.4.6 Quantification of GFP expression using confocal microscopy

Once cells were ready for GFP expression analysis, the nuclei were stained with Hoescht 33342, trihydrochloride, trihydrate (Thermofisher) at a concentration of 1 $\mu g/mL$ for 30 minutes at room temperature in the dark to reduce photobleaching. The nuclear stain was washed with PBS 1x and fresh CM was added. The cells were imaged under the Olympus Fluoview confocal microscope for the cell nucleus at an excitation/emission wavelength of 405/497 nm; and GFP expression of 488/510 nm. A 10x objective was used with a 2x digital zoom. Each well from the 24-well plate was imaged in 3 randomly selected areas.

The images were analysed using ImageJ image processing software, where the blue channel was converted to a binary image by setting the threshold where nuclei have the least overlap. The 'analyse particles' measurement was selected which provides a particle count of the total number of nuclei in the image. Each count was taken as one cell. To measure GFP expression, a manual cell count was performed using the same software after setting the fluorescence intensity threshold to the highest for all images for uniformity. The numbers were tabulated and the percentage of GFP expression relative to number of cells was determined.

4.5 Results

4.5.1 Characterization of NdFeB permanent magnet arrays

The magnefect-nano horizontal oscillating system uses a NdFeB magnet with three arrangements to fit 6- , 24-, and 96-well plates. The permanent magnets increase transfection time and efficiency by pulling MNP transfection complexes towards cells with the presence of magnetic gradients. To assess the effect of magnetic strength and uniformity of magnetic field across the arrays on MNP uptake in cells, the magnet arrays were measured using a MagScan instrument and Hall probe to obtain a magnetic field intensity distribution across each array and the change in magnetic field strength with increasing distance from the surface of the magnet. MNP uptake in HeLa cells in a 96- and 24- well was observed for 'hotspot areas where particles are localized to specific areas in the well and compared with the magnetic characterization of the arrays.

4.5.1.1 Characterization of magnetic field strength

The magnet arrays were characterized for their magnetic strength and the uniformity of field to better understand the magnetic gradients exerted on MNPs during nanomagnetic transfection. The 6-, 24-, and 96-well permanent magnet arrays used in the magnefect-nano system were characterized using the MagScan system which converts magnetic field strength into magnetic field intensity distribution (Figure 4.2 A). Magnetic gradient measurements from the centre and the edge of one magnet from each array were performed using a Hall probe (Figure 4.2 B). MagScan heatmap colours (red and blue) show measurement of opposing magnetic poles and the colour intensity describes the field strength. For all three magnets, the centre of each magnet measured the highest field strength, with 345 mT for 6-well, 234 mT for 24-well and 365 for 96-well magnets. The magnetic strength gradually decreases towards the edge of the magnets.

Hall probe measurements in Figure 4.2 B show the magnetic strength of each magnet at increasing distance from the surface. For all three magnets, the surface has the highest magnetic strength but the value varies between magnet sizes. The 96-well magnet has the highest field strength at the centre at 400 mT, whereas the 24- and 6-well magnets start at 250–300 mT. At the edge of the magnets, the magnetic strength is similar for the 3 magnet types at 350 mT. The drop in magnetic field with increasing distance away from the magnet surface differed between the magnet sizes. The 96-well magnet showed the steepest drop in magnetic strength and a loss of the field at 10 mm. This was followed by 24-well array with 0 mT at 30 mm and 6 well array at 50 mm from both the centre and edge of the magnets.

Hall probe measurements are useful to determine the positioning and distance from the magnet surface required for the cell culture plate for MNP to be influenced by a magnetic field. A study conducted by Fouriki et al. showed that transfection of cells in cell culture plates decreased with increasing distance from the magnet, with 3 mm from the surface of the magnet showing highest transfection and a strong drop in transfection at 8 mm distance from the magnet surface (Fouriki et al., 2010). Based on the MagScan magnetic field intensity distribution, magnets are arranged in alternating magnetizing directions, which can have a positive effect on transfection. Based on a study by Furlani and Xue, the alternating patterns enhance magnetic strength within each well, as well as creating more uniform MNP sedimentation within wells (Furlani and Xue, 2012). The group modelled the magnetic field and force of a 24-well magnet array, shown in Figures 4.3 and 4.4. The study concluded that alternating magnetization produced a stronger downward magnetic force within wells, which is the configuration used in the magnefect-nano system.

4.5.1.2 Assessing the influence of magnetic field on MNP localized distribution

Cells seeded in a 96- and 24- well plate were placed under a static magnet of the same array type and tdMNP-PEI was added into each well. A Prussian blue assay was performed to determine if localization or 'hotspots of particle internalization occurred based on the field strength exerted by the external magnets.

For the 96-well (Figure 4.5 A), cells were stained blue all across the well but there was a higher intensity of blue staining at the centre of the well. This may be the result of stronger field strength at the center of the 96-well magnet pulling MNPs towards the center of the well plate causing localization of MNP uptake. In the 24-well plate (Figure 4.5 B), a loss in cells was observed in the middle ring of the well. The accumulation of particles in a specific spot is not obvious in the 24-well plate, suggesting uniform dispersion of MNPs in the well despite the stronger magnetic field strength at the center of the magnet. To further understand this effect, future studies should include nanomagnetic transfection to probe the occurrence of transfection 'hotspots per well due to the external field gradients of magnets.

A i

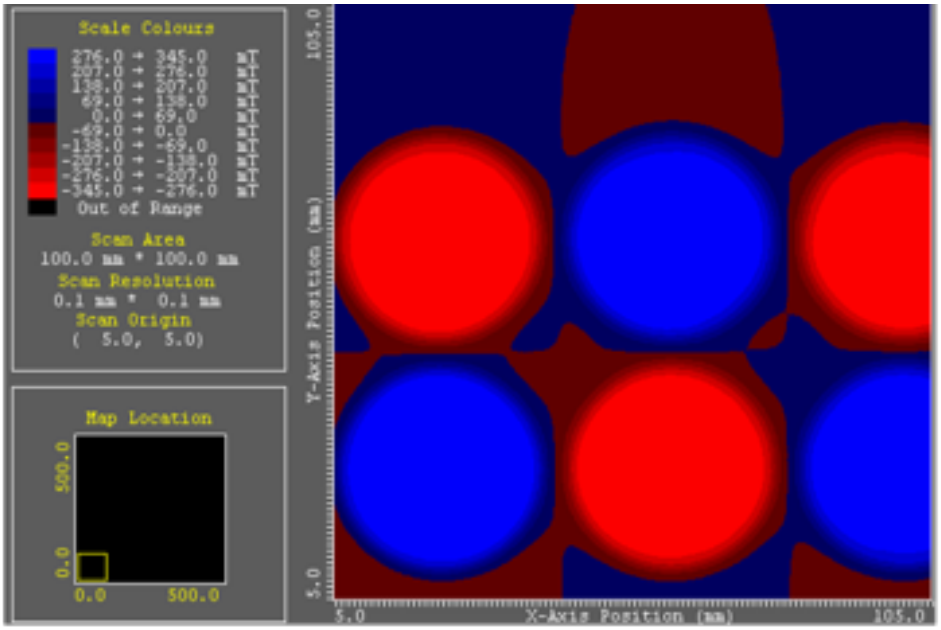
Scale Colours
276.0 → 345.0 mT
207.0 → 276.0 mT
138.0 → 207.0 mT
69.0 → 138.0 mT
0.0 → 69.0 mT
-69.0 → 0.0 mT
-138.0 → -69.0 mT
-207.0 → -138.0 mT
-276.0 → -207.0 mT
-345.0 → -276.0 mT
Out of Range
Scan Area
100.0 mm * 100.0 mm
Scan Resolution
0.1 mm * 0.1 mm
Scan Origin
(5.0, 5.0)
Map Location
500.0
0.0
0.0
500.0
105.0
Y-Axis Position (mm)
5.0
5.0
X-Axis Position (mm)
105.0

ii

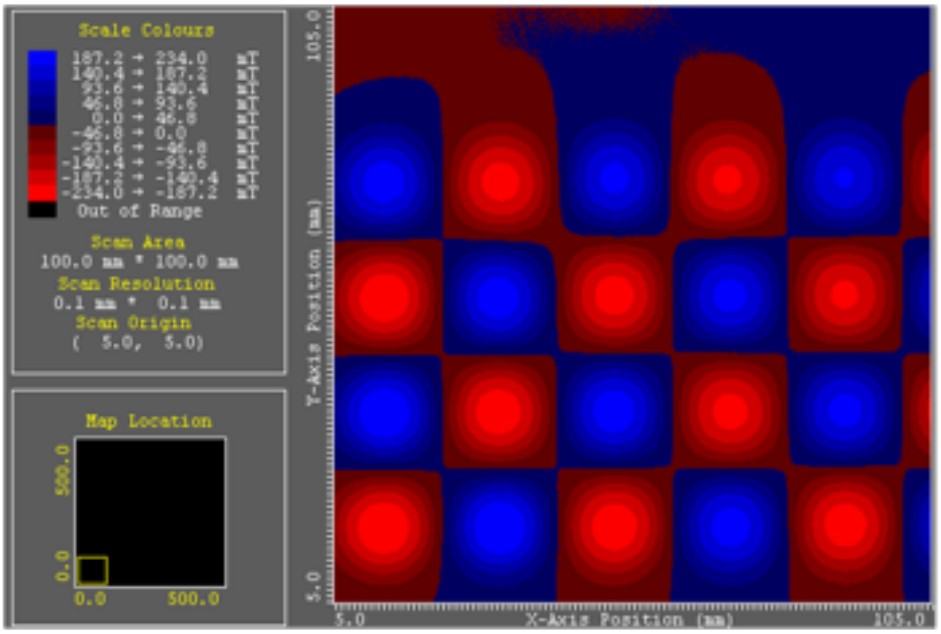
Scale Colours
187.2 → 234.0 mT
140.4 → 187.2 mT
93.6 → 140.4 mT
46.8 → 93.6 mT
0.0 → 46.8 mT
-46.8 → 0.0 mT
-93.6 → -46.8 mT
-140.4 → -93.6 mT
-187.2 → -140.4 mT
-234.0 → -187.2 mT
Out of Range
Scan Area
100.0 mm * 100.0 mm
Scan Resolution
0.1 mm * 0.1 mm
Scan Origin
(5.0, 5.0)
Map Location
500.0
0.0
0.0
500.0
105.0
Y-Axis Position (mm)
5.0
5.0
X-Axis Position (mm)
105.0

iii

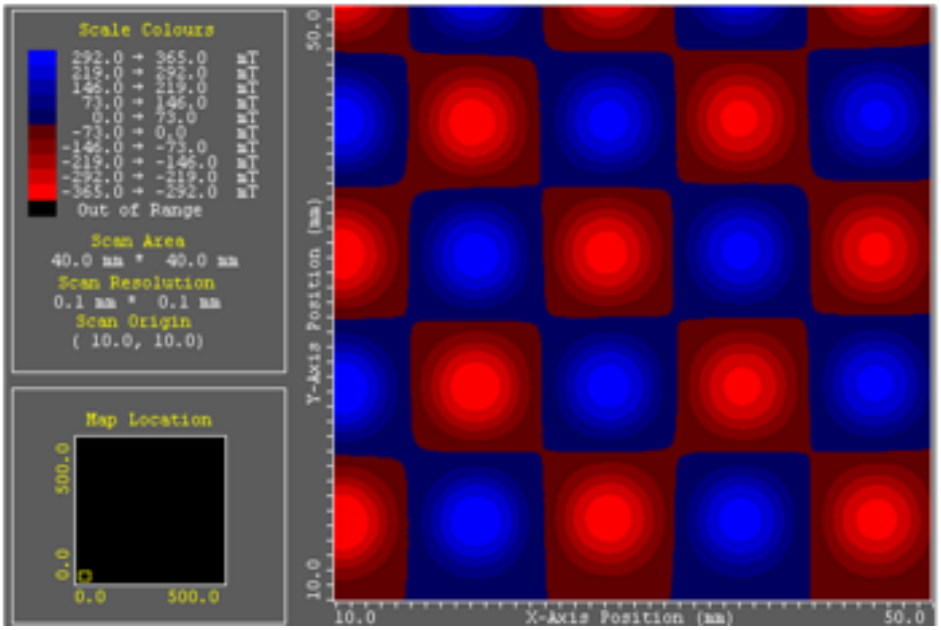
Scale Colours
292.0 → 365.0 mT
219.0 → 292.0 mT
146.0 → 219.0 mT
73.0 → 146.0 mT
0.0 → 73.0 mT
-73.0 → 0.0 mT
-146.0 → -73.0 mT
-219.0 → -146.0 mT
-292.0 → -219.0 mT
-365.0 → -292.0 mT
Out of Range
Scan Area
40.0 mm * 40.0 mm
Scan Resolution
0.1 mm * 0.1 mm
Scan Origin
(10.0, 10.0)
Map Location
500.0
0.0
0.0
500.0
50.0
Y-Axis Position (mm)
10.0
10.0
X-Axis Position (mm)
50.0

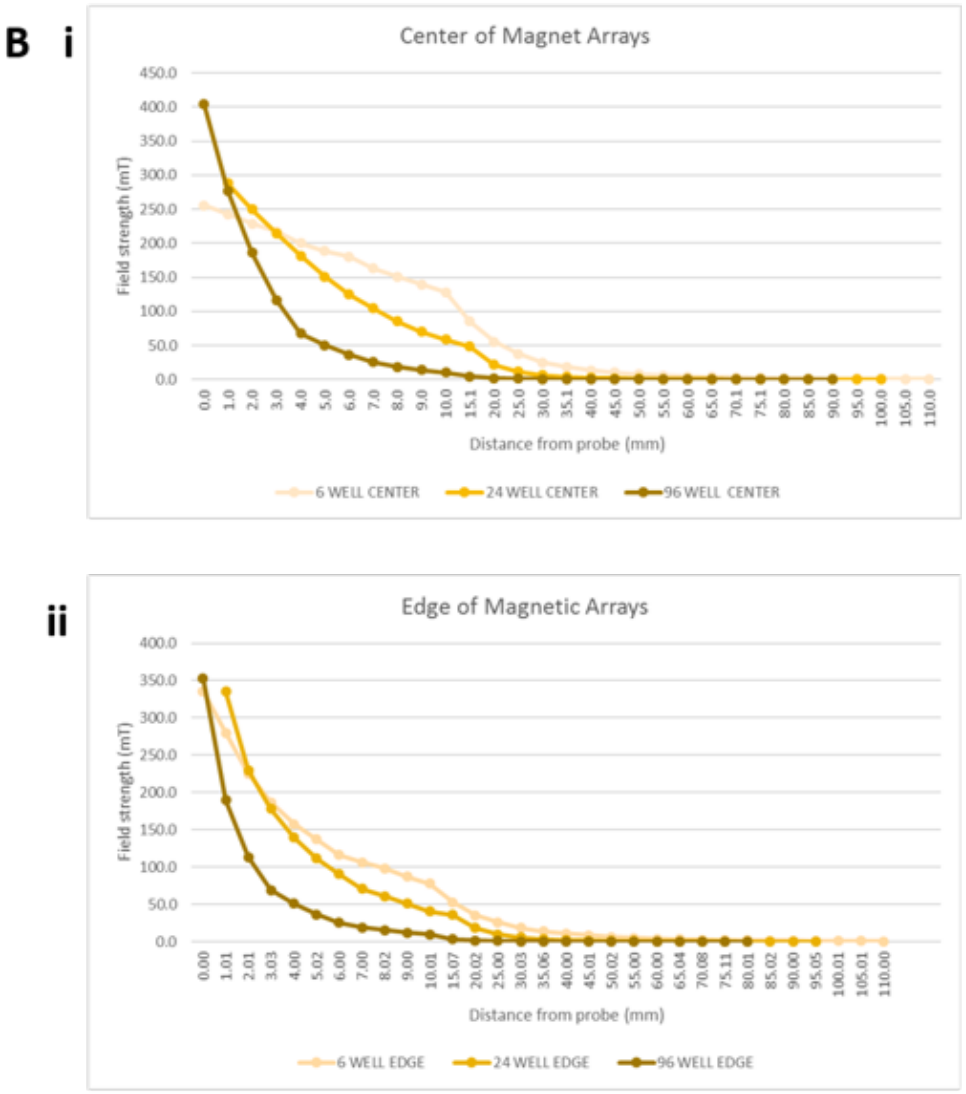

Figure 4.2 (A) MagScan of the permanent magnet arrays used for the magnefect-nano transfection system. Magnetic field intensity distribution showing the field strength of each magnet in the array for (i) 6-well array, (ii) 24-well array, (iii) 96-well array. Red and blue are the alternating poles in the array. (B) Hall probe measurement of the magnetic strength of 6, 24, and 96 single magnet at increasing height from the surface of a magnet from 0 to 100 mm (i) at the centre of a magnet, (ii) at the edge of a magnet.

4.5.2 PEI-coated MNPs: Uptake in cells

Studies have shown MNP internalization rates and the endocytic pathways that MNPs are transported through are dependent on MNP size, shape, and surface coating (Fernandes et al., 2015; Gratton et al., 2008b). To observe this effect, six MNP types were studied for their rate of internalization into HeLa cells. All the particle types were coated with PEI to confer the same charge and polymer type onto the particles, as well as the functionality to transfect cells. The cytotoxicity of particles on cells was also determined.

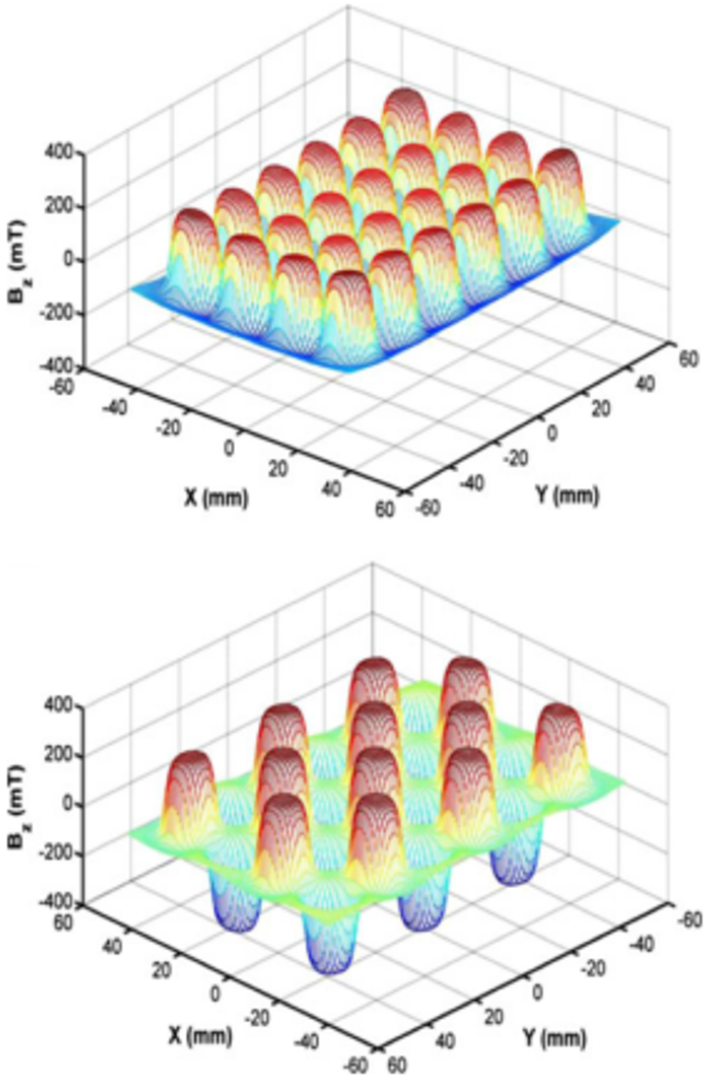

Figure 4.3 Surface plots of the magnetic field **B** for 24-well magnet arrays (top) pointing in the same direction and (bottom) in alternating directions in mT (Furlani and Xue, 2012). Reprinted with permission from Springer publishing group [license number: 4284310696217].

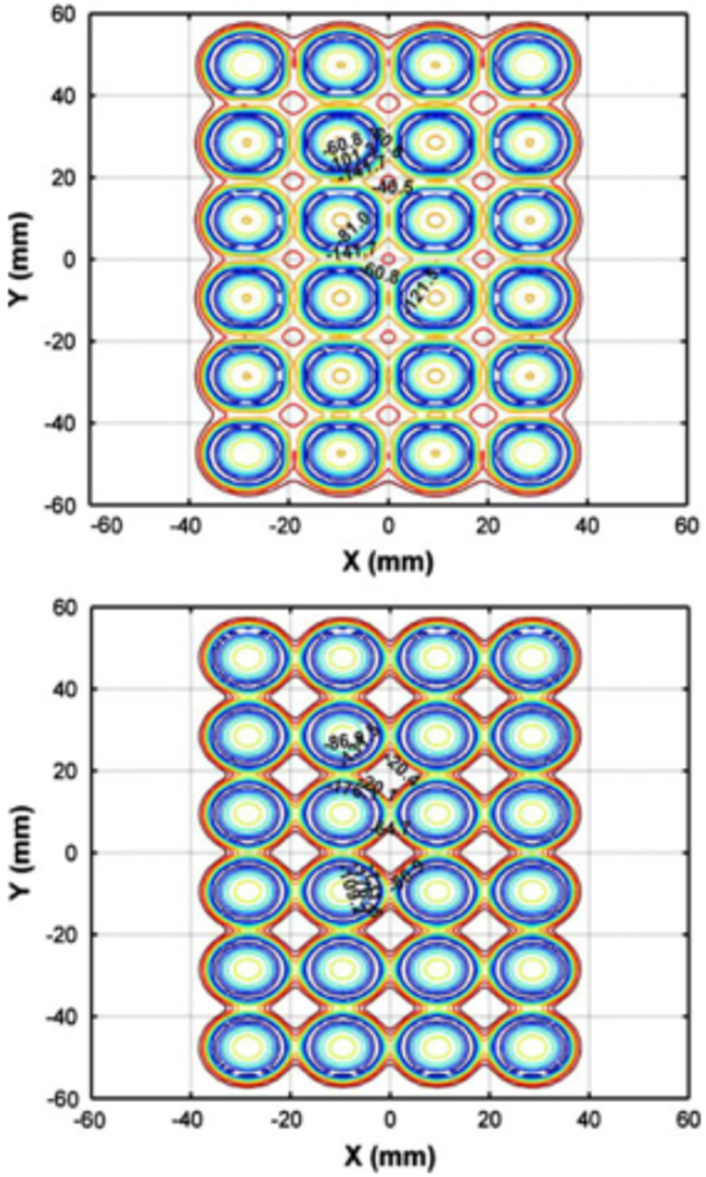

Figure 4.4 Surface plots of the magnetic force **F** for 24-well magnet arrays (top) pointing in the same direction with uniform magnetization and (bottom) in alternating magnetization (Furlani and Xue, 2012). Reprinted with permission from Springer publishing group [license number: 4284310696217].

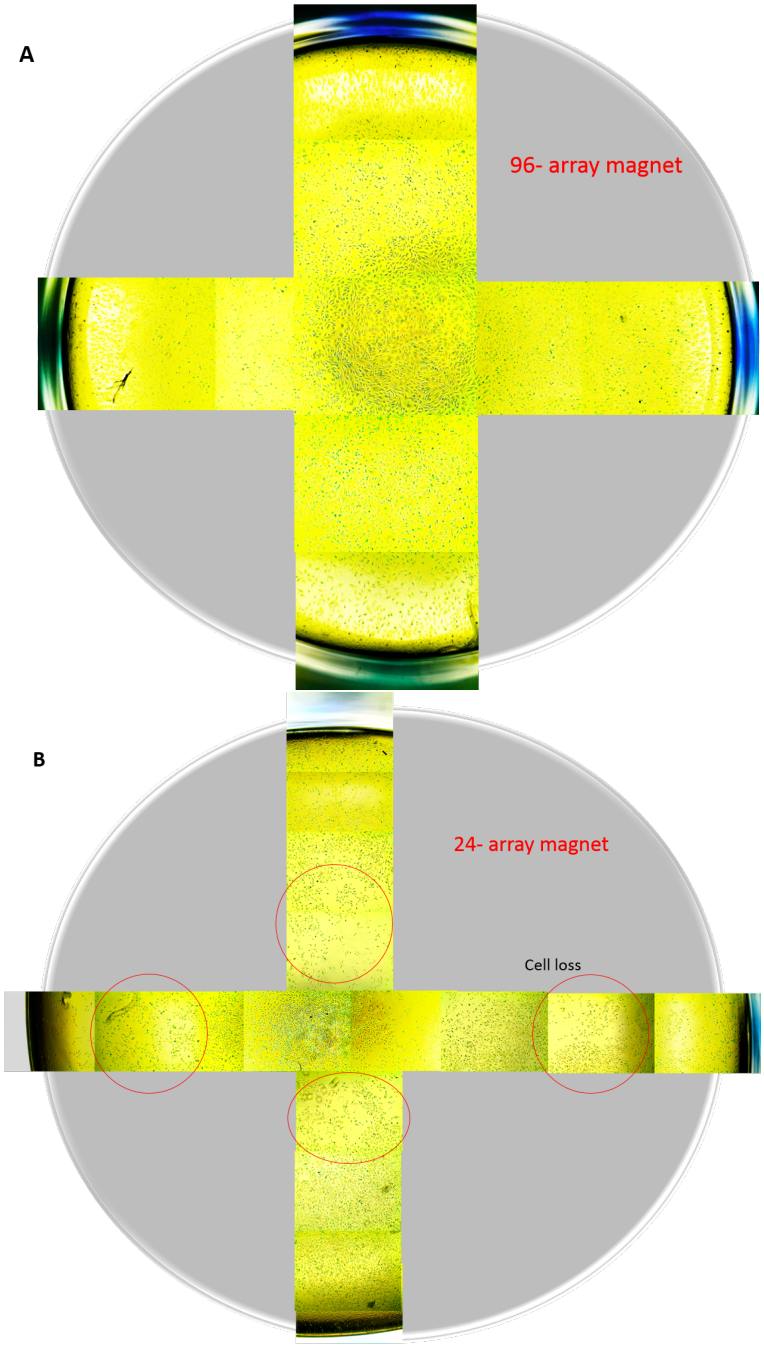

Figure 4.5 Composite brightfield images of prussian blue staining of tdMNP-PEI internalized in cells to visualize 'hotspots' of internalization created by magnet arrays, (A) in a single 96 well, (B) in a single 24 well. Red circles indicate areas of cell loss; n=1

4.5.2.1 Physical and magnetic characterization of PEI-coated MNP

Six types of PEI-coated MNPs were studied for uptake efficiency in HeLa cells as well as their resulting cytotoxicity (Figure 4.6). Flame synthesized maghemite NPs from ETH-Zurich (FS-MNP), co-precipitated maghemite (CoP-MNP) from ETH-Zurich, and commercial maghemite (Sigma-MNP) from Sigma Aldrich were coated with a citric acid coating (detailed in Chapter 2) to confer a negative surface charge with –COOH functional groups followed by a PEI coating by electrostatic physisorption. MNPs synthesized by thermal decomposition were coated with covalently-bound PEI (tdMNP cPEI) (Chapter 3, Materials and Methods), and 2 samples of metallic iron MNPs with carbon shells and surface grafted PEI of 3.4 mmol N/g MNP (SF199) and 7.24 mmol N/g MNP (FB257) were provided by the University of Regensburg (Zeltner et al., 2012).

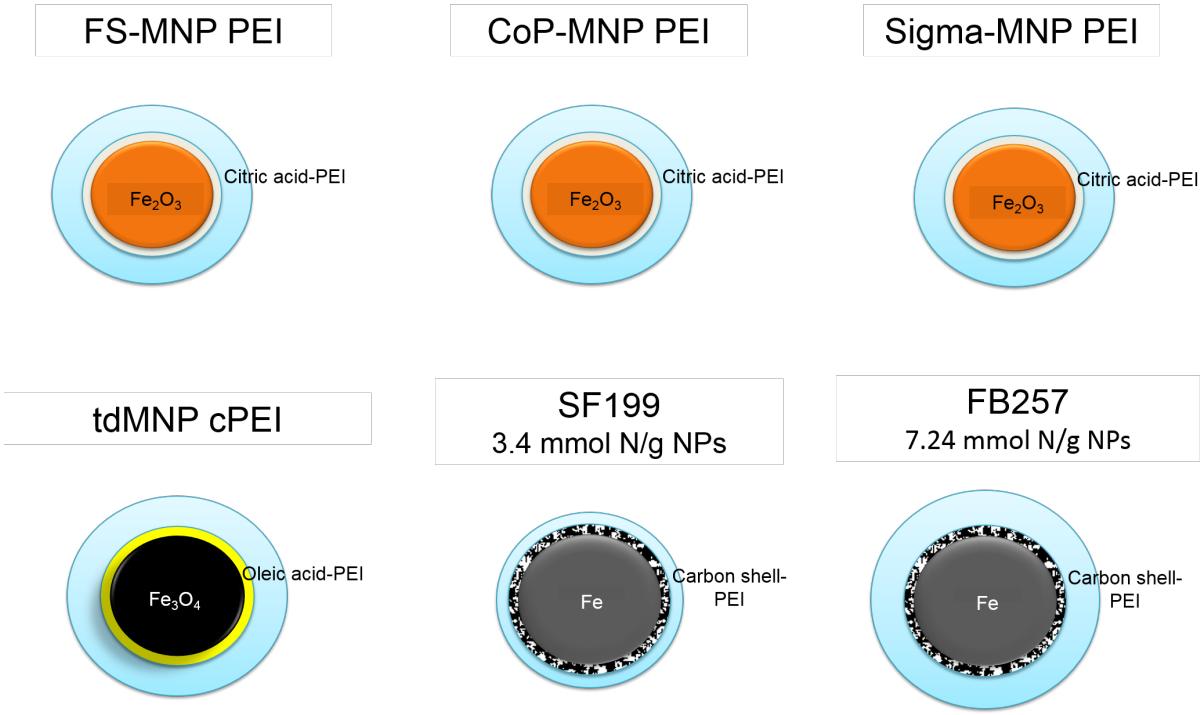

Figure 4.6 Schematic of the six different particle types of maghemite core (orange), magnetite core (black) and metallic iron core (grey), and their different surface coating of either citric acid, oleic acid, or carbon shell. All the particles had an outer PEI polymer coating.

The particles were characterized using AC susceptometry and DLS (Figure 4.7). ACS measurements were obtained for MNP samples before and after PEI coating and changes in the ACS χ" peak were observed, except for SF199 and FB257 which only had measurements with grafted PEI.

Based on ACS measurements, all MNP samples exhibited magnetically blocked properties except for CoP-MNP (Figure 4.7, Row 2) which showed typical superparamagnetic behaviour where the χ" does not show a peak up to frequencies of 500 000 Hz. This is due to the small core size of CoP-MNP, reflected in DLS measurements of PEI coated CoP-MNP, which is only ~30 nm hydrodynamic size.

ACS curves of MNPs exhibiting Brownian relaxation behaviour (FS-MNP, Sigma-MNP, and tdMNP) show shifts in peak positions towards lower frequencies with the addition of PEI. FS-MNP with a strong Brownian peak displayed an increase in hydrodynamic size from 35 nm to 71 nm after PEI coating. DLS measurements of FS-MNP show a measurement nearly identical to the ACS measurement at 73 nm average peak size after PEI coating.

The commercial particles Sigma-MNPs measured a hydrodynamic size of 58 nm, which increased to 103 nm after PEI coating. DLS size distributions shows 2 peaks, one at 85 nm and a small population at 535 nm. tdMNP cPEI exhibiting a partial Brownian relaxation component

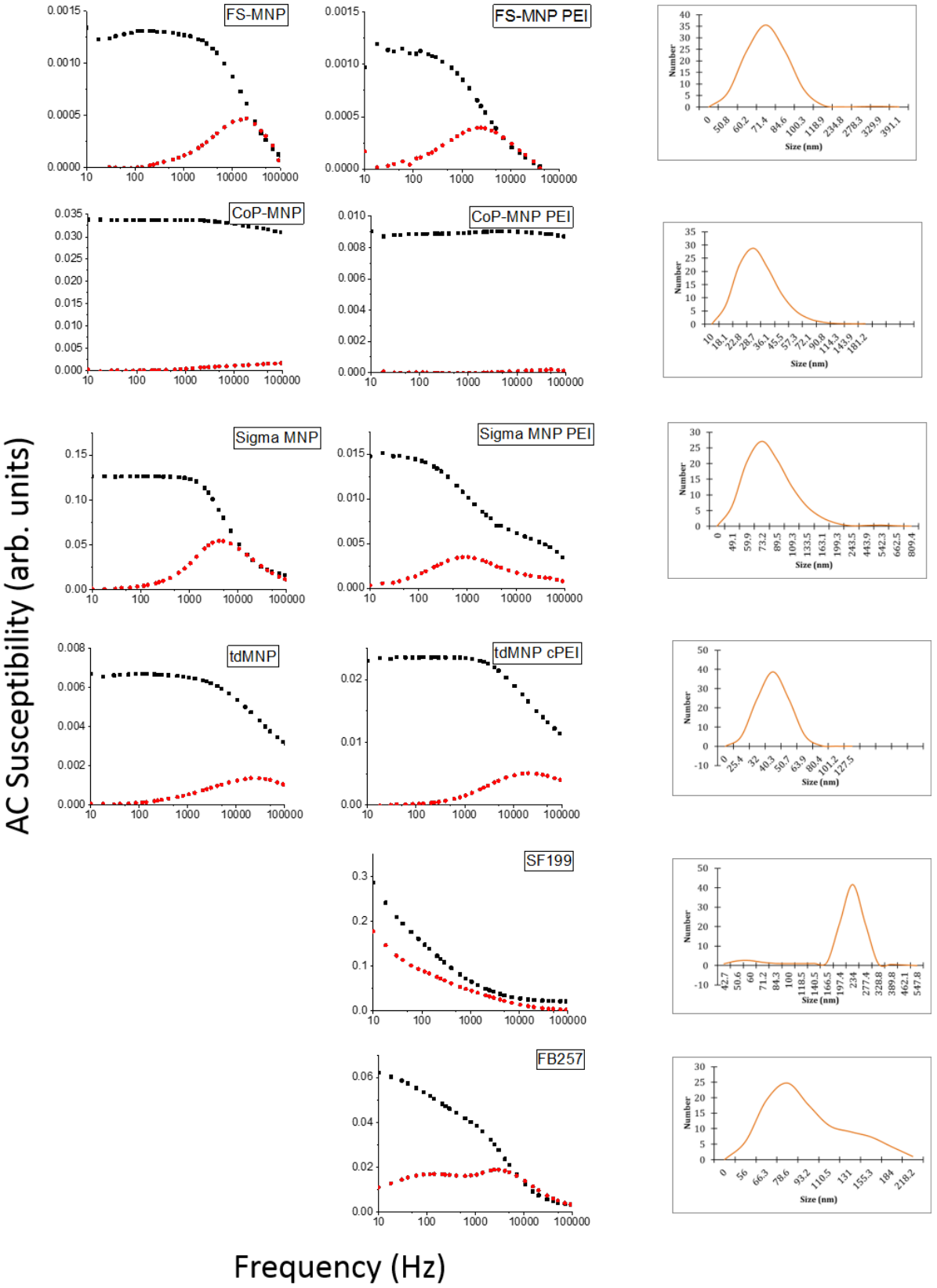

Figure 4.7 AC susceptometry measurements before PEI coating (Column 1) after PEI coating (Column 2), and DLS size measurements after PEI coating (Column 3) of different MNP; n=1.

had a starting hydrodynamic size of 26 nm, and after PEI covalent binding the size increased to 35 nm, and the DLS of tdMNP cPEI was at 42 nm.

Table 4.3 Summary of calculated hydrodynamic sizes of MNP for Brownian peak of ACS, average size of DLS measurements and zeta potential of MNP after coated with PEI.

	Brownian hydrodynamic size (nm)	Average DLS hydrodynamic size (nm)	Zeta potential (mV)
FS-MNP PEI	71	73.2	+ 39.6
CoP-MNP PEI	-	33.4	+ 37.8
Sigma-MNP PEI	103	85.3, 535.1	+ 46.9
tdMNP cPEI	35	41.7	+ 42.9
SF199	> measurable limit	64.8, 233.3	+ 47.1
FB257	66, 184	97.1	+ 59.6

Iron-carbon shell MNP (SF199) measured a large hydrodynamic size and strong Brownian peak, which extended below 10 Hz, and DLS measurements at 233 nm, with a small peak at 64 nm. Therefore, ACS measurements could not be used to calculate the hydrodynamic size of these MNPs. Similarly, FB257 displayed MNPs of large sizes for ACS measurements with two size distributions, one of which extends below 10 Hz. DLS measurements also reflected the dual size distribution of this sample with a wide size distribution of 2 indistinct peaks. Based on the Brownian peak at higher frequency, one population of MNPs were at 66 nm, and the larger population was measured at ∼200 nm. Zeta potential measurements of all samples (Table 4.3) showed positive surface charge after PEI coating indicating successful PEI coating.

4.5.2.2 Internalization of MNP-PEI in HeLa cells

Prussian blue staining was performed to obtain brightfield images of PEI-coated MNPs internalized in HeLa cells, their clustering behaviour as well as the general morphology of cells after uptake of MNPs of different sizes and composition (Figure 4.8). Most of the MNP types (CoP-MNP-PEI, tdMNP cPEI, SF199, FB257) were observed to form dense clusters around the perinuclear region of cells. FS-MNP-PEI at low magnification showed low density of attached cells with poor morphology suggesting MNP-PEI based cytotoxicity. Compared to the other images, FS-MNP-PEI (Figure 4.8 B) were still observed around the outer cytoplasm of the cells and not concentrated around the nucleus, and MNP clusters were not as dense. The same was observed with cells seeded with Sigma-MNP-PEI (Figure 4.8 D) where close inspection show low internalization of MNPs in cells.

CoP-MNP-PEI (Figure 4.8 C) and tdMNP cPEI (Figure 4.8 E) displayed high cell density and MNP clustering around the nucleus with almost uniform uptake of MNPs in cells. FB257 (Figure 4.8 G) had dense but sporadic uptake of MNPs in cells and at low amounts compared to SF199 (Figure 4.8 F), which showed higher uptake of MNPs in cells.

The amount of iron seeded per well and internalized by cells was determined using the ferrozine assay. Figure 4.9 depicts the amount of iron seeded into each well and the amount

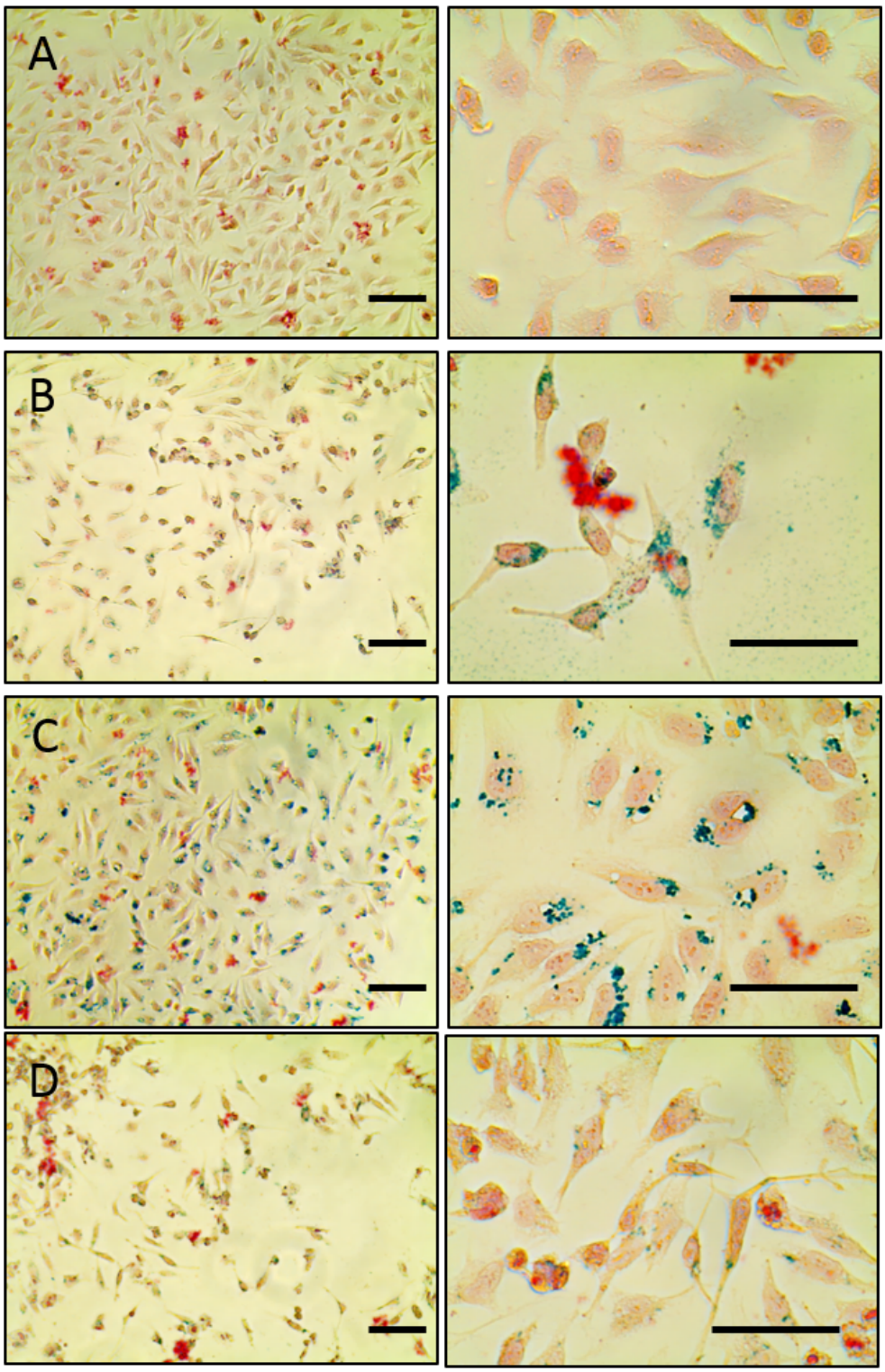
A
B
C
D

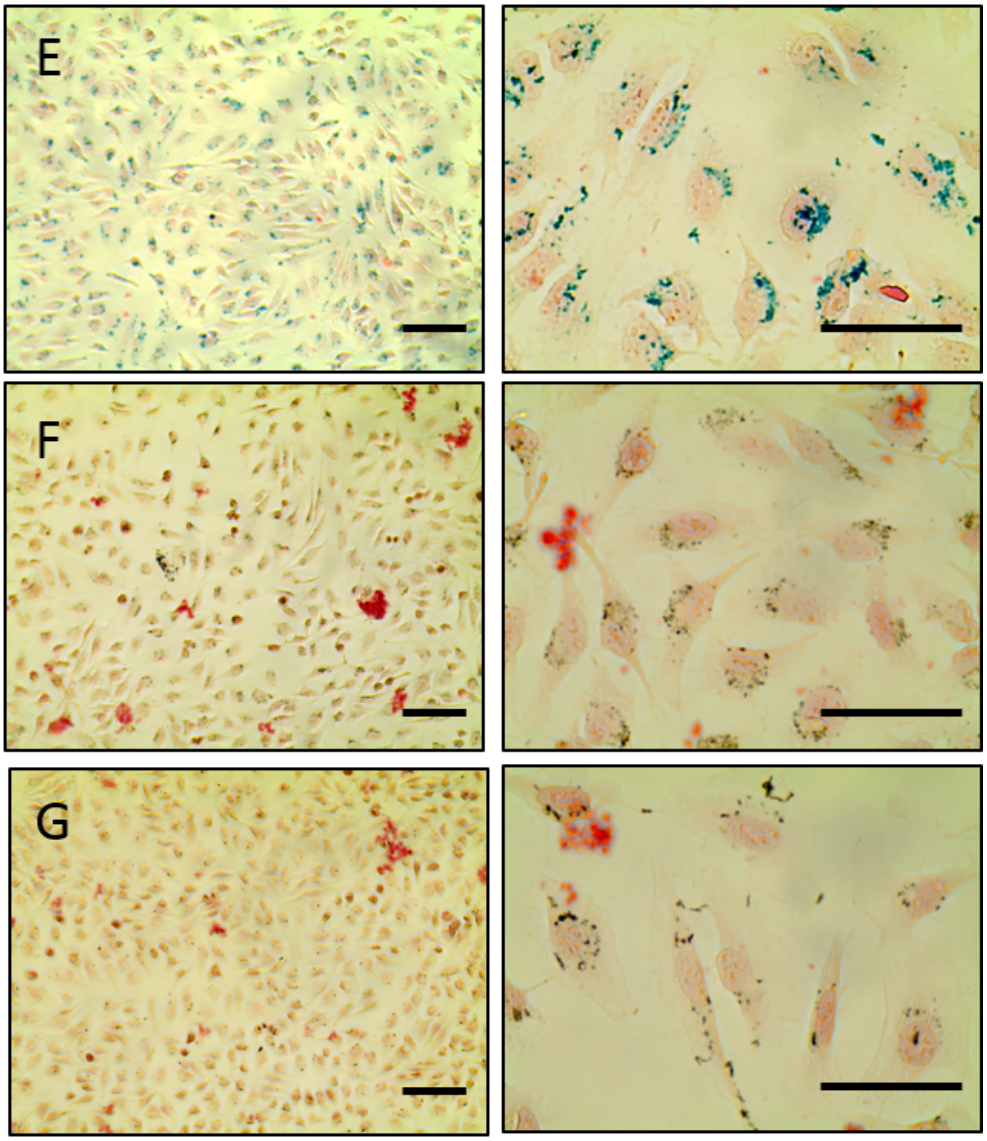

Figure 4.8 Prussian blue staining of iron MNP (blue) in cells and nuclear fast red staining of cells to show contrast. Staining shows (A) HeLa cells, (B) FS-MNP-PEI in cells, (C) CoP-MNP-PEI in cells, (D) Sigma-MNP-PEI in cells, (E) tdMNP cPEI in cells, (F) SF199 in cells, and (G) FB257 in cells. Scale bar=100 μm.

taken up by cells, including cells detached from the cell culture plastic. The amount of MNPs seeded varied from around 0.3 μg to 1.5 μg, however the amount of iron taken up by cells was a narrow range between 0.25 μg (FB257) to 0.6 μg (CoP-MNP-PEI).

The amount of MNPs taken up by cells were not dependent on the amount seeded into cells. The cells seemed to take up a limited amount of material from the external environment, in this case, from around 2-4 pg iron/cell until uptake saturation. The rate limiting step for MNP uptake in cells could be endocytosis, cell size, and duration of MNP incubation in cells. The plasma membrane invaginates to envelop MNPs in an endocytic vesicle, however since the amount of plasma membrane is limited, cells can only perform limited endocytosis, until the plasma membrane is replenished. MNP uptake may be increased by prolonging the duration of MNP incubation with cells. This effect is also discussed in Chapter 6.

The two highest mass of iron internalization in cells were CoP-MNP-PEI and tdMNP cPEI (Figure 4.9 and Table 4.4); however, these samples did not show signs of cell toxicity (Figure 4.10). The cell viability assay (XTT) also reflected the cytotoxicity observed in brightfield images, where FS-MNP-PEI and Sigma-MNP-PEI showed a significant decrease in cell viability compared to cells not treated with MNP-PEI, with Sigma-MNP-PEI causing the highest toxicity to HeLa

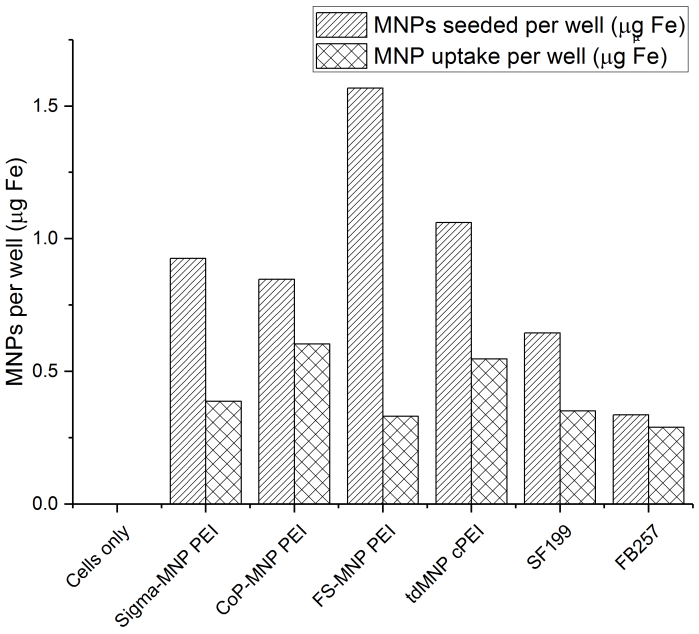

Figure 4.9 Ferrozine assay of iron quantification. Mass of iron (from each MNP-PEI type) added into each well (blue) in a 24-well plate with HeLa cells, and iron (from MNP-PEI) internalized into cells per well after 24 hours (orange); n=1.

Table 4.4 Calculated mass of iron internalized per HeLa cell, n=1.

MNP-PEI type	Cells only	Sigma-MNP	CoP-MNP	FS-MNP	MNP cPEI	SF199	FB257
Uptake Fe/cell (pg)	0	2.58	4.02	2.20	3.64	2.34	1.93

cells.

High magnification brightfield images of Sigma-MNPs (Figure 4.8) also show low amount of MNPs in cells, which could mean that cells that internalized a large amount of MNPs were subject to cytotoxicity and detached from the tissue culture plate, leaving cells that took up little MNPs to remain attached. Figure 4.9 shows a relatively low concentration of iron in cells for both Sigma-MNP and FS-MNP, however they conferred a significantly toxic effect on cells (Figure 4.10). Since the PEI surface coating is the same across all samples, cytotoxicity could be due to the size of particles.

Both Sigma-MNPs and FS-MNPs are more than double the size of CoP-MNPs and tdMNP cPEI. Sigma-MNPs are also larger than FS-MNPs, and cause higher toxicity to cells. The larger size of MNPs could adversely affect endocytosis of cells, placing a heavy burden on the plasma membrane during endocytosis. Samples SF199 and FB257 showed a darker, brownish staining of MNPs instead of blue, possibly due to the influence of carbon shell covering the iron core. Both the carbon-coated MNPs also exhibited low cytotoxicity. Metallic iron exhibits cytotoxicity, however the dense PEI coating and carbon shell may be able to shield the cell from the metal core of the MNPs.

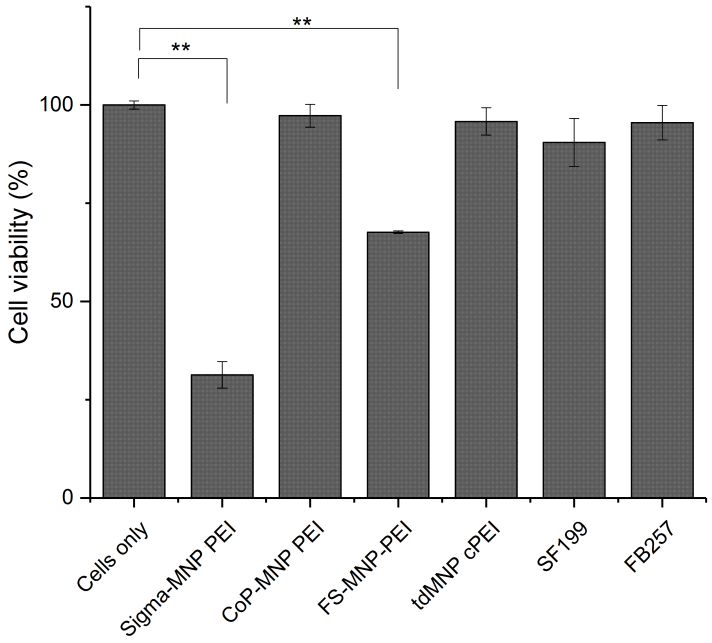

Figure 4.10 Cell viability after MNP-PEI uptake measured using the XTT colourimetric assay, n=3.

4.5.3 Transfection of adherent cells with commercial MNP transfection vectors

nTMag and polyMag are two PEI-coated MNP transfection agents that can be purchased from nanoTherics, along with the magnefect-nano oscillating system. These transfection agents (especially nTMag) are commonly used for nanomagnetic transfection. The MNP to DNA binding curves are studied, and nTMag transfection rates are compared to Lipofectamine 2000 and polyMag.

4.5.3.1 DNA to commercial MNP-PEI binding curve

DNA to nTMag and polyMag binding curves (Figure 4.11) were studied to determine the amount of MNPs needed to completely bind and precipitate 6 μg DNA, based on the protocol and description of the assay in Chapter 4.4. With increasing volume of MNPs added into the DNA solution, more DNA was bound to MNPs and there was a decrease in the detection of free DNA in the supernatant for both particle types. Saturation of DNA bound to particles occurred at 0.5 μL for polyMag, which is lesser than for nTMag, of 0.75 μL particles. After the loss of DNA absorbance signal at complete particle:DNA binding, there was a gradual increase in DNA absorbance measurement with further addition of particles for both polyMag and nTMag. MNP (μL):DNA (μg) ratio for polyMag was 1:12, and 1:8 for nTMag.

4.5.3.2 Transfection of nTMag vs Lipofectamine 2000

The efficiency of nanomagnetic transfection was compared to the conventional lipofectamine method. The effect of static and oscillating magnet arrays on transfection rates were also compared. Lipofectamine transfection was performed according to the protocol described in the methods section. The lipid transfection complex was incubated with cells for 6 hours before being washed off, while nanomagentic transfection was performed for 30 minutes without media change. All treatments contained the same amount of DNA. For the static treatment, well plates were placed on static magnet arrays for 30 minutes, and oscillating magnets were run per the standard protocol of 2 Hz and 2 mm displacement also for 30 minutes. Figure 4.12 shows that the transfection efficiency of nanomagnetic transfection using nTMag was significantly higher than the lipofectamine treatment where transfection was below 20%. nTMag had three times

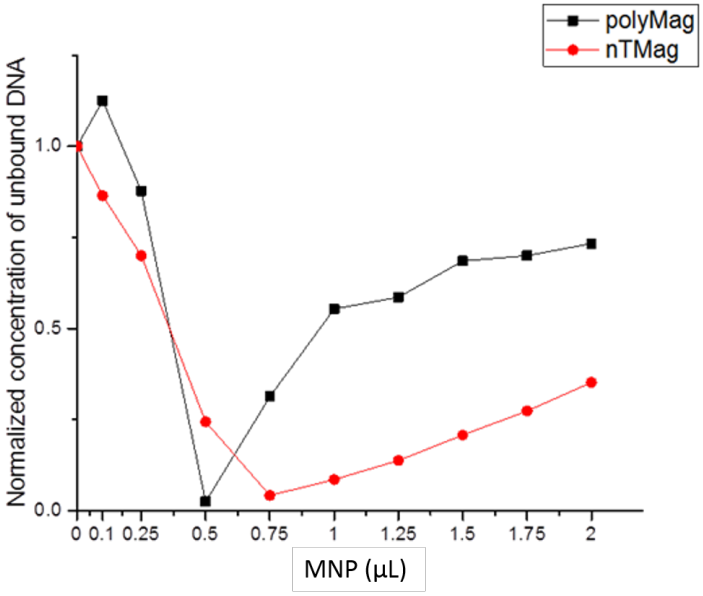

Figure 4.11 Commercial MNP polyMag and nTMag to DNA binding curve of pGFP showing the volume of MNP needed to bind 6 μg of DNA; n=1.

the rate of transfection at ~60%. The GFP expression of static and oscillating magnet arrays for both nanomagnetic transfection and lipofectamine did not differ significantly.

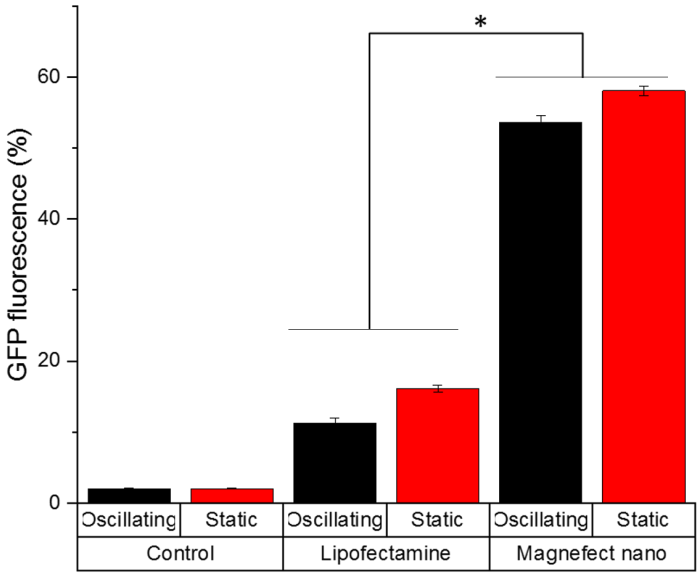

Figure 4.12 Comparision between GFP expression of MG-63 cells transfected using Lipofectamine 2000 and nTMag using oscillating magnefect-nano or static magnet arrays; n=3.

Figure 4.13 is the flow cytometry analysis of the cell population and gating of GFP positive cells. The flow rate of cells in the flow cytometer was the same, however based on the dot plot with each dot representing a cell in the sample, the cell density for nanomagnetic transfection (Figure 4.13 D and E) was lower than the lipofectamine samples (Figure 4.13 B and C). GFP positive cells were determined using a histogram plot (right of the dot plot) and gating the control group as GFP negative (Figure 4.13 A) where all the cells are non-fluorescent. FL1 signals to the right of the fluorescence negative gate were cells expressing GFP fluorescence. The FL1 GFP of nanomagnetic transfection had a noticeably higher signal compared to lipofectamine.

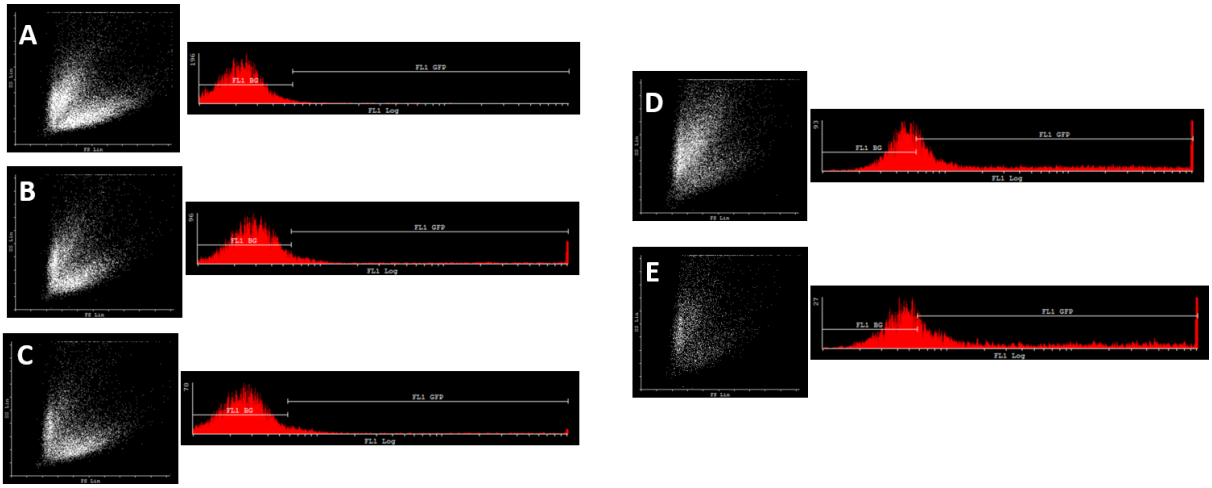

Figure 4.13 Flow cytometry analysis of MG-63 cells expressing GFP. (A) MG-63 control, (B) Lipofectamine with static magnet, (C) Lipofectamine with oscillating magnet, (D) nanomagnetic transfection with static magnet, (E) nanomagnetic transfection with oscillating magnet. FL1 GFP gate represents the number of cells expressing GFP+ signal.

Nanomagnetic transfection utilizes magnetic targeting to direct the magnetic transfection complexes to cells. Compared to the cationic lipid Lipofectamine 2000, nTMag had a significantly higher transfection efficiency (Zhao et al., 2014). Besides that, the time taken to perform the transfection was shorter using nanomagnetic transfection (30 minutes) compared to lipofectamine which takes 6 hours before media is changed. The long incubation time of lipofectamine could affect cell viability due to the toxic nature of the positively charged lipid moieties. Similarly, nTMag contains a high amount of PEI coating which conferred high toxicity to cells. Flow cytometer data show that the nTMag complex group had a lower cell population in the dot plot compared to the lipofectamine group. This effect is from the long incubation time of nTMag with cells, where a media change was not performed. Section 4.5.4.3 describes the improvement in cell viability when media change is performed after the 30 minutes nanomagnetic transfection procedure.

The effect of static and oscillating magnet was not significant on transfection efficiency. Nanomagnetic transfection relies heavily on magnets to improve transfection efficiency by magnetic targeting. For the lipofectamine treatment, the effect of external magnets was negligible as there are no magnetic components in the transfection complexes. Therefore, the difference seen between the oscillating and static magnets in lipofectamine are due to experimental variability.

4.5.4 Parameters influencing transfection rates – optimization of nTMag transfection

nTMag has been shown to be an effective transfection agent compared to the conventional Lipofectamine 2000 reagent and polyMag from nanoTherics. The subsequent sections will discuss parameters that influence nTMag transfection rates and use these parameters to optimize and obtain the highest transfection efficiency.

4.5.4.1 Transfection efficiency of oscillating systems – horizontal vs vertical oscillation

The magnefect-nano and MICA magnetic oscillating systems were studied for their effect on transfection efficiencies. The magnefect-nano is a horizontal oscillating system, whereas the MICA system oscillates vertically. Transfection efficiency was also studied using nTMag-pGFP at two different complex concentrations ($0.3\mu L$:$0.3\mu g$ and $0.8\mu L$:$0.8\mu g$). An nTMag only control was introduced to ensure that transfection analysis was only detected from GFP expression.

Cytotoxicity was also compared between the groups using propidium iodide staining for dead cells and flow cytometry.

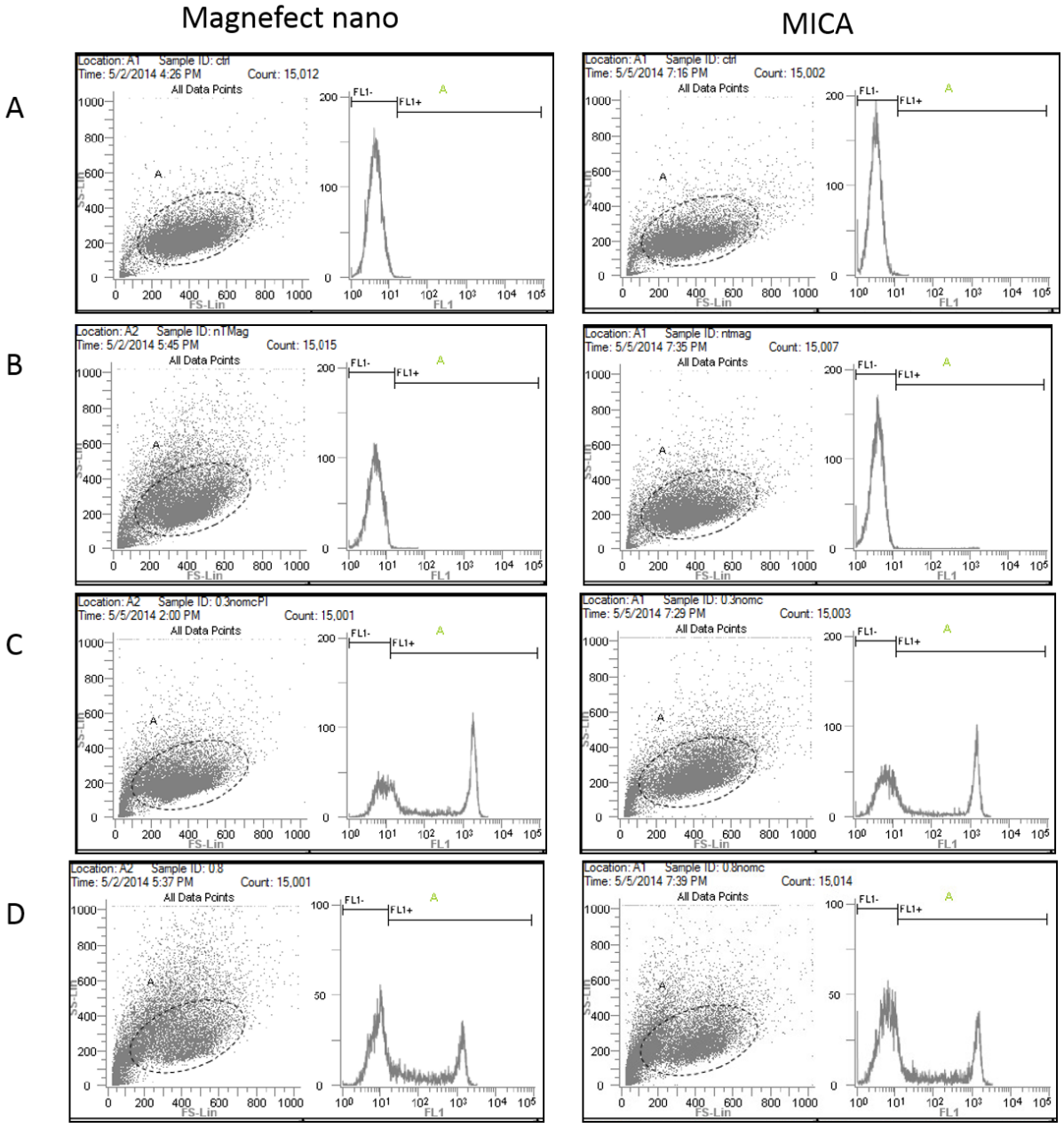

Figure 4.14 Flow cytometry analysis of GFP positive cells between the magnefect-nano (Column 1) and MICA system (Column 2). (A) HeLa cells, (B) nTMag control with no DNA, (C) nTMag:DNA of $0.3\mu L$:$0.3\mu g$, and (D) nTMag:DNA of $0.8\mu L$:$0.8\mu g$; n=3.

Figure 4.14 A shows flow cytometry results of the control group of HeLa cells and gating at a densely-populated region of cells. The negative control nTMag (Figure B) contained only nTMag (without pEGFP) seeded in cells, which was important to show that fluorescence expression was indeed induced by the presence of the nTMag-DNA complex. FL1 signal for this control group is low, indicating no false positives from nTMag internalization alone. Transfection groups include 0.3 μg DNA to 0.3 μL nTMag (low dose) (Figure C) and 0.8 μg DNA to 0.8 μL nTMag (high dose) (Figure D). The dot plot indicates a difference in the forward and side scatter between control group (Fig. A), and nTMag treated groups.

Based on GFP expression results in Figure 4.15 A, nTMag treatment without DNA did not induce a false positive transfection and all the nTMag-DNA complexes successfully transfected HeLa cells at a high rate. The highest transfection rate was the low dose complex +

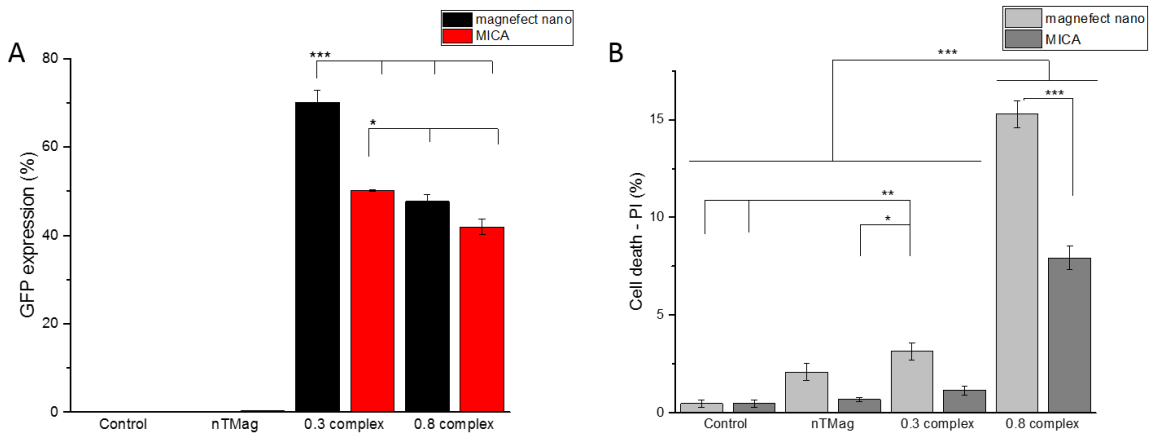

Figure 4.15 Comparison of transfection efficiency between magnefect-nano and MICA system. (A) GFP expression of nanomagnetic transfection of HeLa cells using the horizontal (magnefect-nano) and vertical MICA magnetic oscillating systems at two different nTMag-DNA complex concentrations, (n=3). (B) Percentage of cell death at time of GFP expression analysis determined by propidium iodide staining and flow cytometry, (n=2-3).

magnefect-nano group, at 65% GFP expression, which was highly significant ($p<0.0001$) compared to all other groups. Figure A clearly shows an improved transfection rate when using the magnefect-nano compared to the MICA system for either complex concentrations. Two-way ANOVA determined that the two oscillating systems differed significantly, as well as between the low and high dose complex concentrations, which affected transfection rates. Transfection rates are also heavily dependent on the interaction between complex concentration and type of magnet systems ($p<0.0001$).

Propidium iodide staining Figure 4.15 B showed an increase in cell death with the nTMag + magnefect-nano treatment compared to HeLa control groups ($p=0.17$). The group with the highest rate of transfection (low dose + magnefect-nano) had a relatively low cell death count ($\sim$ 3%) compared to the high dose group, although it was a statistically significant increase compared to the control groups. For both the nTMag 0.3 complex and 0.8 complex groups, magnefect-nano treatment consistently had a higher cell death percentage between the two oscillating magnet arrays. Similarly, the high dose complex concentration had an adverse effect on cells, especially when coupled with the magnefect-nano which resulted in 15% cell death out of the cell population. Two-way ANOVA analysis of the cytotoxicity study revealed that the combined effect between complex concentration and oscillating magnet systems had an effect on cell viability ($p<0.0001$). Complex concentrations alone and the type of magnetic system used also affected cell death.

The effect of complex concentration plays an important role on the transfection efficiency of cells and cytotoxicity. Cells transfected with 0.3 μL MNP complex had a significantly higher transfection rate than with 0.8 μL (high dose) complex for both the magnefect-nano and MICA system (Figure 4.15 D). Cell viability of the high dose transfection was also severely affected as PEI is known to confer a toxic effect on cells due to its positive charge. Increasing the complex concentration also does not improve transfection efficiency, as there is a threshold for effectiveness of increasing complex concentration before cells become saturated and cytotoxicity becomes predominant.

4.5.4.2 Optimization of nTMag:DNA ratio and complex concentration (96- and 24- well plates) for highest transfection efficiency

MNP-DNA complex formulations are important factors in obtaining high transfection rates. To study the effect of complex concentration and MNP:DNA ratio on transfection rates, a

transfection complex formulation procedure was used based on a nanoTherics protocol and nTMag and DNA concentrations are reported in Table 4.1. The study was performed in a 96-well plate to obtain high throughput data and two wells were pooled for flow cytometry analysis.

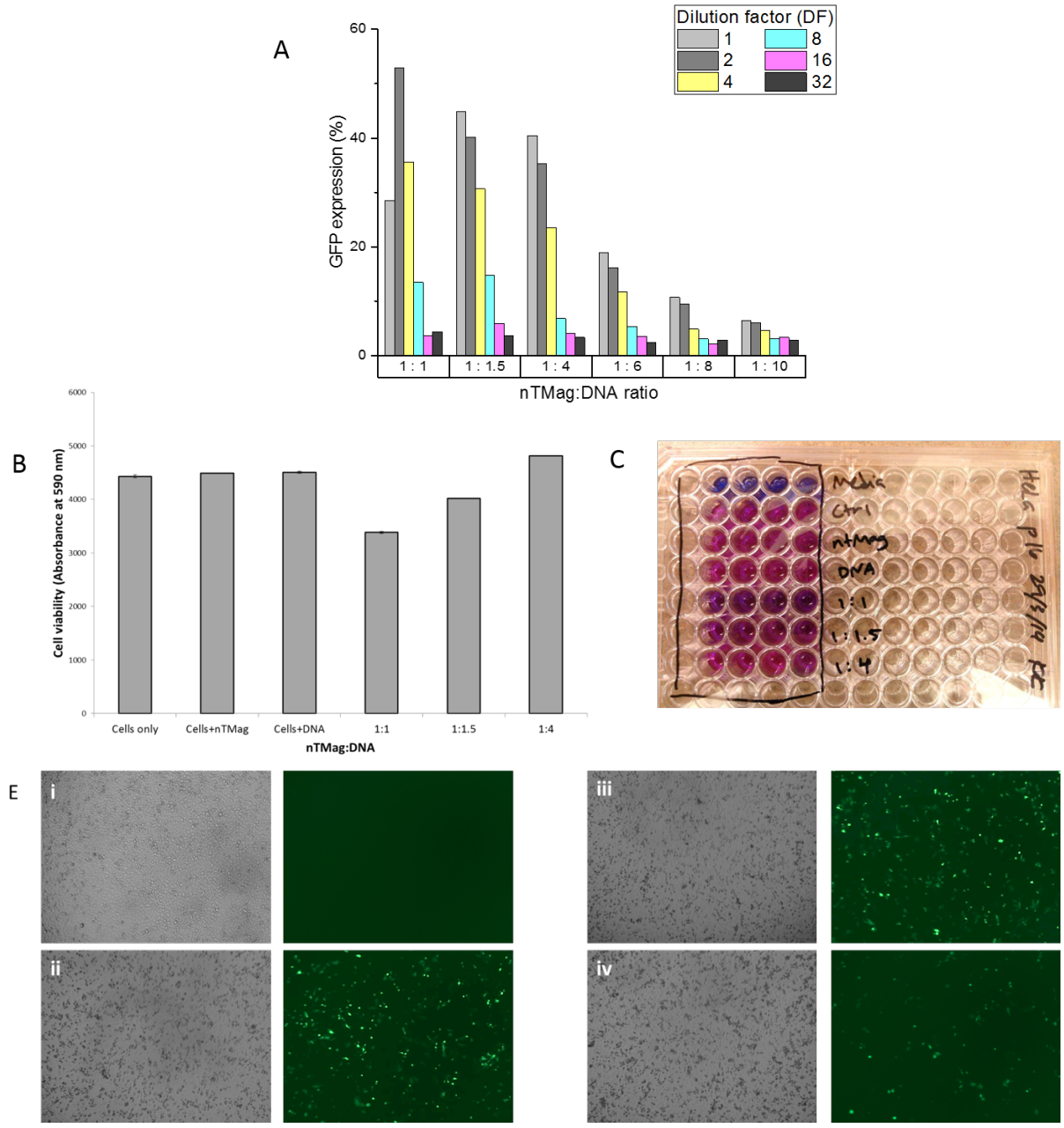

Figure 4.16 (A) Bar graph of GFP expression in HeLa cells at different nTMag:DNA ratios with the highest nTMag volume being 0.4 μL, and different complex concentrations by serial dilutions (Table 4.1). Most efficient ratio was 1:1 at dilution factor (DF) of 2, 1:1.5 at DF 0, and 1:4 at DF 0; n=1. (B) Cell viability of the three complexes with highest transfection rates; n=4. (C) Celltiter blue (resazurin assay) in a 96-well plate for cell viability showing change in colour of the different treatments; n=4. (D) Brightfield (left) and fluorescence (right) images of HeLa cells for celltiter blue assay after transfection (i) HeLa control, (ii) 0.2:0.2, (iii) 0.2:0.3, (iv) 0.4:1.6 showing GFP expression. Scale bar=200 μm; n=4.

GFP expression derived from nTMag:DNA ratios decreased with increasing amount of DNA whereby at ratios of 1:6, 1:8 and 1:10 of nTMag:DNA the transfection rates were lower than 20% (Figure 4.16 A). Furthermore, the effect of concentration of complexes per well on transfection rates were obtained in this study, where high transfection rates were obtained with lower dilution factors, and at DF 8 and above GFP expression was less than 20%. The highest GFP expression occurred at ratio of 1:1 DF 2 (0.2 μL nTMag : 0.2 μg DNA), followed by 1:1.5 DF 0 (0.4 μL : 0.6 μg), 1:4 DF 0 (0.4 μL : 1.6 μg), and 1:1.5 DF 2 (0.2 μL :0.3 μg) with transfection rates of

53%, 45%, 40%, and 40% respectively.

In the cell toxicity assay based on the transfection values of Figure 4.16 A, three complex formulations were chosen which were 0.2:0.2, 0.2:0.3, and 0.4:1.6 of nTMag:DNA, with nTMag only as a reference treatment at 0.2 μL. The cell viability was determined after transfection using celltiter blue. Based on Figure 4.16 B, the complex concentration of 0.2:0.2 had the lowest viability compared to the control group with a 20% decrease (p=0.0045). Figure C shows the colour change of the celltiter blue assay from blue to red with treatment group 1:1 (0.2:0.2) showing the least colour change.

Micrographs of transfected cells (Figure 4.16 D) of brightfield (left) and the corresponding fluorescence images taken on an EVOS microscope of control HeLa cells, transfected cells of nTMag:DNA at 0.2:0.2, 0.2:0.3, and 0.4:0.6 for Figures E i, ii, ii and iv respectively. The lowest observable transfection was in treatment 0.4:0.6, whereas images in Fig. E ii and iii qualitatively had no observable difference in transfection.

To scale-up the effect of complex ratios and concentration, five nTMag:DNA complex formulations were picked based on results in Figure 4.16 and transfection was scaled to 24-well plates. The highest transfection rates were observed at ratios of 1:1 and 1:1.5 in the 96-well plate transfection in Figure 4.16 A. Hence, transfection complex ratios chosen from the 96-well plate study were 0.2:0.2, 0.4:0.6 and 0.2:0.3. The complex amounts were scaled up 4x based on cell seeding density (15 000 cells per 96 well to 60 000 cells per 24 well). Therefore, 24 well complexes were 0.8:0.8, 1.6:2.4, and 0.8:1.2, with two additional complex ratios 0.6:0.6 and 0.6:0.9 which had lower nTMag volumes. The transfection complexes chosen was tabulated in Figure 4.17 A.

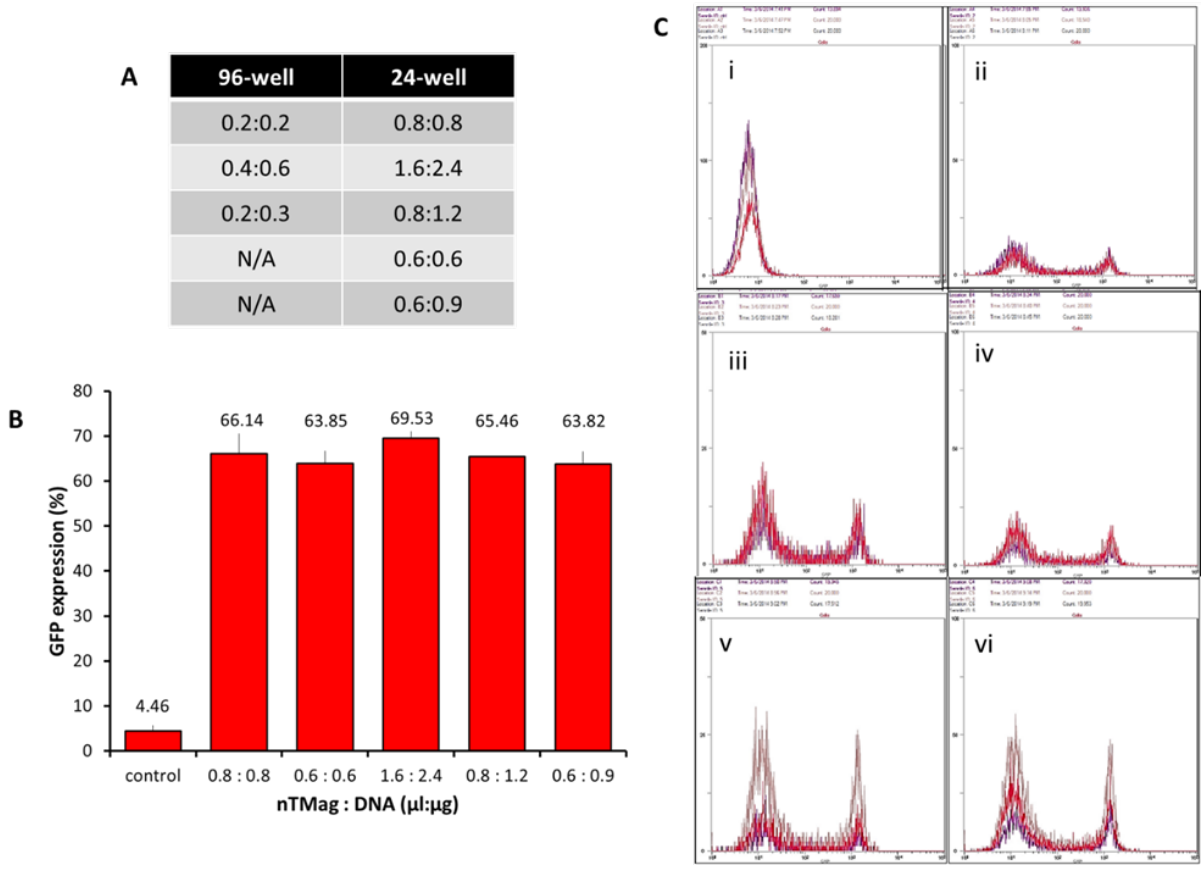

Figure 4.17 (A) Scale-up of transfection complex formulations from 96-well to 24-well. (B) Experiment scale up – GFP expression of HeLa cells transfected in 24-well plates at different nTMag:DNA ratios and complex concentrations formulated based on 96-well transfection (Figure 4.16 A). (C) Flow cytometry analysis of GFP transfected cells: (i) HeLa control, (ii) 0.8:0.8, (iii) 0.6:0.6, (iv) 1.6:2.4, (v) 0.8:1.2, (vi) 0.6:0.9 complex ratios of volume nTMag, Different colour intensities represent replicates, n=3.

GFP expression in Figure 4.17 B show that all the complex formulations had relatively similar transfection rates of ∼60%. Flow cytometry plots (Figure 4.17 C) show population of cells with GFP expression where goups 0.8:0.8 and 1.6:2.4 (Fig. C ii and iv) with the highest transfection rates (66% and 69.5% respectively) also showed lower FL1 peaks, which can qualitatively infer low cell count. Lowering the volume of nTMag to 0.6 μL did not result in a significant change or drop in transfection rates. Similarly, higher DNA mass did not produce higher GFP expression where 0.6 μg was sufficient to maintain transfection values.

Based on the DNA binding curve assay discussed above, the ratio of MNP-PEI to DNA plays an important role in cell uptake efficiency and transfection rates. The particle to DNA ratio was studied further for nTMag and tdMNP-PEI. The nanoTherics protocol for nTMag instructs to use an nTMag:DNA ratio of 1:1 at a concentration of 0.3 μL nTMag to 0.3 μg DNA per 24-well plate. Although this concentration yielded a 50 – 60% transfection rate when particles were newly purchased, the transfection efficiency dropped over time observed in Figure 4.21 and Figure 4.22 where transfection rates dropped to 10%. To overcome the short shelf life of nTMag for transfection rates, the complex formulation was studied in order to increase transfection efficiency to more than 50%.

With the study scaled up to a 24-well plate in Figure 4.17, all the complexes had similar transfection rates, from 63–69%. This value reflects the threshold of transfection that nTMag can achieve with HeLa cells. Besides high transfection rates, cytotoxicity should be considered. Since nTMag is toxic at sufficiently high doses, using a lower volume of MNPs improves cell viability. Therefore 0.6 μL nTMag with 0.6 μg DNA was chosen for subsequent transfection studies, since it has high transfection rates of ∼60% and relatively lower toxicity compared to the 0.8 μL nTMag complexes.

4.5.4.3 Effect of media change after transfection procedure on cell viability

To elucidate the effect of nTMag-DNA transfection complexes on cell viability over time, a study was conducted on the viability of cells after the media was replaced in wells once the transfection procedure on the magnefect-nano was completed.

Three transfection complexes were chosen at nTMag(μL):DNA(μg) of 0.3:0.3, 0.6:0.6 and 0.8:0.8, denoted as 0.3 complex, 0.6 complex and 0.8 complex respectively. The effect of nTMag alone without DNA on transfection and cell viability was also included as a control. Figure 4.18 A shows the GFP expression of cells after transfection with the complexes, where t-test results indicate there was no significant difference in GFP expression (mean=44-48%) between all three complex formulations without media change.

To determine cell viability, a celltiter blue assay was performed on cells with the same treatment as transfected groups in Figure 4.18 A, with one group undergoing media change immediately after 30 minutes transfection on the magnefect-nano to remove unbound transfection complex in wells, and cells in the 'no media change group was incubated with the transfection complex until GFP assay time point of 48 hours. The cell viability assay was performed 48 hours post-transfection. A two-way ANOVA was performed on the data which showed that for cell viability, the effect of complex concentrations was significantly different, where higher concentrations of transfection complex resulted in lower cell viability ($p<0.001$). The effect of media change also showed a significant response, where changing the media after transfection resulted in higher levels of cell viability for all transfection groups, as well as nTMag only control ($p<0.001$) (Figure 4.18 B). Finally, the interaction between transfection complex and media change were significant ($p<0.001$) where a lower complex concentration coupled with media change improved overall cell viability. Although fluorescence micrographs show less GFP expression in the 'media change' group (Fig. 4.18 C), presumably due to the shorter incubation time of the transfection complex compared to the 'no media change' group.

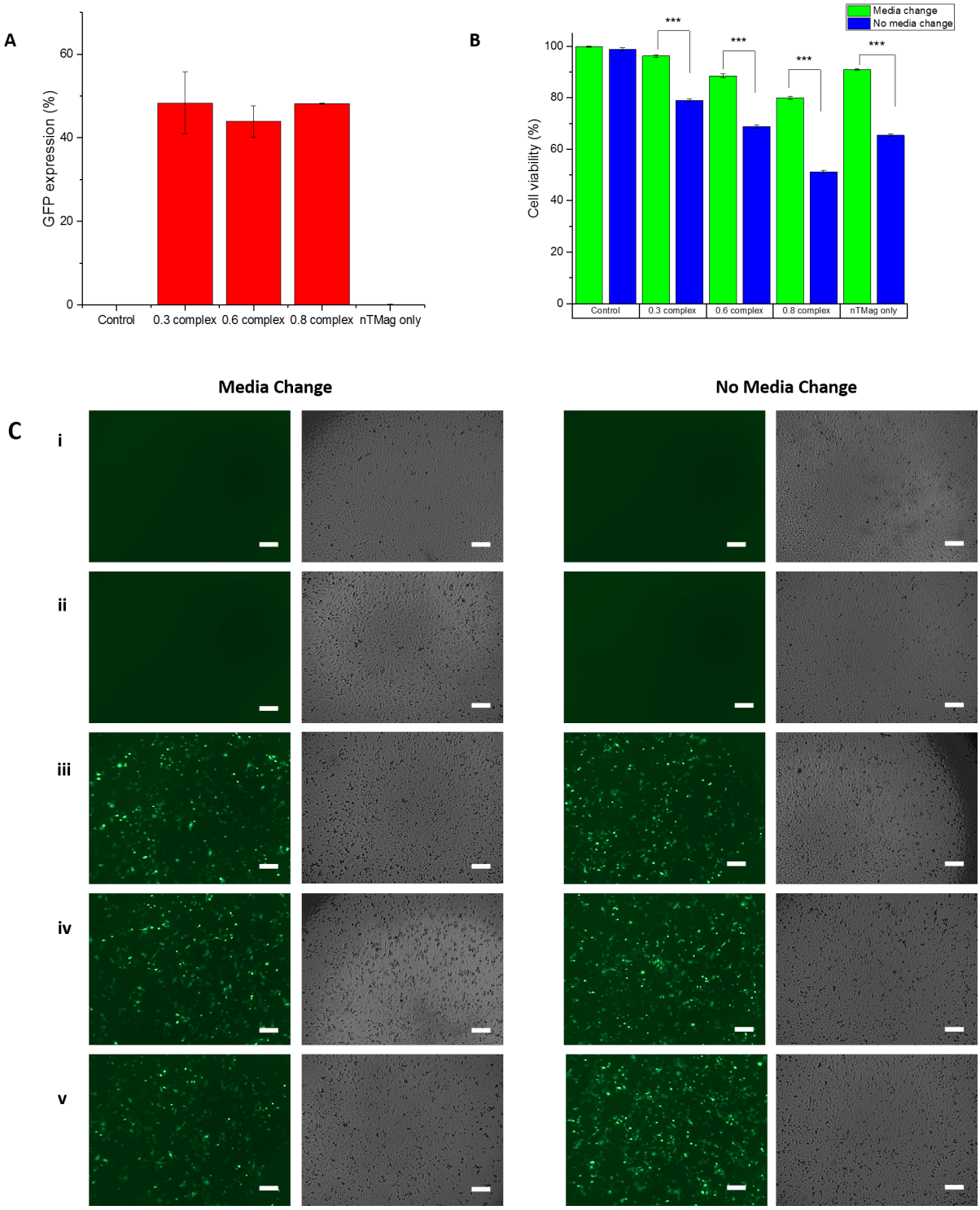

Figure 4.18 (A) Bar graph of GFP expression in HeLa cells at different nTMag:DNA ratios with the highest nTMag volume being 0.4 μL, and different complex concentrations by serial dilutions (Table 4.1). Most efficient ratio was 1:1 at dilution factor (DF) 2, 1:1.5 at DF 0, and 1:4 at DF 0; n=1. (B) Cell viability of the three complexes with highest transfection rates; n=4. (C) Celltiter blue (resazurin assay) in a 96-well plate for cell viability showing change in colour of the different treatments. (D) Brightfield (left) and fluorescence (right) images of HeLa cells for celltiter blue assay after transfection (i) HeLa control, (ii) 0.2:0.2, (iii) 0.2:0.3, (iv) 0.4:1.6 showing GFP expression. Scale bar=200 μm; n=3.

4.5.4.4 Optimization of cell seeding density and GFP expression time points for highest transfection efficiency

Two parameters affecting GFP expression analysis were studied, which were cell seeding density and time of GFP expression analysis after the nanomagnetic transfection procedure. Cells were seeded at 50 000, 70 000 and 90 000 cells per well in a 24 well plate and grown for 24 hours. Nanomagnetic transfection was carried out as detailed in Chapter 2, and GFP expression was analysed on the flow cytometer 24 hours, 48 hours, and 72 hours later.

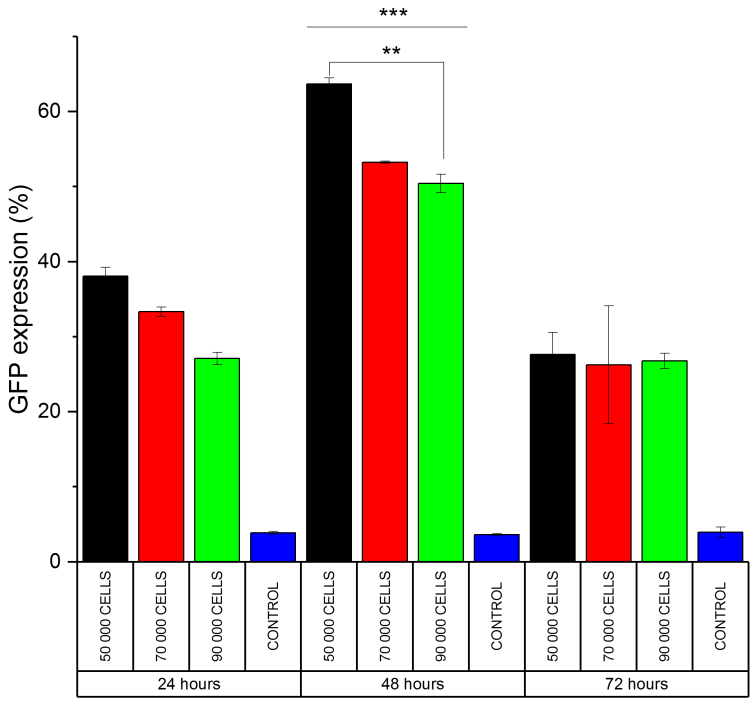

Figure 4.19 GFP expression of transfected cells at seeding densities of 50 000, 70 000 and 90 000 cells per well in a 24 well plate, and quantitation of GFP expression 24, 48 and 72 hours after nanomagnetic transfection procedure; n=3.

Results in Figure 4.19 explains the effect of seeding density and time of highest GFP expression. All transfected groups showed statistically significant transfection compared to the control groups. Comparisons between time points indicate that 24 hours after transfection, cells showed an initial protein expression of about 30-40%; however, the expression peaked at hour 48 after transfection (50-60%) and decreased drastically at 72 hours to ∼30%. Between the seeding density per time point, only 50 000 cells had a significant increase to 90 000 cells in the 48 hours group. However, a trend in groups 24 and 48 hours can be seen where lower seeding density showed higher transfection efficiency, but this effect plateaued at 72 hours.

The two-way ANOVA shows that individually, cell seeding density and expression time point parameters significantly influenced protein expression rates. However, the correlation between both parameters also influenced GFP expression whereby both 70 000 cells per well and expression at 48 hours yielded the best transfection rates.

Optimization of transfection efficiency should ideally be studied for every cell type, where cell doubling time, protein expression time, ease of permeating the plasma membrane, type of endocytic process, and primary or established cell lines could influence transfection efficiency. Cells also have to be healthy and under minimum stress during transfection, therefore cells with low passage number should be used, and transfection should be performed 24 hours after cell seeding to allow cells to attach and recover.

For HeLa cells, 48 hours after transfection showed the strongest protein expression, after which the expression began to decrease. The cell seeding density is also a factor as the confluency at the time of transfection could be a factor for highest percentage of cells taking up complexes, where at around 70-80% confluency, cells showed highest transfection efficiency. This could be attributed to an almost confluent monolayer of cells in the cell culture plate, hence MNP complexes sedimented by the external magnet would have a higher chance of interacting with a cell membrane instead of the tissue culture plastic on the bottom. A higher confluency would probably affect cell viability where after the 48 hours taken for transfection, cells with short doubling times such as HeLa may start to undergo apoptosis from lack of space.

4.5.5 Transfection of adherent cells with MNPs synthesized by thermal decomposition

nTMag and polyMag are proprietary, therefore little information about the particles are available, such as the amount of PEI used, the type of surface coating, the core and hydrodynamic size of particles, to name a few. This chapter will study tdMNP synthesized by thermal decomposition (described in Chapter 3) which are well characterized with the ability to transfect cells. Well characterized MNPs are useful to probe the mechanism of nanomagnetic transfection further and to understand the role of each transfection component. Two tdMNP types with PEI coated covalently (tdMNP cPEI) and electrostatically bonded (tdMNP-PEI) to the surface of tdMNP were compared for transfection efficiency. tdMNP-PEI was also optimized to obtain the highest transfection efficiency, as well as to study the effect of excess PEI in the transfection complex. The magnefect-nano horizontal oscillating system was studied for its effectiveness in inducing transfection by varying the frequency and amplitude of oscillation.

4.5.5.1 Covalently bound PEI: Effect of unbound PEI in tdMNP cPEI suspension on transfection rates

PEI covalently bound to tdMNP (tdMNP cPEI) before and after magnetic separation was used for transfection of HeLa cells. The magnetic separation technique (Chapter 4.3) was used as an additional washing step to remove unbound/free PEI from the suspension that was not removed during centrifugal filtration for the PEI coating procedure (described in Chapter 3.2.2). Using bound PEI on tdMNP by covalent binding ensures that only PEI bound loosely or in suspension will be removed.

Figure 4.20 A i, ii and iii of the respective ACS measurements of tdMNP only, tdMNP cPEI without magnetic separation and tdMNP cPEI after magnetic separation shows shifts in the χ" peak for all 3 samples, based on the vertical line (blue) positioned at the tdMNP only χ" peak as an indicator. In the tdMNP only graph, the χ" peak is higher than 40 000 Hz. After PEI coating on tdMNP, the χ" peak shifts to the left to $\sim$4860 Hz indicating an increase in hydrodynamic size. Finally, the effect of magnetic separation on tdMNP cPEI resulted in a decrease in hydrodynamic size with a small shift back to higher frequencies of $\sim$17 500 Hz.

DLS and zeta potential measurements (Figure 4.20 B) of tdMNP cPEI before magnetic separation (Figure 4.20 B i) and after magnetic separation (Figure 4.20 B ii) show a measured average increase in hydrodynamic size of 5 nm with magnetic separation. However, observable differences in the DLS graph show a tail end in the sample (63–127 nm) before magnetic separation whereas the DLS distribution is narrowed after magnetic separation. Zeta potential analysis shows a positive surface charge for both tdMNP cPEI samples, but the intensity of the charge decreased by almost half after magnetic separation to +24 mV.

Magnetic separation is a suitable washing technique for tdMNP cPEI as the strong covalent bonds between tdMNP and PEI prevents the attached PEI layer from being removed by this harsh technique that could potentially strip surface coatings from shear flow if not bound tightly.

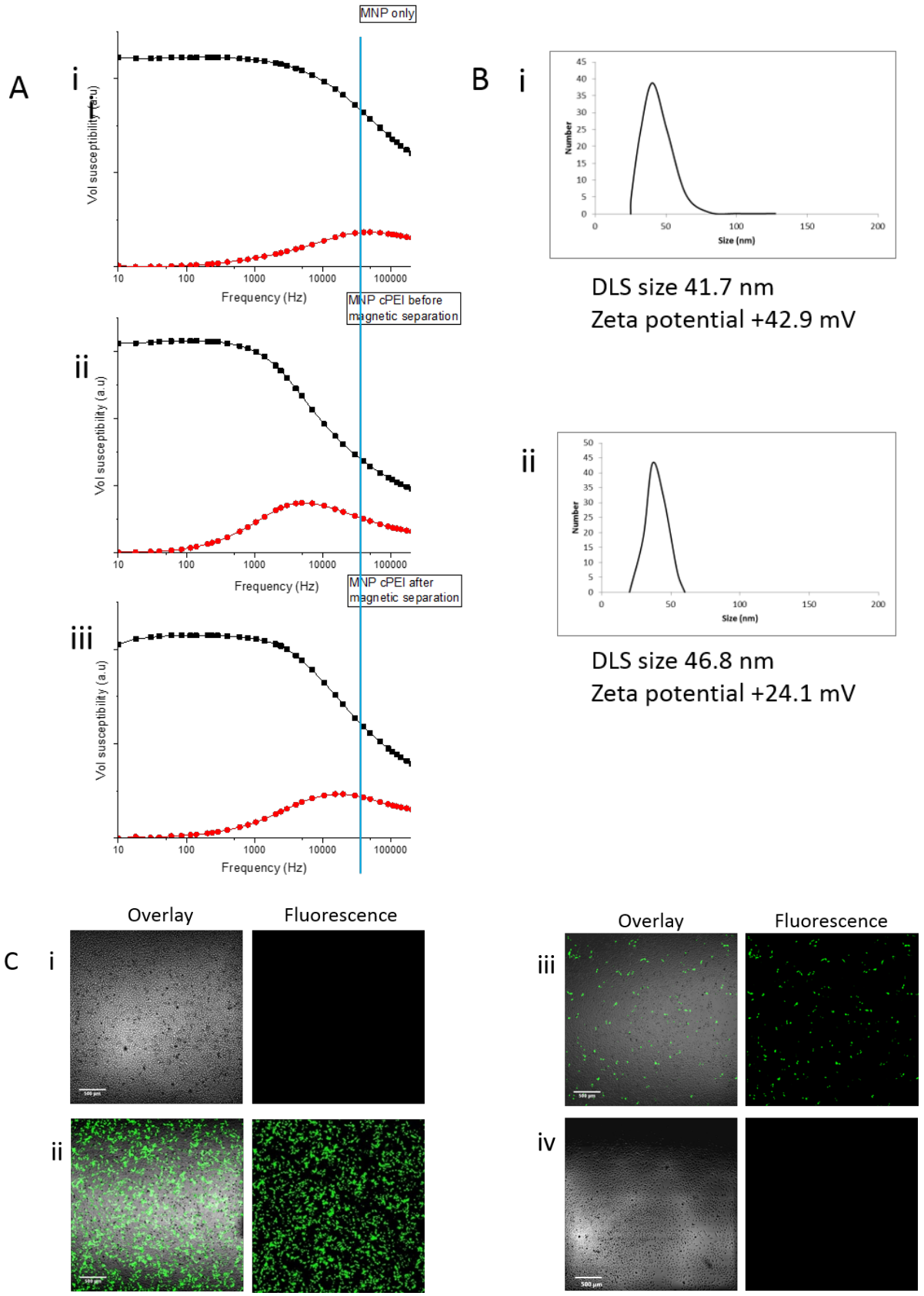

Figure 4.20 (A) ACS measurements of tdMNP cPEI, (top) before PEI conjugation, (middle) after PEI conjugation and before magnetic separation, and (bottom) after PEI conjugation and after magnetic separation. Blue vertical line intercepts at peak of MNP only (top) to indicate shift in ACS peaks in each step. (B) DLS graphs showing hydrodynamic size and zeta potential mesurements of tdMNP cPEI (i) before magnetic separation and (ii) after magnetic separation. (C) Fluorescence and brightfield images qualitatively showing GFP transfection of HeLa cells; (i) control, (ii) nTMag control, (iii) tdMNP cPEI before magnetic separation, (iv) tdMNP cPEI after magnetic separation, scale bar=500μmm; n=3.

ACS measurements show a decrease in size of tdMNP cPEI after magnetic separation possibly due to the loosely bound PEI being removed from tdMNP surface reducing the hydrodynamic size of particles. The smaller size is also characteristic of stable particles, where if the surface coating had become uneven, particles will start to aggregate and form larger clusters. Therefore, it can be assumed that the particles still maintained a uniform surface PEI coating enough to stabilize particles in the suspension and create good ionic and stearic hindrance. DLS measurements also show the loss of the tail end of the size distribution. Loss of the tail end is result from the removal of polyplexes that formed from free PEI in the suspension. This also shows that the centrifugal filtration method is not enough to wash all PEI from the system. Zeta potential measurements show a decrease in the net positive charge, however MNP still possess a positive charge after magnetic separation indicating the covalently bound PEI was still attached to MNP.

The presence of PEI polyplexes during tdMNP coating was also measured using the DLS during ionic binding of PEI to tdMNP in the previous chapter (Chapter 3). Similar to this study, centrifugal filtration and even dialysis is not as effective as magnetic separation to remove unbound PEI. However as mentioned before the shear flow of magnetic separation washing may strip weakly/ionically bound PEI off tdMNP, resulting in an unstable tdMNP-PEI suspension.

tdMNP cPEI samples were used for transfection of HeLa cells to determine the effect of removing unbound/free PEI in an MNP-PEI suspension. Figure 4.20 C shows fluorescence and brightfield overlayed images of cells after GFP transfection of control group, nTMag, tdMNP cPEI before magnetic separation and tdMNP cPEI after magnetic separation. nTMag served as a positive control for successful transfection. Cells transfected with tdMNP cPEI before magnetic separation showed some GFP expression, indicating a low amount of transfection. However, the magnetic separation treatment on tdMNP cPEI clearly resulted in no GFP expression and hence unsuccessful transfection.

Covalently bound PEI on MNP (tdMNP cPEI) provides strong binding forces to tether PEI on MNP surface and prevents PEI from detaching from MNP during transfection. By studying the type of interaction between tdMNP and PEI, the mechanism of PEI-mediated transfection when internalized in cells can be understood, in terms of whether PEI needs to be allowed to dissociate from MNP in cells or if the whole tdMNP cPEI complex can facilitate the complete transfection process. The obvious decline in transfection after magnetic separation treatment could indicate that nanomagnetic transfection requires PEI to be able to dissociate from MNPs in order to facilitate transport of DNA to the nucleus for successful transfection.

In the subsequent sections, the transfection parameters of PEI ionically bound to MNPs (tdMNP-PEI) are reported.

4.5.6 Transfection parameters of ionically bound PEI on MNPs (tdMNP-PEI)

4.5.6.1 DNA binding curve with tdMNP-PEI

The DNA binding curve assay described in Chapter 4.4 and previously studied with polyMag and nTMag in Section 4.5.3.1 was performed using synthesized tdMNP coated with electrostatically bound PEI (tdMNP-PEI). The ratio of particles needed to fully bind and precipitate 6 μg of DNA was 2.4 μL of 0.03 μg Fe / μL (Figure 4.21 A). Gradual addition of tdMNP-PEI saw a decrease in DNA absorbance measurement until a saturation ratio was achieved. Above that concentration, the Nanodrop measured a gradual increase in DNA absorbance signal with particle loading.

With reference to the DNA binding study in Figure 4.21 A, 14 points were chosen and the ratio of tdMNP-PEI:DNA were used for transfection of HeLa cells. This study was in effect to find the ratio of particles to DNA needed to provide the highest transfection and to understand

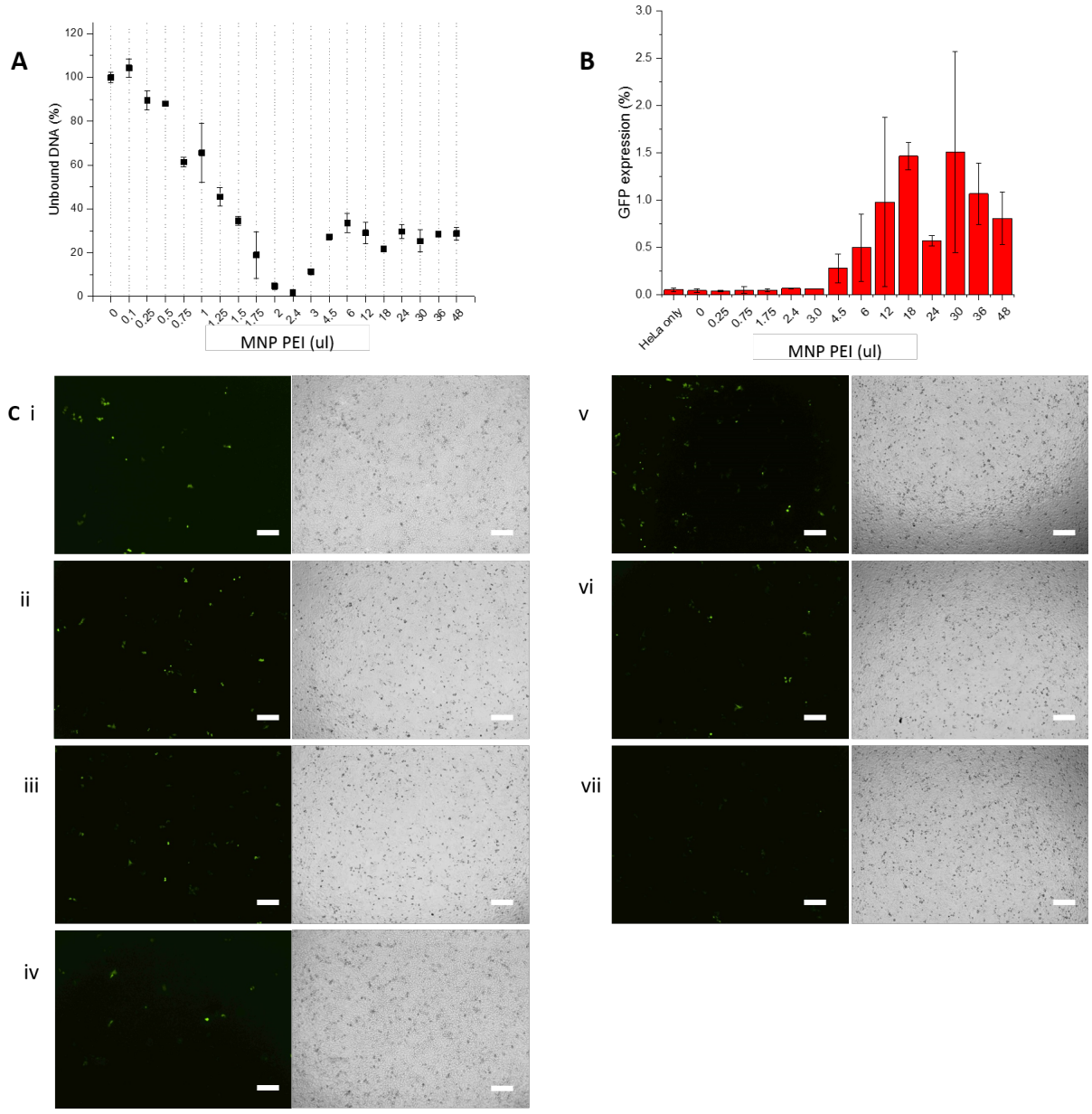

Figure 4.21 (A) DNA binding curve of tdMNP-PEI with increasing MNP-PEI volume, n=1; (B) transfection of MNP-PEI:DNA ratios based on values from DNA binding curve, n=3; and (C) fluorescence images of GFP positive HeLa cells and brightfield image of transfected cells for MNP-PEI volume of (i) 4.5 μL, (ii) 6 μL, (iii) 18 μL, (iv) 24 μL, (v) 30 μL, (vi) 36 μL, and (vii) 48 μL, scale bar=400 μm; n=3.

the effect of surface charge of transfection complexes on cell uptake. Figure 4.21 B shows the transfection efficiency at different tdMNP-PEI:DNA ratios. Transfection efficiency was unusually low compared to previously conducted experiments, where in this case it was at ~2% GFP expression, also observed in micrographs (Figure 4.21 C). An inverse lognormal distribution was observed where at low tdMNP-PEI concentration, cells did not transfect at low tdMNP-PEI loading, until a ratio of 4.5 μL MNP-PEI to 6 μL DNA was reached. The highest transfection was obtained at tdMNP-PEI:DNA 3:1 (18 μL MNP-PEI) and 5:1 (30 μL MNP-PEI). Between these 2 points at 24 μL tdMNP-PEI the transfection drops, possibly due to experimental error.

4.5.6.2 Assembly of transfection complex components and effect with magnet treatments

Complex formation of nanomagnetic transfection usually takes place with MNPs as starting material, followed by the coating of PEI on MNPs and lastly the addition of DNA into the

MNP-PEI suspension. This study was conducted to determine the effect of the order of formation of the three transfection components (MNPs, PEI and DNA) that affect transfection efficiency. Four transfection complexes (transfection agent with plasmid) types using tdMNP-PEI were assembled and used for transfection of HeLa cells with three external magnet treatments (oscillating magnet, static magnet, no magnet), with the nTMag-DNA transfection complex as a positive control for transfection.

Table 4.5 Formation of transfection complexes with different tdMNP, PEI and DNA assemblies

nTMag DNA	nTMag + DNA
PEI DNA	PEI only + DNA
(MNP-PEI) DNA	tdMNP coated with PEI + DNA
MNP DNA	tdMNP only (oleic acid surface) + DNA
(PEI DNA) MNP	PEI only complexed with DNA + tdMNP only (oleic acid surface)

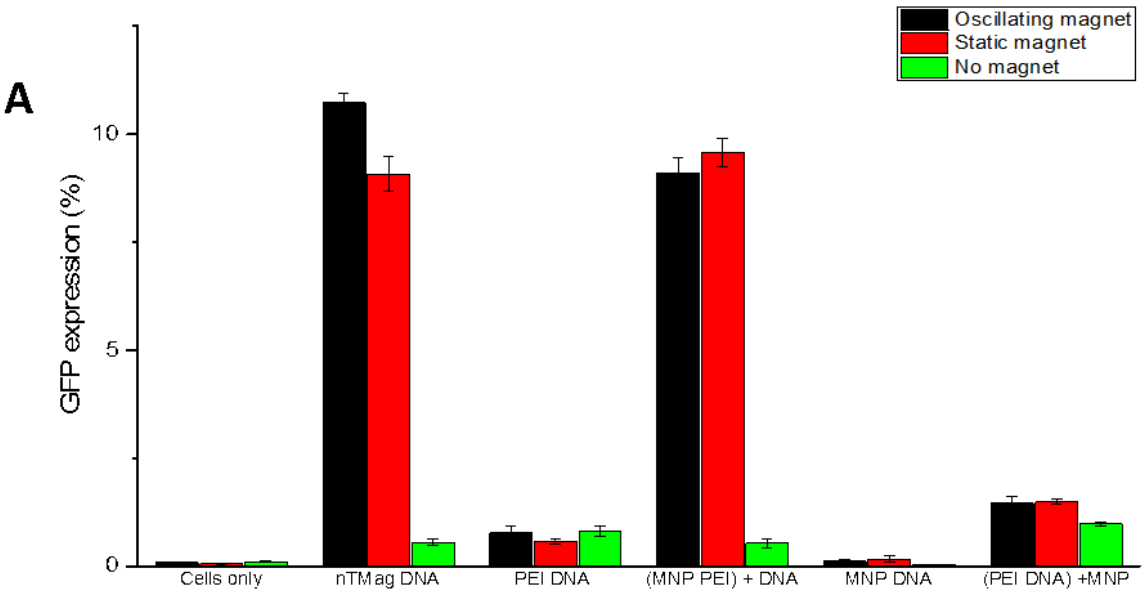

Figure 4.22 (A) GFP expression of complexes made up by assembling transfection components in different order and combinations, and transfection using three magnet treatmentns, n=4. (Figure continued on the following page.)

The assembly of tdMNP, PEI and DNA components that make up the transfection complex is shown in Table 4.5. Figure 4.22 A shows the GFP expression of cells transfected with different complex assemblies. nTMag transfected 10.7% of cells with the oscillating magnefect-nano, and 9% with the static magnet. The next group with successful nanomagnetic transfection was the tdMNP-PEI vector with DNA added subsequently, with a 9% transfection rate. Without an external magnet to pull the magnetic complex towards cells, the transfection rate was close to zero for nTMag and tdMNP-PEI groups, which shows that the presence of a permanent magnet heavily influenced nanomagnetic transfection. With only the PEI polymer as a vector, transfection occurred at ∼2% but was much lower than nanomagnetic transfection. The presence of external magnets did not have an influence on PEI only transfection due to no magnetic material in the transfection complex. tdMNP only without the presence of PEI was unable to transfect cells due to the absence of a cationic moiety to bind DNA. Formation of PEI-DNA and subsequently the addition of tdMNP into the transfection complex also resulted in low transfection rates of 1.4% in the presence of external magnets.

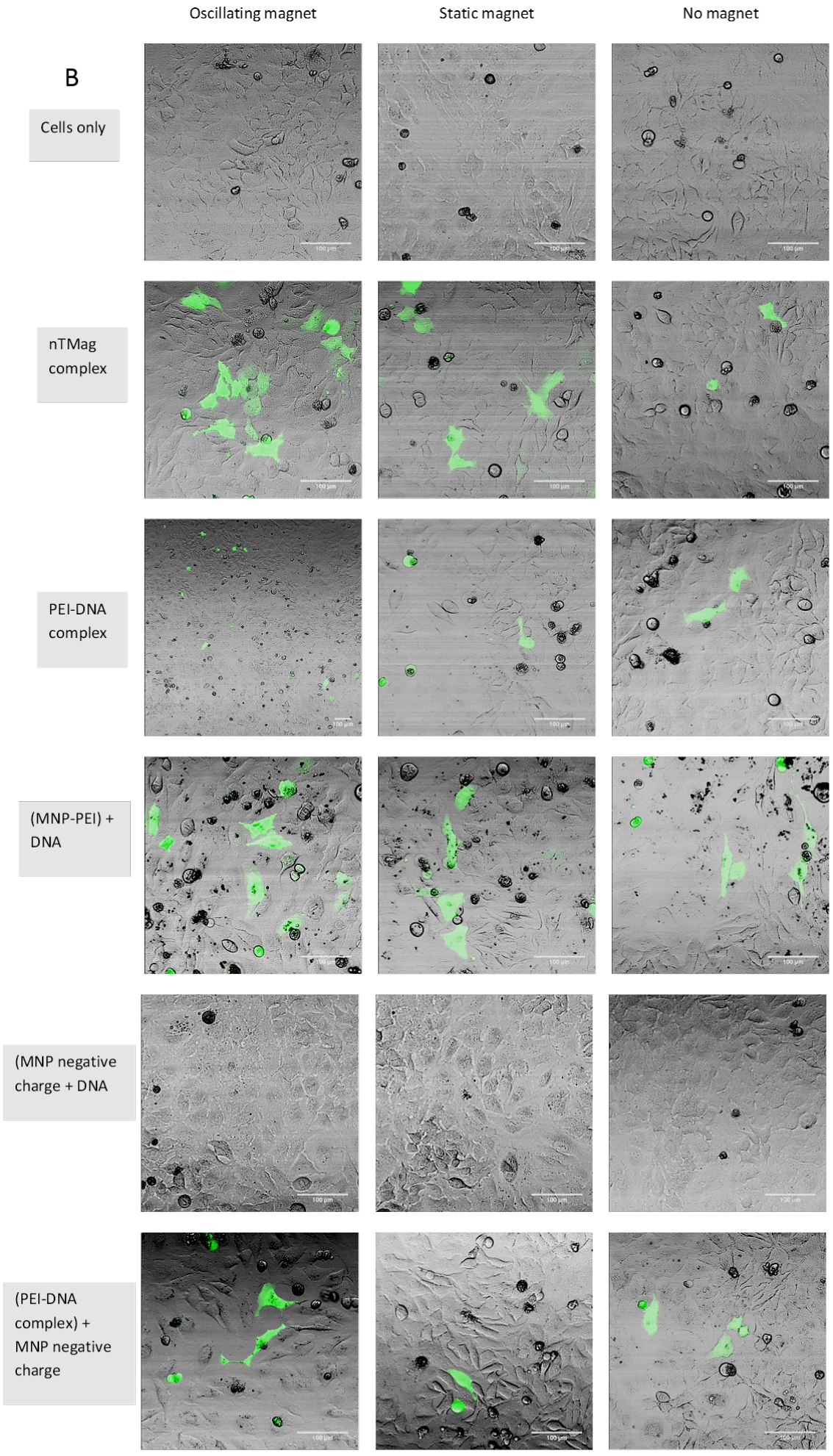
Oscillating magnet
Static magnet
No magnet
B
Cells only
nTMag complex
PEI-DNA complex
(MNP-PEI) + DNA
(MNP negative charge + DNA
(PEI-DNA complex) + MNP negative charge

Figure 4.22 (B) Overlay fluorescence and brightfield images of cells expressing GFP for all treatments; (i) Control cells, (ii) nTMag-DNA, (iii) PEI-DNA, (iv) (MNP-PEI)+DNA, (v) MNP-DNA, (vi) (PEI-DNA)+MNP, scale bar=100μm; n=4.

A two-way ANOVA performed on the transfection groups showed that the presence of an external magnet had a significant effect on transfection rates, as well as the type of transfection complex. The combined effect of both the magnetic field and type of transfection complex significantly influenced transfection ($p < 0.0001$). Based on these results, the rate of nanomagnetic transfection was higher as the time taken to transfect cells was reduced due to the presence of external magnets. PEI alone was less effective as a transfection agent during the 30-minutes transfection procedure but the transfection rate could improve with longer incubation time. There was a significant difference in the static and oscillating magnet fields for group nTMag-DNA, where the oscillating field improved transfection efficiency of nTMag ($p=1.2e^{-6}$) however there was no difference between these two magnet types for other transfection groups.

Overlaid brightfield and fluorescence micrographs (Figure 4.22) show GFP expression within a small field of view, where nTMag (Fig. B ii), PEI-DNA (Fig. B iii), (MNP-PEI)+DNA (Fig. B iv), and (PEI-DNA)+MNP (Fig. B vi) show GFP expression in cells. Transfection group (MNP-PEI)+DNA show dark spots in cells, which can be attributed to tdMNP clusters within the cell cytoplasm.

4.5.6.3 Optimization of tdMNP-PEI to DNA ratio and complex concentration (96- and 24- well plates) for highest transfection efficiency

To achieve highest transfection efficiency, an important parameter is the ratio between tdMNP-PEI (ionic binding) and DNA, and concurrently its concentration per well. Different tdMNP-PEI and DNA ratios were used for transfection as well as a serial dilution to obtain a change in concentration for transfecting HeLa cells,described in Table 4.2. Besides transfection efficiency, cytotoxicity of transfected cells was taken into account (Figure 4.23).

The highest transfection rate obtained was 29% for treatment A4 at 0.96 μL:0.96 μg of tdMNP-PEI to DNA. The second highest transfection was at the same ratio of 1:1 but with the concentration halved (0.48 μL:0.48 μg) in treatment B4. The transfection efficiency was only 3% lower than the highest transfection. Both the groups had high cell viability.

Using PEI-coated tdMNP, lower dosage of PEI can be used due to magnetic targeting into cells, which reduces excessive cell interaction with the toxic polymer. Transfection rates can be increased using higher concentrations of PEI, however it compromises cell viability. To determine if increasing PEI concentrations improves transfection, free/unbound PEI was added into the tdMNP-PEI transfection complex to study transfection efficiency and cell viability. tdMNP-PEI:DNA complex groups were the same as in Figure 4.23, but with the addition of excess PEI into the tdMNP-PEI suspension (Table 4.2).

In Figure 4.24, transfection efficiency was at almost 40% for treatments A5, A6, B5, and C5, which was ∼10% higher than the transfection obtained without free PEI (Figure 4.23 A). Although the transfection rates were high in these groups, they were largely toxic to cells with only 10 – 20% cells surviving in A5, A6, and B5. In well C5, transfection was still almost 40% and cell viability improved to more than half the cells surviving (∼55% cell viability). The effect of free PEI did boost transfection by 10% although cell viability was reduced.

Scale up from 96- to 24 well plates

Two tdMNP-PEI:DNA formulations were chosen from the experiment above and scaled up 6x to a 24-well plate shown in Table 4.6. The 6x scale-up is based on the surface area of the well

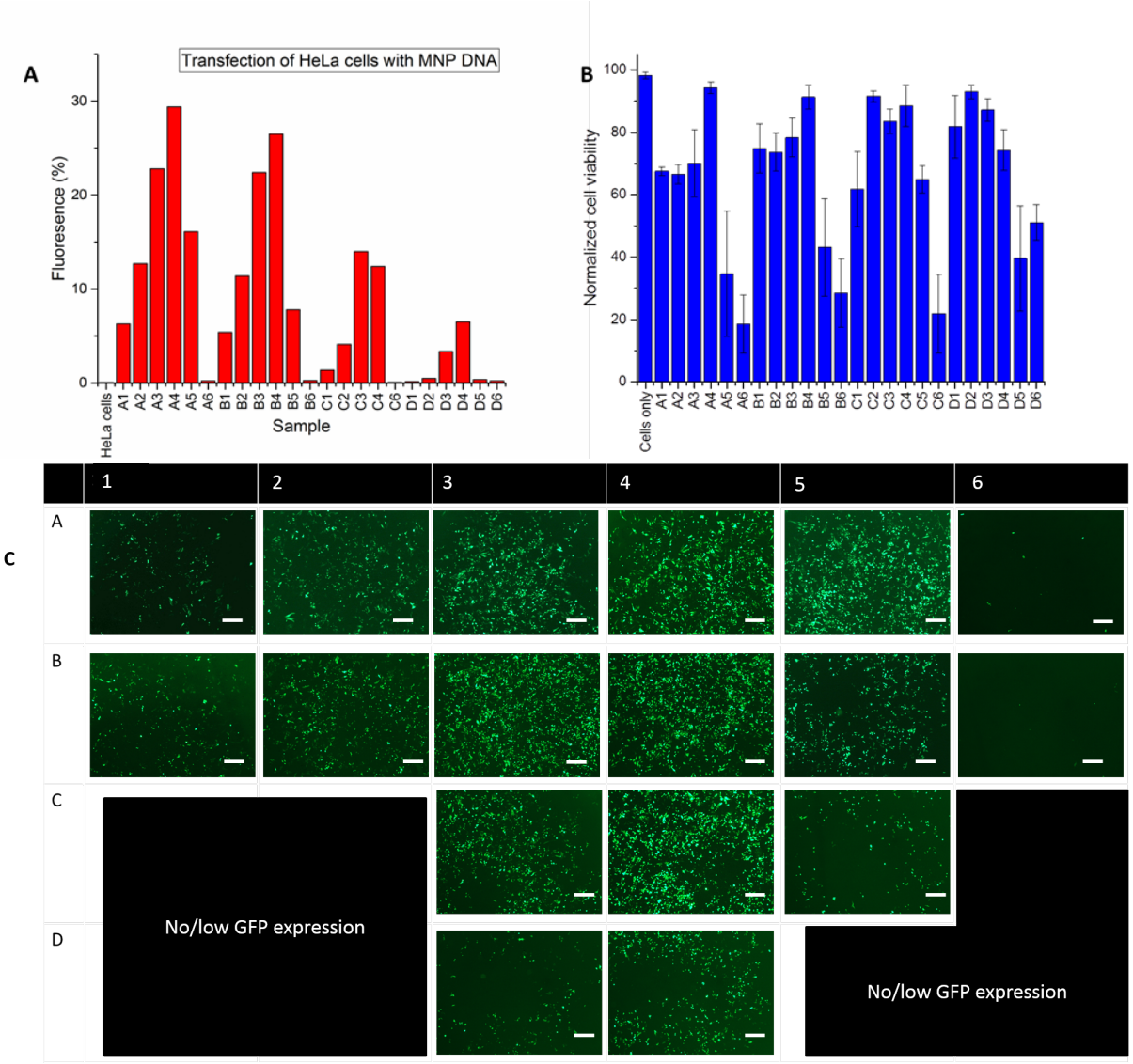

Figure 4.23 (A) GFP expression in HeLa cells at different tdMNP-PEI to DNA ratios (no free PEI) and different complex concentrations by serial dilutions (see Table 4.2 in methods section for labelling scheme); n=3. (B) Cell viability of tdMNP-PEI DNA complexes; n=3. (C) Fluorescence images of HeLa cells of transfection in each well in a 96 well format, scale bar=500 μm; n=3.

plates where the 96 well is 0.32 mm^2 and the 24 well is 2 mm^2. A 2x dilution factor was also calculated for the values. The four complex formulations were studied without and with the presence of excess PEI. These values are given in Table 4.7.

Table 4.6 Scale-up values of transfection complexes to 24 well plate for tdMNP-PEI μL to DNA μg

96 well ratio	24 well ratio
0.48:0.24	2.88:1.44
0.24:0.24	2.88:2.88

Based on Figure 4.25, the highest transfection was at 2.88:2.88 of tdMNP-PEI to DNA without free PEI. The presence of free PEI improved transfection efficiency for groups 1.44:0.72 and 2.88:1.44 (ratio 2:1). The opposite was observed for groups with ratio 1:1, where 1.44:1.44 and 2.88:2.88 had higher transfection without free PEI. Based on the two-way ANOVA, the effect of tdMNP-PEI to DNA ratios are significant, as is the effect of free PEI for transfection. The combined effect of ratio of components as well as free PEI should be taken into account when preparing a transfection complex.

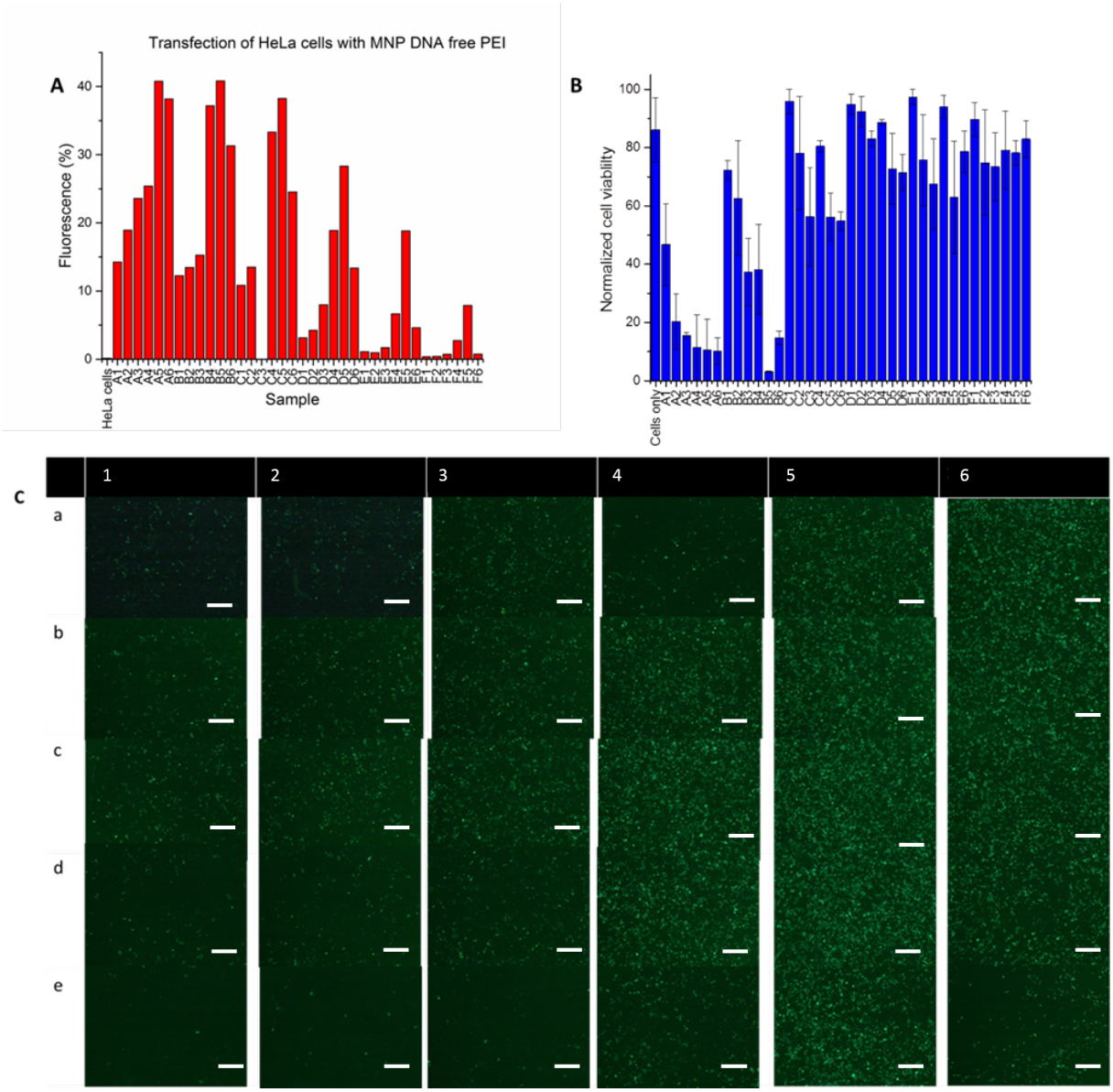

Figure 4.24 (A) GFP expression in HeLa cells at different tdMNP-PEI: DNA: free PEI ratios and different complex concentrations by serial dilutions (Table 4.2). (B) Cell viability of tdMNP-PEI:DNA:free PEI complexes; n=3. (C) Fluorescence images of HeLa cells of transfection in each well in a 96 well format, scale bar=500 μm; n=3

Although the highest transfection efficiency for tdMNP-PEI was 30% with transfection complex ratio of 2.88:2.88, it was still only half the efficiency compared to the nTMag complex. Furthermore, the amount of DNA used for tdMNP-PEI was 4.8 times higher than that used for nTMag transfection with only 0.6 μg DNA. nTMag was more effective in delivering DNA into cells for protein expression. Hence, the lower complex concentration of 1.44 μL:1.44 μg of tdMNP-PEI:DNA was used for subsequent transfection experiments.

4.5.6.4 Effect of frequency and amplitude of magnefect-nano oscillation on transfection efficiency

The nTMag protocol states that the highest transfection efficiency occurs at an oscillation frequency of 2 Hz and 0.2 mm displacement on the magnefect-nano. To study if transfection efficiency on the magnefect-nano changes with a different MNP type, the effect of frequency and amplitude of oscillation on the magnefect-nano for transfection efficiency of tdMNP-PEI was determined. Transfection was also compared for tdMNP-PEI before dialysis and after dialysis (detailed experiments on dialysis in Appendix).

Table 4.7 Dilution factor for 24 well transfection complexes for tdMNP-PEI μL to DNA μg

DF 1	DF 2
2.88:1.44	1.44:0.72
2.88:2.88	1.44:1.44
Free PEI	
1 μg	0.5 μg

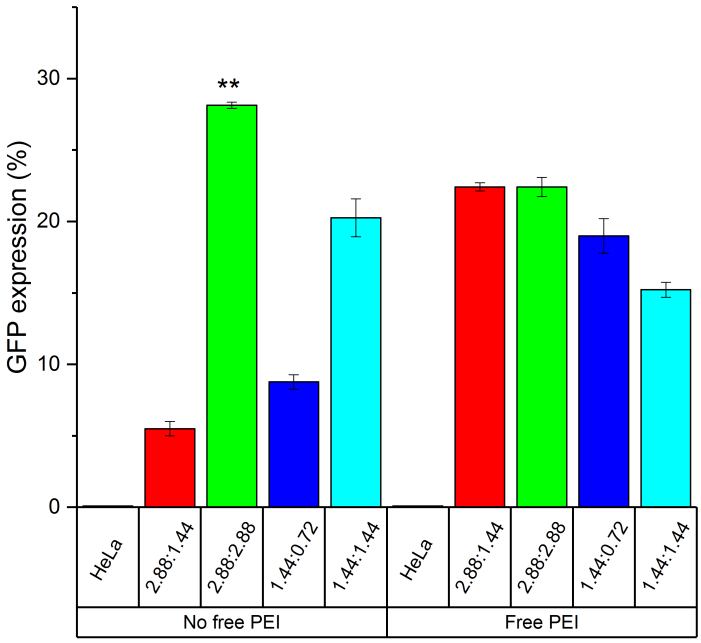

Figure 4.25 Scale-up from 96 well to 24 well plates of MNP-PEI:DNA transfection ratios, with and without addition of free PEI. The ratios are 1.44:0.72, 1.44:1.44, 2.88:1.44, and 2.88:2.88. Free PEI was added at mass of 1 μg or 0.5 μg; n=3.

Figure 4.26 shows the effect on GFP expression with a change in frequency of oscillation at a constant amplitude of 0.2 mm. Transfection was studied for HeLa cells without a magnet, a static magnet, and magnet with oscillation at 0.5 Hz, 2 Hz, and 5 Hz. Based on Figure 4.26 A, highest transfection was at 20% for tdMNP-PEI after dialysis at 2 Hz frequency and 2 mm amplitude. The transfection dropped dramatically at 5 Hz. The effect of dialysis is negligible but there is a pronounced effect at 2 Hz and 5 Hz where dialyzed particles had higher transfection. Without the presence of an external magnet, transfection was less than 5% but the introduction of a static magnet increased transfection by 2x. Cell counts (Figure 4.26 B and C) show high nuclear cell counts for all groups, suggesting low toxicity. The effect of oscillation had significantly improved transfection efficiencies, where oscillation at 2 Hz obtained the highest transfection for tdMNP-PEI after dialysis.

The change in oscillation amplitude was studied to determine the best parameters for the magnefect-nano for tdMNP-PEI transfection agent (Figure 4.27). The frequency of oscillation was kept constant at 2 Hz and treatment groups were no magnet, static magnet, 0.1 mm, 0.2 mm, and 0.5 mm displacement. The highest transfection efficiency at ~30% for the 0.2 mm amplitude group was significantly higher to other groups except for 0.1 mm amplitude. Nanomagnetic transfection without a magnet resulted in a low transfection of ~5%, similar to Figure 4.26 above. In this study, the effect of dialysis was not significant but amplitude of oscillation affected transfection efficiency. Based on the two-way ANOVA, there was also no correlation between dialysis and amplitude of oscillation.

Therefore, the effect of dialysis in this study was inconclusive but the highest transfection

A

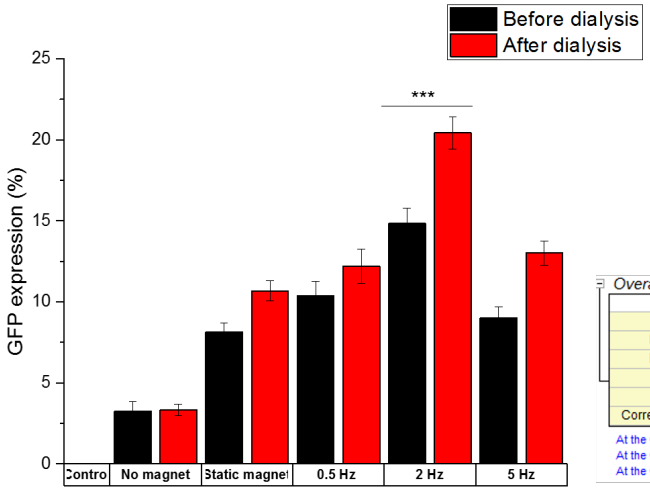

Overall ANOVA

	DF	Sum of Squares	Mean Square	F Value	P Value
Dialysis	1	3.49462E-5	3.49462E-5	8.02614E-6	0.99775
Frequency	5	1321.15888	264.23178	60.68654	0
Interaction	5	58.28071	11.65614	2.67709	0.02779
Model	11	2415.75851	219.61441	50.4392	0
Error	76	330.90721	4.35404	--	--
Corrected Total	87	2746.66572	--	--	--

At the 0.05 level, the population means of **Dialysis** are **not significantly** different.
At the 0.05 level, the population means of **Frequency** are **significantly** different.
At the 0.05 level, the interaction between **Dialysis** and **Frequency** is **significant**.

B

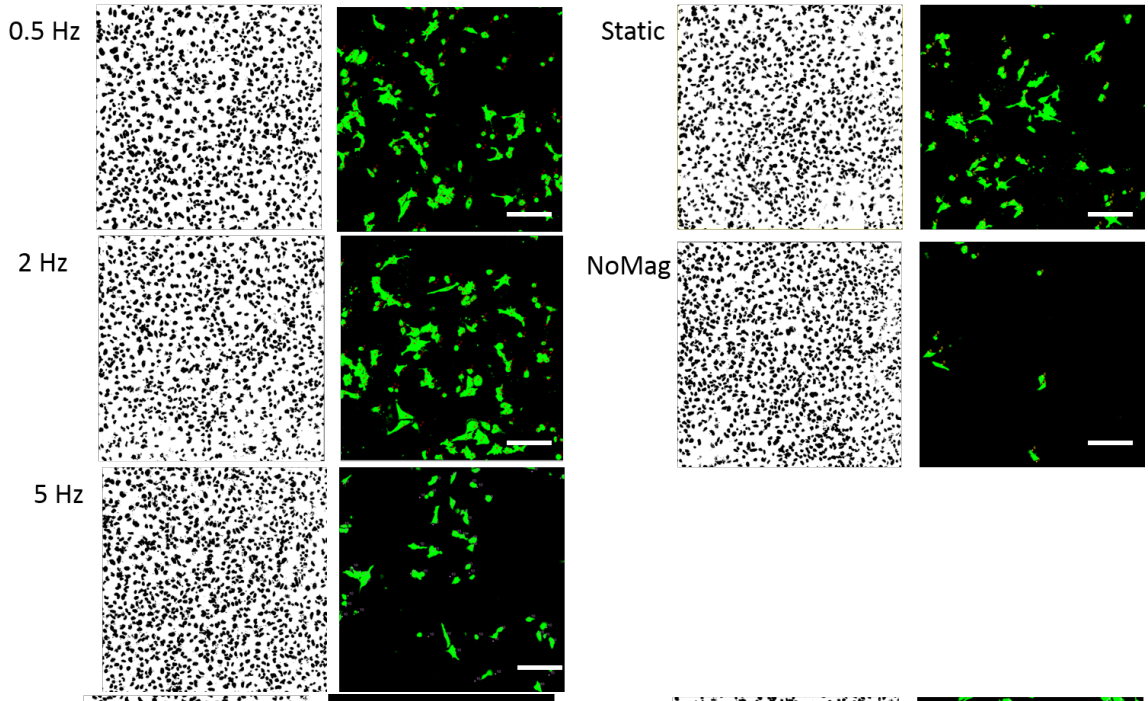

C

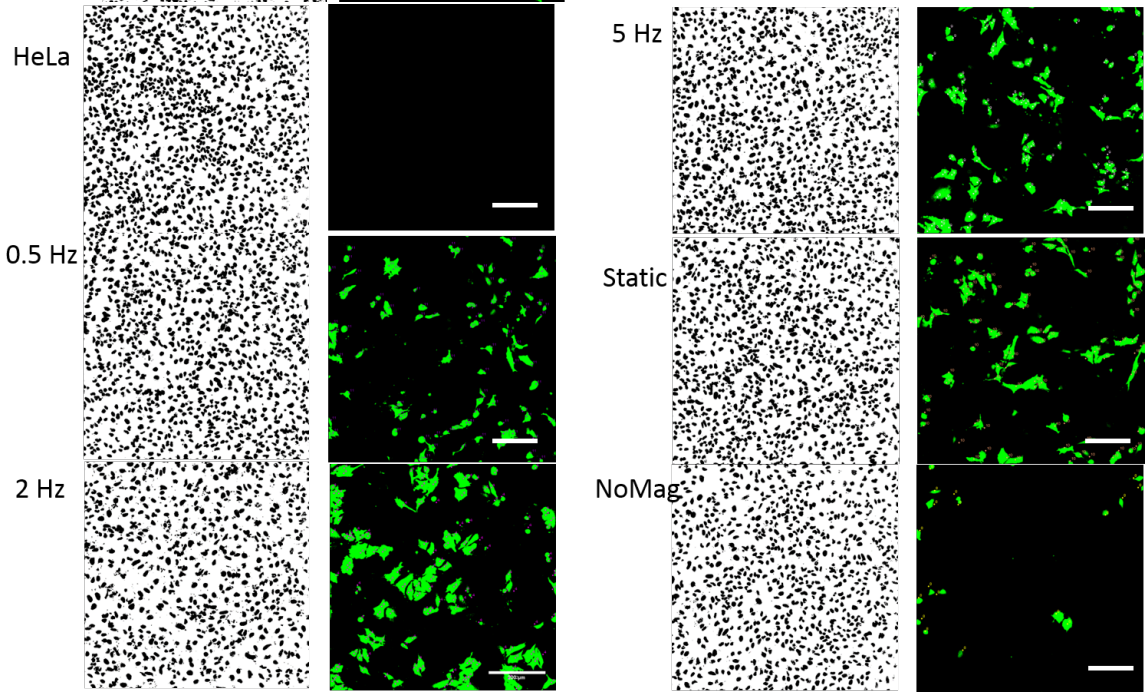

Figure 4.26 Transfection of HeLa cells at different frequencies of magnefect-nano oscillation and 0.2 mm amplitude. (A) GFP expression of transfected cells at different magnefect-nano frequencies, and cell nuclear count (left) and fluorescent GFP expression (right) images of HeLa cells for (B) tdMNP-PEI before dialysis and (C) tdMNP-PEI after dialysis. Scale bar 200 μm; n=4.

efficiency obtained with tdMNP-PEI was similar to oscillation parameters of nTMag, which is 2 Hz frequency and 0.2 mm amplitude.

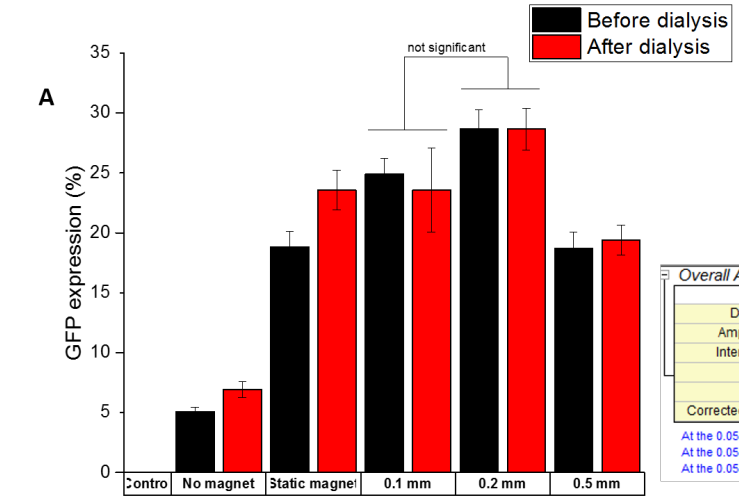

Overall ANOVA

	DF	Sum of Squares	Mean Square	F Value	P Value
Dialysis	1	0.00374	0.00374	1.60713E-4	0.98991
Amplitude	5	5239.12709	1047.82542	45.04719	0
Interaction	5	94.58923	18.91785	0.8133	0.54337
Model	11	8585.83695	780.53063	33.55589	0
Error	87	2023.67367	23.26062	--	--
Corrected Total	98	10609.51062	--	--	--

At the 0.05 level, the population means of **Dialysis** are **not significantly** different.
At the 0.05 level, the population means of **Amplitude** are **significantly** different.
At the 0.05 level, the interaction between **Dialysis** and **Amplitude** is **not significant**.

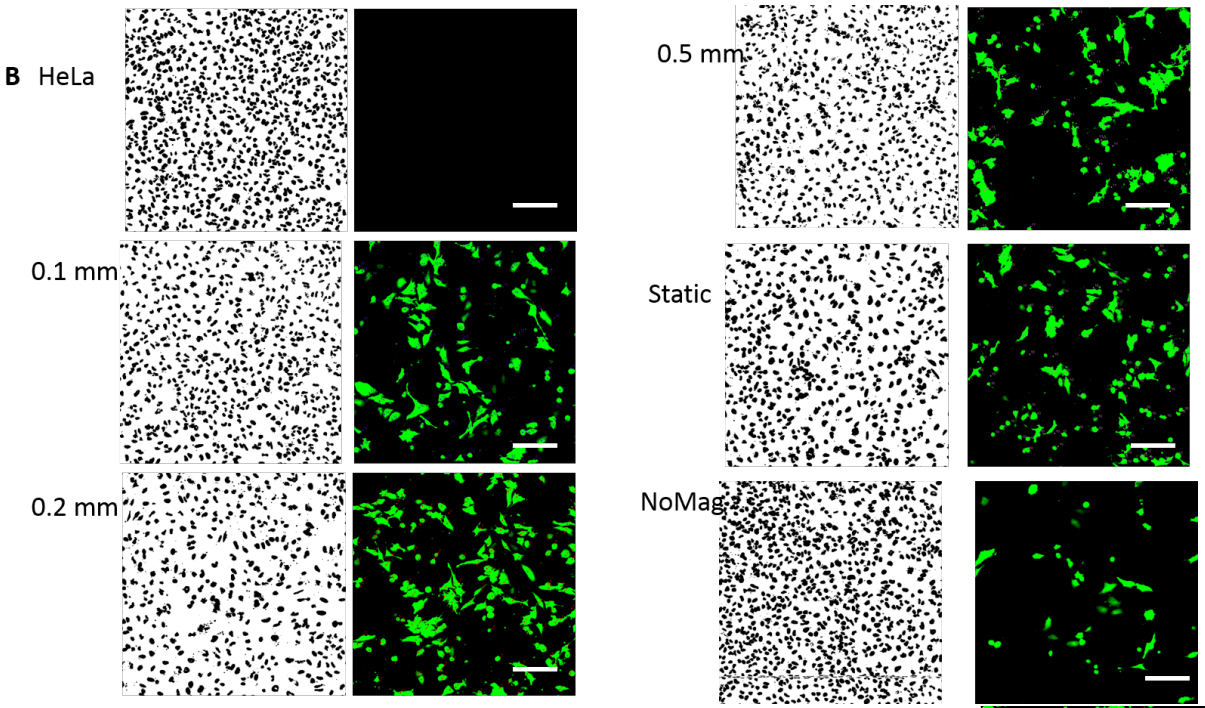

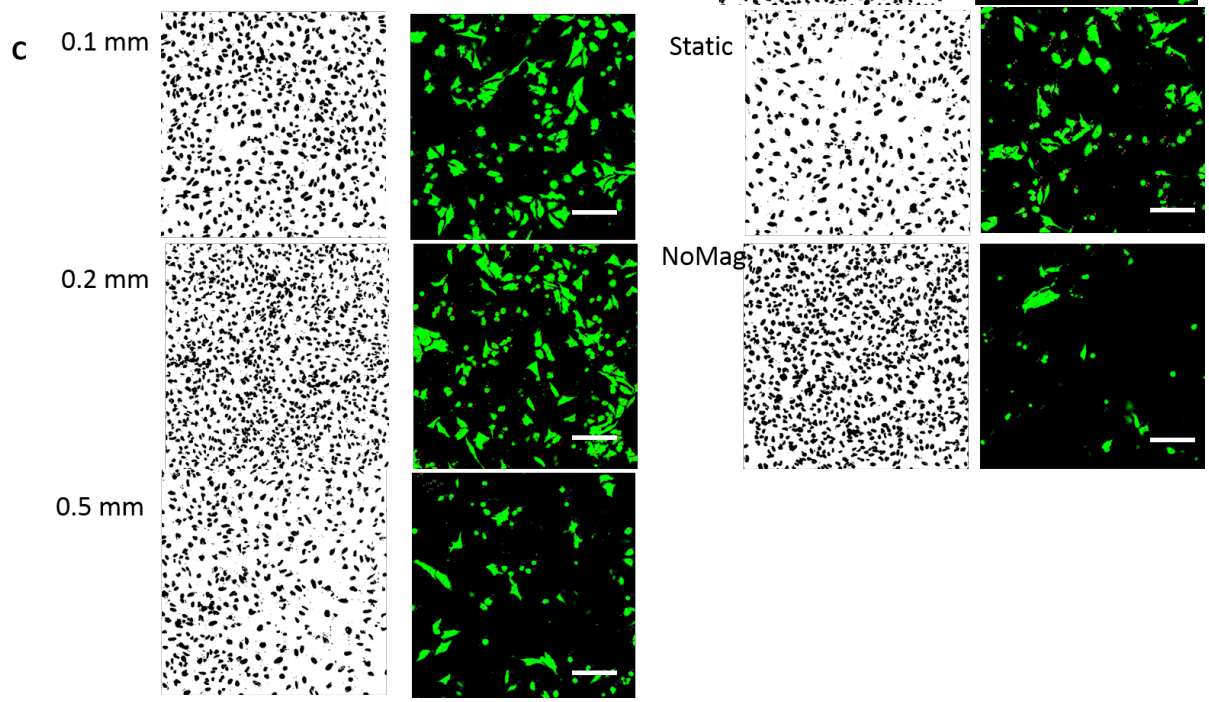

Figure 4.27 Transfection of HeLa cells at different amplitude of magnefect-nano oscillation and 2 Hz frequency. (A) GFP expression of transfected cells at different magnefect-nano amplitude, and cell nuclear count (left) and fluorescent GFP expression (right) images of HeLa cells for (B) tdMNP-PEI before dialysis and (C) tdMNP-PEI after dialysis. Scale bar 200 μm, n=4.

4.6 Discussion

4.6.1 Effect of size on MNP-PEI uptake and toxicity in cells

Citric acid coating of iron oxide MNP is used widely for various applications requiring an aqueous suspension of MNP. The relative ease of the coating method of bare particles make it a favourable choice, especially when bare MNP have no surface functional groups to attach a coating to. This coating process is especially favoured during synthesis of MNP by co-precipitation as it produces bare particles. In Chapter 4.5.2, bare MNP were coated with citric acid to form surface carboxylic groups.

Citric acid molecules contain 1 hydroxide group, and 3 carboxylic groups, each with a different acid dissociation constant (pKa), where above a certain pH, the carboxylic group deprotonates to release a hydrogen ion. The pKa of each carboxylic group in a citric acid molecule are 3.13, 4.76, and 6.4. Conjugation of citric acid onto bare iron oxide particles occurs with the deprotonation of the carboxylic groups on citric acid to form $–COO^-$ by adjusting the pH to 5.2. At this pH, the carboxylic groups with pKa 3.13 and 4.76 are dissociated and able to attach to the surface of iron oxide particles by chemical adsorption. The remaining –COOH group which is not dissociated at pH 5.2 is free to confer stearic and electrostatic stability to MNP in suspension at a pH above 6.4, where it dissociates and MNP become negatively charged, however Campelj et al. showed that the highest percentage of MNP suspended as a stable colloid was at pH 10. Bare maghemite particles have an isoelectric point at pH 7 (Campelj et al., 2008). Therefore, the acidification step at pH 2 before citric acid coating and at pH 5.2 during coating confers a positive charge across the surface of MNP, which reacts with the $–COO^-$ groups of citric acid during chemisorption with the influence of temperature to promote bond formation.

A study conducted by de Sousa et al. to measure the stability of citric acid coated particles found that higher stability was achieved when one COO- group was anchored to the MNP with two free carboxylic groups for electrostatic stability (de Sousa et al., 2013). The three particles coated with citric acid were Sigma-MNP, FS-MNP and CoP-MNP. Citric acid coating provided particle stability shown in the ACS measurements. MNP-cPEI by thermal decomposition also showed good stability in water.

PEI coating on citric acid coated particles was performed using electrostatic adsorption, whereas tdMNP-cPEI had covalently bound PEI using carbodiimide crosslinking, while PEI was grafted onto the amine groups on the carbon shell of SF199 and FB257 using aziridine. Cells take up particles by endocytosis based on size, surface charge, and shape. Studies found that cells can even take up particles up to 3 μm in size, and the endocytic pathway through which particles are taken up is not size-dependent (Gratton et al., 2008b). There is currently no consensus on NP size dependent internalization. Lerch et al. found that cells take up the same amount of material regardless of particle size (Lerch et al., 2013), however Leclerc found that smaller aggregates had higher internalization (Leclerc et al., 2012). The mechanism of uptake was also determined to be different based on particle size, where small NPs adhere to the cell membrane before internalization whereas larger NPs are immediately internalized (Shang et al., 2014), therefore the rate of internalization of larger particles is higher (Sabuncu et al., 2012).

Besides uptake in cells, particle size also affects cytotoxicity. Toxicity of MNP could be observed in the Prussian blue images (Figure 4.8), where MNP type affected cell density after treatment. The highest cell density after internalization was treatment with CoP-MNP and MNP-cPEI, suggesting low cytotoxicity. This was reflected in the viability assay, where there

was not a significant difference in cell viability between CoP-MNP and MNP-cPEI treated cells compared to the control cells. Interestingly, the particles which caused low toxicity also had the highest uptake in cells. Toxicity studies of NPs are also inconclusive, with reports of larger silica particles or aggregates being more toxic (Leclerc et al., 2012), and the opposite effect observed with silver NPs (Park et al., 2011), and even that particle size is a small factor in cytotoxicity (Zhang et al., 2011). In this study, a relationship between MNP size and cytotoxicity was observed. MNP with a carbon shell had low cytotoxicity which may suggest that either grafted PEI had lower toxicity compared to the commercial polymer, or that the carbon shell provided protection against the cell interacting with the metallic iron core.

4.6.2 MNP-PEI to DNA ratio for efficient transfection

The DNA binding assay was performed to study the concentration of MNP-PEI needed to bind a fixed amount of DNA to obtain a MNP-PEI to DNA ratio of complete binding. The positively charged surface of PEI coated onto MNP binds to the negatively charged phosphate backbone of DNA by electrostatic interaction, therefore bound DNA undergoes flocculation during centrifugation and DNA that is unbound due to MNP-PEI to DNA saturation will remain in the suspension. The DNA that remains in suspension can be measured by UV spectrometry. MNP-PEI was added in gradual increasing concentrations until all DNA in the suspension is bound.

In Figure 4.11 and Figure 4.21, the ratio for the minimum amount of particles to bind free DNA is at an MNP-PEI:DNA ratio of 1:8 for nTMag, 1:12 for polyMag and 3:1 for tdMNP-PEI. At this ideal complex ratio, the complete binding of the DNA phosphate backbone to the amine groups of PEI negates both charges, leaving the transfection complexes at a neutral charge. Below this complex ratio (left side of x-axis), there is a lack of amine groups from PEI to bind all DNA in suspension, therefore DNA exists unbound in the solution. Above the complex ratio (right side of x-axis), there is an excess of amine groups/PEI and the net charge should be positive. DNA absorbance measured above this ratio should be close to zero due to excess PEI binding all free DNA. However, from the binding curve, there is an increase in DNA absorbance signal beyond the ideal MNP-PEI to DNA ratio. Since all DNA in suspension should be completely bound to MNP above the values stated above, the reading picked up by the Nanodrop instrument could be due to contamination from other material such as excess PEI from MNP surface.

Different ratios of tdMNP-PEI to DNA were studied for their transfection efficiency. Based on Figure 4.21 B, transfection only occurs above the ideal complex ratio. When the net charge of complexes is close to zero at tdMNP-PEI 2.4, no transfection occurred. The same was observed with nTMag. The transfection rates increased when the amount of nTMag was increased, and was most efficient at a ratio of 1:1 where the amount of PEI exceeded DNA. This effect could be based on the surface charge of complexes which affects cell interaction and internalization. Internalization of positive charged particles in cells is more efficient compared to negatively charged and neutral charged particles (Chen et al., 2011). Positive charged materials are endocytosed more easily and have better interaction with the negatively charged plasma membrane. Negatively charged particles take a long time to be endocytosed, but with a protein corona the toxicity effect is reduced (Mbeh et al., 2015). Particles without a surface charge take a long time to be endocytosed, possibly due to low ionic interaction with biomolecules on the plasma membrane. Besides uptake in cells, success of transfection is dependent on the ability of transfection complexes to either bypass the endocytic trafficking pathways or to escape from the endosome. One hypothesis for the suitability of PEI as a transfection agent is its buffering capacity, which induces a proton-sponge effect causing endosome rupture and release of transfection complexes (discussed in Chapter 1) (Behr, 1997; Kurtulus et al., 2014).

At different ratios of tdMNP-PEI to DNA, it is assumed that the size of complexes change. It has been reported that at low PEI:DNA ratio, complex diameters are large but decrease with increasing PEI in the system. The higher PEI:DNA ratios also resulted in better transfection

except until cytotoxicity became the dominant factor (Xie et al., 2013; Zhao et al., 2014). This same effect was reported in liposomes for transfection where a higher charge density created smaller complexes with better transfection efficiency (Brgles et al., 2012). Gold NPs conjugated with PEI showed better transfection with smaller aggregates whereas larger NP complexes were trapped in endocytic vesicles (Cebrián et al., 2011). The results obtained here is in line with previous studies, where a higher charge density of PEI complexes induce better transfection success (Xie et al., 2013; Zhao et al., 2014). This may be due to their smaller size and higher positive charge density which improves buffering capacity to escape from endosomes (Cebrián et al., 2011). The DNA binding curve is only a guide to obtain correct transfection ratios, where transfection occurs above the ratio where DNA absorbance is zero.

4.6.3 Assembly of transfection components

The three components involved in nanomagnetic transfection are MNPs, cationic agent (polymer or lipid), and plasmid of interest. Commonly, the cationic agent is coated onto MNPs and DNA is condensed on the surface of this structure before delivery into cells. In the study in Section 4.5.6.2, the different components are ordered differently in order to systematically elucidate the importance of each component for successful transfection. The three types of magnet treatments show that external magnets exert a strong influence on magnetic materials in cell culture plates. When nTMag and tdMNP-PEI carrying DNA were used to transfect cells, the presence of permanent magnets at the bottom of plates significantly increased transfection rates. External magnets do not have influence on treatments without magnetic material such as PEI + DNA. The effect of oscillation was only significant for nTMag and not for tdMNP-PEI. Two possible differences in the particle types are that nTMag is superparamagnetic and tdMNP-PEI are magnetically blocked, and nTMag has a higher amount of PEI per volume of suspension, inferred from the higher loss of cells during transfection at lower volume compared to tdMNP-PEI. Therefore the size and charge of the resulting complex are different between the two particle types. The smaller size of nTMag could induce a larger movement on the cell membrane during oscillation, promoting endocytosis.

For a 30-minute transfection, PEI-DNA was ineffective as PEI-mediated transfection usually takes 6 hours to transfect cells at maximum capacity. Therefore MNPs are effective in reducing transfection time while obtaining high transfection capacities. Based on the assemblies of components, MNPs alone were not able to carry out transfection without PEI. tdMNPs with a negative charge do not have the ability to bind and condense DNA on its surface. Even if this is able to occur, MNPs cannot protect the DNA from the harsh internal environment of the cell such as degradation by nucleases and endosomal lysis. Negatively-charged MNPs are also internalized slower than positively-charged MNPs (Fukumoto et al., 2010; Calatayud et al., 2014), therefore during the 30 minutes of transfection, tdMNPs alone will have less uptake in cells than the tdMNP-PEI.

When the components of transfection are reversed, where PEI is complexed with DNA and tdMNPs are added into the suspension after complexation has taken place, transfection rates were low. PEI condenses DNA to form large aggregates of PEI-DNA structures. With the binding of DNA to PEI, the amount of positively-charged groups on PEI is reduced. The low charge density of PEI complexes coupled with the large complex sizes make it difficult for PEI-DNA complexes to attach to MNPs. This in effect may reduce the chances of MNPs being able to act as a carrier to sediment the PEI-DNA complexes in the presence of an external magnet. A similar study conducted by Arsianti and colleagues found that MNP-PEI + DNA complex had highest internalization in cells but it was the PEI-DNA + MNP complex that showed highest expression (Arsianti et al., 2010).

In summary, the design of a magnetic vector for transfection was most suitable using the conventional coating of PEI onto MNP surface before complexation to DNA to obtain high transfection efficiencies for nanomagnetic transfection.

4.6.4 Frequency and amplitude of the magnefect-nano oscillating system

One of the parameters that could influence transfection efficiency is the magnetic oscillating system. As discussed in Chapter 1, there are various magnetic oscillating systems developed for improving transfection rates. When the magnefect-nano and MICA system was tested against each other in Section 4.4.5, the horizontal system was shown to have higher transfection. The effect of the external magnet movement on MNP movement in cell culture wells and the interaction between cells may provide an explanation to the difference in transfection rates. The magnefect-nano moves in a horizontal oscillating fashion, therefore the MNP complex gets pulled towards the cell monolayer and maintains contact with the plasma membrane throughout the 30-minute duration, besides creating a small lateral movement on the cell surface. The MICA system in contrast, moves up and down on the z-axis. With the well plates on the top of the stage, movement of the magnet towards and away from the wells creates a on and off magnetic field where the magnetic field gradient gets weaker in the cell culture wells when moving downwards. The effect on MNP complexes would be that they get pulled towards cells when the magnet moves towards the well plates and goes back into suspension when the magnet moves away. This type of magnetic pulse makes it more difficult for MNP complexes to reach cells and attach to the plasma membrane. Complexes that quickly sediment on to of adherent cells have a higher chance of being internalized but the movement up and down of the MNP complex possibly does not help with internalization, especially if the complex has not adhered to the cell membrane. Therefore, higher internalization of MNP complexes and concurrently transfection rates are dependent on continuous attachment of MNP complexes on cells for the duration of the transfection.

The frequency and amplitude of oscillation of the external magnet showed a positive correlation to transfection efficiency. For both nTMag and tdMNP-PEI, the same parameters provided the highest GFP expression, at 2 Hz and 0.2 mm oscillation. tdMNP-PEI also had significantly higher transfection compared to the static magnet, suggesting a positive effect of the magnefect-nano oscillation on transfection. This evidence suggests that the oscillation of the external magnet causes improved internalization of MNP complex into cells by stimulation endocytosis. Another possibility is that oscillation causes movement of MNP inside endocytic vesicles which ruptures the vesicles to promote MNP complex escape. Since both nTMag and tdMNP showed highest transfection at the same oscillating parameters, the difference in size and magnetic anisotropy of both the MNP types did not influence the rate of oscillation for MNP uptake. However, not all oscillating nanomagentic transfections provide highest transfection at the default parameters. A study by Pickard and Chari showed that not only did the magnefect-nano system improve transfection of astrocytes compared to the static magnet, the highest transfection efficiency was obtained at a lower frequency of 1 Hz with 0.2 mm amplitude (Pickard and Chari, 2010a). To study this effect further, different sizes, particles types, and cell types should be studied to understand the mechanism of magnetic oscillation on the uptake efficiency of MNP into cells.

4.6.5 Effect of PEI on cellular toxicity

During cell transfection, maintaining viable cell populations is important to obtain high cell counts and healthy cells expressing the protein of interest. Transfection efficiency has to be weighed against cell health because successful transfection using toxic particles will result in decrease of cell numbers and a change in cell processes, which is highly undesirable if the method were to be applied for genetic engineering of cells.

Toxicity of tdMNP-PEI transfection complexes have been observed in HeLa cells at long complex incubation time and addition of excess PEI. To understand the effect of incubation time of transfection complexes in cells on cytotoxicity, cells either underwent a media change 30 minutes or 48 hours after transfection complex addition. Figure 4.18 B clearly shows that media change significantly improves cell viability for all treatment groups. During the optimiza-

tion of MNP-PEI to DNA ratio in Section 4.5.6.3, highest transfection efficiency obtained by tdMNP-PEI is 30% but the addition of free PEI improves transfection efficiency by 10%. At the tdMNP-PEI:DNA ratio where transfection was 26% (Group B4), the addition of free PEI into the group increased GFP expression but cell viability dropped to below 50%. The addition of free PEI increased transfection but cells suffered a large loss in viability.

Because PEI-coated particles are toxic, a shorter incubation time of complexes in media improves cell viability greatly. PEI-mediated gene delivery is known for causing toxicity to cells. Research suggests that the high density positive charges of PEI causes apoptosis, especially when coupled with DNA (Lee, 2007). When DNA is coupled to PEI to form complexes, these complexes have reduced toxicity due to the lower net positive charge compared to free PEI. However, in the cell the DNA dissociates from PEI creating free PEI which attaches to cellular or nuclear compartments and causes cytotoxicity. For successful transfection, PEI relies on the proton sponge effect for endosomal escape. This mechanism however causes cell stress which triggers an inflammatory or apoptotic response (Beyerle et al., 2010). PEI toxicity has also been attributed to its destabilizing effects on the cell plasma membrane (Aravindan et al., 2009). The toxicity conferred by PEI is also dependent on its structure, where branches PEI are more toxic compared to the linear structure (Kafil and Omidi, 2011). This effect could be related to the charge density on each PEI type, where branched PEI have higher amine group content and therefore has a stronger positive charge, inducing apoptosis in cells. An inflammatory or apoptotic response in cells are reported to be induced by the production of reactive oxygen species (ROS) which causes oxidative cell stress (Beyerle et al., 2010). The effects of ROS on cells are discussed further in Chapter 6.

The effect of high MW PEI on cell viability is well known, especially concerning cationic polymer transfection. Godbey et al. studied the effect of free PEI and PEI complexed with DNA on cell viability (Godbey et al., 2001). It was found that both free and complexed conferred toxicity on cells inducing apoptosis, however the time taken to inflict toxicity differed where complexed PEI took ∼7 hours longer to show a cytotoxic effect compared to cells treated with free PEI. Removing free PEI during PEI-DNA complexation also reduced cytotoxic effects (Godbey et al., 1999a). Free PEI was shown to inflict plasma membrane destabilization, which is an immediate effect when PEI makes contact with cells, however the PEI-DNA complexes are taken in safely by cells but show delayed toxicity when the complex unfurls in the cell and the released PEI inflicts toxicity in the cell.

4.7 Conclusion

nTMag was able to obtain high transfection efficiencies of 50 – 60% in HeLa cells after optimization of parameters was performed. The nuclear count for cells treated with nTMag was lower than the control, suggesting high cytotoxicity. After optimization, tdMNP-PEI was able to transfect 20 – 30% of HeLa cells while maintaining cytotoxicity at low levels. To improve transfection rates similar to nTMag, one option is to increase the PEI concentration in the MNP suspension, however this will adversely affect cell viability. tdMNP-PEI transfection also had low transfection reproducibility of studies involving the frequency and amplitude of oscillation.

Ideally, optimization of transfection parameters should be performed for different cell types and MNP transfection agents. The parameters studied here were the MNP to DNA binding curve, the ratio of MNP to DNA complex formulation, complex concentration, cell seeding density, time of maximum protein expression, effect of media change, effect of storage time on MNP transfection activity (Appendix), presence of excess PEI, and the frequency and amplitude of oscillation on the magnefect-nano. Over time, the nTMag transfection efficiency decreased to 10% when cells were transfected according to the nanoTherics protocol. Optimization of nTMag transfection improved efficiency to 60%. Synthesized tdMNP-PEI was also able to perform transfection after the transfection parameters were optimized, with 30% highest transfection efficiency and low cytotoxicity.

The formulations for preparing lab-syntheiszed MNP transfection agent was also determined, where PEI transfected well at neutral pH with good buffering capacity. PEI was also found to work well when the binding strength to MNPs was low (high dissociation). When PEI was covalently bound to MNPs, transfection was unsuccessful. The addition of free PEI did improve transfection efficiency; however, cell viability was negatively affected.

Based on this study, MNPs synthesized in the lab can be designed to perform gene delivery functions by functionalization with a chemical transfection vector. The binding between MNPs and surface transfection agents as well as MNP transfection vector to the DNA has to be studied to facilitate endocytosis, endosomal escape, nucleic acid protection, and transport of nucleic acid into the nucleus. To improve transfection efficiency, cell viability becomes compromised. The next chapter investigates the mechanism of nanomagnetic transfection using ACS measurements and Raman spectroscopy.

Chapter 5

Developing methods to investigate the mechanism of nanomagnetic transfection

5.1 Introduction

As discussed in Chapter 1, nanomagnetic transfection involves the initial attachment of MNP transfection complexes onto the cell membrane, subsequently the endocytosis and entrapment of the MNPs in the endocytic vesicle, follwed by endocytic escape and detachment of the PEI-DNA complex into the nucleus and finally protein expression (Figure 5.1).

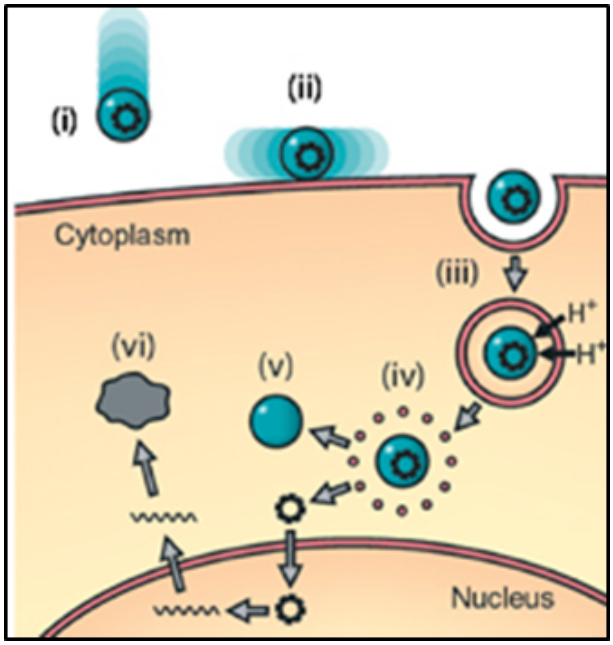

Figure 5.1 Mechanism of nanomagnetic transfection in cells from attachment to cell membrane to protein expression (Fouriki et al., 2010). Reprinted with permission under the terms of the Creative Commons Attribution-Noncommercial 3.0 Unported License.

In Chapter 4, nanomagnetic transfection was optimized to achieve the highest efficiency by studying the parameters affecting nanomagnetic transfection. Quantification was performed at the end-point of the transfection method to determine GFP expression, however the mechanism of nanomagnetic transfection was not established. In this chapter, experiments were performed to examine the movement of the nanomagnetic transfection complex in cells from cell attachment to GFP expression using AC susceptometry, fluorescence confocal imaging, and Raman spectroscopy.

Using AC susceptometry to study blocked particles, changes in the relaxation behaviour of

particles can be monitored by observing changes to the χ' and χ" Brownian signals of particles before and after internalization in cells (Soukup et al., 2015) and even at different time points in cells. When MNPs are immobilized in a viscous suspension or dried on a matrix, blocked particles lose their magnetic susceptibility signal and the χ" Brownian peak is diminished due to their inability to physically rotate. ACS simulations were performed and illustrated in Figure 5.2 using constant parameters with anisotropy of 7200 Jm^{-3}, temperature of 310 K, particle size of 20 nm with polydispersity of 0.3 and a cluster diameter population of 60 nm with a polydispersity of 03. The difference between the two simulations is the use of a viscosity of 0.0007 Pa.s for 'no immobilization' and 1.0000 Pa.s for 'immobilization' simulations.

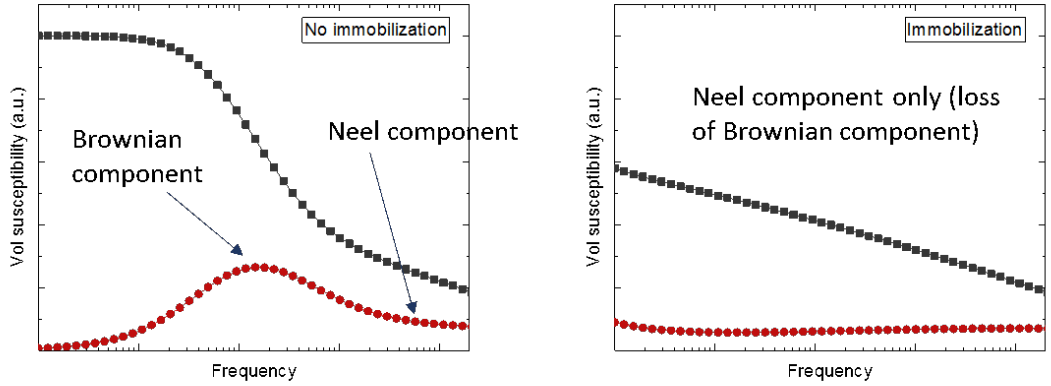

Figure 5.2 ACS simulation of MNPs with partial Brownian and Néel relaxation components. (Left) MNP in suspension with complete mobility showing both relaxation components. (Right) Immobilization of MNPs causes loss of Brownian relaxation component with only Néel relaxation ACS signal.

The remaining susceptibility signal after Brownian immobilization is contributed by Néel relaxed particles, which are unaffected by the external suspension/environment due to their intrinsic magnetic spins (Figure 5.2 right). This effect was simulated using the computational model. Therefore using MNPs with a Brownian component, the loss in a Brownian signal indicates particle immobility due to MNPs attachment to the cell, entrapment in the endocytic vesicle, or the formation of large clusters below dectable limits. The appearance of a Brownian peak in the cell, however would indicate particle endosomal escape and movement of mobile MNPs to the nucleus to deliver the PEI-DNA cargo for transfection. By observing changes in the Brownian relaxation signal of MNP, AC susceptometry would be a useful technique to probe endosomal escape in cells for PEI-coated MNPs.

Optical microscopy can complement AC susceptometry techniqies, as the ACS measures overall average mobility/clustering over population of cells whilst optical microscopy measures local effects (e.g. for individual cells). Confocal fluorescence images were presented in this chapter to obtain a visual understanding of the interaction and movement of tdMNP-PEI transfection complexes in cells.

Besides AC susceptometry, Raman spectroscopy was also utilized to observe particle movement in cells. Raman spectroscopy provides *in situ* cell analysis without labelling of the species of interest. By obtaining Raman fingerprint peaks of MNPs or PEI, the location of MNPs and PEI in cells can be identified by analyzing the cell and MNP peaks in a Raman chemical map. Two laser wavelengths and two PEI-coated MNP types were used to study the identification of MNP and PEI in HeLa cells.

Furthermore, two MNP types were used in this study. tdMNP PEI were the particles synthesized by thermal decomposition and used for transfection (Chapter 3 and Chapter 4). Due to the large Néel component in the suspension, a different magnetite MNP suspension was

prepared which had a stronger Brownian signal due to a larger proportion of blocked particles. This suspension, referred to subsequently as MN4, was functionalized with citric acid and coated with PEI, which was also used for AC susceptometry and Raman spectroscopy.

Objectives

1. **Changes in Brownian relaxation behaviour of MNPs before and after internalization in cells.** To determine changes in the mobility of blocked MNP-PEI before, during and after internalization in cells using AC susceptometry by observing the Brownian relaxation peak.

2. **Changes in the Brownian relaxation behaviour of MNPs in cells during the transfection procedure.** To determine the attachment and endosomal escape of MNP PEI in cells during transfection by observing changes in the ACS Brownian relaxation measurements of blocked particles at different time points during transfection.

3. **To observe the movement of MNP transfection complexes in cells during the transfection procedure.** To determine localization of the MNP-complexes in cells during transfection and the interaction between MNP, PEI, and DNA using fluorescent tags and confocal microscopy.

4. **To observe localization of MNPs in cells using Raman spectroscopy.** To determine the individual Raman spectra of MNPs and PEI as well as HeLa cells and finally to observe the localization of MNPs in cells using Raman spectroscopy.

5.2 Materials and Methods

5.2.1 Preparation of tdMNP-complexes

tdMNP, tdMNP PEI, and tdMNP PEI DNA were prepared for adding into the cell monolayer. 50 μL of 0.03 $\mu gFe/\mu L$ tdMNPs were pipetted into three glass vials. For the tdMNP-PEI vials, 500 μg of PEI (1 mg/mL) was added and for the tdMNP-PEI-DNA vials, 500 μg PEI and 125 μg DNA (1 mg/ml) were added. All the samples were made up to a final volume of 675 μL with distilled water. Final concentration of tdMNPs were 0.02 $\mu gFe/\mu l$, PEI was 0.74 $\mu g/\mu l$, and DNA was 0.19 $\mu g/\mu l$. The vials were sonicated in the waterbath for 1 hour. After sonication, the tdMNP transfection complexes suspended in water were measured on the AC susceptometer.

5.2.2 Treatment of HeLa cells with tdMNP-complexes and ACS measurements

HeLa cells were grown in a T75 flask to a confluency of 70 - 80% after 24 hours. The media was removed and 10 mL fresh CM was added into the flasks. 400 μL of 0.03 $\mu gFe/\mu L$ of tdMNP suspensions were added into their respective flasks. The flasks were oscillated on the magnefect nano using a 24 well magnet array for 30 minutes at 2 Hz and 2 mm displacement and tdMNP supplemented media was replaced with fresh CM in the flasks.

For ACS measurements, HeLa cells were treated with 5 mL trypsin until complete cell detachment. The trypsin was neutralized with 5 mL CM and centrifuged at 900 rpm for 5 minutes to pellet the cells. The supernatant was aspirated and cells were resuspended in 200 μL of CM and pipetted into ACS glass vials. The cells were left for 15 minutes to precipitate to the bottom of the vials and measured on the AC susceptometer.

Normalization of ACS data was performed by dividing the χ' and χ" values with the largest value from the χ' data, so that the highest value is scaled to 1.

5.2.3 Lysis and sonication of tdMNP treated HeLa cells

Cell lysis was performed to disrupt the membrane bilayer and separate the tdMNPs from the cell cytoplasm. After ACS measurements, cells samples were lysed by freeze-thaw treatment. Samples in ACS glass vials were pipetted into microcentrifuge tubes. The tubes were placed in the $-20\,^{\circ}\mathrm{C}$ freezer for 30 minutes to freeze and transferred to a $37\,^{\circ}\mathrm{C}$ incubator to thaw. The process was repeated 3 times to lyse cells. The particles were then sonicated in the waterbath for 1 hour to disperse particles and lyse any remaining intact cells. The suspension was transferred to ACS vials and measured on the AC susceptometer.

5.2.4 Preparation of Raman samples on a silicon wafer

2 μL of an MNP in a suspension was dropped onto a silicon wafer and allowed to dry. More MNP was added until 3–4 layers of dried sample was obtained. The same procedure was employed for MNP-PEI. To obtain the SERS effect (discussed in Chapter 1), 10 μL of gold NP (Sigma-Aldrich, 100 nm in citrate buffer) was dropped onto the dry MNP sample and left to dry at room temperature. For the PEI sample, a small amount of the PEI stock (Sigma Aldrich, 25 kDa branched) was dropped onto the silicon wafer using a pipette tip. Due to the high viscosity of the sample, the volume cannot be specified. The samples were measured using Raman spectroscopy.

5.2.5 Preparation of cell samples on a CaF_2 coverslip

Calcium fluoride coverslips provide lower fluorescence emission and therefore reduces the Raman background noise. The CaF_2 coverslips were washed with 1% SDS for 10 minutes, sterilized using 70% ethanol and rinsed with PBS.

The slide was placed in a 12-well plate for cell seeding. For cells with MNP-PEI uptake, the HeLa cells were seeded at a density of 10 000 cells/cm^2 and after 24 hours, MNP or MNP-PEI was added at 5 μL in 500 μL CM. The plate was placed on a static magnet for 1 hour after which media was changed. After 24 hours, the CaF_2 coverslip was washed with PBS and cells were fixed with 4% paraformaldehyde, washed with PBS and finally rinsed with water to prevent salt deposition. The coverslip was measured on the Raman spectrometer.

Cells without MNP or MNP-PEI uptake were deposited onto the CaF_2 coverslip using a cytospin. Briefly, HeLa cells in T75 flasks were trypsinized and resuspended in CM. 200 μL of cells (5 000 cells/μL) was pipetted into the cytospin and spun onto the coverslip at 700 rpm for 1 minute. The cells deposited onto the coverslip were fixed with 4% paraformaldehyde, washed with PBS, and rinsed with water. The coverslips with cells could be stored at $4\,^{\circ}\mathrm{C}$ for a week.

5.2.6 Raman spectroscopy sampling

The instrument used was a Thermo Fisher DXR Raman Microscope. When the lasers were changed, laser calibration and alignment was performed according to the OMNICS software instructions. All samples used a 50 μm slit aperture and 50x objective lens unless stated otherwise. For acquisition of MNP and MNP-PEI samples, the laser power had to be at a minimum to prevent sample burning. Therefore, particle sampling was at a laser power of 1.0 mW for 5 seconds and 5 exposures per point. PEI sampling was performed using the same setup but with a 4 mW laser power. For HeLa cell sampling, an area was chosen with 1x1 or 2x1 μm points that did not exceed 24 hours of sampling time. Each point was sampled for more than 5 minutes to obtain enough spectral information from each point, where the exposure time was 30 minutes and the number of exposures was 15. Since cells were able to maintain membrane integrity at high laser power, it was set to 10 mW.

The data obtained was analysed using the OMNICS software provided by Thermo Fisher for baseline correction, smoothing, peak identification, and multivariate curve analysis (MCA) of area map scan. The MCA or multivariate curve resolution uses matrix decomposition to extract components that represent the chamistry of the spectral map. The analysis identifies chemical

components within the map as well as the concentration of the chemical (Noothalapati et al., 2017).

5.3 Results

5.3.1 AC Susceptometry to monitor the mobility of MNP-complexes during the transfection process

This study was performed to determine particle mobility in cells using ACS measurements. tdMNP and MN4 particles dispersed in water were measured to determine their Brownian relaxation component. Cells were then treated with the particles and ACS was performed to determine changes in the Brownian component of internalized particles, to determine particle mobility after cellular interaction.

5.3.1.1 Measuring uptake and mobility of three MNP-complex assemblies in cells

The three tdMNP-complex assemblies measured in this study were tdMNP only, tdMNP-PEI, and tdMNP-PEI-DNA. As discussed in Chapter 4, different surface charges of particles and sizes affect their interaction with cells. Furthermore this section looks at the mechanism of nanomagentic transfection. Therefore negatively charged tdMNP only, PEI-coated tdMNP and the complete transfection complex tdMNP-PEI carrying DNA was monitored to determine differences between the assemblies during and after cell internalization.

Adherent HeLa cells were treated with high concentrations of 3 tdMNP-complexes – tdMNP, tdMNP-PEI, and tdMNP-PEI-DNA. Cells were imaged for GFP expression after 48 hours of MNP treatment (Fig. 5.3 A). Cells treated with tdMNP were confluent and maintained a healthy population with normal spreading and radial attachment (Fig. 5.3 Ai). Cells treated with tdMNP-PEI and tdMNP-PEI-DNA (Fig. 5.3 Aii & iii) showed low cell density with some cells showing healthy attachment based on their elongated morphology, while other cells appeared to have a rounded morphology and low attachment to the substrate exhibiting unhealthy/dying cells. The dark contrast and granularity indicate internalization of MNP-complexes in cells and MNP deposition on the plastic substrate. Cells treated with tdMNP-PEI-DNA transfection complex also showed a small population of cells expressing GFP (Fig. 5.3 A iii), indicating that some of the MNP-complexes were still functional at high dosage. Cells treated with tdMNP-PEI and tdMNP-PEI-DNA showed low confluency due to high internalization into cells because of their positive charge which conferred high toxicity to cells (Fig. 5.3 A ii&iii).

Cells were then detached from flasks and pipetted into vials for ACS measurements. Figure 5.3 B show ACS vials of HeLa cell samples with tdMNPs (left), tdMNP-PEI (middle), and tdMNP-PEI-DNA (right). Efficiency of particle internalization can be deduced from the staining intensity of particles. Cells treated with tdMNP showed little colouring with a translucent cell pellet, whereas cells with tdMNP-PEI and tdMNP-PEI-DNA showed a darker colour of cells indicating higher internalization of particles compared to MNP without PEI coating. The PEI coating improved internalization of tdMNPs into cells as the positive surface charge interacts with the negatively charged lipid bilayer (discussed in Chapter 4), hence improving internalization compared to the negative surface charge of tdMNPs (Gratton et al., 2008a).

After imaging and cell detachment, cells internalized with tdMNP-complexes were measured on the AC susceptometer to monitor changes in magnetic susceptibility of particles before and after cell uptake. Changes in ACS measurements of tdMNP-complexes suspended in water (Figure 5.4 A) were compared tdMNP-complexes internalized in cells (Figure 5.4 B).

tdMNPs only in Figure 5.4 A i showed a χ" Brownian peak at 34 kHz, corresponding to a hydrodynamic diameter of approximately 26 nm. After PEI surface coating, the particles increased in size to 36 nm (Figure 5.4 Aii), and the addition of DNA to form tdMNP-PEI-DNA increased the hydrodynamic diameter to 38 nm. The broadening of the χ" peak also indicates

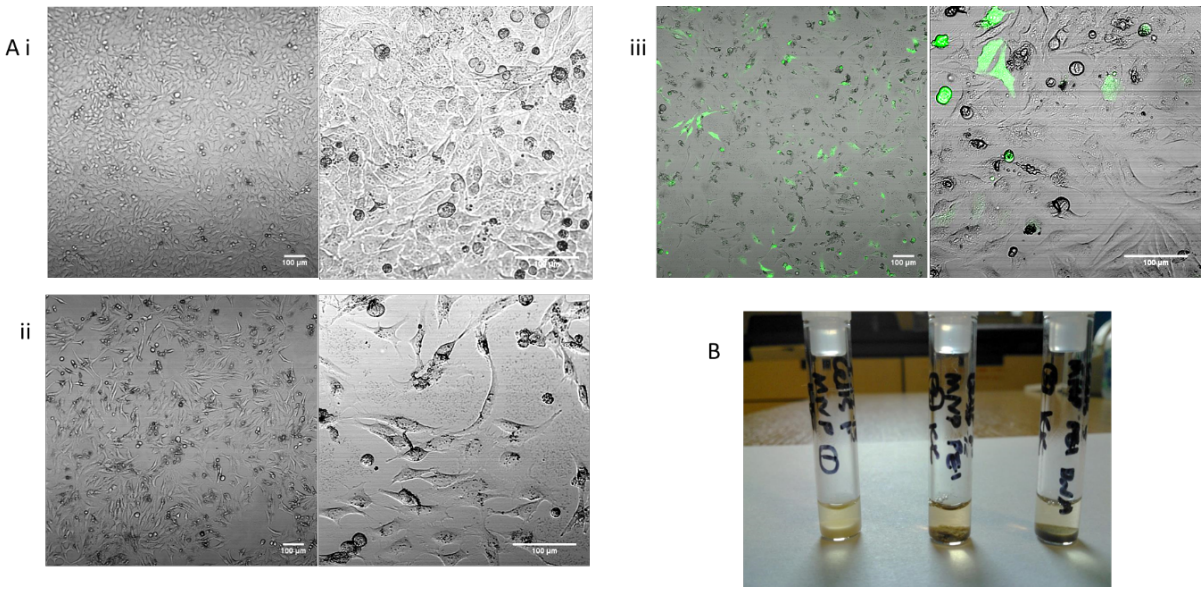

Figure 5.3 (A) Brightfield and fluorescent overlay images of particle uptake in HeLa cells after 48 hours with (i) tdMNP only, (ii) tdMNP-PEI, and (iii) tdMNP-PEI-DNA. (B) Detached HeLa cell pellets in ACS vials used in ACS measurements with cells-tdMNP (left), cells-tdMNP-PEI (middle) and cells-tdMNP-PEI-DNA (right).

incresed polydispersivity. It was not feasible to perform simulations on all ACS measurements, however trends can be inferred from the simulations performed in Chapter 3.

Once the particles were internalized in cells, there was a drastic change to their magnetic susceptibility. Figure 5.4 B indicates that all three particle types had lost their Brownian relaxation component based on the loss of the peak position in the χ" signal. Besides that, both the χ components for tdMNP were very weak (Figure 5.4 B i), which signified low uptake of tdMNP in cells. This result was consistent with the low staining intensity of HeLa cells in ACS vials observed in Figure 5.3 A. Since a small population of tdMNP particles show Néel relaxation behaviour, a χ' signal should be observed even in an immobilized state if particles are present in the sample. Therefore, tdMNP was not able to be internalized efficiently in cells.

tdMNP-PEI and tdMNP-PEI-DNA complexes in cells (Figure 5.4 B ii&iii) showed a higher χ' susceptibility signal compared to tdMNP in cells indicating better uptake efficiency in cells. tdMNP-PEI-DNA showed the highest χ' susceptibility signal ($\sim$0.0007) at low frequency which indicate a larger particle mass in the sample compared to the other groups due to either higher cell numbers in the group having taken up MNPs or from increased MNP-PEI-DNA uptake per cell. Increased MNP uptake is likely as the larger size of the tdMNP-PEI-DNA complexes improves sedimentation onto cells and therefore increases the rate of internalization, which was consistent with previous work (Rodriguez-Lorenzo et al., 2015).

The normalized values of χ' and χ" ACS measurements of each particle group in cells were plotted on the same graph to obtain a comparison between the sample measurements (Figure 5.4 C) (Normalization described in Methods). All three samples show the same gradient of signal loss for the χ' plots (Figure 5.4 Ci). tdMNP (black plot) shows a jagged curve indicating high background noise during sample measurement which is due to low MNP sample amount. The χ" ACS plot does not indicate a clear presence of a Brownian peak for any of the complex assemblies (Figure 5.4 Cii). Therefore, all three MNP groups are concluded to be immobilized in cells after 48 hours of internalization.

Confocal fluorescence images were obtained to understand the morphology of the transfection components (tdMNP-PEI, DNA only and tdMNP-PEI-DNA) in cells. tdMNP-PEI was tagged with green fluorescent dye, DNA with a Cy3 dye (Mirius) and the cell nucleus was stained with Hoescht 33342. HeLa cells were treated with either tdMNP-PEI (green) (Figure 5.5 A), DNA

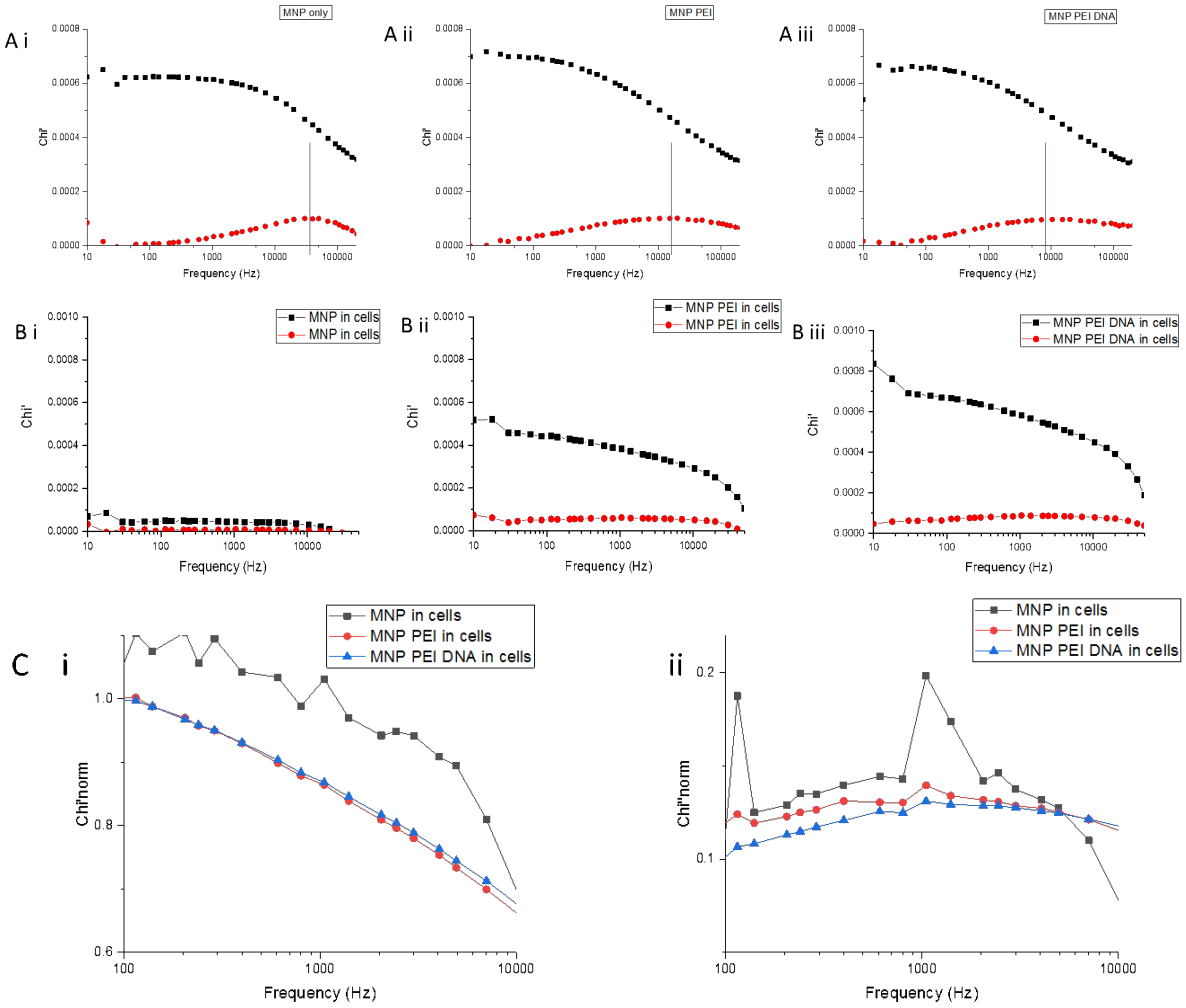

Figure 5.4 ACS measurements of (A) particles of different complexes in water (i) tdMNP only, (ii) tdMNP-PEI, and (iii) tdMNP-PEI-DNA. (B) Particles internalized in cells (i) tdMNP only, (ii) tdMNP-PEI, and (iii) tdMNP-PEI-DNA. (C) Normalized values of the three particle types in cells with (i) χ' normalization (ii) χ" normalization (described in Methods).

only (red) (Figure 5.5 B), or tdMNP-PEI-DNA complex (green and red) (Figure 5.5 C). Cells were visualized under the microscope 24 hours after treatment.

In Figure 5.5 A, tdMNP-PEI particles were successfully taken up by cells and can be seen distributed throughout the cell cytoplasm. Cells treated with DNA only (Figure 5.5 B) are observed to show no red fluorescence around the nucleus of cells (blue), indicating the absence of DNA in cells. The absence of DNA could primarily be due the presence of nucleases in cell culture media and in the cells which degrade naked nucleic acids. The negative surface charge of DNA also reduces the uptake efficiency into cells, as well as the low concentration of DNA in the well reduces the probability of DNA-cell membrane interaction. Delivery of DNA into cells ultimately requires a transport vector to protect naked DNA from degradation and facilitate its transport to the nucleus.

In Figure 5.5 C, the characteristics of the tdMNP-PEI-DNA transfection agent could be observed when internalized in cells. Without DNA, the tdMN-PEI particles were uniformly distributed within the cytoplasm and showed small granule size (Fig. 5.5 A). When complexed with DNA, however, the presence of large clusters was observed where tdMNP-PEI particles combined with DNA to form large particle clusters of varying size. The combination of the tdMNP-PEI labelled in green and the DNA labelled in red formed yellow clusters, confirming that the particles and DNA were indeed complexing and interacting. This observation was in accordance with ACS measurements, where tdMNP-PEI-DNA transfection complex was larger

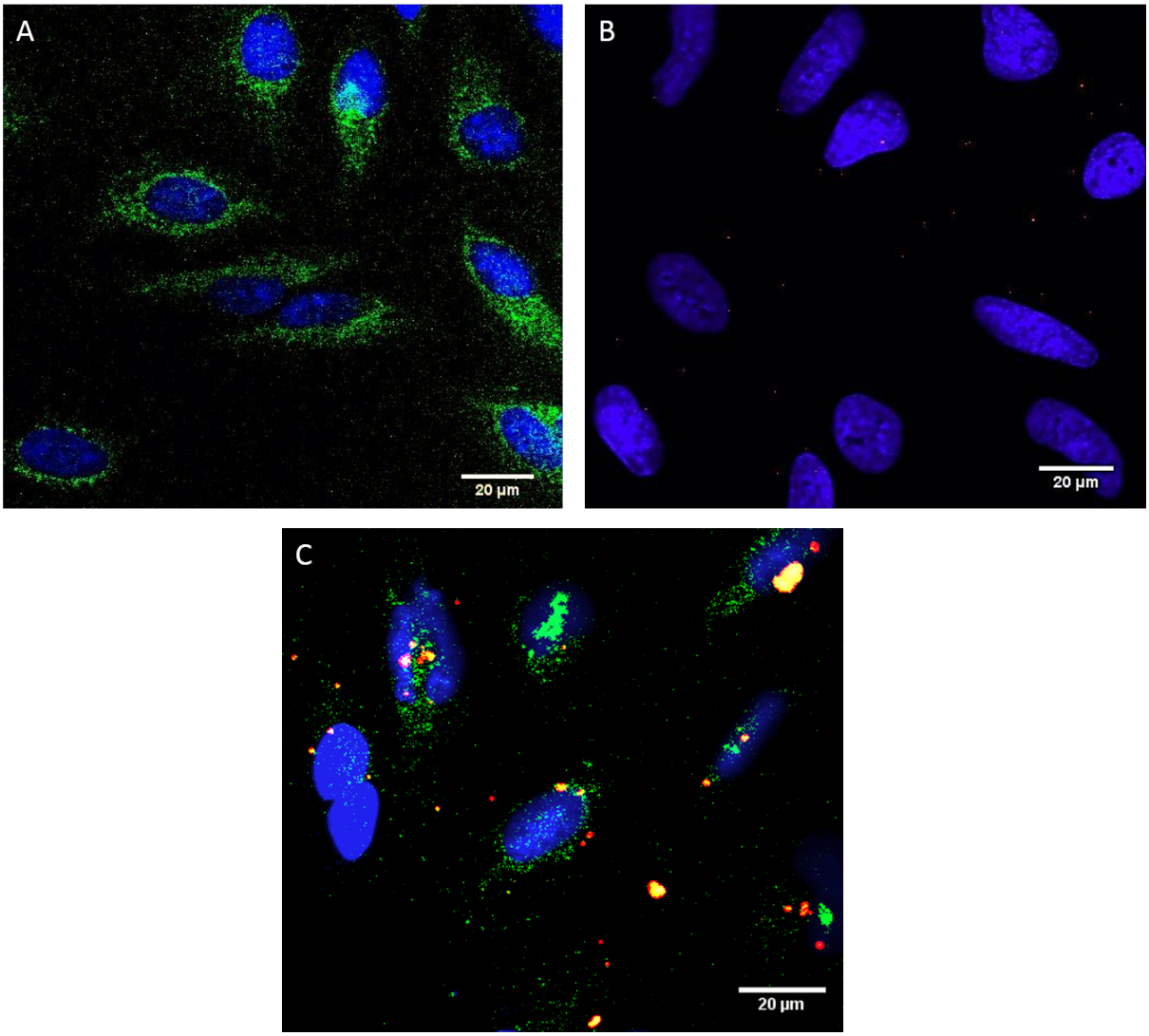

Figure 5.5 Fluorescence images of (A) HeLa cells treated with tdMNP-PEI only (Fluorescein sodium salt), (B) cells with DNA only (Cy3), and (C) cells with tdMNP-PEI-DNA complex, nucleus stained with Hoescht 33342.

compared MNP-PEI samples without DNA (Figure 5.4 A) and had high polydispersivity based on the broad χ" peak.

5.3.1.2 Effect of cell lysis and sonication of cells containing tdMNP-complexes

AC susceptometry was used to monitor changes in MNP susceptibility before, during, and after interaction with HeLa cells. Three MNP-complexes – tdMNP, tdMNP-PEI, and tdMNP-PEI-DNA were measured on the AC susceptometer before cell uptake (suspended in distilled water), after internalization in cells, and after lysis of cells and sonication to disperse particles in the cell suspension (Fig. 5.6). The effect of cell lysis and sonication to disperse particles was to monitor a re-emergence of a Brownian peak (particle stablilty and mobility) once released from the cytoplasm.

Figure 5.6 A are ACS measurements of tdMNP samples. Similar to previous measurements, tdMNP samples were a stable colloid in water with a hydrodynamic diameter of 26 nm (Figure 5.6 A i). After internalization into cells, the magnetic signal (χ') drops due to low MNP uptake (Figure 5.6 A ii). Once the particles are released from the cells by lysis and sonication, the magnetic susceptibility signal decreased even further from loss of particles from handling during the freeze-thaw and sonication treatments. Normalization of the ACS measurements in Figure 5.6 A iv show that tdMNPs in water were mobile, where the presence of a Brownian relaxation peak was observed with the gradual increase of the χ" signal with higher frequency. The loss of the peak indicates that tdMNP after cell uptake caused particle immobilization. Lysis of cells to free the MNPs and sonication did not restore the Brownian movement of tdMNP particles. However, at such low susceptibility signal, the ACS measurements of tdMNP samples are difficult the be deciphered and therefore is unreliable. This result differs from that reported by Soukup et al. (2015), whereby negatively-charged MNPs coated with a protein corona show re-emergence of a Brownian component when the particles were released from cells by lysis.

ACS measurements of tdMNP PEI group in cells show a higher magnetic susceptibility signal compared to the tdMNP treatment group in cells (Figure 5.6 B ii&iii). Normalization of the ACS measurements in Figure 5.6 B iv does not show a clear indication of a Brownian signal for tdMNP-PEI samples after internalization in cells and lysis of cells to free the trapped particles. A similar result was observed for cells treated with tdMNP-PEI-DNA (Figure 5.6 C) where interaction with cells cause a loss in the Brownian relaxation signal in ACS measurements, signifying MNP immobilization. The loss of the ACS Brownian relaxation peak for all samples indicate immobilization in cells. Lysis of the cells and sonication of the samples to resuspend particles did not result in the re-emergence of a Brownian peak. This could be due to the loss of PEI coating and stickiness of the cell debris causing MNP clustering and loss of coating stability.

Before ACS measurements (Figure 5.6), cells treated with MNP-complexes were imaged using brightfield and fluorescence microscopy (Figure 5.7). Control cells and cells treated with tdMNP showed high cell density and healthy cell morphology. Cells with tdMNP-PEI and tdMNP-PEI-DNA had lower cell density than the control group and a rounded cell morphology with lower cell-cell contact. The transfection complex tdMNP-PEI-DNA retained some transfection activity (not quantified). In terms of particle uptake, cells with dark granular structures seen in tdMNP-PEI and tdMNP-PEI-DNA treatment indicated higher particle uptake compared to tdMNP only. This result was similar to Figure 5.3 A.

HeLa cells treated with tdMNP, tdMNP-PEI, and tdMNP-PEI-DNA respectively were detached from cell culture plates and seeded onto glass coverslips for microscopy studies of cytotoxicity and morphology. Cells seeded on glass coverslips were treated with a Live/Dead cell viability assay (Figure 5.8).

Control cells and cells treated with tdMNP showed high cell viability (green) with and low cell death (red). The detachment and reseeding of cells onto glass coverslips did not affect cell

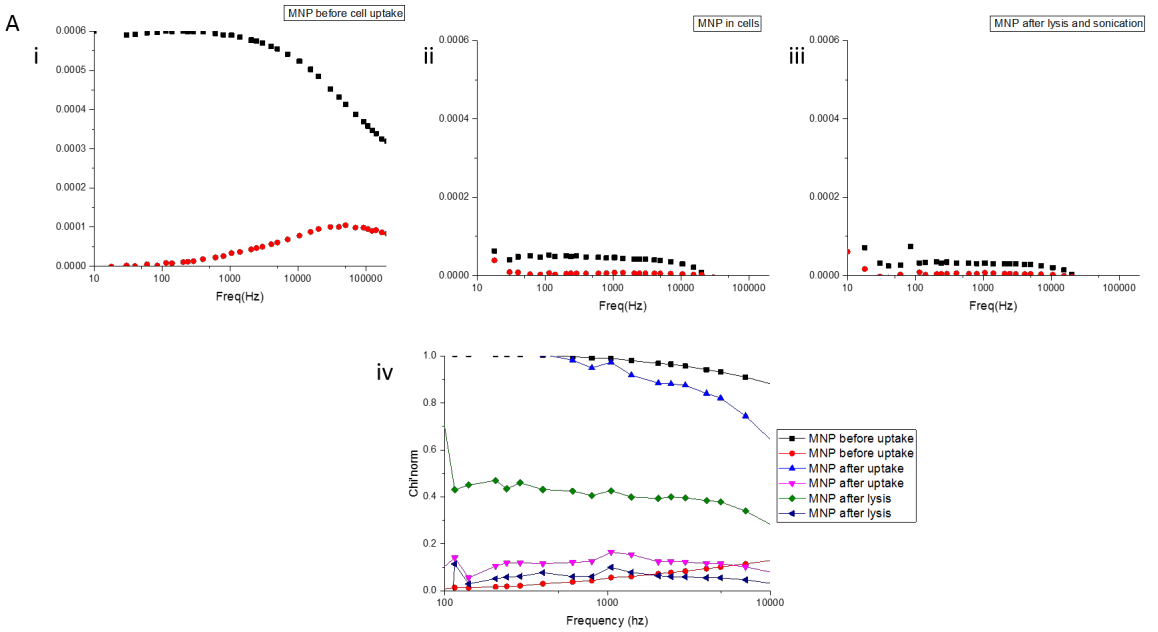
A
i
MNP before cell uptake
Freq(Hz)
ii
MNP in cells
Freq(Hz)
iii
MNP after lysis and sonication
Freq(Hz)
iv
Chi'norm
Frequency (hz)
MNP before uptake
MNP before uptake
MNP after uptake
MNP after uptake
MNP after lysis
MNP after lysis

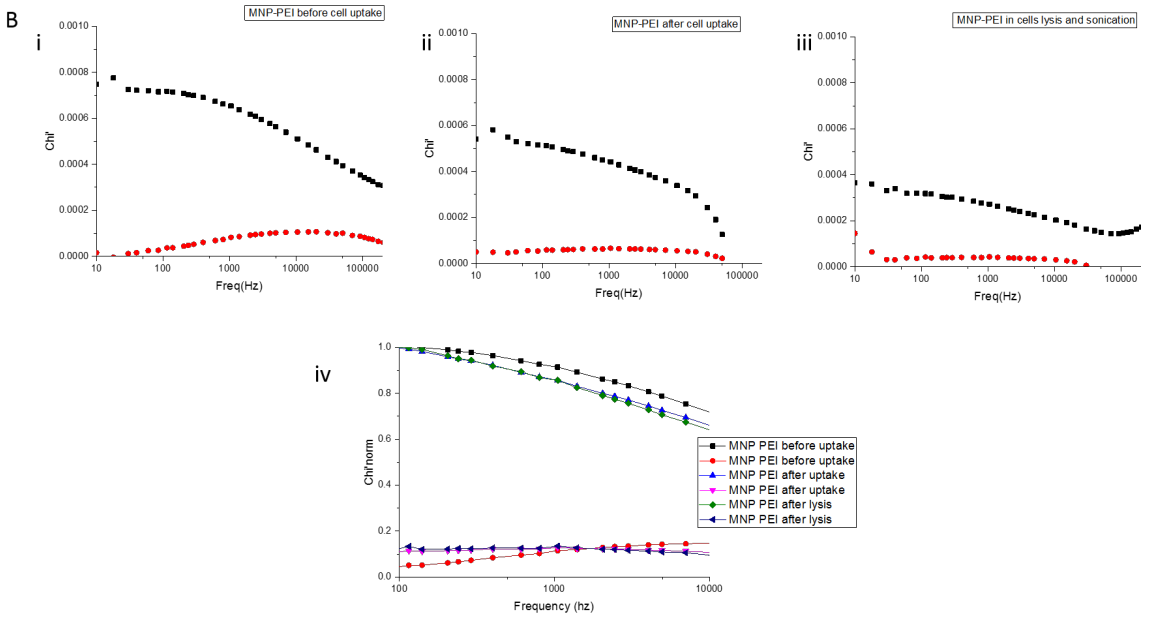
B
i
MNP-PEI before cell uptake
Chi'
Freq(Hz)
ii
MNP-PEI after cell uptake
Chi'
Freq(Hz)
iii
MNP-PEI in cells lysis and sonication
Chi'
Freq(Hz)
iv
Chi'norm
Frequency (hz)
MNP PEI before uptake
MNP PEI before uptake
MNP PEI after uptake
MNP PEI after uptake
MNP PEI after lysis
MNP PEI after lysis

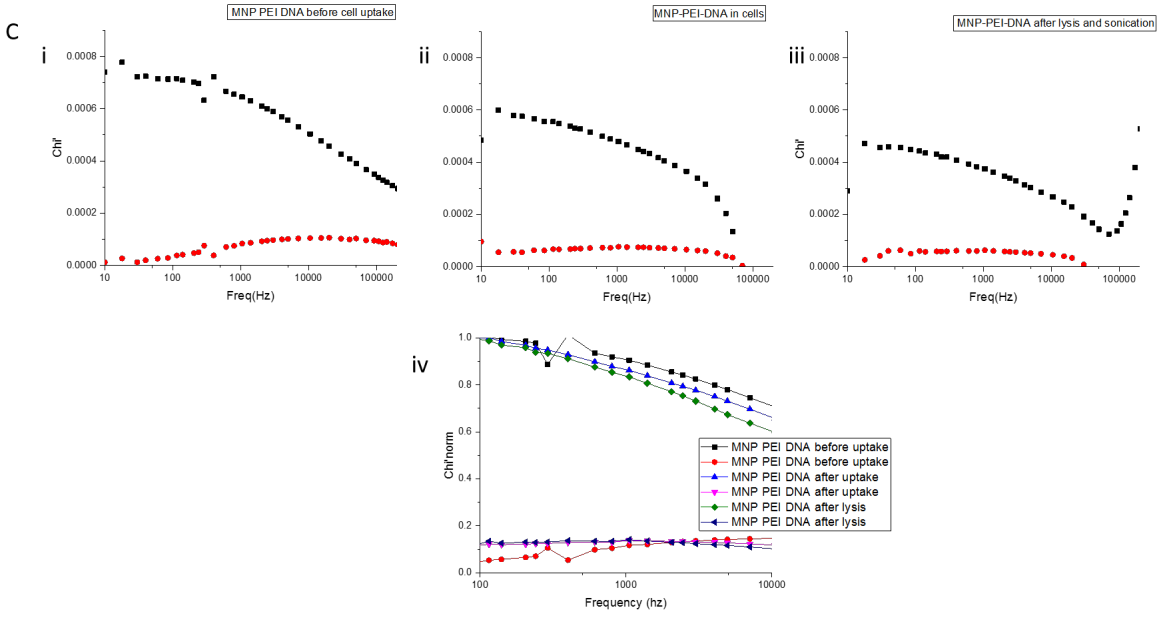
C
i
MNP PEI DNA before cell uptake
Chi'
Freq(Hz)
ii
MNP-PEI-DNA in cells
Freq(Hz)
iii
MNP-PEI-DNA after lysis and sonication
Chi'
Freq(Hz)
iv
Chi'norm
Frequency (hz)
MNP PEI DNA before uptake
MNP PEI DNA before uptake
MNP PEI DNA after uptake
MNP PEI DNA after uptake
MNP PEI DNA after lysis
MNP PEI DNA after lysis

Figure 5.6 ACS measurements of internalized particle complexes in HeLa cells for (A) tdMNP only, (B) tdMNP-PEI and (C) tdMNP-PEI-DNA. Cells with particles were subjected to lysis reagents and sonication to free particles from the cytoplasm and disperse them. ACS measurements show (i) particles in water before cell uptake, (ii) after cell uptake, and (iii) after lysis and sonication. (iv) The ACS measurements for all 3 treatments were normalized and compared.

health as the cells were observed to show good attachment and cell spreading. Cells treated with tdMNP-PEI and tdMNP-PEI-DNA however, showed low viability after reseeding onto coverslips based on the low green fluorescence intensity. tdMNP-PEI-DNA was found to have the highest cell death followed by tdMNP-PEI. Calcein AM (non-fluorescent) permeates into the cell through the cell membrane and is hydrolysed into the fluorescent green dye by esterases in the cell. Therefore, the low fluorescence intensity is an indicator that the cells were unhealthy and lacked the capacity to carry out the intracellular chemical conversion. After detachment from flasks, cells still retained the particles in their cytoplasm, observed in the brightfield images (left). The high uptake of MNP in these two treatment groups (tdMNP-PEI and tdMNP-PEI-DNA) could be the cause for damaged cells and inability to regain attachment and spreading functions.

F-actin (Phalloidin 568) and nucleus (Hoescht 33342) of cells were stained to observe their internal morphology (Figure 5.9). Fluorescent images of reseeded cells show that cells treated with tdMNP only had higher cell number per area and high cell-cell contact compared to tdMNP-PEI and tdMNP-PEI-DNA. Unlike cells treated with tdMNP, both the PEI-coated MNP treated cells show fine actin filaments radiating laterally from the cell membrane onto the substrate, which was also observed in previous studies (Smith et al., 2010). These protrusions are known as filopodia or microspikes which are plasma membrane protrusions formed by thin actin filaments and function as a probe to the external environment, as cell-cell adhesions and for cell migration (Litman et al., 2000; Mattila and Lappalainen, 2008). Cells also showed the presence of actin stress fibres, where dorsal, ventral and transverse arcs (Pellegrin and Mellor, 2007) are clearly observable in the tdMNP-PEI treated cells in Fig. 5.9. Brightfield images show no observable MNP in cells in the tdMNP group, however both PEI-coated MNP groups (tdMNP-PEI and tdMNP-PEI-DNA) show dark contrast and high granularity due to internalized MNP in the cell cytoplasm. This finding is similar to that observed in Figure 5.3.

5.3.1.3 Time point ACS measurements of tdMNP-PEI internalized in cells

To track the spatio-temporal behaviour of MNPs over time and endosomal escape using ACS, 4 time points were chosen between the beginning of the transfection procedure to the time of GFP expression (0.5h, 2h, 17h, and 48h). HeLa cells treated with tdMNP-PEI were detached from the flasks during the time points and measured on the ACS. The changes in χ' and χ" during the process of nanomagnetic transfection were compared.

The transfection process begins from the end of the magnefect-nano oscillating treatment to 48 hours where GFP expression is at its peak, which was determined in Chapter 4. In this study, only tdMNP-PEI was used to study endosomal escape after endocytosis. Figure 5.10 shows the ACS measurements of tdMNP-PEI in suspension (Figure Ai), and 30 minutes (Figure Aii), 2 hours (Figure Aiii), 17 hours (Figure Aiv), and 48 hours (Figure Av) after magnefect-nano treatment. tdMNP-PEI was added into cells and oscillated on the magnefect-nano, and particles that were unattached were washed off. A magnetic signal for all time points were observed at around 0.001 volume susceptibility, except for the time point at 2 hours which had a slightly higher signal. This could be due to replicate variability, either from an increase in particle uptake or more cells collected from the flask into the ACS glass vial. Normalization was performed to determine if there was subtle differences in the χ' and χ" magnetic susceptibility peaks of the different time points.

Figure 5.10 B shows the normalized ACS measurements for all time points and tdMNP-PEI

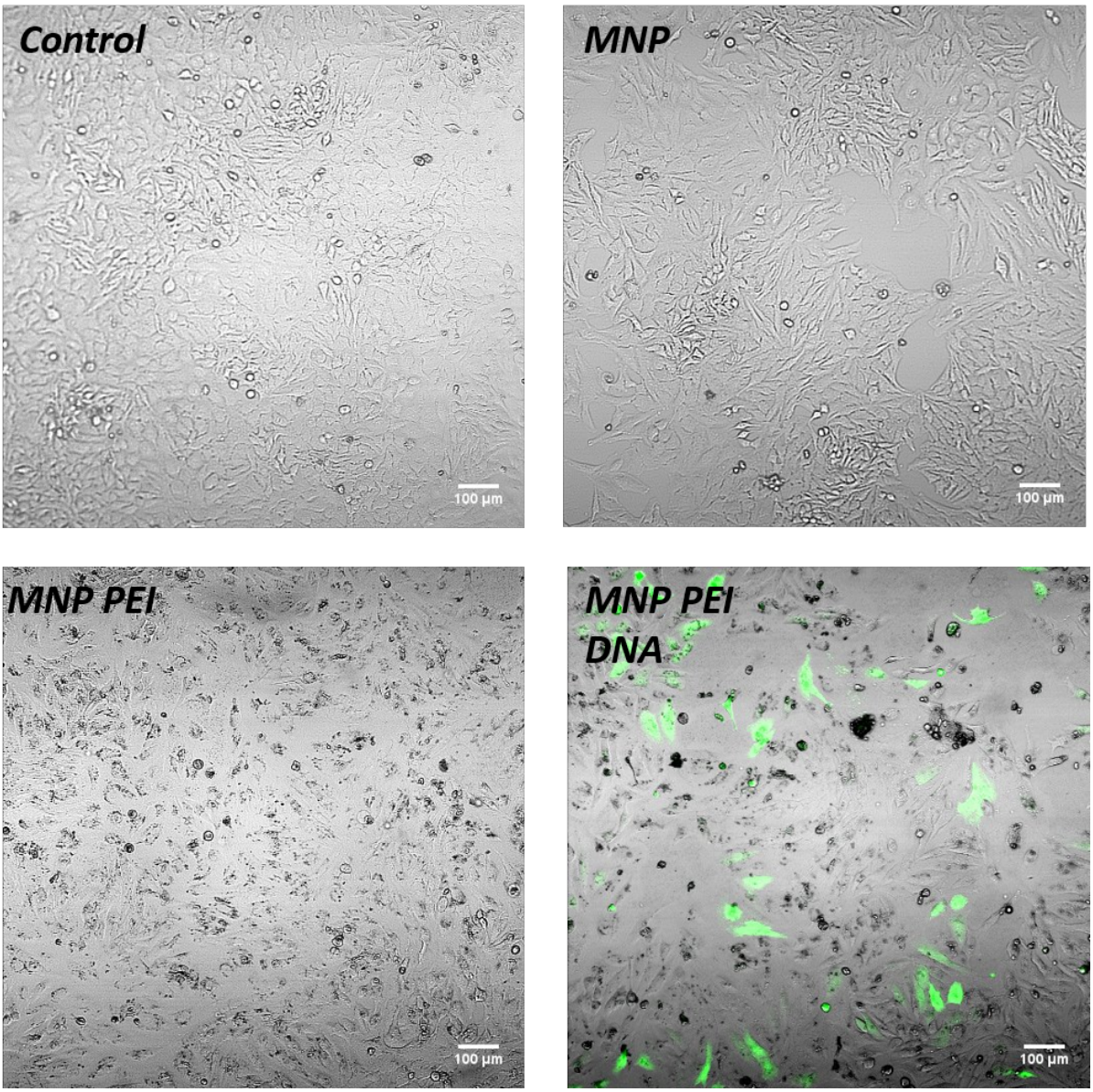

Figure 5.7 Images of HeLa cells with internalized MNP-complexes measured previously on the ACS (Fig. 5.6). Cells were imaged on the brightfield to show internalization and transfection of particle complexes.

in suspension, with both normalized χ' and χ" ACS measurements (Figure Bi), normalized χ" comparison (Figure Bii) and normalized χ' comparison (Figure Biii) for all time points. From the χ" slopes, there is no observable difference between time point groups. The decrease in χ" signal with increasing frequency indicates immobilization of particles after interaction and uptake in cells. Similarly, the normalized χ' signal shows no difference between the time points. The absence of an observable Brownian signal indicates that most of the MNPs are immobilized in cells. Furthermore, since only a portion of the particles exhibit Brownian relaxation behaviour in the suspension, a small loss in mobility causes a significant drop in the signal. Therefore if there are particles that are able to exhibit Brownian relaxation in the cell, the signal is too small to detect.

To visualize the mechanism of nanomagnetic transfection in cells, tdMNP-PEI-DNA was fluorescently-tagged and the spatio-temporal behaviour was observed during the transfection, at 0.5h, 15h, 24h, and 48h after the magnefect nano treatment (Figure 5.11).

The PEI attached to tdMNP was tagged with a fluorescein sodium salt dye, DNA with Cy3 fluorescence and F-actin was stained with Phalloidin 405. 30 minutes after the magnefect-nano treatment (Figure 5.11, 0.5 h) the tdMNP-PEI-DNA was observed as yellow complexes either in the extracellular matrix or attached to the cell membrane. The magnefect-nano treatment helps

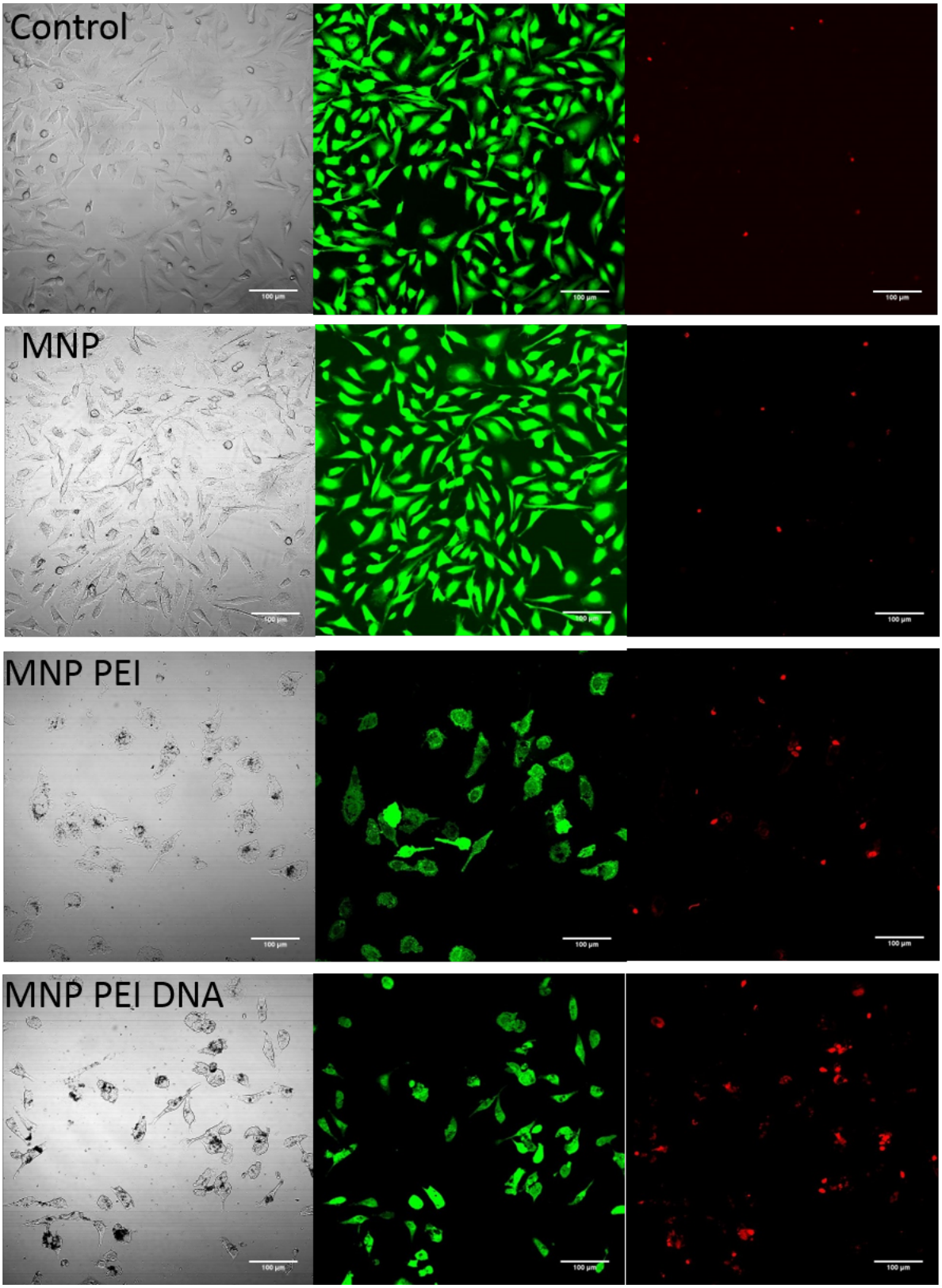

Figure 5.8 HeLa cells with internalized MNP-complexes measured on the ACS 5.6 after reseeding on glass coverslips. Live/dead assay of cells treated with the different particle complexes, and fluorescently imaged for live (green) and dead (red) cells; scale bar 100 μm.

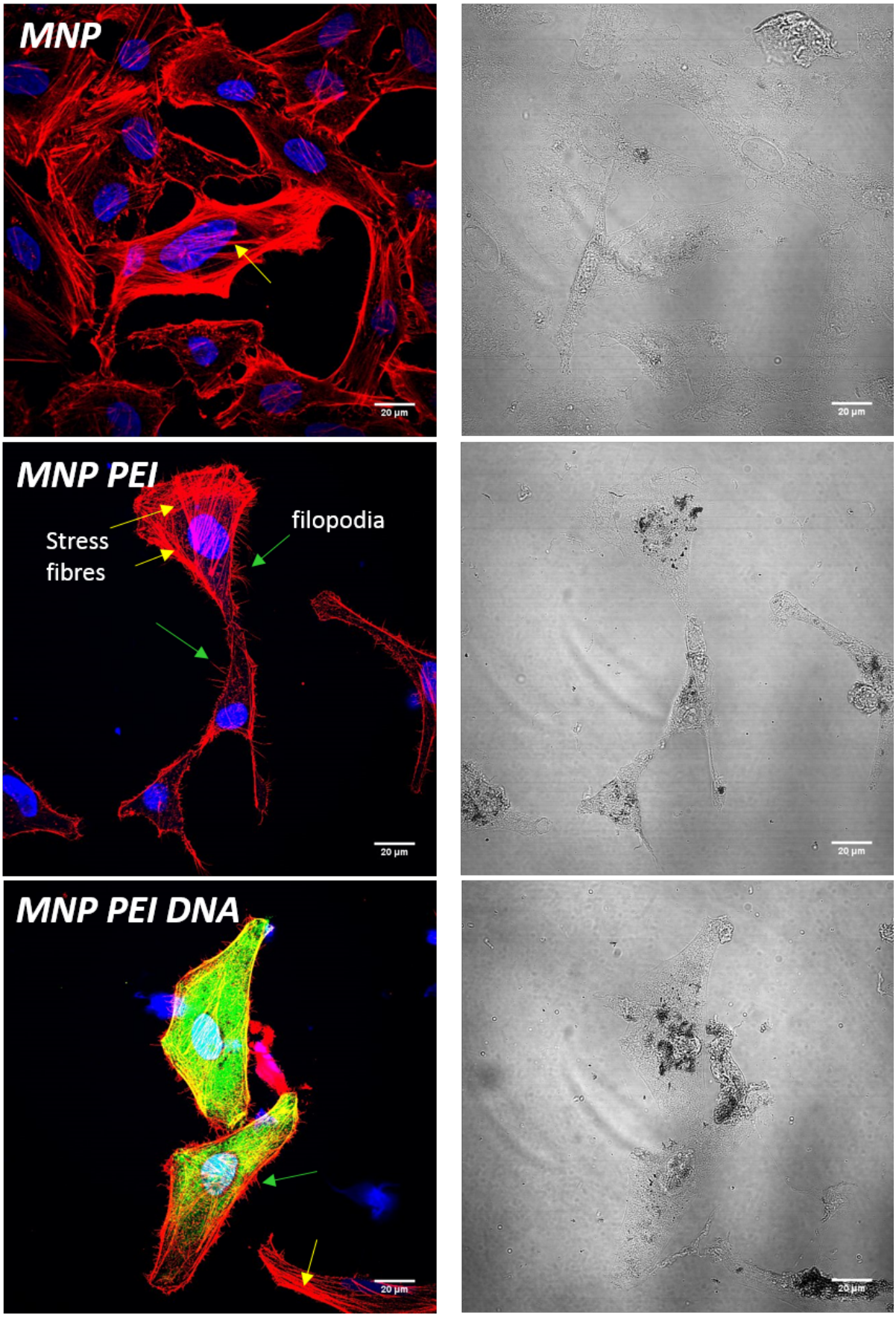

Figure 5.9 Images of HeLa cells with internalized MNP-complexes measured on the ACS 5.6 after reseeding on glass coverslips. Fluorescence and brightfield images of cells showing the actin cytoskeleton (Phalloidin 568 in red), nucleus (Hoescht 33342 in blue) and cells expressing GFP (in green). Stress fibres indicated in yellow arrows and filopodia in green arrows. Scale bar 20 μm.

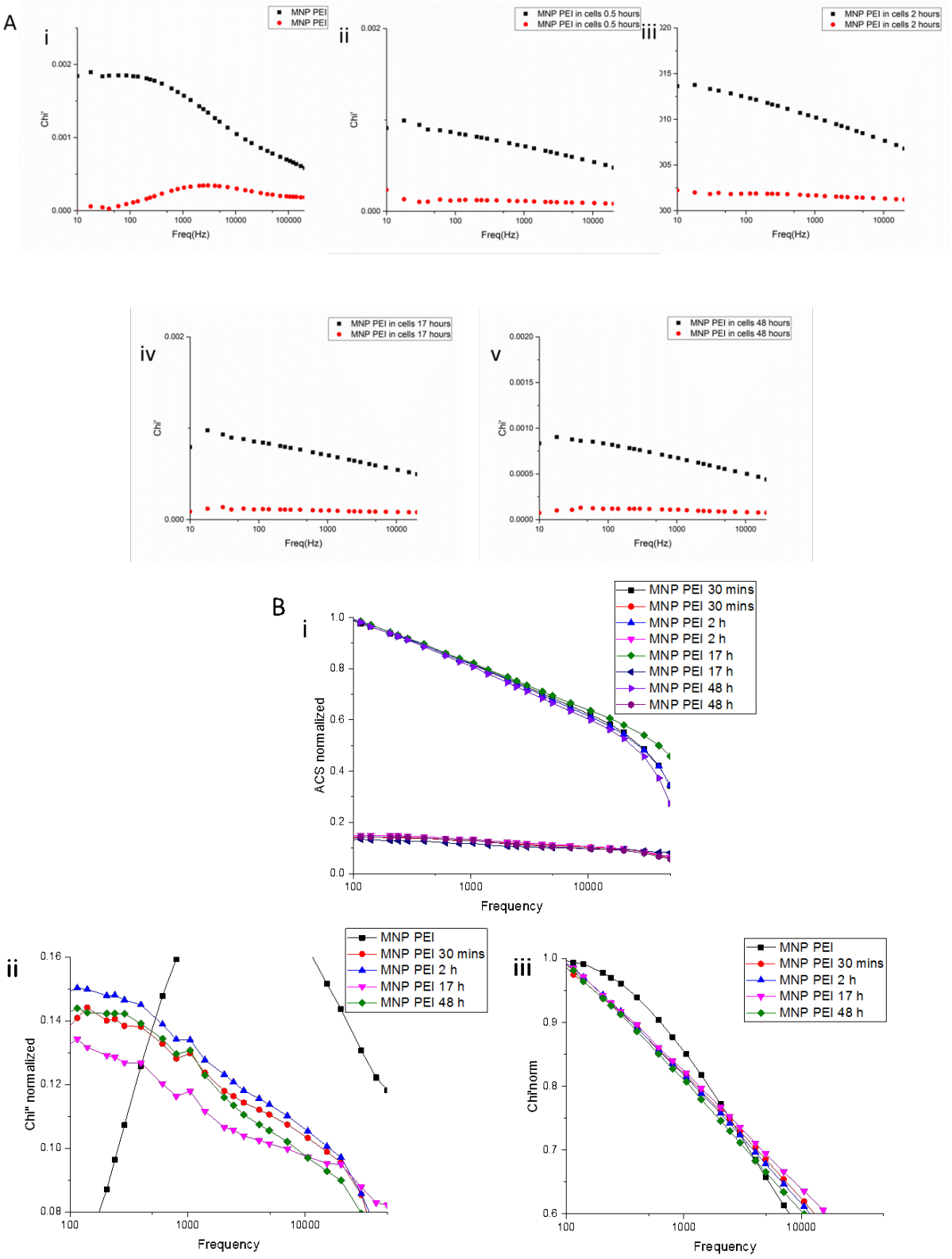

Figure 5.10 (A) ACS measurements of tdMNP-PEI internalized in cells and measured at different time points based on time taken for transfection. Measurements show (i) tdMNP-PEI before cell uptake, (ii) cells at 30 minutes, (iii) cells at 2 hours, (iv) cells at 17 hours, and (v) cells at 48 hours after nanomagentic transfection. (B) normalized graphs of (i) χ'and (ii) χ" of time points.

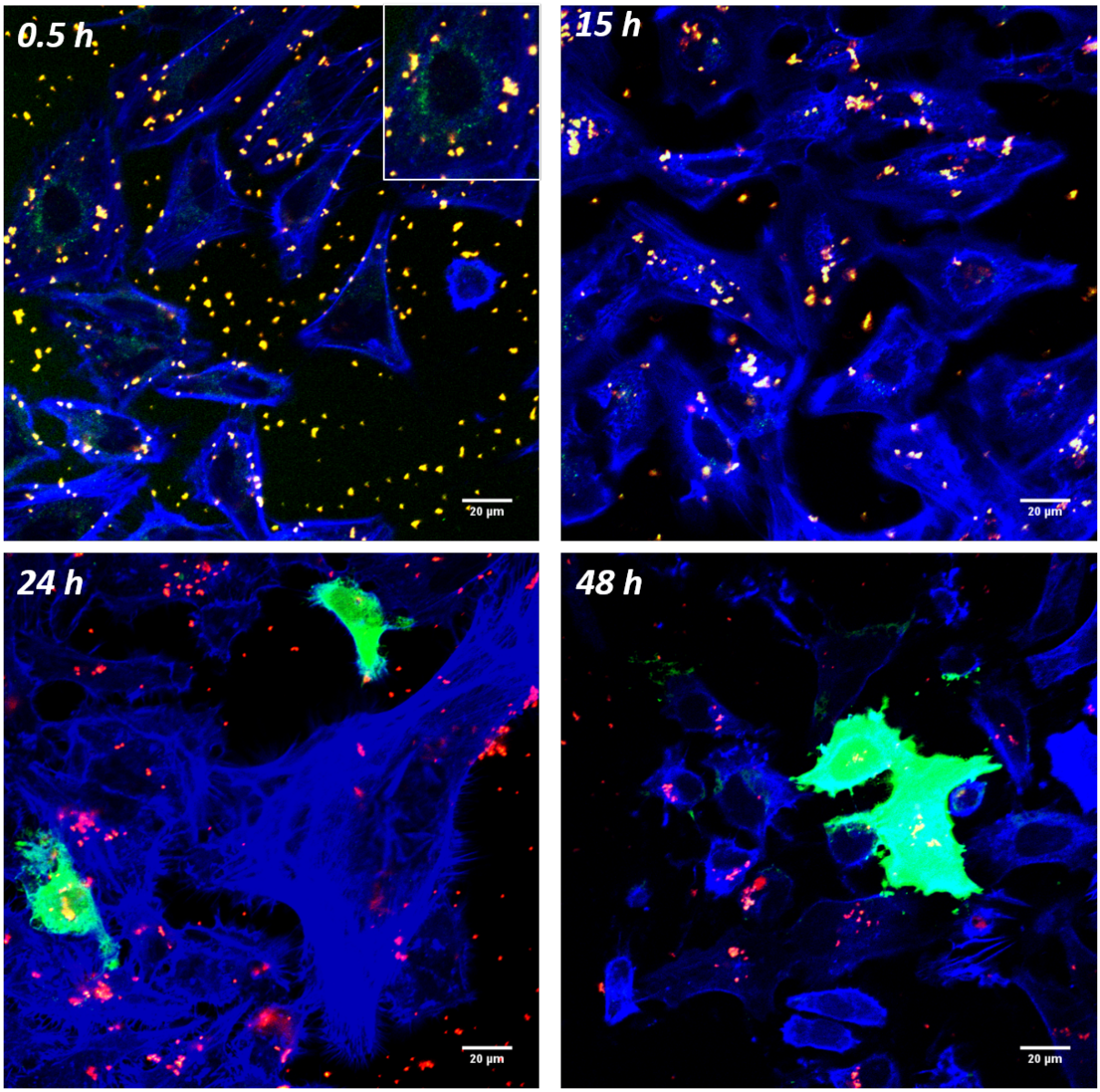

Figure 5.11 Fluorescence images of HeLa cells transfected with tdMNP-PEI-DNA complexes using the nanomagnetic transfection method and imaged at time points of 30 minutes, 15 hours, 24 hours and 48 hours. Images show movement of tdMNP-PEI (green) and DNA (red) complexes towards cells visualized by the actin cytoskeleton (blue). Cells expressing GFP are in green at 24 and 48 hours. Scale bar 20 μm.

increase MNP to cell contact by the sedimentation of magnetic components in the well plates toward the external magnet on the bottom of the plate. Once attachment occurs, the cell can take up the transfection complexes by endocytosis. In the same image, smaller green dots can be seen in the cell cytoplasm (inset). These structures are tdMNP-PEI that did not complex with DNA but still gained entry into the cell.

At 15 hours after magnefect-nano treatment (Fig. 5.11), most of the transfection complexes in the extracellular fluid have disappeared, either from being internalized into the cell or degraded by extracellular nucleases. The tdMNP-PEI-DNA transfection complexes can be seen in the middle of the cell and near the perinuclear region. The complexes migrate towards the cell nucleus and can be seen to form larger clusters. Possibly, complexes that are immobilized in the cytoplasm of the cell are unable to escape from endocytic vesicles and complexes that did escape are able to migrate closer to the nucleus. At the 24 hour time point, transfection has begun to occur and some cells show low intensity GFP expression. At this point the complexes are few and located in the perinuclear region of the cell. The cells seem to show signs of stress, based on bundling and tensioning of the actin cytoskeleton and the formation of filopodia radiating from the cell membrane.

At 48 hours, cells were observed to show higher intensity of GFP expression. The number of complexes are reduced and the green fluorescent dye attached to PEI is absent either due to photobleaching or masked due to the higher intensity of GFP fluorescence. Cells that have been transfected show complexes in the nuclear region of the cell. MNPs have been shown in previous studies to localize within the nucleus (Arsianti et al., 2010; Xu et al., 2008). However the complexes in the nucleus is likely PEI and DNA, whereas the presence of MNPs in the nucleus were not determined in this study. The mechanism of transfection is likely due to the detachment of PEI and DNA complex from MNPs and translocation of the PEI-DNA to the nucleus, whereas MNPs are trapped in lysosomes (Arsianti et al., 2010).

5.3.2 Studying changes in AC susceptibility of MNPs showing strong Brownian relaxation in cells

To properly elucidate the spatio-temporal changes in MNP relaxation behaviour during the transfection process using AC susceptometry, a strong Brownian relaxation component is required. For example, if the particles are superparamagnetic, no change in susceptibility can be observed at the measured frequencies due to their internal magnetic spins contributing to the magnetic signal. However magnetic susceptibility changes of a blocked particle can be monitored using ACS measurements. ACS measurements show that the tdMNP particles used had a Néel relaxation component which contributed to a constant magnetic signal and therefore small changes in the ACS measurements are difficult to observe.

In this study, a *different* iron oxide magnetite MNP with a strong Brownian relaxation component was studied to observe a significant ACS signal during cell internalization. These particles were coated with citric acid and PEI and used for a similar time point study. The particles are referred to as MN4 based on their fraction in the washing step during citric acid coating.

5.3.2.1 ACS characterization of MN4 with different coatings and suspensions

The MN4 particles were first characterised using AC susceptibility to study their relaxation properties. Based on Figure 5.12 A i&ii, MN4 had predominantly blocked particles and the Brownian relaxation peak was more defined than tdMNP. The MN4 particles were however not completely blocked and still contained a small superparamagnetic population. MN4 coated with citric acid and stabilized in water had a hydrodynamic diameter of 59 nm with negative surface charge. These particles were much larger than tdMNP and were blocked at a frequency of ∼3000 Hz. When

the MN4 particles were coated with PEI on top of the citric acid coating and dialyzed to remove free PEI (MN4-PEI), the peak shifted towards a lower frequency with an increase in size to 58 nm.

To better understand the behaviour of these particles when immobilized and to study the χ' and χ" pattern in high viscosity, MN4-PEI was suspended in a pure glycerol suspension with a viscosity of 0.28 Pa.s. Based on Figure 5.12 B i, there was a shift in the relaxation time with the emergence of a tail end of the Brownian relaxation peak at low frequency. The actual peak was well below the measurable frequency of 10 Hz. This meant that the particles were not completely immobilized and still maintained a small degree of rotational diffusivity.

A stock PEI solution at higher viscosity of 13–18 kPa.s was used to fully immobilize the MN4 particles. Similar to the glycerol suspension, MN4-PEI in a PEI matrix was measured on the AC susceptometer. In this PEI matrix, the MN4-PEI Brownian peak has completely disappeared. The remaining signal is from the Néel relaxation component of the suspension. Therefore, in this suspension MN4-PEI is completely immobilized.

In Figure 5.12 C i, ii, and iii, the normalized ACS plots of MN4-PEI in glycerol and PEI matrix was compared. The χ' of the MN4-PEI in glycerol sample (black) showed a steeper gradient (loss of signal) than particles in the PEI matrix (red) (Figure 5.12 C ii). In the normalized χ" graph (Figure C iii) MN4-PEI in glycerol showed a strong Brownian signal at the lower frequency of oscillation. MN4-PEI in the PEI matrix shows a slight upward trend with increasing frequency, which is due to small signal variations in the ACS measurements. Therefore, MN4 samples in a viscous suspension will show lower mobility and a Brownian peak at low frequencies. When MN4 particles are measured in cells, ideally ACS measurements will show immobilization based on a flat χ" signal, and with release of MN4 from endocytic vesicles, particles will gain mobility in the cytoplasm and a Brownian peak will form similar to the peak observed in the glycerol suspension.

5.3.2.2 Time series ACS measurements of MN4-PEI internalized in cells

Once the behaviour of MN4-PEI in suspensions of different viscosities had been established, ACS measurements of MN4 in cells were studied at 4 time points. In this study, MN4-PEI particles were taken up by HeLa cells using the magnefect nano which were then measured on the ACS at 5 hours, 10 hours, 15 hours, and 24 hours after particle uptake. All time points show the same magnetic susceptibility signal strength except Figure 5.13 A ii at 10 hours, due to sample variability. There are no observable differences between the 4 time points in Figure 5.13 A.

χ' values for each time point was normalized and compared between each group (Figure 5.13 Bi). There was no observable difference in the χ' susceptibility signal with increasing frequency between all 4 time points. When the χ" normalized signal was studied (Figure 5.13 Bii), there was high background noise in the measurements due to low MNP content in the samples. However, by performing the LOESS smoothing for 3 points, χ" measurement trends were more visible (Figure 5.13 Biii). While the 3 time points (5 h, 10 h, and 24 h) showed similar trends indicating immobilization of MN4-PEI, at 15 hours (blue) there is a steeper downward gradient at low frequency (100–600 Hz) before assuming the same signal form as the other groups. This steep gradient, similar to the tail-end Brownian peak observed for MN4-PEI in glycerol could indicate partial mobility of MN4-PEI in cells had been restored at 15 hours. However, the ACS signal is too weak and with high background noise, the assumption that there is particle mobility is unreliable.

HeLa cells treated with MN4-PEI were imaged on brightfield to observe morphological differences and particle localization within the cytoplasm at 5 h, 10 h, 15 h and 24 h after internalization (Figure 5.14). At 5 hours, the MN4-PEI particles were only faintly noticeable in cells due to light contrast, indicating low particle clustering. At 10 hours, there were more granular dark structures in the cells with a higher degree of clustering compared to the group at

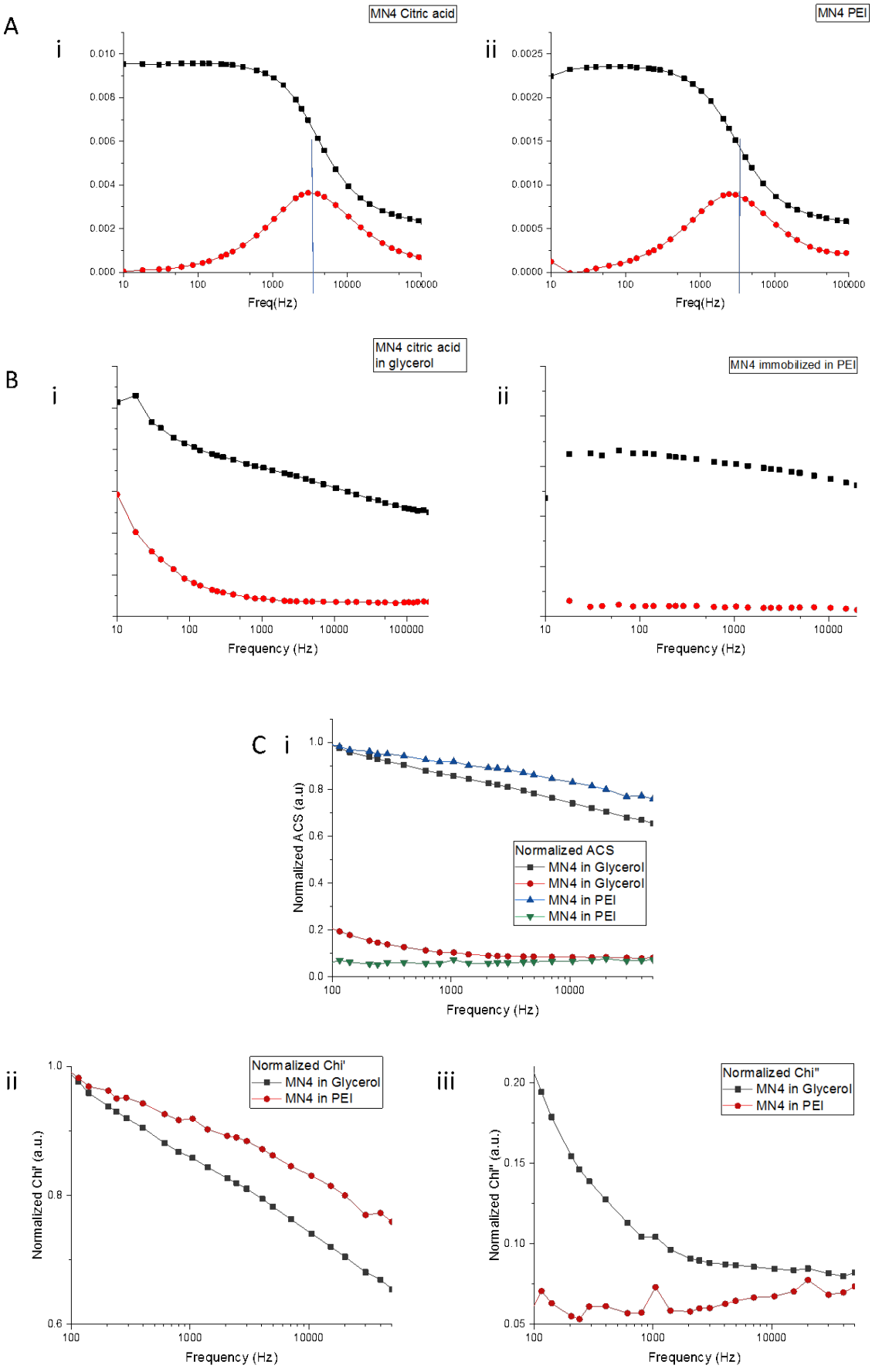

Figure 5.12 ACS measurements of MN4 (A) (i) coated in citric acid and (ii) coated in PEI, showing the peak position in both χ" curves. In figure (B), MN4 was immobilized in a (i) glycerol suspension and (ii) viscous PEI suspension. (C) (i) is the comparison of ACS curves of immobilized MN4 in glycerol and viscous PEI, (ii) are the normalized curves of χ', and (iii) is the normalized curves of χ" in either glycerol or viscous PEI.

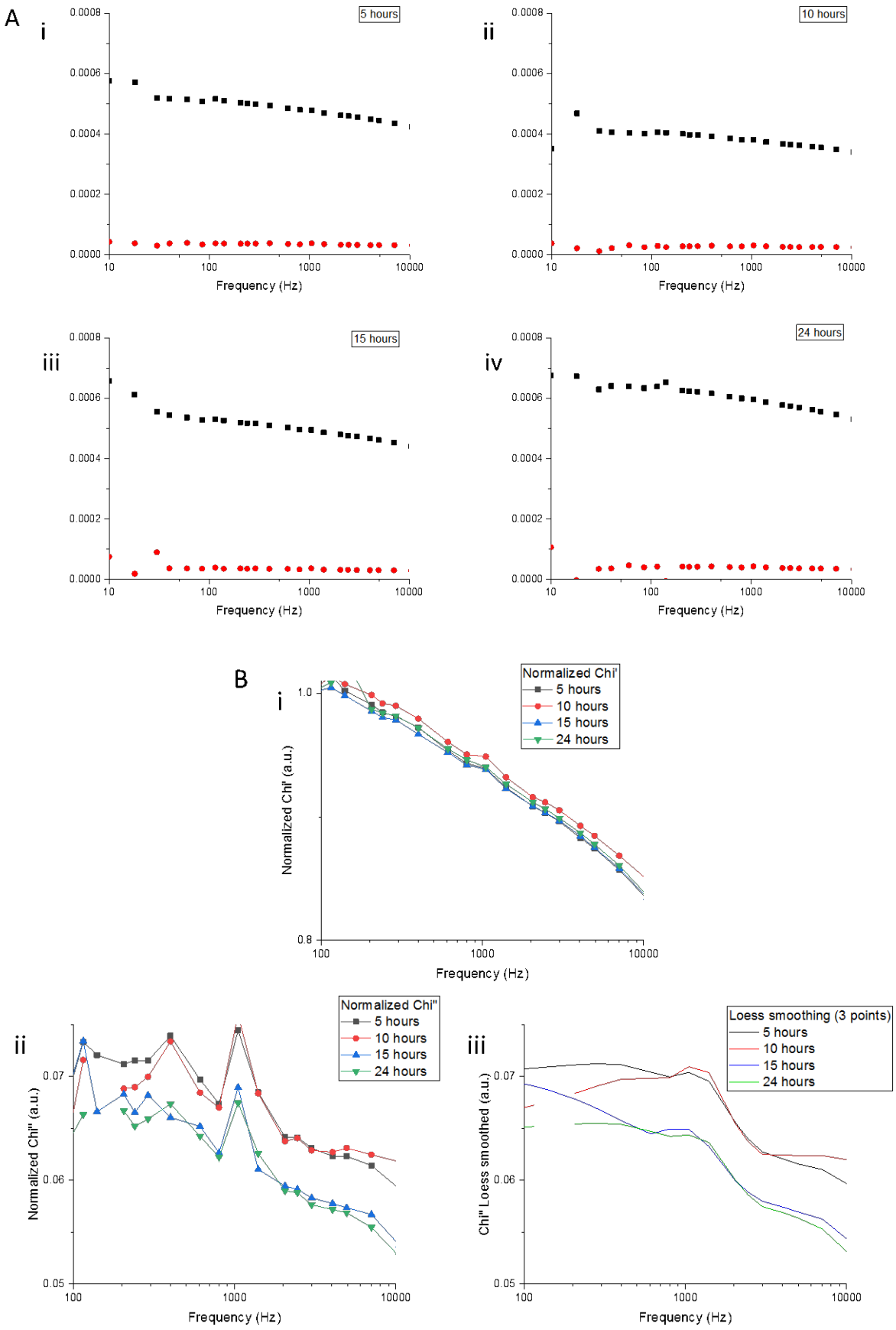

Figure 5.13 (A) ACS measurements of MN4-PEI internalized in HeLa cells at different time points after nanomagnetic transfection for (i) 5 hours, (ii) 10 hours, (iii) 15 hours, and (iv) 24 hours. (B) Comparison between normalized time point curves for (i) χ' and (ii) χ".

5 hours. At 15 hours, particles were moving closer to the perinuclear region of the cell and at 24 hours, the particle clusters had increased in size with dark contrast. At this point, the particles had reached the perinuclear region and were aggregating around this area. Therefore, MN4-PEI particles move towards the nuclear region of the cell with time and were observed to increase in cluster sizer closer to the nuclear region.

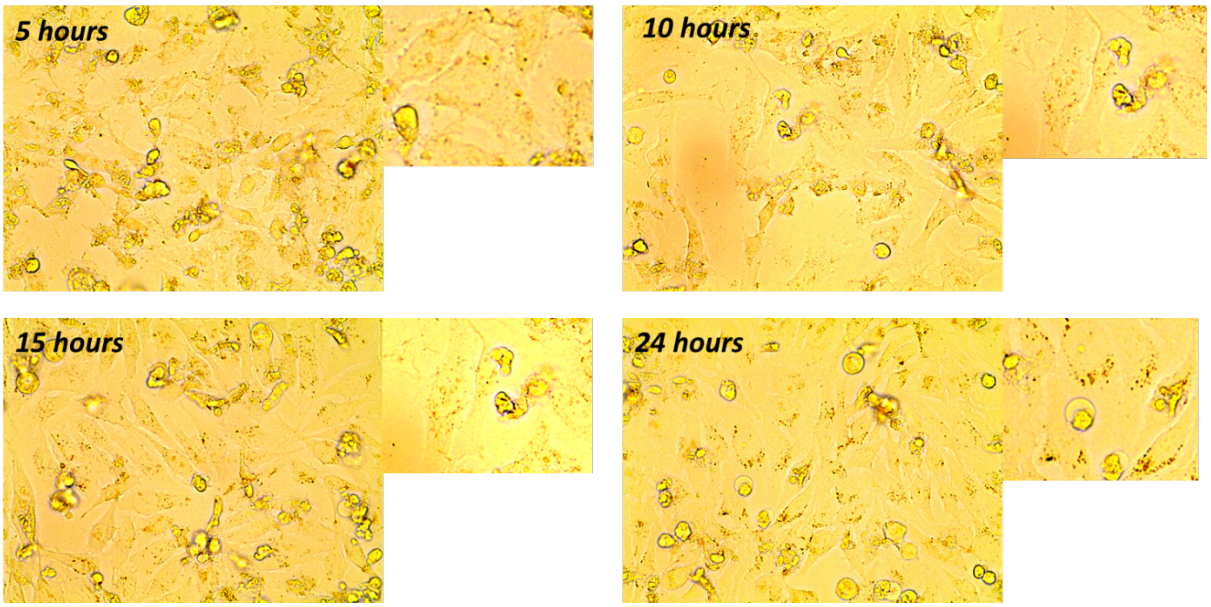

Figure 5.14 Brightfield images with enhanced contrast showing HeLa cells with MN4-PEI at different time points after internalization. Images on the right are zoomed in to show changes in particle morphology in cells for 5 hours, 10 hours, 15 hours and 24 hours.

5.3.3 Raman spectroscopy of tdMNP-PEI localization in HeLa cells

To understand the mechanism of MNP-PEI movement in cells through the cytoplasm, Raman spectroscopy was employed as an analysis technique. Recent advances in Raman spectroscopy instruments created a boost in Raman spectroscopy analysis to study chemical and structural properties of various material by looking at the fundamental spectra and their peak positions, as well as resolve an area of different chemical compositions (Browne and McGarvey, 2007; Ferrari and Basko, 2013). Raman spectroscopy is also gaining ground as a sensitive technique in studying biological processes in cells and cellular organelles (Moreira et al., 2008; Movasaghi et al., 2007).

To determine the movement of tdMNP and PEI components within a cell, the individual components and their characteristics had to be identifiable in different systems. To this end, two laser types–the 532 nm and 780 nm lasers were compared to obtain clearer and more sensitive detections of the materials of interest. Once the spectral fingerprints and identifiable peaks for each component (tdMNP, PEI, tdMNP-PEI, and HeLa cell) were obtained, tdMNP-PEI was internalized in cells and a spectral map was measured to determine localization of the MNP in the cytoplasm using Multivariate Curve Analysis (MCA). Besides that, the Surface Enhanced Raman Spectroscopy (SERS) technique was studied to observe if the plasmon effect was able to enhance the spectra of tdMNP and tdMNP-PEI using the 532 nm laser.

5.3.3.1 532 nm laser for the identification of tdMNP, PEI, and HeLa cells

Raman spectroscopy of the transfection components on a silicon wafer

tdMNPs only were measured on the Raman spectrometer using a 532 nm laser to obtain fingerprint spectra. The particles were measured in the presence of gold nanoparticles to improve the spectral signal using the plasmon effect, shown in Figure 5.15 A. tdMNP with gold NP samples

measured twice showed similar peaks attributing to uniformity of the particles at different points. Pronounced peaks were observed at 674 cm^{-1} and 1398 cm^{-1}.

In Figure 5.15 B, tdMNPs measured with and without SERS (described in Chapter 1) were compared. tdMNPs with gold NP dispersed across the sample showed clear and well-defined peaks, especially at 1398 cm^{-1}. The peak positions were different with and without the SERS effect, where tdMNPs without SERS showed the identifiable silicon wafer peak at 520 cm^{-1} which was absent with the presence of gold NP in the sample. This may be due to gold NP enhancing the tdMNPs signal as they were directly in contact with the tdMNPs and therefore the Raman signal of the silicon wafer was diminished. The tdMNP SERS effect however produced a peak at 674 cm^{-1} which may be the silicon wafer peak which is based on the vibrations of Si-O-Si (Anadolu, 2014).

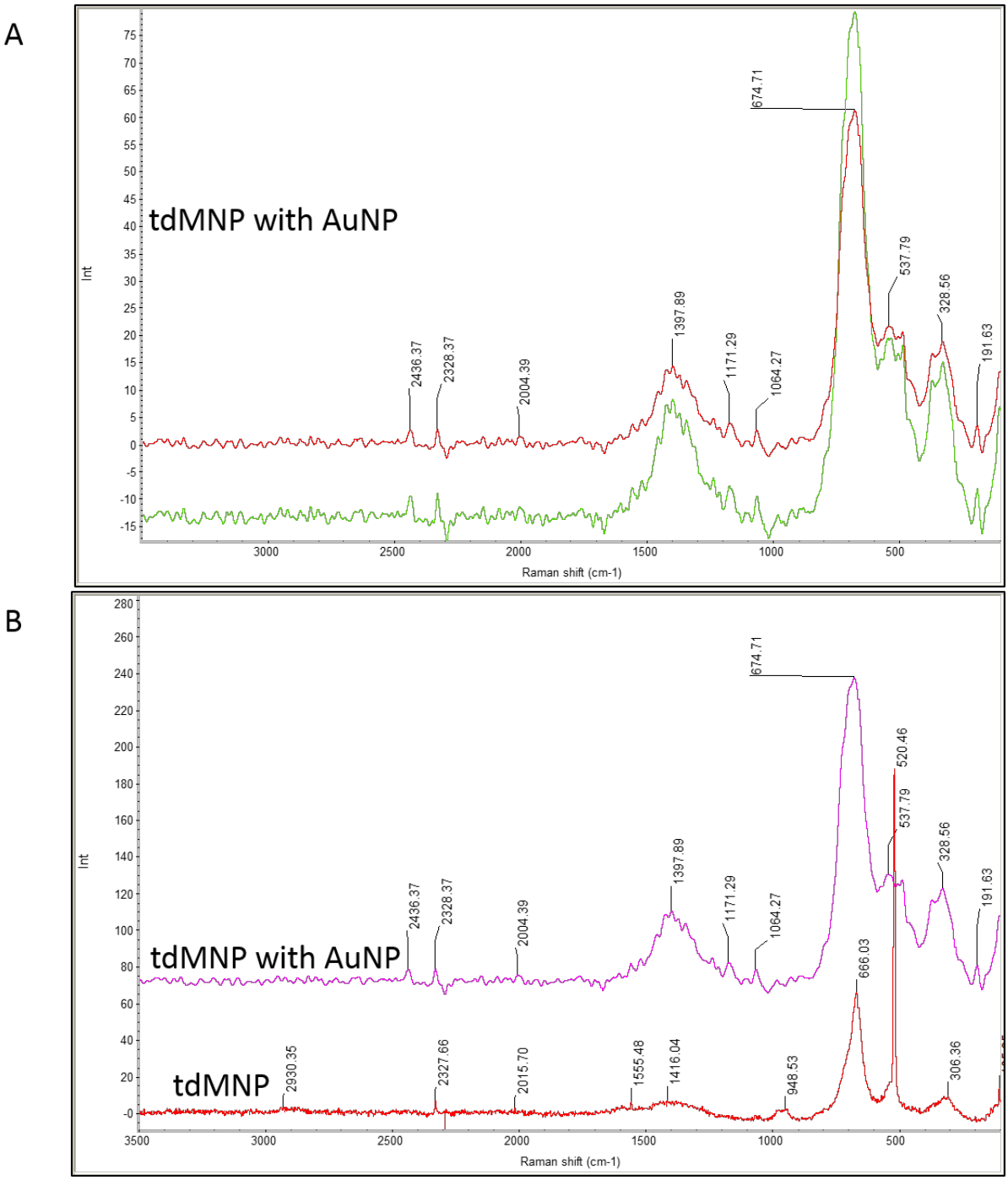

Figure 5.15 Raman spectra of tdMNP dried on a silicon wafer with and without the SERS effect. (A) two spectra of tdMNP-SERS using gold NP at different points on the sample and (B) spectral comparison between tdMNP-SERS (pink) and tdMNP without SERS (red).

In Figure 5.16, PEI polymer on a silicon wafer was measured on the Raman spectrometer using two different objective lenses. The 50x lens which provided higher magnification showed less defined peaks (green) compared to the 10x objective lens (red). Peaks at 520 cm^{-1} are from the silicon waffer. The spectra obtained with the 10x objective lens showed peaks similar to the 50x spectra except at 972 cm^{-1} seen only in the 50x lens. Additional peaks were also observed for 10x magnification at 868, 1037, 1126, and 1384 cm^{-1}. The most distinct peaks for the PEI polymer were at 1455, 2836, 2938, and 3300 cm^{-1}. The 10x objective lens was able to collect stronger signal from the Raman scattering. Raman spectra of PEI was also studied by Lin et al. using SERS, which showed similar spectral peaks to Fig. 5.16 at 877, 1067, 1112, 1305, 1456, 1601, 2854, 2923, and 3309 cm^{-1} (Lin et al., 2009).

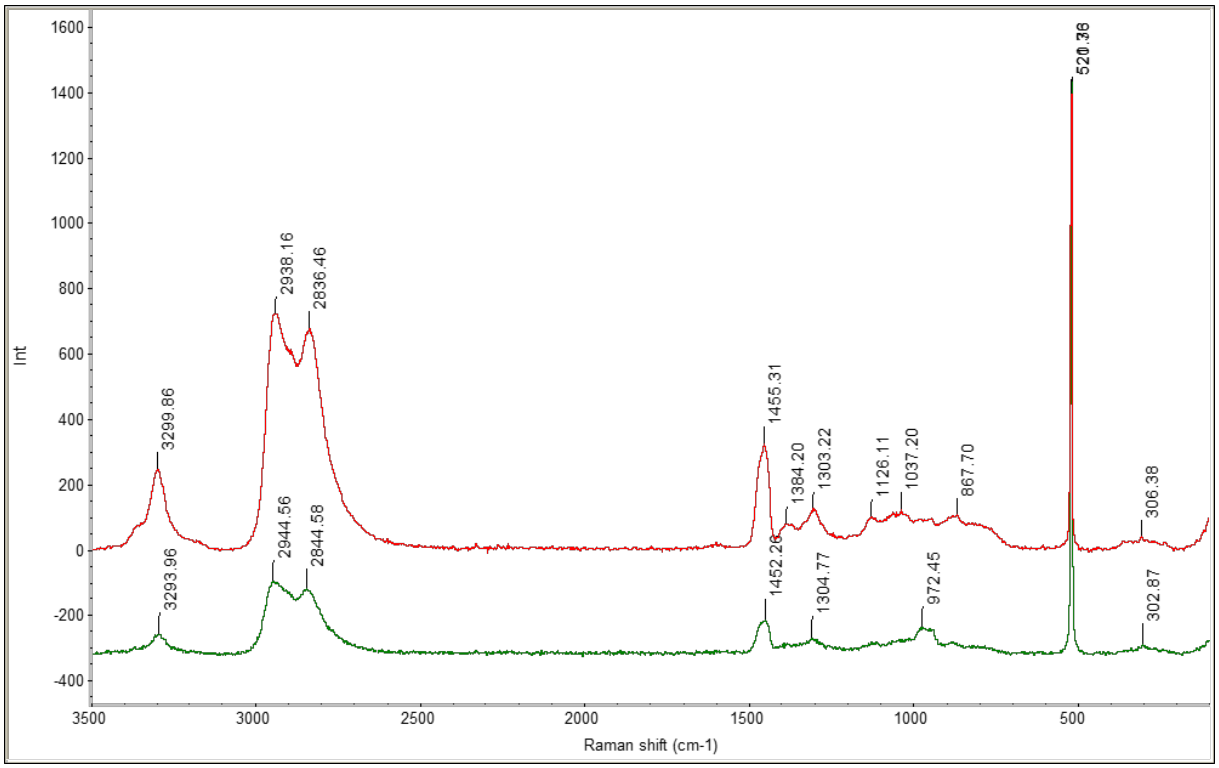

Figure 5.16 Raman spectra of PEI polymer without dilution on a silicon wafer with a 10x objective lens (red) and 50x objective lens (green).

Before the localization of tdMNP-PEI in cells can be studied, a tdMNP-PEI spectral fingerprint has to be obtained. PEI-coated tdMNP dried on a silicon wafer was measured using SERS (Figure 5.17 A) and without SERS (Figure 5.17 B). With SERS, the four spectra obtained had high background noise with ill-defined peaks. The silicon wafer peak was present at ~520 cm^{-1}. Out of the 4 spectra obtained from different points on the sample, three spectra showed similar peak positions (orange, red, and blue).

When comparing with tdMNP sample measurements in Figure 5.15, the peak at 671 cm^{-1} was still present for both tdMNP and tdMNP-PEI spectra. The peak observed at 1398 cm^{-1} for tdMNP (Figure 5.15 A) was absent in the tdMNP-PEI samples (Figure 5.17 A) but seemed to split into two peaks at ~1350 cm^{-1} and ~1560 cm^{-1}. Peaks were observed at 2879 cm^{-1} and 2931 cm^{-1} in tdMNP-PEI, comparable to the peaks 2836 cm^{-1} and 2938 cm^{-1} in Figure 4.12 of the PEI spectra. Using SERS, tdMNP-PEI spectra show peaks that occur in tdMNP and PEI sample spectra.

tdMNP-PEI dried on a silicon wafer was also measured without the SERS effect shown in Figure 5.17 B. The resulting spectra showed low Raman signal and high background noise, and the only clear peak was at 520 cm^{-1} of the silicon wafer. Therefore, SERS was required to enhance the spectra of tdMNP-PEI and without the presence of gold NP, the Raman spectrometer was unable to detect scattering from the MNP sample, resulting in noisy spectra.

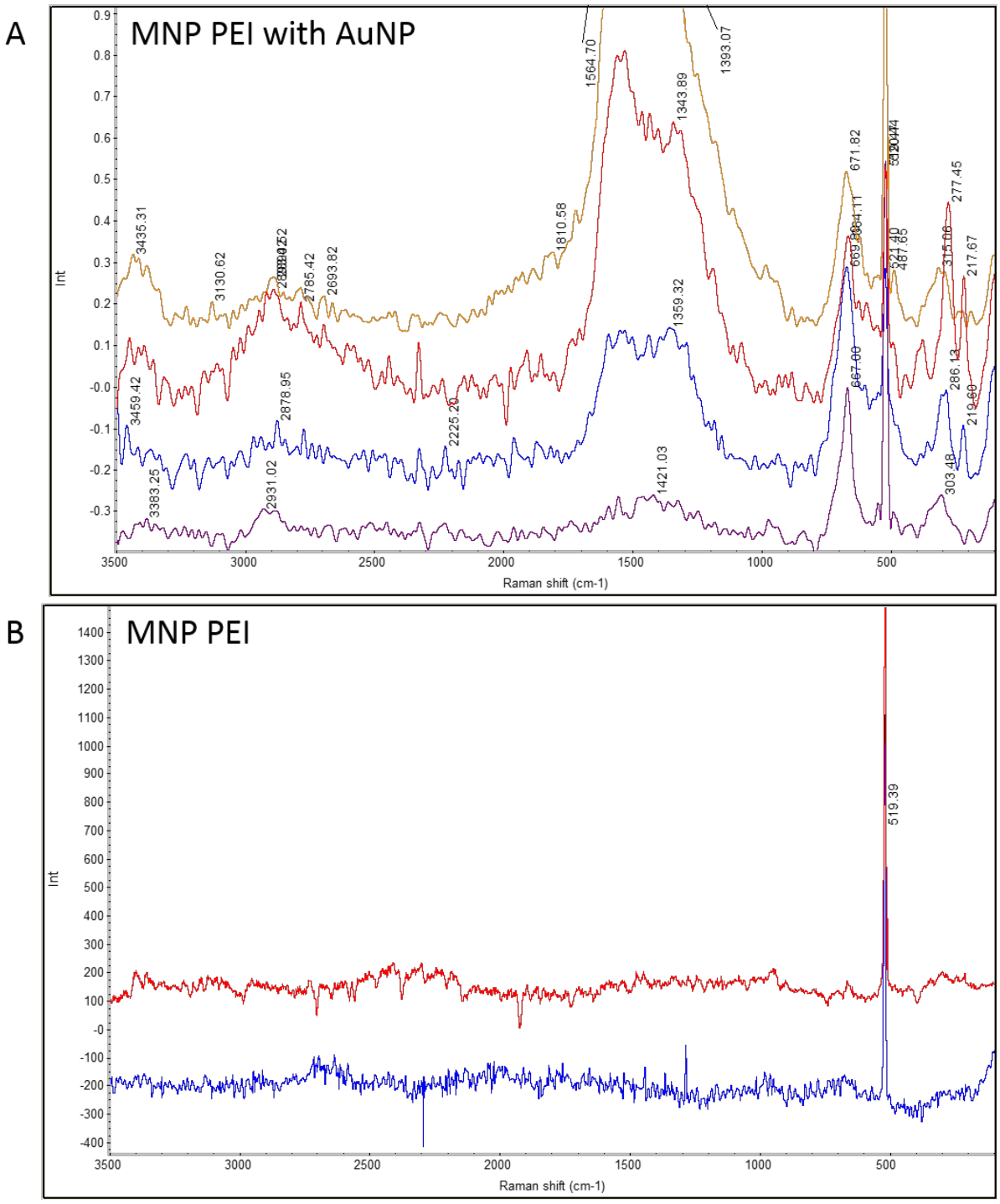

Figure 5.17 Raman spectra of tdMNP-PEI dried on a silicon wafer (A) using SERS with four spectra at different points on the sample and (B) without SERS and two spectra at different points of the sample.

Raman spectroscopy of tdMNP-PEI in HeLa cells

To identify localization of tdMNP-PEI internalized in HeLa cells, spectra of each tdMNP-PEI component (tdMNP and PEI, respectively) including the tdMNP-PEI complex were determined above to identify their localization in cells. Furthermore, Raman mapping can detect the nuclear region of the cell so a map of the chemical components in the same area can be correlated with it. In this section, a Raman chemical map of a HeLa cell before uptake of tdMNP-PEI was measured. Figure 5.18 A shows the brightfield image of the HeLa cell and the location at which the measurement was performed in the cell (red box). The nucleus and cytoplasm of the cell was incorporated into the measured area to study the change in the Raman spectra due to chemical differences between the nucleus and cytoplasm.

When studying the Raman spectra of the HeLa cell, a peak indicative of the biological component lies between 2800–3050 cm^{-1}. This peak can be attributed to lipids and proteins with C–H stretching bands (Boyd et al., 2010), which confirms the presence of a cell sample. When the peak at 2800–3050 cm^{-1} is highlighted in Figure 5.18 Aii, a chemical map of the scanned cell area was produced shown in Figure 5.18 Aiii. Figure 5.18 Aiv is a close-up of the scanned area of the cell, showing a proportion of the cytoplasm on the right and nucleus on the left in the red box. The overlay of the chemical map on the cell brightfield image (Figure 5.18 Av) shows an accurate depiction of the cytoplasmic and nuclear area of the cell. The red intensity decreases with lower protein and lipid content or density. The multivariate curve analysis (MCA) shows 4 identifiable components in Fig. 5.19 A, with the fourth component highlighting the nuclear compartment of the cell (Fig 5.19 B).

HeLa cells were treated with tdMNP-PEI. The cells were measured on the Raman spectrometer after 24 hours, once cells had completely internalized the particles. In Figure 5.20, the HeLa cells were focused using darkfield imaging to observe tdMNP-PEI localization clearly. Figure 5.20 A i shows the HeLa cell with tdMNP-PEI in darkfield and the area of the cell which was scanned. A transverse area of the cell was chosen to incorporate a majority of the cell area from the cytoplasm to the nucleus to ensure MNP-PEI in the cell was effectively captured during measurements. In Figure 5.20 ii, the Raman spectrum of a point on the cell scan is shown and the peak that is highlighted corresponds to the lipid and protein peak area of 2800–3050 cm^{-1}. The spectrum is identical to the one taken with HeLa cell only in Figure 5.18. Figure 5.20 iii, iv, and v showing the chemical map of the cell at 2950 cm^{-1}, the zoomed in image of the cell area and the overlay of the chemical map and darkfield image respectively. Because the image of the cell is in darkfield, the nucleus and cytoplasm cannot be defined from the image alone. From the chemical heat map, the nucleus is located at the dense red area on the left of the cell.

Similar to Figure 5.20, the Raman map of the HeLa cell with tdMNP-PEI uptake was studied at 655 cm^{-1} peak position (Figure 5.21). This peak may correspond to the peaks observed in tdMNP and tdMNP-PEI spectra in Fig. 5.15 and Fig. 5.17 at 675 cm^{-1}. A pattern in the chemical map was obtained which could correspond to MNP localization in cells at the red areas. However upon closer inspection, HeLa cell without tdMNP-PEI Raman spectra also had this peak in its spectrum. Also Raman measurements of dried tdMNP and tdMNP-PEI samples on silicon wafers showed strong noise and was undetectable without SERS. Therefore the peak cannot be attributed to MNP-PEI in cells.

5.3.3.2 780nm laser for the identification of tdMNP and PEI

From the previous sub-chapter, it is obvious that the 532 nm laser was not able to pick up signals from tdMNP in cells. The laser was changed to 780 nm and the measurements were performed on the same sample types to obtain a clearer signal.

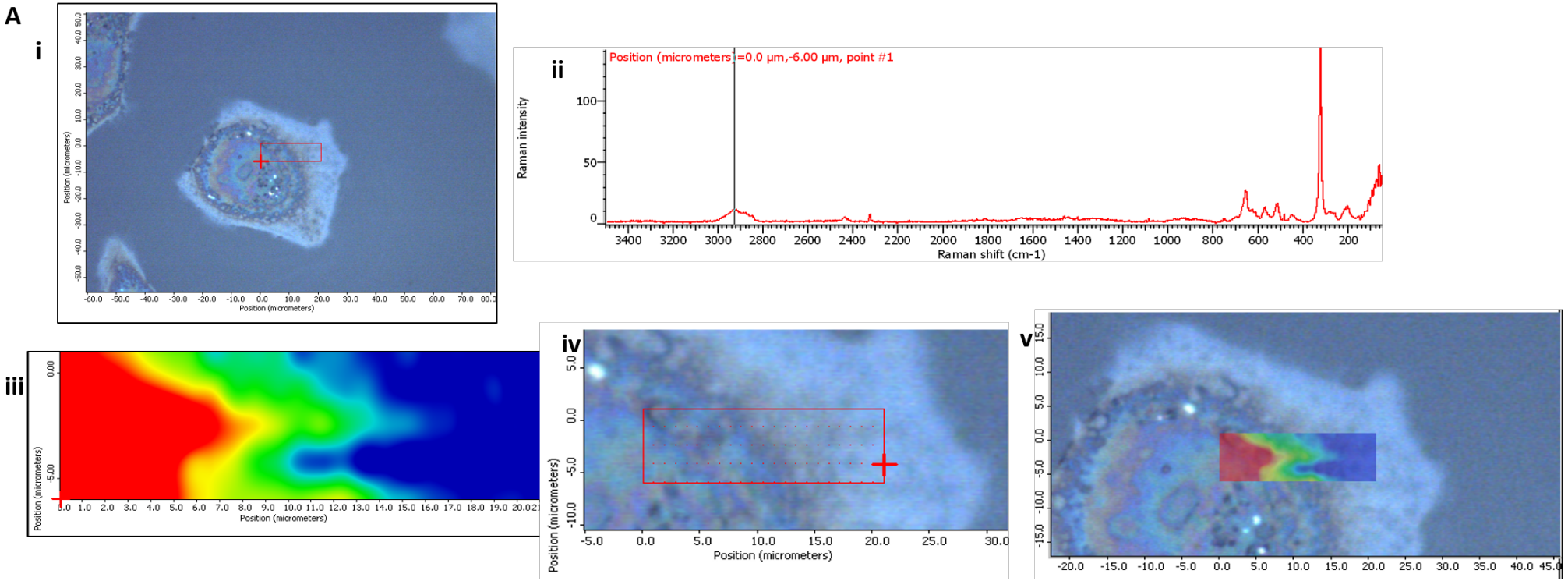

Figure 5.18 (A) Raman spectra area map of a HeLa cell. (i) Brightfield image of the cell and the area which was scanned in the red box, (ii) spectra of a point in the area map focusing on wavelength 2950 cm^{-1}, (iii) chemical map of the Raman map at position 2950 cm^{-1} in the spectra, (iv) a zoomed in view of the scanned area showing each scanned point, and (v) an overlay of the Raman chemical map and brightfield image.

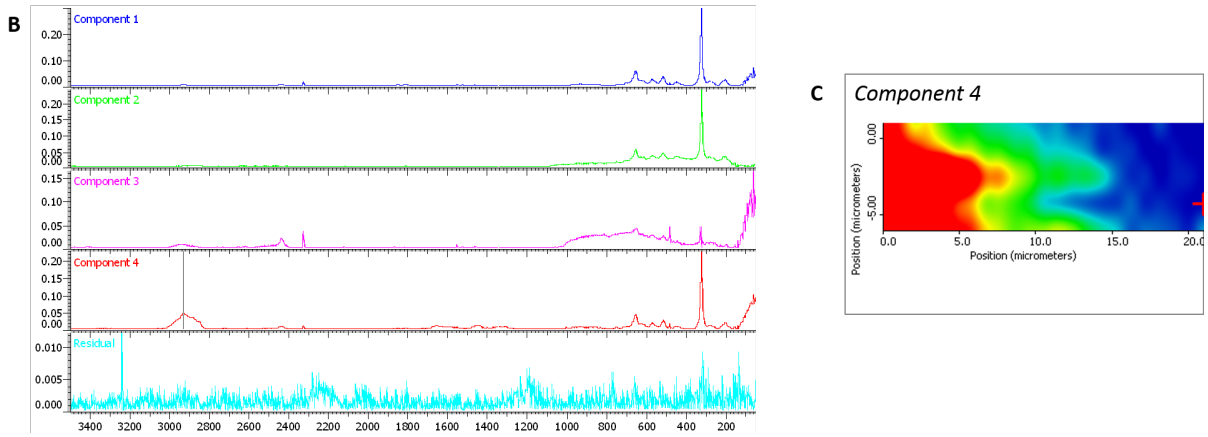

Figure 5.19 (A) Spectra from Multivariate curve analysis (MCA) of four components from HeLa cell (Fig. 5.18) and, (B) heat map of component 4 of the MCA.

tdMNP dried on a silicon wafer was measured using a line map where 10 points were obtained. Figure 5.22 Ai shows the brightfield image of the MNP sample and the line at which the measurements were obtained. The spectra in Figure Aii and the numbers on the right corresponds to the points at which the spectrum was taken on the line map. Besides the silicon wafer peak at 522 cm^{-1}, tdMNP shows three clear peaks at 306, 671, and 943 cm^{-1}. Spectral points 9 and 10 lost the peak at 671 cm^{-1} because these points lay outside the sample area, but it still showed the two other peaks although smaller in intensity.

Since this measurement was performed without SERS, the 780 nm laser was more suitable for studying iron oxide MNP as it provided a clear signal with low noise and well-defined peaks.

To determine if the Raman spectrometer is able to detect tdMNP in the form of an area map, dried tdMNP on a silicon wafer was studied to compare the chemical map to the brightfield image of tdMNP localization within the measured area. The characteristic peak at 670 cm^{-1} of iron oxide magnetite was chosen to locate MNPs within a 2-D area. The chemical heat map (Figure 5.23 iii) shows that there was localization of areas of intensity corresponding to the chosen peak. However the overlay image of the chemical map and brightfield image does not overlap with each other as the dark spots on the image corresponding to MNP did not have a similar pattern to the chemical map. The darkest spot in the centre of the scanned area was shown to be less intense on the chemical map. Therefore although the line map was able to correctly measure the Raman scattering of tdMNP, the area scan was not able to show localization of tdMNP based on the characteristic iron oxide peak.

MCA was performed on the sample for three components 5.24 but the chemical maps for each component still did not reflect the localization of tdMNP on the silicon wafer.

Since tdMNPs were not able to be detected in an area map, another iron oxide magnetite was used. The MNP MN4 coated with citric acid was studied similarly. MN4 was dried on a silicon wafer and was imaged using darkfield for better contrast (Figure 5.25 A i). A line map was scanned for 10 different points and 5 of those points were illustrated in Figure 5.25 A ii. There are three peaks corresponding to MN4 measurements; 305, 623, and 944 cm^{-1}. Since the 623 cm^{-1} peak was too small to define, the 944 cm^{-1} peak was used to study MN4 localization using the Raman area map scanning.

Once the peak position was defined, a Raman spectroscopy area map of the MN4 on silicon wafer was performed (Figure 5.26). Using the peak position 944 cm^{-1}, the chemical map was defined and overlay onto the darkfield image of the scan area. Similar to the results obtained for tdMNP in Figure 5.23, the chemical heat map did not correspond to the darkfield image of MN4, where the changes in colour intensity was not reflective of the dark spots on the silicon wafer where more MN4 had been deposited.

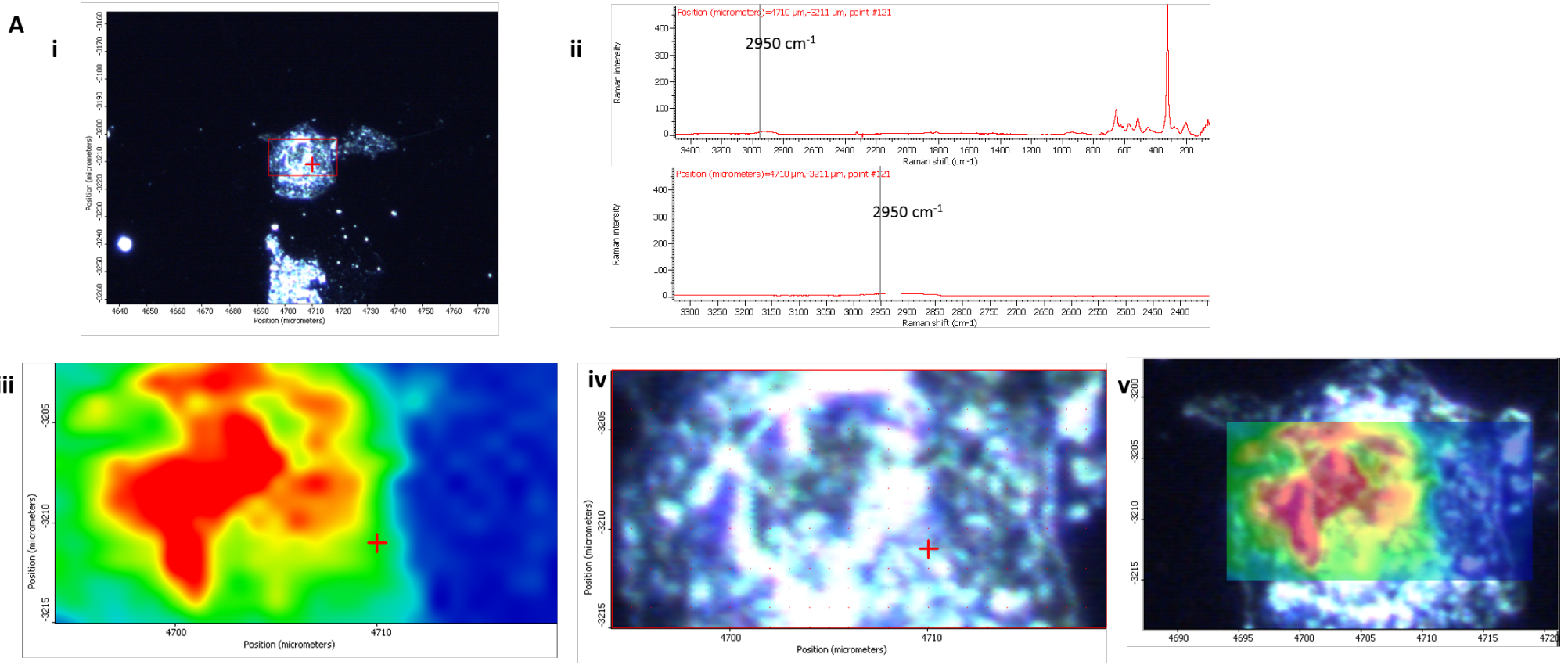

Figure 5.20 Raman spectra of an area map of HeLa cells with internalized tdMNP-PEI highlighting peak position 2950 cm^{-1}. (A) (i) Darkfield image of the HeLa cell showing the scanned area map (red box). (ii) The cell spectra at a single point on the map with the bar at position 2950 cm^{-1} (top) and a zoomed spectra at the wavelength of interest (bottom). (iii) Chemical map of the scanned area at position 2950 cm^{-1}, (iv) a zoomed in view of the scanned darkfield area of the cell, and (v) an overlay of the chemical map image and darkfield image.

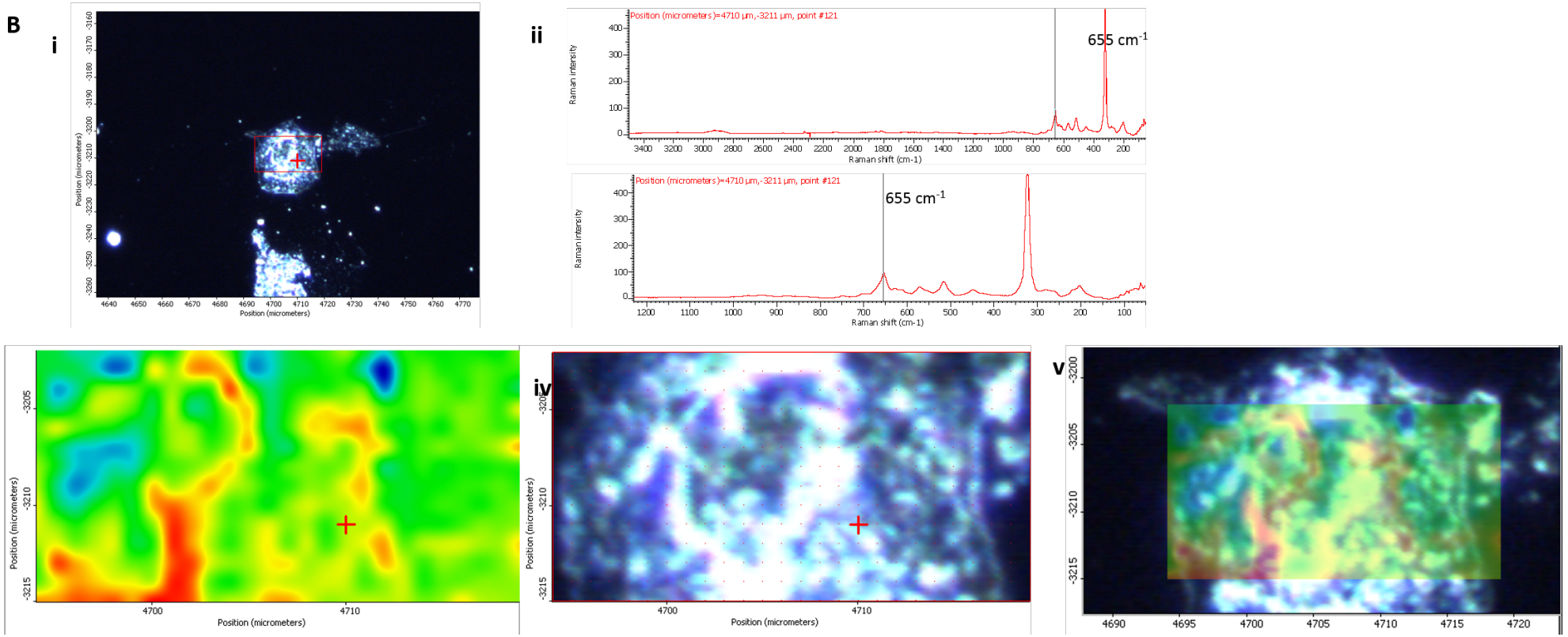

Figure 5.21 Raman spectra of an area map of HeLa cells with internalized tdMNP-PEI highlighting peak position at 655 cm^{-1}. (A) (i) Darkfield image of the HeLa cell showing the scanned area map (red box). (ii) the cell spectra at a single point on the map with the bar at position 655 cm^{-1} (top) and a zoomed spectra at the wavelength of interest (bottom). (iii) Chemical map of the scanned area at position 655 cm^{-1}, (iv) a zoomed in view of the scanned darkfield area of the cell, and (v) an overlay of the chemical map image and darkfield image.

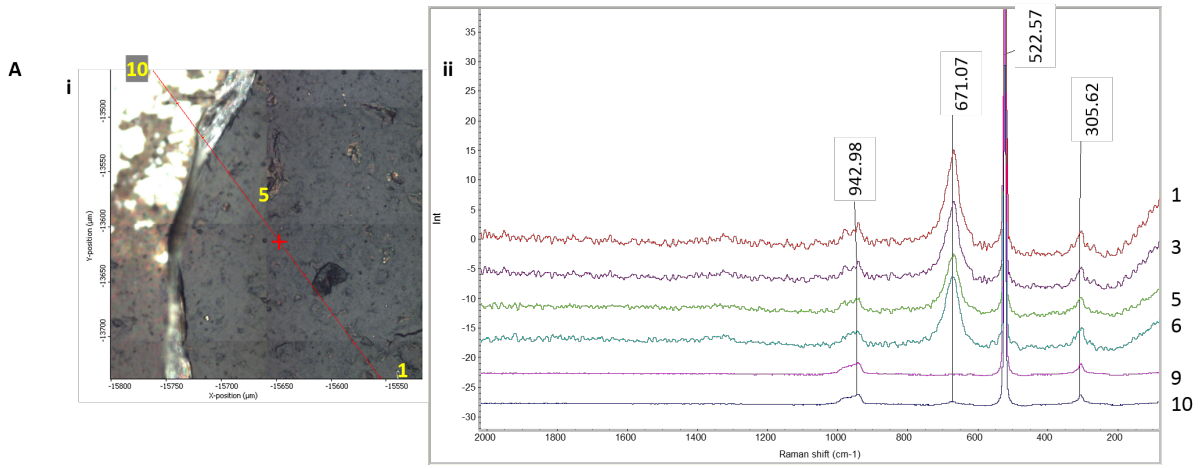

Figure 5.22 Raman spectra of a line map of tdMNP dried onto a silicon wafer. (A) (i) brightfield image of tdMNP and 10 points on the line map for 10 spectra and (ii) Raman spectra from the line map for points 1, 3, 5, 6, 9 ,10.

MCA was also performed on sample MN4 *(data not included)* for 2 components. Again, it did not reflect the localization of MN4 on the silicon wafer. Further studies were not performed.

5.4 Discussion

5.4.1 AC susceptibility for MNP tracking in cells

AC suceptometry is a non-invasive technique that can study the *in situ* magnetic particle susceptibility behaviour in live cells and without requiring chemical labelling or extensive cell sample preparation (Soukup et al., 2015). Since nanomagnetic transfection utilizes MNPs for gene delivery, the changes in MNP and attached PEI Brownian relaxation behaviour can be tracked in time until transfection occurs. Previous studies utilize different techniques to study the trafficking of nanoparticles and their interaction with organelles, such as the use of live-cell imaging and TEM (Bertoli et al., 2014).

In this study changes in the MNP Brownian peak were monitored to understand endosomal escape of tdMNP-PEI and MN4-PEI in cells. Particles in suspension are observed to have both Brownian and Néel relaxation behaviour. Since MNPs that relax by the Néel mechanism utilize intrinsic magnetic spins to sync with the external magnetic field, the external environment (except temperature) of these particles do not influence their magnetic susceptibility. Hence, these superparamagnetic particles have a constant magnetic signal even when there is a change in viscosity, particle immobilization, and clustering. Unlike the Néel relaxation signal, the monitoring of the Brownian relaxation signal would provide information about the internal environment of the cell and particle behaviour with regard to changes in interacting cellular processes.

The low rate of tdMNP only particles taken up by HeLa cells compared to tdMNP-PEI was observed in Figure 5.3 B where the low intensity of colour are signs of low iron oxide uptake, also reflected by the ACS signals in Figure 5.4 and Figure 5.6 A showing low susceptibility signal. Although the same concentration of magnetic material was added into the cell culture, only a fraction was taken up by cells. This reinforces previous studies that the surface charge of MNP is important in inducing higher uptake in cells. Neutral charged and negatively charged MNPs are less favoured compared to cationic particles during cell internalization (Villanueva et al., 2009), whereby particles with no surface charge reduces its interaction with biological molecules such as proteins and the cell membrane. Negatively charged particles interact with cationic surface membrane receptors for cell internalization, however these cationic sites are few on the

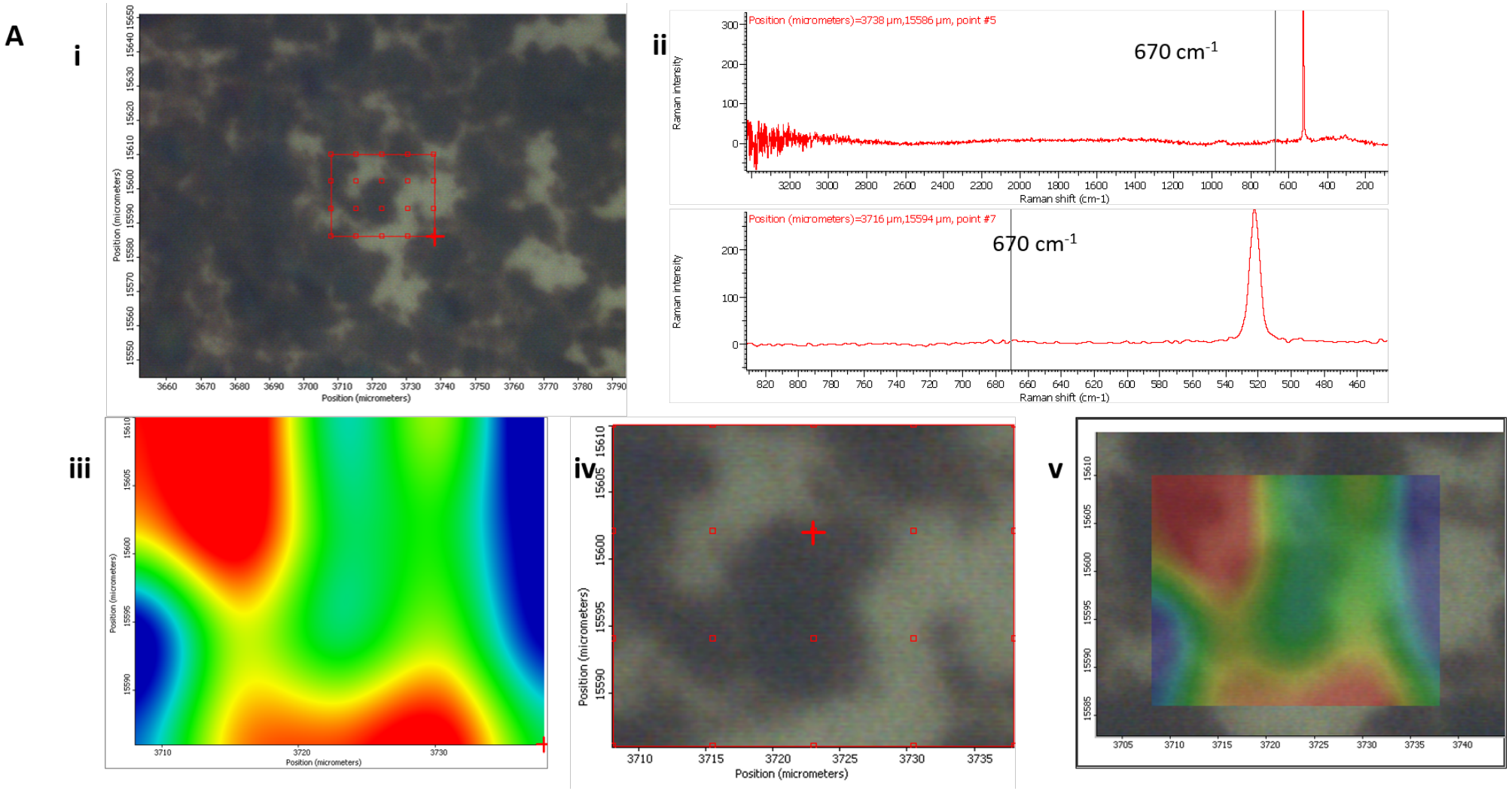

Figure 5.23 Raman spectra of an area map of tdMNP dried onto a silicon wafer. (A) (i) brightfield image of the tdMNP showing the scanned area, (ii) tdMNP spectra of a point on the map with the bar at 670 cm^{-1}, (iii) chemical map of tdMNP area scan at 670 cm^{-1}, (iv) zoomed in area map of tdMNP, and (v) overlay image of the chemical map and brightfield image.

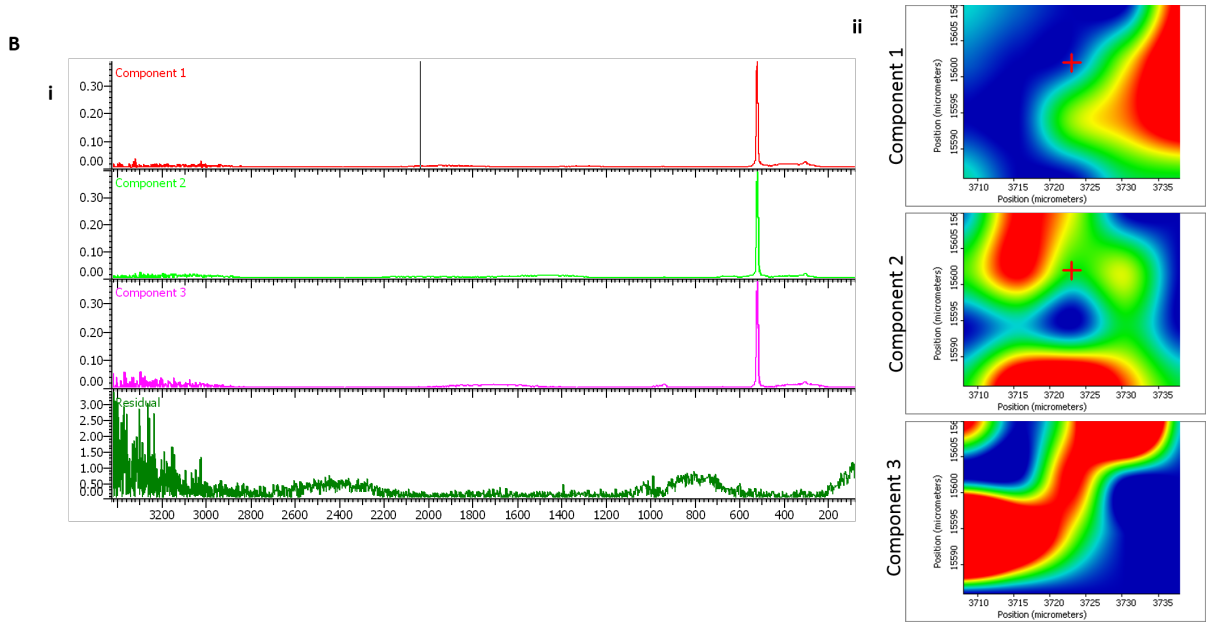

Figure 5.24 (A) Multivariate curve analysis from area scan in Fig. 5.23 (i) MCA spectra of 3 components and (ii) chemical map of each component calculated from MCA.

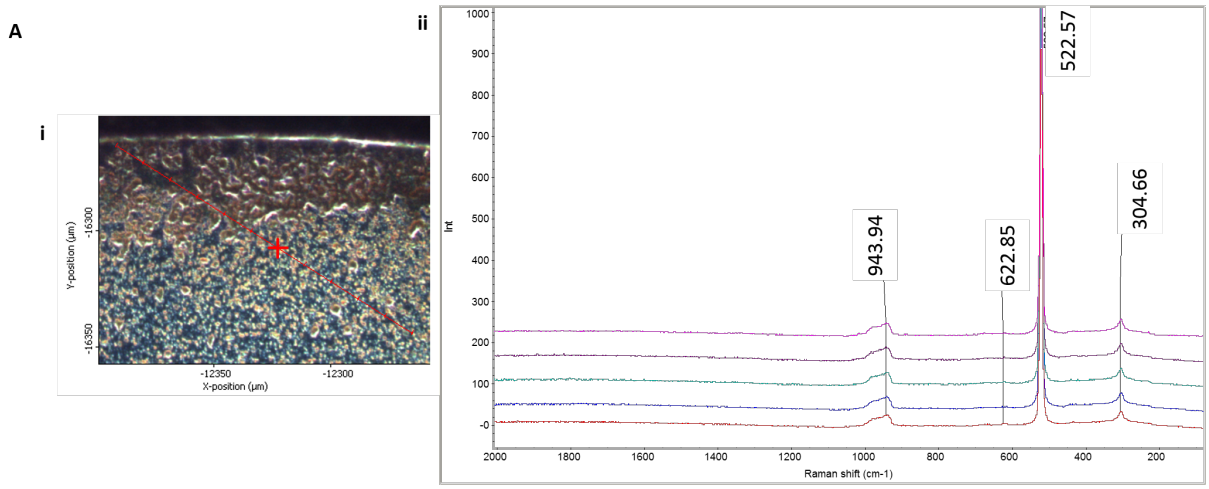

Figure 5.25 Raman spectra line map of magnetite MN4-citric acid (A) (i) darkfield image of MN4 and 10 points on the line map for 10 spectra and (ii) Raman spectra from the line map from 5 different points.

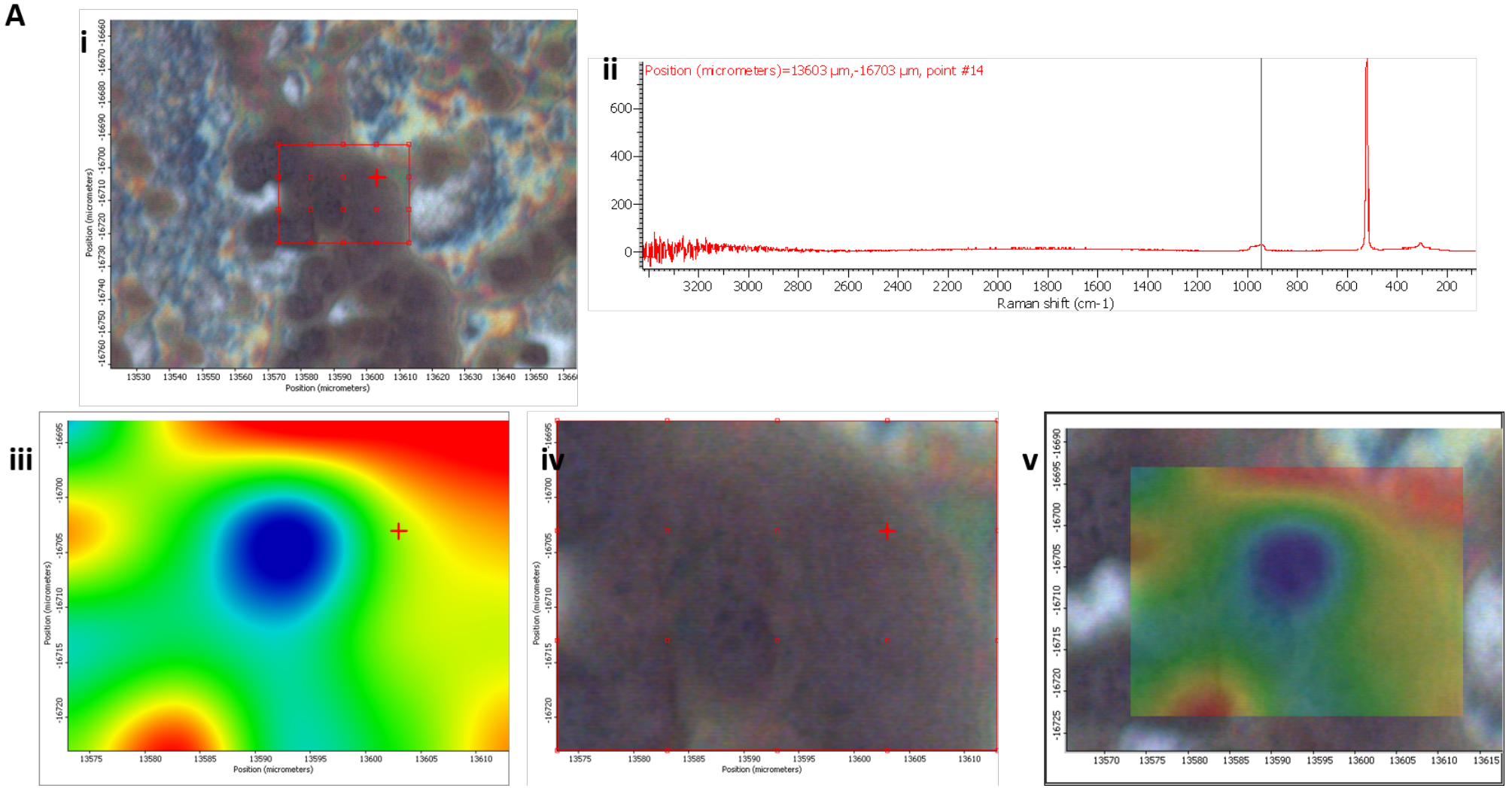

Figure 5.26 Raman spectra of an area map of MN4-citric acid coated dried onto a silicon wafer. (A) (i) brightfield image of MN4 showing the scanned area, (ii) MN4 spectra of a point on the map with the bar at 9500 cm^{-1}, (iii) chemical map of MN4 area scan at 9500 cm^{-1}, (iv) zoomed in area map of MN4, and (v) overlay image of the chemical map and brightfield image.

cell membrane (Verma and Stellacci, 2010).

Uncoated iron oxide MNPs are especially toxic to cells as MNP coating acts as a protective layer to reduce the dissolution of the particles to form soluble metals and production of reactive oxygen species (ROS) (Baber et al., 2011). Therefore most studies utilizing negatively charged MNPs coat them with a protein corona to facilitate uptake and reduce cytotoxicity, as well as increase the time of particle-cell interaction by increasing incubation time of MNP in the cell culture. In the case of MNP-PEI, positively charged particles are attracted to cell membranes and forms a sticky interaction which makes them difficult to come off by washing. Positively charged surfaces interact strongly with the cell membrane and with anionic receptors such as proteoglycans and lipopolyamines which improves uptake efficiency (Fröhlich, 2012). Therefore, PEI is an attractive choice for coating MNP for gene delivery functions, as the cationic charge of PEI coupled with magnetic targeting reduces transfection time from 4–6 hours to 30 minutes.

MNPs added into a cell monolayer culture are pulled down towards cells using the magnefect-nano transfection system, which then attaches to the cell membrane before being endocytosed into the cell. When ACS measurements were obtained 30 minutes after the magnefect-nano treatment, the Brownian relaxation peak was absent suggesting particle immobilization. Since complete endocytosis of all particles may not have occurred immediately after treatment on the magenfect-nano, the loss of a Brownian relaxation signal may indicate immobilization due to the attachment of MNP onto the cell membrane prior to internalization, preventing particle rotation. Once the particles attach to the cell membrane, invagination occurs through one of the many endocytic pathways and the MNP-PEI are taken in by the cell encapsulated in a lipid bilayer membrane.

After 2 hours of ACS measurements, the Brownian signal is still low, which is evidence that the particles are trapped inside endocytic vesicles and are being trafficked through the endocytic pathway. If the Brownian signal reappeared at 2 hours post-transfection, the mechanism of entry may be through cell wounding, where particles that are in cells have regained movement without being trapped in vesicles. Previous studies have determined that the mechanism of nanomagnetic transfection for internalization is through endocytosis and not membrane wounding (Ang et al., 2011).

After time point 10–17 hours, particles may have regained some Brownian movement in the cells relative to the other time points measured. After particle entrapment in endocytic vesicles, the proton sponge effect should occur where the buffering capacity of PEI causes endosomal lysis which releases the MNP-complex into the cytoplasm. ACS measurements in the MN4 treated cells did show a slight emergence of a Brownian peak, although the results were inconclusive. On the whole, ACS measurements did not show the appearance of a Brownian peak. Based on the continued immobilization of MNP, it can be deduced that the majority of MNP was not able to escape from the endosomes, and thus were trafficked for exocytosis or were aggregated within the perinuclear region of the cell. Other evidence to suggest MNP entrapment in the cell is the low transfection efficiency of tdMNP-PEI, which was only able to transfect HeLa cells at 20% efficiency, based on the study in Chapter 4. Therefore the population of particles that were able to escape from vesicles were low and did not significantly contribute to a Brownian relaxation signal in the ACS measurements.

Another possibility is during endosomal entrapment MNPs were aggregated, and when released from the endosomes through lysis, the MNPs were not able to break-up into smaller clusters. This effect was observed in Figure 5.6 where during cell lysis and sonication to separate MNPs from the cell, an ACS Brownian signal was not obtained possibly from the mash-up of MNPs, PEI and cellular residue. Similarly the endosomal lysis may cause particle coating detabilization and result in large unstable agglomerates. These clusters are too large for a detectable χ' peak to be measured on the ACS, even if they became mobile (i.e. by the endosome breaking). Therefore a Brownian peak will not be observed. Based on simulations, MNP clusters at $\sim$ 300 nm are not detectable for ACS instruments measuring at the lowest frequency of 10 Hz.

At 48 hours, the particles were immobilized again based on the loss of Brownian relaxation. From Figure 5.14 the MN4 particles head in the same direction towards the centre of the cell. Therefore during particle migration there is a possibility of particle clustering occurring at the perinuclear region of cells. These large particle clusters at a confined space causes particle immobilization. Another route that MNP may take is the particles are expelled from the cell either through exocytosis or during cell division when particles are released onto the extracellular matrix and are taken up by different cells which may cause immobilization due to the endocytic pathway. With the second uptake occurring, it is possible that PEI had been stripped off from the MNP surface or the buffering capacity may not work for endocytic vesicle escape.

A study by Zhao et al. describes the live tracking of PEI-coated MNP for nanomagnetic transfection in cells over time. ACS measurements reflect observations in this study, where at 2 hours the particles were localized on the cell membrane, and are internalized at 6 hours. Interestingly, MNPs were shown to traverse the nuclear membrane and localize in the nucleus (Zhao et al., 2014), since previously MNPs were thought to be unable to enter into the nucleus due to their size (Villanueva et al., 2009). The mechanism of entry into the nucleus can be by two ways: through the nuclear pore, which is NP size dependent, or entry during mitosis where the nuclear membrane breaks down. Nabeshi et al. had also determined that the NP entry into the nucleus is surface charge dependent, where amine and carboxylic functionalized NPs were unable to enter the nucleus and most MNPs localize in the perinuclear regions of the cell (Nabeshi et al., 2011).

In Fig. 5.11, cells that expressed GFP are shown to contain the transfection complex in their nucleus. The presence of MNPs in the nucleus however is unknown as the complex in the nucleus may just be made up of PEI and DNA. Besides that, the study in Chapter 4 determined that PEI covalently bound to MNPs was unable to transfect cells as efficiently as PEI bound electrostatically to MNPs. This suggests that PEI requires detachment from MNP surface for transfection to occur. Cells treated with MN4 in Fig. 5.14 show particle localization at the perinuclear region of the cells. Although evidence based on this particle type suggests MNPs does not enter the nucleus, it is inconclusive in this study if MNPs cross the nuclear membrane and deliver DNA in the nucleus during nanomagnetic transfection.

5.4.2 Raman spectroscopy for MNP tracking in cells

Raman spectroscopy has been used in various biological applications such as general scans of biological material (Boyd et al., 2010; Kang et al., 2013) or specific monitoring of biomolecules such as the monitoring of cytochrome c in apoptotic cells (Okada et al., 2012). It had also been used to detect inorganic samples such as graphene (Ferrari and Basko, 2013) and magnetic material (Chourpa et al., 2005). This technique is useful to detect specific chemicals fingerprints in a concoction of materials based on the Raman scattering of the sample.

Over the years, Raman spectroscopy has been developed enough to be sensitive to various signals. Single cell Raman spectroscopy is commonly used to study cell processes such as cytokinesis and apoptosis. In this study, we aim to perform particle tracking in cells. Chourpa et al. mapped the Raman signal for magnetite and maghemite nanoparticles using a 632.8 nm laser (Chourpa et al., 2005), which provided identifiable peaks comparable to the studies performed in this chapter. Magnetite fingerprints were found at 662 cm^{-1}, which was in accordance to the peak obtained in this study for the 532 nm laser at 674 cm^{-1} using SERS and 666 cm^{-1} without SERS, whereas the peak was at 671 cm^{-1} for the 782 nm laser. The peak formation at 671 cm^{-1} may be attributed to the crystalline phase the MNP which is rich in magnetite.

The two different lasers used, 532 nm and 780 nm, had a significant difference on the iron oxide MNP spectra. With the 532 nm laser, the spectrum obtained from MNPs was noisy with indistinct peaks. The spectrum was difficult to obtain and the MNP sample burnt quickly at this wavelength due to the dark colour of the sample. To overcome this, a lower laser power was used,

however this reduced the sensitivity of sample detection leading to a longer acquisition time and a low signal-to-noise ratio. When SERS was employed to improve the MNP spectra, clearer peaks were obtained with less noise. However this method was not suitable for this study as using gold NP with MNP-PEI may change the interaction with cells and the uptake and release pathway, much less the ability to transfect cells. With the 780 nm laser, the signal-to-noise ratio of MNP was higher compared to the 532 nm laser and an MNP spectra was obtained without SERS. There was strong noise at the higher end of the Raman shift but this can be neglected as the identifiable peaks are in the 200–1000 cm^{-1} range. The difference between the two lasers when measuring the MNP sample could be from the high fluorescence background emitted with the 532 nm laser. The 532 nm laser emits Raman signals in the visible light region where fluorescence is also detected. The 782 nm laser however excites molecules at a near infrared wavelength, which is too weak to induce fluorescence signals (Wahadoszamen et al., 2015). Therefore MNP samples are better measured at 782 nm to obtain a larger signal-to-noise ratio.

When performing cellular analysis, the most relevant shift is from 600–1800 cm^{-1} where the Raman peak for phospholipids, nucleic acid, lipid and protein can be found (Votteler et al., 2012). When MNPs were internalized in cells and a Raman map of an area obtained, the MCA was unable to detect an identifiable MNP or PEI spectra within the Raman spectra of the cell when overlapping the MNP and PEI spectrum obtained from samples on the silicon wafer using a 532 nm laser. Even at 782 nm laser wavelength, when the MNP spectra was clearer than the 532 nm laser, it was unable to accurately obtain a chemical map of MNP dried onto the wafer. The characteristic magnetite peak at 671 cm^{-1} was also unidentifiable. This technique for particle tracking in live cells has been performed using a specialized Raman spectrometer and also gold NP (Kang et al., 2013). Therefore, the Raman spectrometer used is either not sensitive enough for the detection of single particle tracking in cells, or various background corrections and normalization should be performed to obtain an MNP signal, and the use of SERS is recommended to improve effectiveness and signal strength.

Fourier Transform Infrared Spectroscopy (FTIR) is commonly used for probing fingerprints of materials. Unlike Raman spectroscopy which detects the molecular vibrations of materials, FTIR detects the transmittance or reflectance of infrared light after adsorption by the sample. The main reason FTIR was not used in this study is due to its unsuitablilty of sample preparation, which requires destruction of the biological sample. Furthermore, the presence of water in the sample causes signal interference. Unlike Raman spectroscopy which can map the single molecule chemistry of a cell using an area scan to determine local differences within a cell, FTIR requires the cell sample to be processed and dehydrated. However, FTIR studeis with biological sample can be undertaken using synchrotron-based instruments and attenuated total reflection-FTIR (ATR-FTIR), where sample preparation is not a limiting factor.

5.5 Conclusion

ACS measurements are a useful technique to determine changes in MNP relaxation behaviour in cells, to determine particle immobilization, loss or retention of coating, and even complex is measuring changes in viscosity in cells. In the study of the mechanism of transfection, the population of MNPs that were able to escape the endosome and resume Brownian relaxation was too low to be detectable by the AC susceptometer. Furthermore, the MNPs showed agglomeration in the cytoplasm which lowers the frequency of Brownian relaxation which again is below detectable levels of the ACS instrument.

The Raman spectrometer was able to detect MNPs and PEI spectral fingerprints when combined with SERS. Overall, the 780 nm laser had a better signal-to-noise ratio when measuring MNPs. However, the Raman spectrometer was not able to detect MNPs or PEI in cells using the chemical map area scan, although the cytoplasm and nucleus was able to be distinguished.

To improve this study, MNPs with higher transfection efficiency should be used to obtain a high population of transfecting MNP-complexes, which can then emit a stronger magnetic signal. Besides that, time point measurements are not ideal as different MNP-cell samples were used for each time point and limited temporal data is generated. The strongest Brownian signal generation was likely not measured at any of the 4 time points. Therefore continuous susceptibility measurements during the 48 hour transfection procedure are preferred to observe changes in MNP relaxation behaviour, especially in real time. In terms of studying the Raman signal of MNP in cells, a more sensitive Raman spectrometer suitable for cell samples should be used. Besides that, SERS technique can be easily employed for MNP internalization due to the ease of MNP fuctionalization, where gold NPs can be attached to MNPs. This method prevents gold NPs from separating from the MNPs of interest as they are internalized and trafficked within the cell. Future studies could also include fluorescence tagging of transfection components, and the fluorescence and brightfield live imaging of the migration of the MNP transfection complex in the cell up to gene expression.

Chapter 6

Effect of MNP-PEI on the Regulation of Cell Focal Adhesions and Actin Stress Fibres

6.1 Introduction

Iron oxide MNPs are regarded to have good biocompatibility *in vivo* as the body is able to metabolize and incorporate iron for cellular functions such as in haemoglobin and ferritin, although an excessive amount of stored iron has been known to cause toxicity (Weir et al., 1984). Iron oxide MNPs injected into animal models have shown clearance from the body through the reticuloendothelial system, where MNPs are observed to accumulate mainly in the liver and spleen, where it undergoes clearance or degradation (Edge et al., 2016; Jain et al., 2008), which suggests biocompatibility. There is also contrasting evidence that MNPs *in vivo* cause the production of ROS which caused neural damage (Mehta et al., 2004).

Studies have shown increased cytotoxicity of uncoated or bare MNPs. Therefore surface coating of MNPs are not only used to enhance functionality, but to also to enhance biocompatibility and protect cells from rapid biodegradation of MNP and the production of ROS. Baber et al. (2011) demonstrated that a silica shell around uncoated MNPs reduces the formation of soluble iron which improves cell viability. Although many surface coatings improve biocompatibility of MNPs, toxicity is also size and surface charge dependent (Yang et al., 2013). PEI, for example, has been known to confer high cytotoxicity, especially at high positive surface charge density. Therefore studies have shown the incorporation of PEG with PEI to reduce cytotoxicity (Hoskins et al., 2012).

For *in vitro* studies, MNPs are used commercially in applications such as transfection, cell labelling, cell separation, and recently magnetic 3D cell culturing by Greiner-BioOne. Many of the companies selling MNP for commercial purposes state that the particles are safe and elicit low to no cytotoxic effect on cells. This effect was usually demonstrated through cell viability or cell death assays, which report a good response towards MNP internalization. These findings however do not take into account disruptions in cellular processes or downstream changes in cell behaviour which might affect the outcome of an experiment or application, hence an understanding of these changes is especially important when used for potential therapeutic applications. Hoskins et al. have stressed the importance of conducting the correct assay for cell viability and toxicity determination as some commercially available kits record inaccurate assay readings due to interaction of the chemical with MNPs (Hoskins et al., 2012), whereby MNPs have been known to quench fluorescence signals, or bind to assay molecules.

In many cases, MNPs do not elicit a live or dead toxicity result, but cause underlying disruptions in cellular processes. In Chapter 5, changes in the magnetic relaxation behaviour of tdMNP-PEI in the cell was explored using AC susceptometry by treating HeLa cells with high concentrations of tdMNP-PEI. An unexpected finding during this work were changes in the

cell behaviour during treatment with trypsin, whereby the presence of tdMNP-PEI inhibited detachment from tissue culture plastic. In this chapter, the phenomenon surrounding increased cell adhesion in cells treated with PEI coated tdMNPs was examined.

To this end, the vinculin molecule was studied to determine changes in cell adhesion of tdMNP-PEI treated cells. Vinculin is commonly associated with focal adhesion studies and the mechanism of vinculin association with actin and integrins as well as vinculin binding sites and active conformation has been widely reported (Humphries et al., 2007; Le Clainche et al., 2010). Vinculin and F-actin is commonly studied in cell adhesion research, as one factor causing F-actin stiffness is its binding to vinculin which initiates actin bundling and cross-linking (Goldmann et al., 1998). Therefore, an increase in vinculin biomolecule production also increases actin stiffness. To date, four main stress fibres have been identified, which are the dorsal and ventral stress fibres, transverse arcs, and the perinuclear actin cap (Figure 6.1) (Small et al., 1998). The formation of filopodia or microspikes, which are small actin fibres radiating from the cell membrane have been observed mainly in cell migration (Mattila and Lappalainen, 2008).

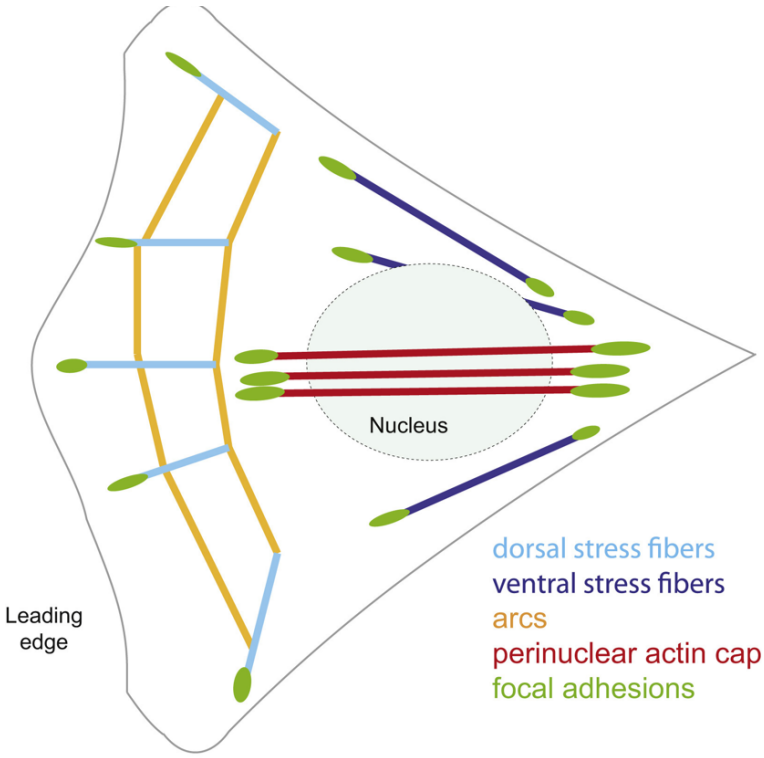

Figure 6.1 Schematic of the 4 main stress fibres and their interaction with focal adhesions in a cell (Burridge and Guilluy, 2016). Reprinted with permission from Elsevier publishing group [under a Creative Common licence CC BY-NC-ND 4.0].

Furthermore the changes in gene regulation were studied for ACTA2, ACTN1, VCL, MVCL, P4HA2, PCDHB12, SVIL, and TGFBI, which functions are described below.

Alpha actinin plays an important function in the development of focal adhesion, whereby it binds to other adhesion molecules such as integrins and intracellular adhesion molecule-1 (ICAM-1). Similar to vinculin, it is a protein associated with actin, along with adhesion proteins talin and paxillin (Alenghat and Ingber, 2002; Sjöblom et al., 2008). Besides its function as an adhesion protein, alpha-actinin acts as an actin crosslinking protein which promotes the formation of actin stress fibres (Sjöblom et al., 2008; Feng et al., 2013). The upregulation of ACTN1 gene signifies the increase in cell adhesion by the formation of focal adhesions through vinculin and possibly other adhesion proteins, as well as the observable increase in actin stress fibre formation with increasing MNP-PEI dosage.

Metavinculin is a splice variant of vinculin which localizes in muscle tissue. Although the specific function of metavinculin is still being discovered, and the differences between vinculin

and metavinculin function is unknown, metavinculin expression is observed to respond positively to mechanotransductive stimuli (Thompson et al., 2013; Thoss et al., 2013).

The gene P4HA2 encodes for the enzyme prolyl-4-hydroxylase which functions in the synthesis of collagen, specifically in the formation of the triple helix structure of collagen (Myllyharju, 2003). Transforming-growth-factor-beta-induced (TGFBI) is an extracellular matrix (ECM) protein found in many cell types. It can bind with various collagen types and forms cell-cell and cell-matrix interactions (Lee et al., 2014). It is also involved in many cell processes such as growth, apoptosis (Kim et al., 2003), and migration (LeBaron et al., 1995).

The cadherin superfamily is comprised of three subgroups; classical cadherins, protocadheris and atypical cadherins. Protocadherins, like classical cadherins are transmembrane proteins involved in Ca^{2+} mediated cell adhesion. Primarily, cadherins function in cell-cell adhesion, however their roles also extend to tissue morphogenesis (Halbleib and Nelson, 2006). Protocadherins display weak cell-cell adhesion functions but they also regulate various other cell processes. PCDHB12 which is also known as VE-cadherin-2 have a role in cell adhesion as a means to regulate cellular migration, and this adhesion is subsequently broken down by ADAM10 metalloprotease protein to initiate cell migration (Bouillot et al., 2011).

The protein supervillin was characterized by Pestonjamasp et. al in 1997, which was found to bind to F-actin filaments and localize at focal adhesions in the presence of E-cadherin at the cell membrane (Pestonjamasp et al., 1997; Wulfkuhle et al., 1999). Supervillin is found to regulate cytoskeleton activity by binding to F-actin and myosin-II filaments and performing actin crosslinking which increases membrane protrusions (Wulfkuhle et al., 1999), however this interaction negatively facilitates cell spreading (Takizawa et al., 2007). The presence of supervillin at focal adhesion sites either prevents the formation of mature focal adhesions or promotes the disassembly of mature focal adhesions, specifically focal adhesions that contains vinculin. Therefore, the amount of supervillin in cells is positively correlated with formation of focal adhesion sites and vinculin (Takizawa et al., 2006).

In this study, MG-63 and HeLa cells were treated with increasing doses of tdMNP-PEI to study their adhesion to tissue culture plastic. Changes in vinculin expression were also quantified with tdMNP-PEI treatment and the formation of actin stress fibres were observed. To determine the individual components of tdMNP-PEI causing changes in cell behaviour, an adhesion assay was performed. Finally the genes involved in actin fibre and focal adhesion formation were identified and their regulation with tdMNP-PEI treatment was studied.

Objectives

1. **Relationship between tdMNP-PEI dosage and uptake in cells.** To determine if the uptake efficiency of tdMNP-PEI in cells were dependent on loading volume of tdMNP-PEI in cultured cells.

2. **Dose dependent vinculin expression and stress fibre formation.** To quantify vinculin expression and observe changes in stress fibre formation with relation to tdMNP-PEI dose response.

3. **Effect of cell type on adhesion and MNP and PEI components affecting adhesion.** To compare the effect of tdMNP-PEI induced cell adhesion on MG-63 and HeLa and to study the contribution of individual components of MNP-PEI on cell adhesion.

4. **Identify genes involved in tdMNP-PEI induced cell adhesion.**To identify adhesion- and actin-associated genes that are upregulated after tdMNP-PEI treatment.

6.2 Materials and Methods

6.2.1 tdMNP-PEI treatment on MG-63 or HeLa cells

In a T75 tissue culture flask, cells are seeded at a density of 35 000 cells/cm^2 and grown to a confluency of 70 – 80% in 24 hours. 3 tubes of 10 mL of fresh CM was prepared and tdMNP-PEI (0.35 μg Fe/μL) was added into it at volumes of 20 μL, 50 μL and 100 μL. The media in flasks were replaced with the tdMNP-PEI supplemented CM and oscillated on the magnefect nano for 30 minutes. The media was then removed and replaced with fresh CM. Cells were incubated for 24 hours until treatment with trypsin. For trypsin treatment, cells were first imaged on the microscope in brightfield. CM was removed, cells washed with PBS and 5 mL trypsin solution was added into each flask. The flasks were incubated for 5 minutes and imaged on the microscope.

In a 24-well plate, cells were seeded at the same seeding density as detailed above. CM supplemented with 0.2 μL, 0.6 μL, and 1.0 μL of tdMNP-PEI of the same concentration was added into the cells, oscillated on the magnefect nano for 30 minutes and incubated for 24 hours. Assays were performed subsequently.

For gene expression studies, MG-63 cells were seeded in 6-well plates at the same density. Cells were treated the same as detailed above, with 1.5 μL (low dose) and 3.0 μL (high dose) of tdMNP-PEI at the same concentration.

6.2.2 Immunocytochemistry (ICC) for vinculin

Glass coverslips were soaked in 70% industrial methylated spirits (IMS) overnight and washed with PBS 3 times and seeded with cells. Cells were fixed in 10% formaldehyde (Fisher Scientific) in PBS or 100% ice cold methanol (Sigma), for 15 minutes at room temperature. For the ICC staining, cells were washed with PBS and permeabilized with 0.01% Triton-X 100 (Sigma) in PBS for 15 minutes at room temperature, followed by 2 washes in PBS-0.1% Tween 20 (Sigma). Cells were then blocked in 1% bovine serum albumin (BSA) (Sigma) for 1 hour at room temperature and washed with PBS-0.1% Tween 20. Primary antibody incubations (anti-Human/Mouse/Rat Vinculin mouse monoclonal from R&D systems) diluted to 1.25 μg/mL in 0.1% BSA in PBS-0.1% Tween 20 were performed at 4 °C overnight. Following the incubation, cells were washed with PBS-0.1% Tween 20 for 5 minutes on a shaker, twice. Then secondary antibody staining was performed, where 2 μL/mL Alexa Fluor 488-anti mouse (0.1% BSA in PBS-0.1% Tween 20) (Abcam) was incubated on cells for 1 hour at room temperature in the dark followed by 2 washes with PBS-0.1% Tween 20. Nuclei were stained with Hoescht 33342, trihydrochloride, trihydrate (Thermofisher) at a concentration of 1 μg/mL for 30 minutes at room temperature in the dark, and F-actin were stained with 1X Cytopainter 555 phalloidin (Abcam) for 1 hour at room temperature in the dark. Cells on coverslips were mounted onto microscope slides using Fluoromount Aqueous Mounting Media (Sigma) and dried at room temperature in the dark.

Samples were imaged on the confocal microscope and processed using ImageJ. The Green Fire Blue pseudo-colour filter was applied for vinculin staining and Red Hot for actin staining to observe the intensity and localization of biomolecule expression. The biomolecule intensity is shown in Figure 6.2 below.

6.2.3 Fluorescence quantification

Samples were imaged using the confocal microscope under the same laser power and gain settings to obtain comparable fluorescence images. Each cell membrane and nucleus was outlined by drawing boundaries around the area of interest. The mean fluorescence intensity per area within the outline was determined using ImageJ image processing software. The raw fluorescence intensity values of the nucleus were subtracted from the cytoplasmic values, as well as the subtraction of the nuclear area from the cytoplasmic area to obtain the ratio of nuclear to cytoplasmic

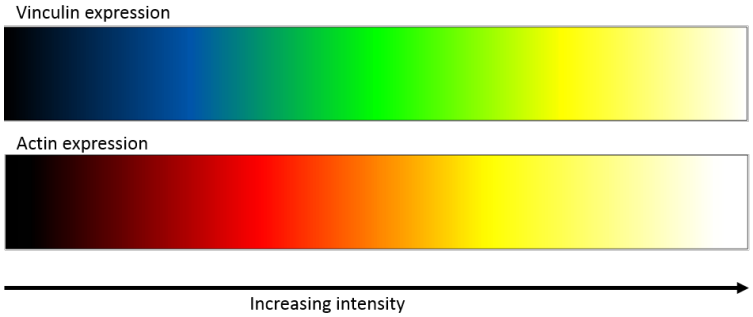

Figure 6.2 Colour map showing intensity of biomolecule expression obtained from pseudo-colour filters from ImageJ.

fluorescence intensity and the area of the cytoplasm and nucleus, respectively. The fluorescence intensity was divided over the total area to obtain the fluorescence intensity/unit area for the nucleus and cytoplasm.

6.2.4 PicoGreen cell adhesion study

PicoGreen dsDNA is an assay to quantify double-stranded DNA (dsDNA) which binds to DNA strands to form a highly fluorescent complex. The measured fluorescence intensity is relative to the amount of dsDNA in the sample. To study cell adhesion, the cell monolayer was treated with trypsin to detach cells and cells that remained attached were subjected to the PicoGreen assay. Intensity of fluoresecence indicated dsDNA amount, corresponding to the number of cells that remained attached to the cell culture plastic.

Cells were seeded into 24 well plates and MNPs were seeded after 24 hours at different loading densities per well and incubated for another 24 hours. The cells were then aspirated of media and washed with PBS once, and trypsinized with 1x, 0.5x, or 0.25x trypsin for 5 minutes. The plates were shaken to detach cells and trypsin with detached cells was aspirated off the wells. Pico Green assay (Quant-iT PicoGreen dsDNA reagent) (Life Technologies) was then performed to quantify the relative amount of cells left in each well. This assay quantitatively measures the fluorescence of double stranded DNA in a solution corresponding to the amount of cells. Cells that were adherent in wells were washed with PBS and lysed with 300 μL DNAzol reagent overnight at 4 °C followed by 200 μL of 100% ethanol. The solution is left to stand for 30 minutes until DNA condensation was visible. The solution was pipetted into Eppendorf tubes and centrifuged at 2320 rcf for 15 seconds. The supernatant was discarded and DNA pellet resuspended in 100 μL 1x TE buffer in a 96-well plate followed by equal volume of PicoGreen reagent per well. The reaction was incubated for 5 minutes and fluorescence was measured on a plate reader at an excitation wavelength of 480 nm and emission wavelength of 520 nm.

6.2.5 Gene expression study

Total RNA extraction for cell adhesion study

MG-63 cells with tdMNP-PEI after 24 hours were lysed and RNA extracted for qPCR analysis. The RNA extraction kit used was the miRNeasy Mini Kit from Qiagen. MG-63 cells in a 6 well plate were removed using a cell scraper and transferred into a PCR clean Eppendorf tube. 700 μL of QIAzol lysis reagent was added to the sample and vortexed to lyse cells. Samples were incubated at room temperature for 5 minutes. 140 μL of chloroform (Sigma) was added and tube shaken vigorously for 15 seconds before incubation for 3 minutes. Centrifugation was performed at 12 000 g for 15 minutes at 4 °C. The solution contained 3 layers and the upper aqueous phase was transferred into a new collection tube. 525 μL of 100% ethanol (Sigma) was added and mixed by pipetting. The sample was pipetted into an RNeasy Mini column and centrifuged at 13 000 g for 15 seconds at room temperature. The flow through was discarded. DNase digest

was performed by adding DNase enzyme (RNase-free DNase set; Qiagen) to the column and incubating for 15 minutes at room temperature. The column was washed with RWT and RDD buffers and finally with 80% ethanol. The RNA is eluted with 30-50 μL of RNase free water and RNA concentration was measured using a Nanodrop 2000. RNA samples were stored in $-20\,^{\circ}\mathrm{C}$ until further use.

Microarray data

A microarray was performed to identify gene expressions affected by tdMNP-PEI treatments. The microarray assay on control and tdMNP-PEI treated MG-63 cells were outsourced to Cambridge Genomic Services, UK. The assay was performed on a Human Oligo Chip mRNA from Toray International U.K. Ltd. The microarray results were filtered to identify genes associated with cell adhesion and actin fibres. From these genes, the ones that showed an increase in expression after tdMNP-PEI treatment were chosen for qPCR studies.

Primer design and preparation

From the initial microarray data, genes were chosen based on their upregulation after treatment with tdMNP-PEI and their function with relation to cell adhesion. The gene was searched in the NCBI database and the NCBI accession number or locus is used to perform searches on BLAST-primer selection. The primer size was between 100 – 400 bases. The melting temperatures chosen was between 50 – 60 °C with a difference of 3 °C between the forward and reverse primers. From the list of available primers from the BLAST results, a primer which sits between two exons with a PCR product length of ∼250 bases was chosen. The forward and reverse primer sequences were ordered on the Thermo Fisher website. The housekeeping gene used was GAPDH.

The primers arrived in desiccated form. To resuspend them, PCR grade water (QIAGEN) was used. The primers were suspended into a concentration of 100 nM. The working solution was prepared by diluting 10 μL of primer stock solution with 90 μL of PCR grade water. The suspensions were stored at $-80\,^{\circ}\mathrm{C}$.

Quantitative real-time polymerase chain reaction (qPCR)

Quantitative polymerase chain reaction or real-time PCR measures the exponential amplification of DNA with each amplification cycle. The quantification is measured by the fluorescence, where a fluorescence signal is generated when a PCR product is generated. The measurements can determine the amount of starting material of the sample.

qPCR was performed using a one-step reaction, without the synthesis of cDNA using the Quantifast SYBR Green RT-PCR Kit (Qiagen). Preparation of qPCR reactions were done on ice. The Master Mix was prepared by adding 6.25 μL SYBR Green, 1.25 μL forward and 1.25 μL reverse primers, and 0.125 μL enzyme per reaction tube. 3.5 μL of 100 mM RNA sample was pipetted into PCR tubes, and 8.8 μL Master Mix was added per tube. The tubes were spun down and placed on the qPCR system Agilent Stratagene MX3000P. Amplification and melting curve procedure was set to 50 °C for 10 minutes, 95 °C for 5 minutes, 95 °C for 10 seconds and 60 °C 30 seconds (40 cycles), 95 °C for 1 minute, 60 °C for 30 seconds and 95 °C for 30 seconds.

The dissociation curve or melting curve of qPCR is to determine if a primer produces one PCR product, to ensure gene specificity and absence of primer dimers. The dissociation of a dsDNA (double stranded DNA) is dependent on length, GC content, and presence of base mismatches. Therefore more than one dissociation peak indicates the primer is non-specific to the gene of interest or forms primer-dimers, and therefore the data and primer is disregarded. In the qPCR study, primers producing one dissociation peak is chosen for subsequent analysis.

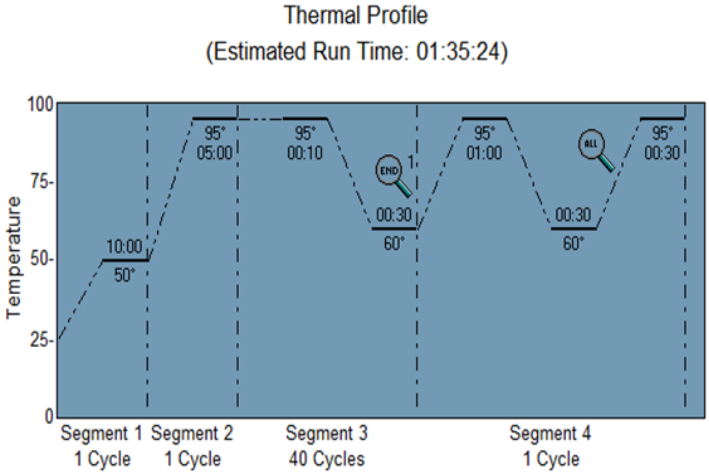

Figure 6.3 Thermal profile of qPCR procedure.

Determination of ΔΔ Ct values

The ΔΔ Ct (Cycles to Threshold) method was used to analyse qPCR data for statistical analysis and gene expression fold change. The housekeeping gene used was GAPDH. To calculate ΔΔ cT, the following equations were used:
Δ Ct = Ct gene of interest – Ct of housekeeping gene
ΔΔ Ct = Δ Ct of treatment gene – Δ Ct of control gene
Gene expression fold change was obtained by the log base 2 of ΔΔ Ct ($2^{-\Delta\Delta\ Ct}$).
Statistical significance was calculated by first performing an F test to determine equal or unequal variance. Based on the F tests, the appropriate t-tests were performed on Δ Ct values.

DNA polyacrylamide gel electrophoresis

Agarose gel was prepared by dissolving 20 g agarose (Fisher Scientific) in 150 mL 1x TAE buffer in the microwave for 3 minutes. 5 μL ethidium bromide was added and the liquid gel was poured into a mould and combs inserted. Once the gel had dried, the qPCR product was mixed with loading buffer and the sample was loaded into the wells, along with a 1 Kbp ladder. The gel was run at 100 A for 45 minutes and observed in a UV chamber and images of the bands were taken.

6.2.6 Statistical analysis

A 2-way ANOVA statistical analysis was performed for ferrozine assay data, fluorescence quantification data, and PicoGreen data. A t-test was performed on the Δ Ct values for gene expression to determine statistical significance.

6.3 Results

6.3.1 Effect of tdMNP-PEI dosage on cell adhesion

Trypsin is a proteolytic enzyme which breaks down proteins to detach adherent cells from tissue culture plastic. Brightfield images of HeLa cells are depicted before and after treatment with trypsin, treated without and with tdMNP-PEI for 30 minutes and the particles were washed off subsequently (Figure 6.4). HeLa cells grown in T75 flasks were treated with tdMNP-PEI at 20, 50, and 100 μL per flask at a concentration of 5.75 $\mu g/\mu L$ for 30 minutes. The cells were then treated with trypsin 24 hours later for 5 minutes and brightfield images of cells were obtained.

Figure 6.4 A (left column) shows that cells were confluent, with a typical spread morphology before trypsin treatment, and completely detached after trypsin treatment (Figure 6.4 A, right

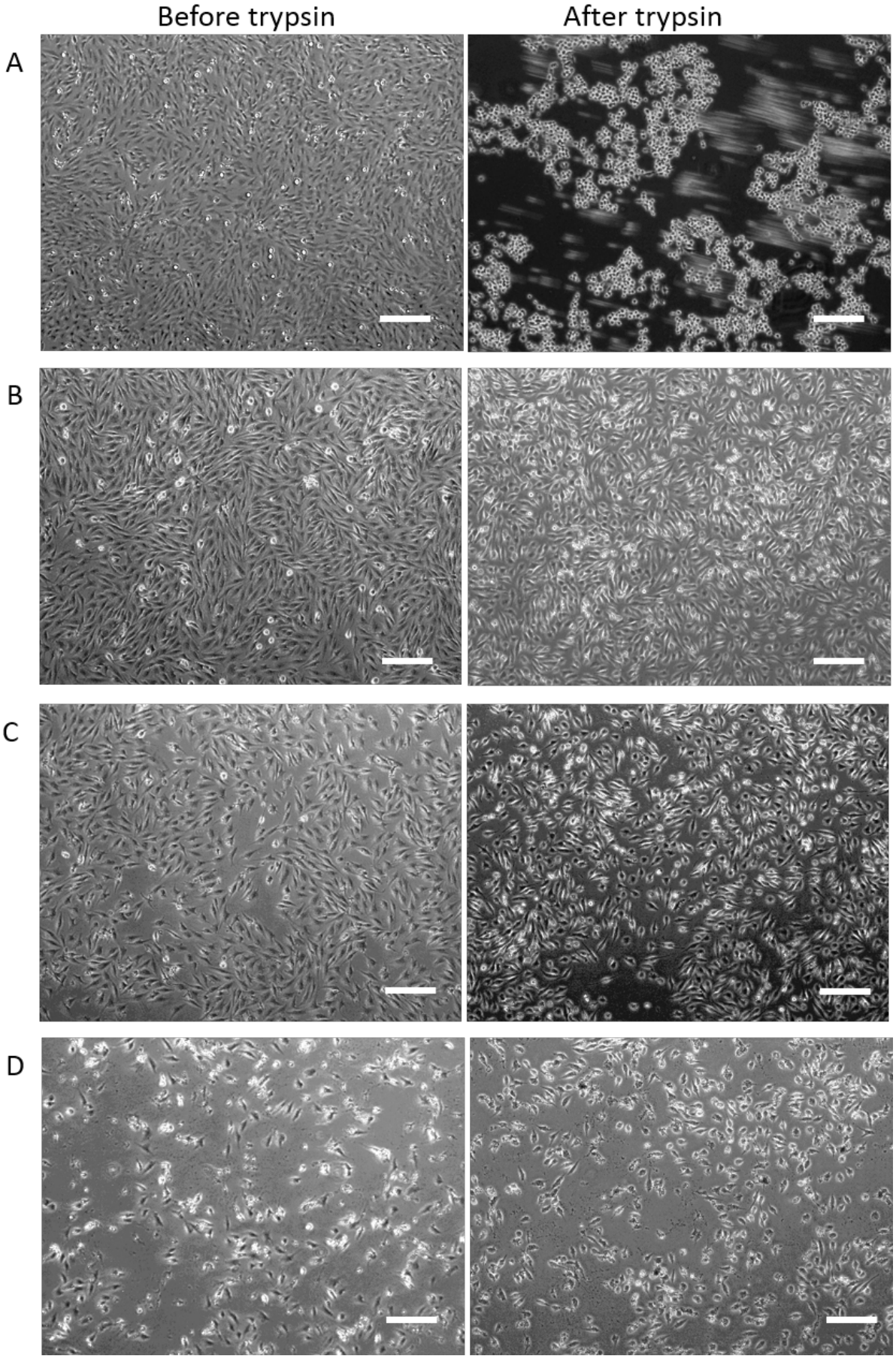

Figure 6.4 Brightfield images of MG-63 cells with tdMNP-PEI in T75 flasks before and after treatment with trypsin for cell detachment. Treatment groups are (A) control cells without tdMNP-PEI, (B) cells with 20 μL tdMNP-PEI, (C) cells with 50 μL tdMNP-PEI, (D) cells with 100 μL tdMNP-PEI. Cells were completely detached in the control group but not in the flasks containing tdMNP-PEI, scale bar=500 μm; scale bar 50 μm, n=1.

column) which can be observed from the spherical morphology of cells floating in the culture media. By contrast, whilst cells treated with 20 μL tdMNP-PEI were also confluent and had a typical spread morphology, they did not show detachment after trypsin, retaining a spread morphology. At 50 μL tdMNP-PEI, cells were less confluent but also showed little to no detachment following treatment with trypsin. In the 100 μL MNP-PEI group, the cells were visibly stressed based on their rounded and uneven shaped morphology, and had low confluency. Similar to the 20 μL and 50 μL tdMNP-PEI groups, treatment with trypsin had little effect on cell detachment in the 100 μL group.

At a lower dosage of tdMNP-PEI, cells maintained a typical spread morphology but with increasing tdMNP-PEI dosage, cells did not proliferate and had a more rounded morphology when compared with untreated controls (Figure 6.4 D). Despite signs of cell stress with the addition of 100 μL tdMNP-PEI, the adherence of cells onto the cell culture flask was noticeable compared to untreated controls. The high dose resulted in a loss of cells possibly due to PEI toxicity but the cells that survived adhered strongly to the flask.

Different doses of tdMNP-PEI in MG-63 cells were studied for their internalization in 24-well plates using Prussian blue assay to stain iron blue. Figure 6.5 shows control cells having high confluency and no visible blue stain, suggesting no iron content in cells. At 0.2 μL tdMNP-PEI per well (Figure 6.5 A ii), cells were less confluent than the control group (Figure 6.5 A i) and showed little to no blue staining in the cell cytoplasm signifying very little iron uptake. At 0.6 μL and 1.0 μL tdMNP-PEI in cells, strong positive staining was found in the cytoplasm of cells, with the latter showing higher blue intensity and more clustering of particles in the perinuclear region. The ferrozine assay (Figure 6.5 B) shows a significant increase (p=0.0013) in particle uptake of cells for each concentration of tdMNP-PEI seeded in wells with the lowest mass of iron at 0.065 μg, followed by 0.18 μL and 0.3 μL per 24-well respective to the increasing dosage. tdMNP-PEI 1.0 μL also shows a significant difference between the amount of particles added into wells and particles taken up by cells.

The mass of tdMNP-PEI taken up by cells appeared to be dose dependent. At low concentrations of tdMNP-PEI, particles were not visible in cells using Prussian blue staining. The ferrozine assay, however, shows that cells contained a small amount of iron by the end of the experiment at 24 hours, which when quantified was comparable to the mass of iron initially seeded. This suggests the uptake efficiency was higher at low concentrations of tdMNP-PEI. At higher concentrations of tdMNP-PEI (0.6 μL), the particles were discernible as fine blue particulate distributed within the cytoplasm. At the highest dose (1 μL tdMNP-PEI), the particles were visible as large aggregates, indicated by granular regions in cells which clustered around the perinuclear region. Two-way ANOVA shows that the uptake of particles increased significantly (p=0.0028) with each tdMNP-PEI dosage. As expected, the amount of tdMNP-PEI taken up by cells was relative to the initial concentration of tdMNP-PEI that was seeded in wells. This effect however was finite at concentration of tdMNP-PEI 1.0 μL due to a significant difference between the particles seeded in cells and the mass of iron taken up by cells (p=0.0004). Based on these observations it is likely that at this concentration and an incubation time of 30 minutes, the amount of particles that can be taken up by cells may be close to saturation.

Based on the cell seeding density per well in the 24 well plate (70 000 cells/well) and the doubling time of MG-63 of 48 h (Mohseny et al., 2011), the mass of iron taken up by cells was determined to be approximately 2.9 pg/cell for the 1.0 μL tdMNP-PEI group (Figure 5.2 B). This value falls between the range of iron uptake in HeLa cells studied in Chapter 4, Table 4.4. Previous studies reported variable amounts of iron uptake from 55 to 140 pg Fe/cell for different MNP types (Soenen et al., 2010). The huge difference in iron uptake in this study compared to previous findings can be attributed to the concentration of MNP seeded into the cell monolayer and the time of incubation with MNP. At 30 minutes of incubation time and with a small concentration of MNP in HeLa cells, the cells were able to take up most of the particles, which suggests that with a longer incubation time and a higher concentration of MNP-PEI, cells would be able to increase uptake, but at the cost of cell health.

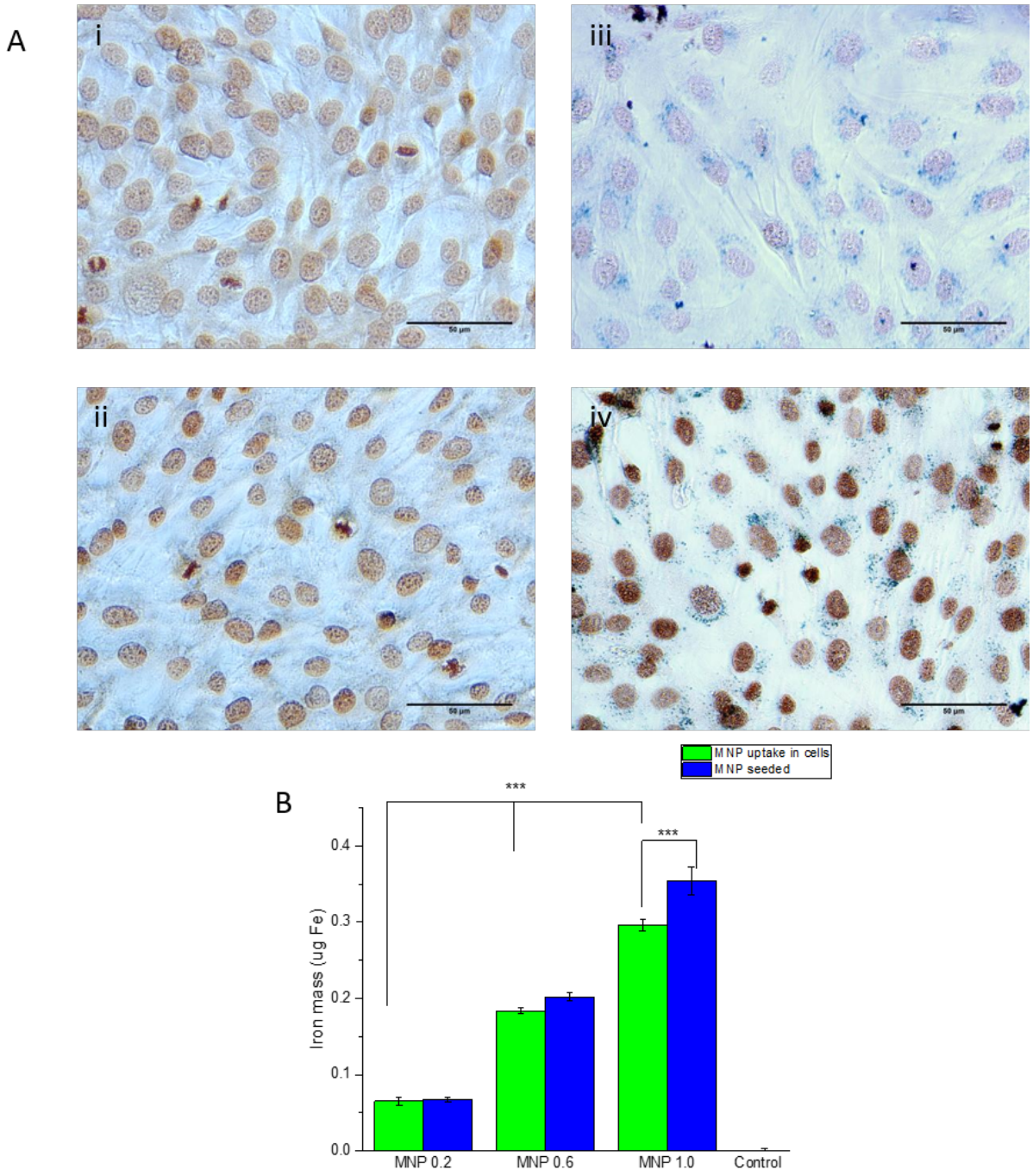

Figure 6.5 (A) Brightfield images of MG-63 cells with MNP-PEI treated with Prussian blue for visualization of iron uptake in cells (blue) and counterstained with nuclear fast red. (i) Control, (ii) 0.2 μL MNP-PEI, (iii) 0.6 μL tdMNP-PEI, (iv) 1.0 μL tdMNP-PEI, scale bar=50 μm. (B) Quantification of uptake of tdMNP-PEI in cells by mass of iron per well in a 24 well plate using ferrozine assay. tdMNP uptake is significantly different in each treatment; n=3.

6.3.2 Effect of tdMNP-PEI dosage on vinculin and actin stress fibre formation

The effect of tdMNP-PEI on cell adhesion was assessed using immunostaining for vinculin, an adhesion protein shown to be a component in the formation of focal adhesions in cells (DePasquale and Izzard, 1987; Humphries et al., 2007). Additionally, phalloidin based F-actin staining was employed to assess actin stress fibre formation. Cells treated with different concentrations of tdMNP-PEI were labelled for the two biomolecules, imaged using confocal microscopy and processed using ImageJ (described in Section 6.2.2). Vinculin fluorescence intensity was quantified as described in Materials and Methods (Figure 6.6 A). Control cells show predominantly low vinculin intensity in the cytoplasm (indicated by blue regions), with a high intensity (indicated by yellow regions) present at nuclear regions. Cells with 0.2 μL tdMNP-PEI had a similar staining profile to control cells. Increasing tdMNP-PEI dose (0.6 μL and 1.0 μL) significantly increased vinculin fluorescence intensity compared to control cells ($p=6.4e^{-7}$) and vinculin was localised predominantly around the nucleus and in the cytoplasm. Fluorescence imaging of F-actin (Figure 6.6 A, right column) showed a comparable difference between the control and 0.2 μL groups (Figure 6.6 A i and ii) with the 0.6 μL and 1.0 μL groups (Figure 6.6 A iii and iv), where initially there was randomly ordered actin cytoskeleton, preceding a reorganization of the actin cytoskeleton to form parallel stress fibres. Dendritic protrusions of F-actin from the cell membrane was observed in tdMNP-PEI groups.

The fluorescence intensity of vinculin in cells was quantified and compared between the cytoplasm area and nucleus area to determine whether vinculin formation during cell stress occurs randomly within the cell or is localized at the centre or periphery of the cell. Overall, the expression of vinculin was higher in the nuclear region of cells compared to the cytoplasm in all groups (Figure 6.6 B). A significant increase in vinculin expression was observed in the cytoplasm with higher dosage of tdMNP-PEI in cells (0.6 μL and 1.0 μL) ($p<0.001$) compared to the control and 0.2 μL tdMNP-PEI groups, however vinculin expression in the nuclear region remained relatively unchanged until treated with 1.0 μL tdMNP-PEI ($p<0.005$).

The difference in vinculin expression between the cytoplasm and nucleus per treatment group was only significant in the control and 0.2 μL groups ($p<0.005$), whereby at higher tdMNP-PEI dosage (0.6 and 1.0 μL), the intensity of vinculin expression increased in the nucleus comparable to cytoplasmic intensity. Overall, treatment of tdMNP-PEI 1.0 μL showed the highest expression of vinculin, followed by 0.6 μL tdMNP-PEI. Analysis via two-way ANOVA showed that the population means for each variable was significantly different (tdMNP-PEI dosage, $p=5e^{-15}$; cytoplasm to nucleus intensity, $p=2.6e^{-8}$), but the tdMNP-PEI dosage in cells is not significant to the localization of vinculin expression. The increase in vinculin intensity surrounding the nucleus may be due to a specific set of stress fibres – the perinuclear actin cap. These stress fibres attached to focal adhesions form around the nuclear region (Figure 6.1) and function to maintain the shape and position of the nucleus in the cell, as well as transmit forces from the ECM to the nucleus (Khatau et al., 2009; Tojkander et al., 2012).

A live/dead assay was performed on MG-63 cells to qualitatively assess the cytotoxicity of tdMNP-PEI on cells (Fig. 6.7). From TGA results in Chapter 3, PEI coating comprises 60% of the tdMNP-PEI mass. Therefore, 0.2 μL of tdMNP-PEI = 0.7 μg PEI, 0.6 μL tdMNP-PEI = 2.1 μg PEI, and 1.0 μL tdMNP-PEI =3.45 μg PEI. The PEI treatment group in Figure 5.4 E is 1.0 μg PEI, which has slightly higher PEI than the 0.2 μL tdMNP-PEI treatment group.

Figure 6.7 showed a higher rate of cell death in all treated groups compared to the untreated control (Figure 6.7 A). Even at low concentrations of tdMNP-PEI, cells were observed to have higher cell death than untreated controls. PEI treated cells (1.0 μg) (Figure E) show more cell death than cells with tdMNP-PEI (Figure B – D). Brightfield imaging (third column) showed cells with 0.6 μL and 1.0 μL tdMNP-PEI were also more granular (Figure C&D) than

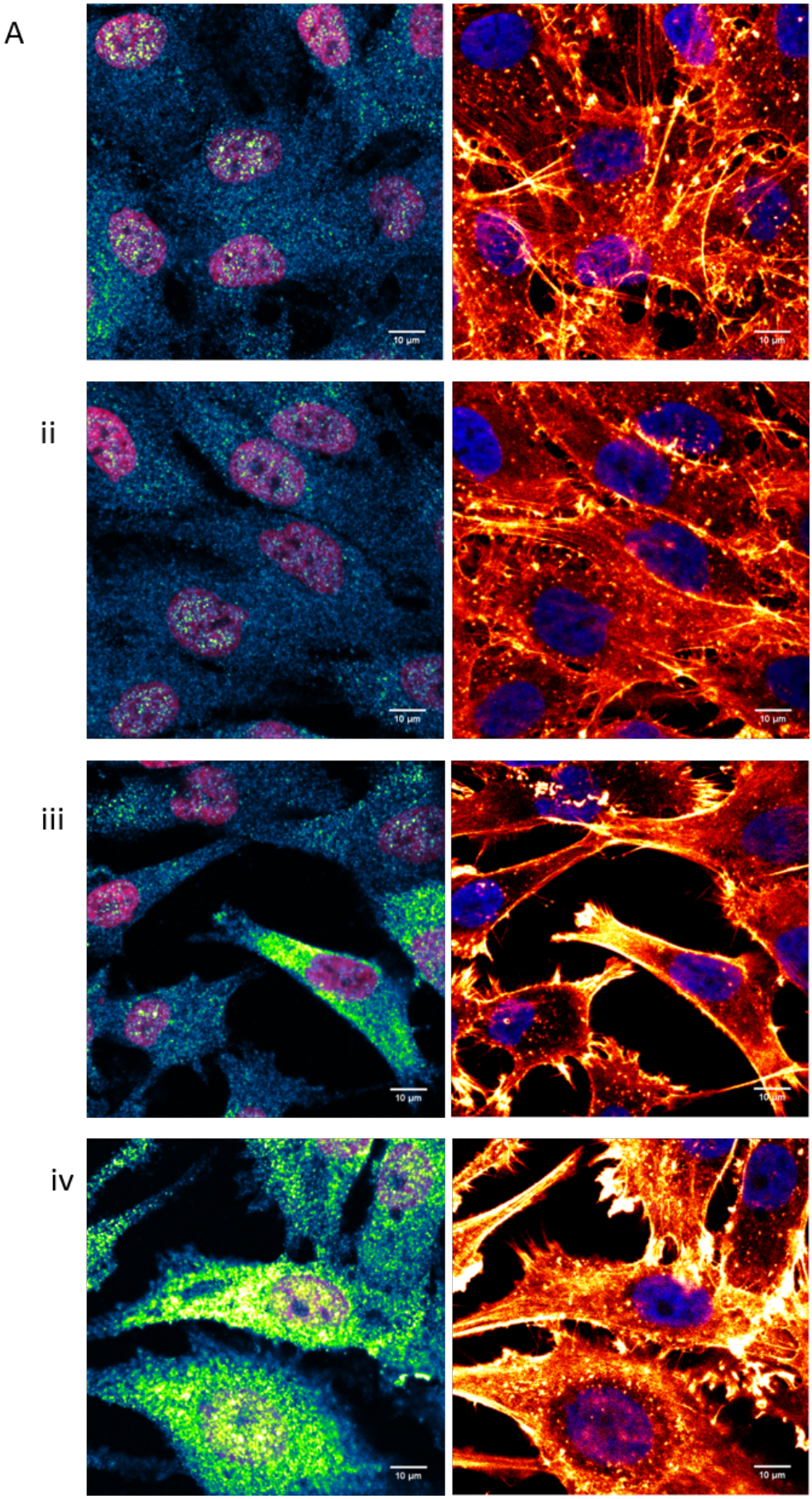
A
ii
iii
iv
10 µm

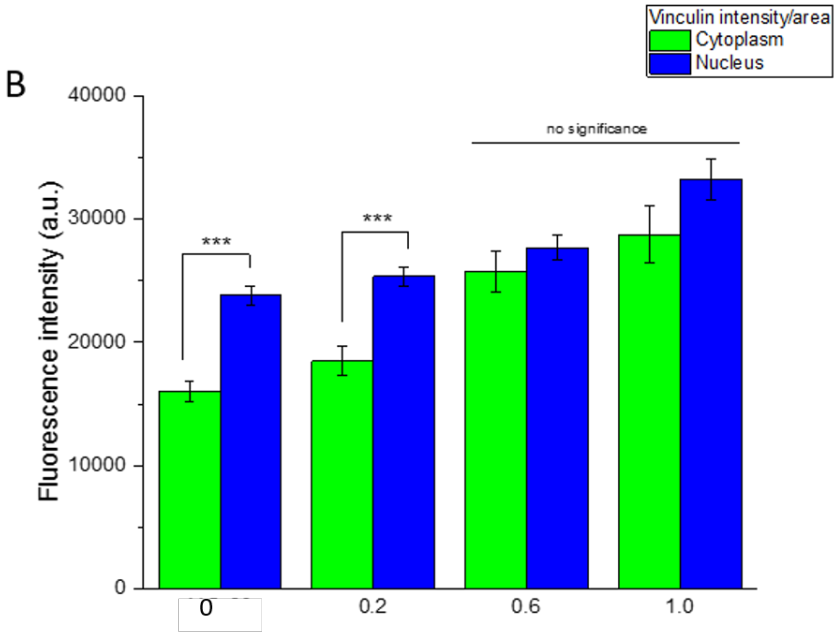

Figure 6.6 (A) Fluorescence images of nucleus (purple), vinculin in blue-green (left), and F-actin in red (right) processed with intensity filters in ImageJ processing software. Treatments are MG-63 (i) control, (ii) with 0.2 μL tdMNP-PEI, (iii) with 0.6 μL tdMNP-PEI and (iv) with 1.0 μL tdMNP-PEI, scale bar=10 μm. The change from blue to green to yellow indicates increasing vinculin intensity. (B) Quantification of vinculin intensity per area in the nucleus and cytoplasm in 25 – 40 cells with significantly increased vinculin expression at high tdMNP-PEI doses (0.6 μL and 1.0 μL); n=25–40 cells, two-way ANOVA.

the other groups, suggesting the formation of endocytic vesicles taking up material from the media.

6.3.3 Magnetic transfection vector components that induce adhesion

A simple determination of cell adhesion is the PicoGreen assay to quantify the cells remaining in wells after cells treated with tdMNP-PEI, PEI, and tdMNP were treated with trypsin to detach cells from the ECM and wash them away. The amount of DNA quantified represents the amount of cells remaining in the cell culture plate after treatment with trypsin. Therefore, higher PicoGreen fluorescence intensity indicates stronger cell adhesion.

Figure 6.8 A i and ii compares between the adhesion intensity of HeLa and MG-63 cells when detached with 1x trypsin concentration after 24 hours treatment with tdMNP-PEI. Both cell types showed the same effect when treated with tdMNP-PEI where cells treated with 2, 1, and 0.5 μL tdMNP-PEI were not significantly different from total cells (not trypsinized), whereas doses of 0.25, 0.125, and 0 tdMNP-PEI μL per well had higher detachment of cells after trypsinization (HeLa cells $p \leq 0.006$, MG-63 cells $p \leq 1.3e^{-6}$). The dosage of tdMNP-PEI on cell adhesion was the same in both cell types, however HeLa cells exhibited lower cell adhesion compared to MG-63 indicated by the lower fluorescence intensity in HeLa cell groups.

To test the effects of the two components in the tdMNP-PEI complex, the effect of each individual component on cell adhesion was studied. MG-63 cells were treated with MNP only without PEI coating and stimulated for 30 minutes on the magnefect nano. Figure 6.8 Bi shows cells treated with trypsin immediately after oscillation on the magnefect-nano and Fig. B ii was after 24 hours of tdMNP-PEI incubation. With the 30-minute incubation time group, changes in cell adhesion was small compared with untreated control cells, however tdMNPs 30 μL and 15 μL showed significant differences to the other treatment groups ($p \leq 0.04$). When tdMNPs were incubated with the cells for 24 hours (Figure 6.8 B ii), there was a significant increase in cell adhesion for the 3 treatment groups with the highest seeded tdMNPs ($p \leq 7.6e^{-4}$).

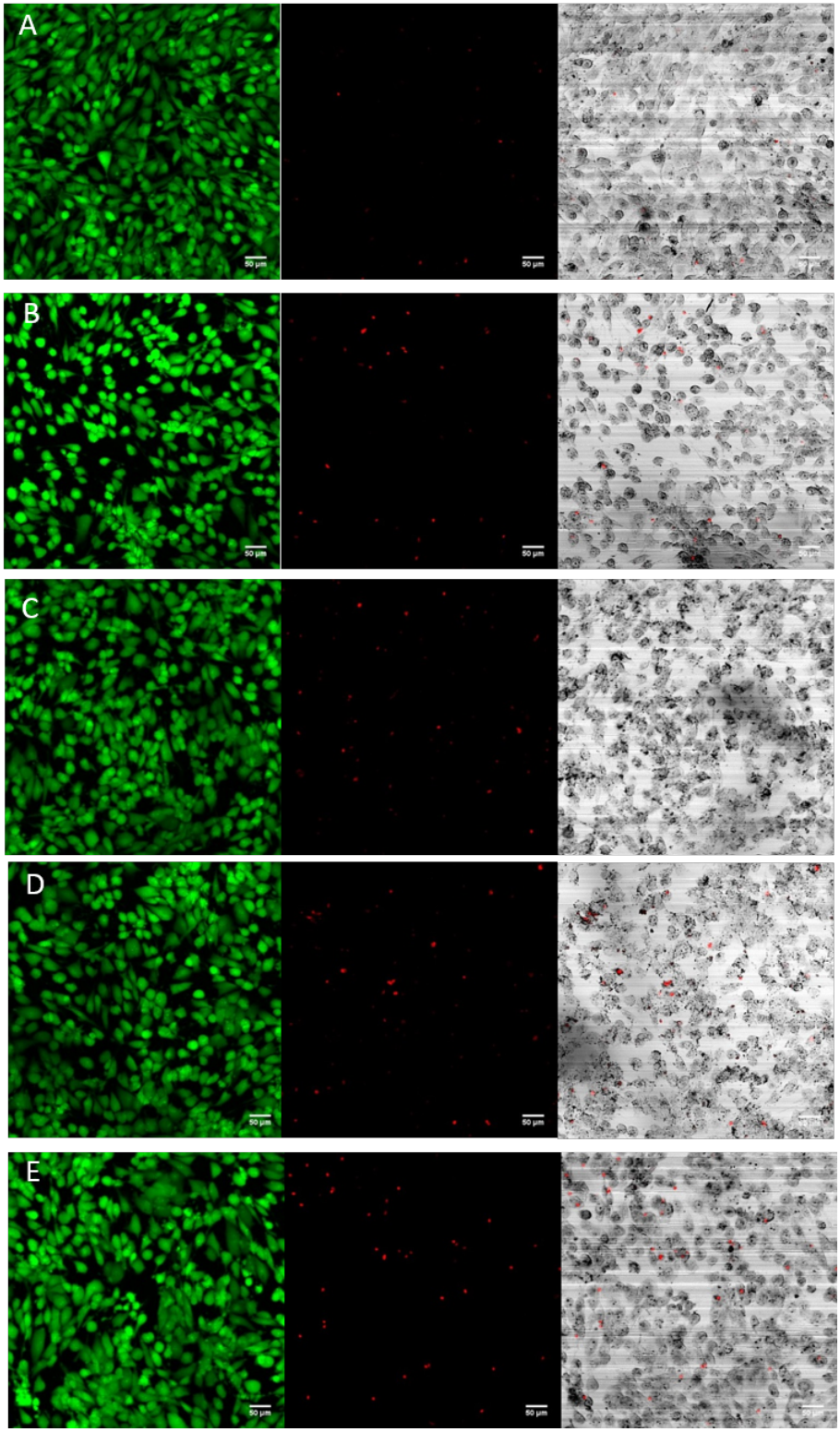

Figure 6.7 Live/dead assay for cell viability of MG-63 cells treated with (A) control, (B) 0.2 μL tdMNP PEI, (C) 0.6 μL MNP PEI, (D) 1.0 μL tdMNP PEI, (E) 1.0 μg PEI. Live cells stained in green (first column), dead cells stained red (second column), and overlay of dead cells and brightfield image (third column), scale bar= 50 μm; n=3.

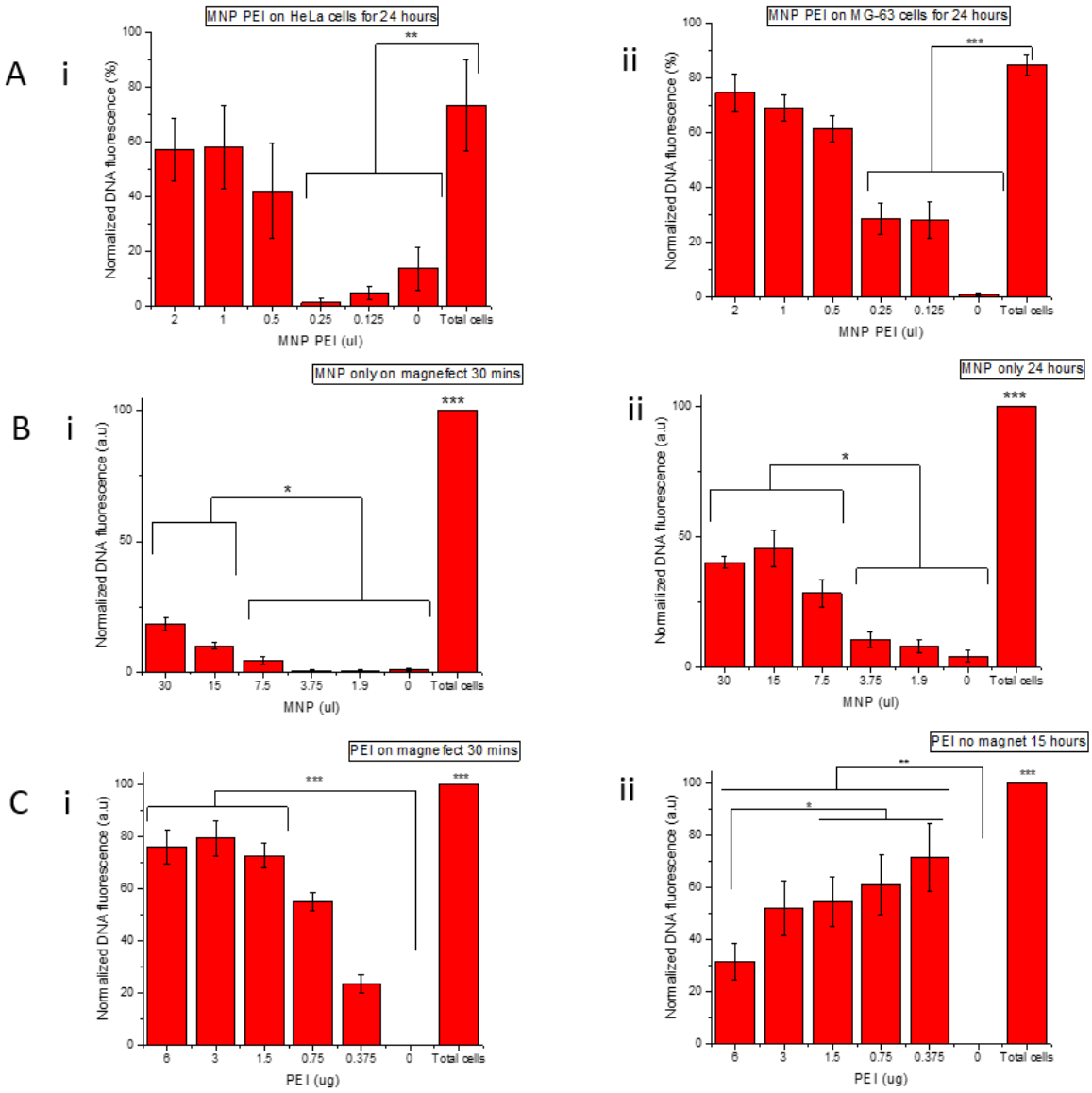

Figure 6.8 Pico green assay to determine relative cell numbers adhered in wells after trypsin treatment of cells loaded with different concentrations of tdMNP-PEI, tdMNP or PEI. (A) Cells seeded with tdMNP-PEI for 30 minutes on magnefect nano and 24 hours without magnet (i) HeLa cells (ii) MG-63 (B) MG-63 cells with MNP only (i) 30 minutes on the magnefect nano (ii) 30 minutes on magnefect nano and 24 hours without magnet. (C) MG-63 cells with PEI (i) 30 minutes on the magnefect nano (ii) 24 hours without magnet; n=3.

Figure 6.8 C shows cells treated with PEI polymer on the magnefect nano for 30 minutes and immediate PicoGreen assay (Fig. 6.8 C i or 30 minutes on the magnefect nano and 15 hours incubation prior to the assay (Fig. 6.8 C ii. MG-63 cells were treated with 6 PEI doses from 0 μg to 6 μg. The effect of PEI after 30 minutes treatment in cells was significant on cell adhesion for PEI doses 6 μg, 3 μg and 1.5 μg ($p \leq 9.5e^{-7}$). Interestingly, cells treated with PEI for 15 hours had an opposite effect on cell adhesion whereby the highest PEI loading of 6 μg had significantly lower amounts of DNA compared with PEI 1.5, 0.75, and 0.375 μg ($p \leq 0.034$) (Figure 6.8 C ii). This observation, along with the lower DNA content in the 15-hour treatment compared to 30 minutes for all PEI groups indicate a cytotoxic effect of PEI at high dosage and long incubation time. Low dosage of PEI (0.75 and 0.375 μg) incubated in the cell culture for 15 hours had a stronger effect on cell adhesion contrary to the 30 minute treatment where changes in cell adhesion were minimal.

The effect of the individual components of tdMNP-PEI on increased cell adhesion was clearly observed in this study. While cells displayed increased adhesion with a minimum of 0.5 μL tdMNP-PEI treatment, the same effect was not observed when cells were treated with tdMNPs only at the same concentration. At 2 μL tdMNP-PEI, cells exhibited strong adhesion, but tdMNPs alone did not elicit this effect in cells even at >2 μL tdMNPs (0.35 μg Fe/μL). Cells treated with PEI, however, showed the opposite effect, where low concentrations of PEI were able to cause a strong cell adhesion response in a short time. To compare both treatment types, 0.5 μL tdMNP-PEI ($\sim$2 μg PEI) induced cell adhesion after 24 hours, however after 15 hours incubation time, only 0.375 μL PEI was sufficient to increase cell adhesion. Therefore, the key factor of tdMNP-PEI induced cell adhesion is PEI.

6.3.4 Genes involved in tdMNP-PEI induced cell adhesion

To further elucidate the effect of tdMNP-PEI on cell adhesion, gene expression analysis by qPCR was performed on cells treated with a low (1.5 μL) and high (3.0 μL) dose of tdMNP-PEI in 6 well plates. Seventeen genes (22 primers in total) were selected from an initial microarray test performed on the treatment groups. From the microarray results, upregulated genes were identified and correlated with genes associated with the cell adhesion pathway and actin fibre remodelling.

The reported known functions of the genes analysed by qPCR in Figure 6.9 are described in Table 6.1, of which the information was found in genome databases such as NCBI and UniProt (Leary et al., 2016; The UniProt Consortium, 2017).

qPCR data of the gene expressions (Figure 6.9 A i and ii) show significant upregulation in a number of genes in groups treated with tdMNP-PEI and which primers only have a one peak dissociation curve of the qPCR products (described in Section 6.2.5). Out of the 17 genes, 8 were significantly upregulated compared to untreated controls ($p<0.05$), however particle dosage (low and high) did not have a significant difference in gene upregulation. Compared to the untreated controls, ACTA2 expression was upregulated 4-fold while ACTN1 shows a 2.5-fold upregulation. MVCL and VCL expression showed a 2.2 – 2.6 and $\sim$3 fold change respectively versus untreated controls, however low dose MVCL did not have a significant increase in gene upregulation relative to untreated controls. From Figure 6.9 A ii, P4HA2 had the highest fold change in gene expression, with a 4.6-fold increase at high dose MNP-PEI of 0.6 μL. Genes PCDHB12, TGFBI, and SVIL-high dose had significant increase in gene regulation except for SVIL-low dose which was upregulated to an almost 3-fold change but was not statistically significant ($p=0.067$).

To determine the specificity of the primers used for qPCR a melt curve was obtained from the qPCR instrument. The qPCR products were then run on agarose gel electrophoresis. GAPDH was used as a housekeeping gene. A primer that binds and amplifies a specific product has only a single peak in the melt curve, as well as a single band in the agarose gel electrophoresis. Double DNA bands indicate non-specific binding of primer and amplification of sample. Based on Figure 6.9 B i and ii, all the products of qPCR reactions showed a single band except for

Table 6.1 Genes selected for qPCR assay and their functions in cell adhesion and the cytoskeleton.

Genes	Gene Name	Function
ACTA2	Alpha actin 2	Alpha actin is mainly found in skeletal muscle and is involved in motility, structure and cellular integrity
ACTN1	Alpha actinin 1	Codes for an actin-binding protein that crosslinks F-actin to cellular structures. Actin-binding, crosslinking and organiation, vinculin binding, focal adhesion assembly (Leary et al., 2016; The UniProt Consortium, 2017)
MVCL	Metavinculin	A splice-variant isoform of vinculin performing the same function (Thompson et al., 2013)
VCL	Vinculin	Involved in cell-cell adhesion and cell-matrix adhesion by binding to F-actin (The UniProt Consortium, 2017). Acts as a linker that connects focal adhesion molecules (integrins) to the cytoskeleton (Thompson et al., 2013; Zemljic-Harpf et al., 2009)
P4HA2	Prolyl hydroxylase subunit alpha 2	An enzyme component that is involved in collagen synthesis (Leary et al., 2016)
PCDHB12	Protocadherin beta 12	Protocadherins are a member of the cadherins superfamily and function in cell adhesion (Leary et al., 2016)
SVIL	Supervillin	Involved in linking actin filaments to the plasma membrane and diassembly of focal adhesions (The UniProt Consortium, 2017; Leary et al., 2016)
TGFBI	Transforming growth factor beta induced	Encodes and RGD motif that binds collagen and is involved in cell adhesion (Leary et al., 2016)

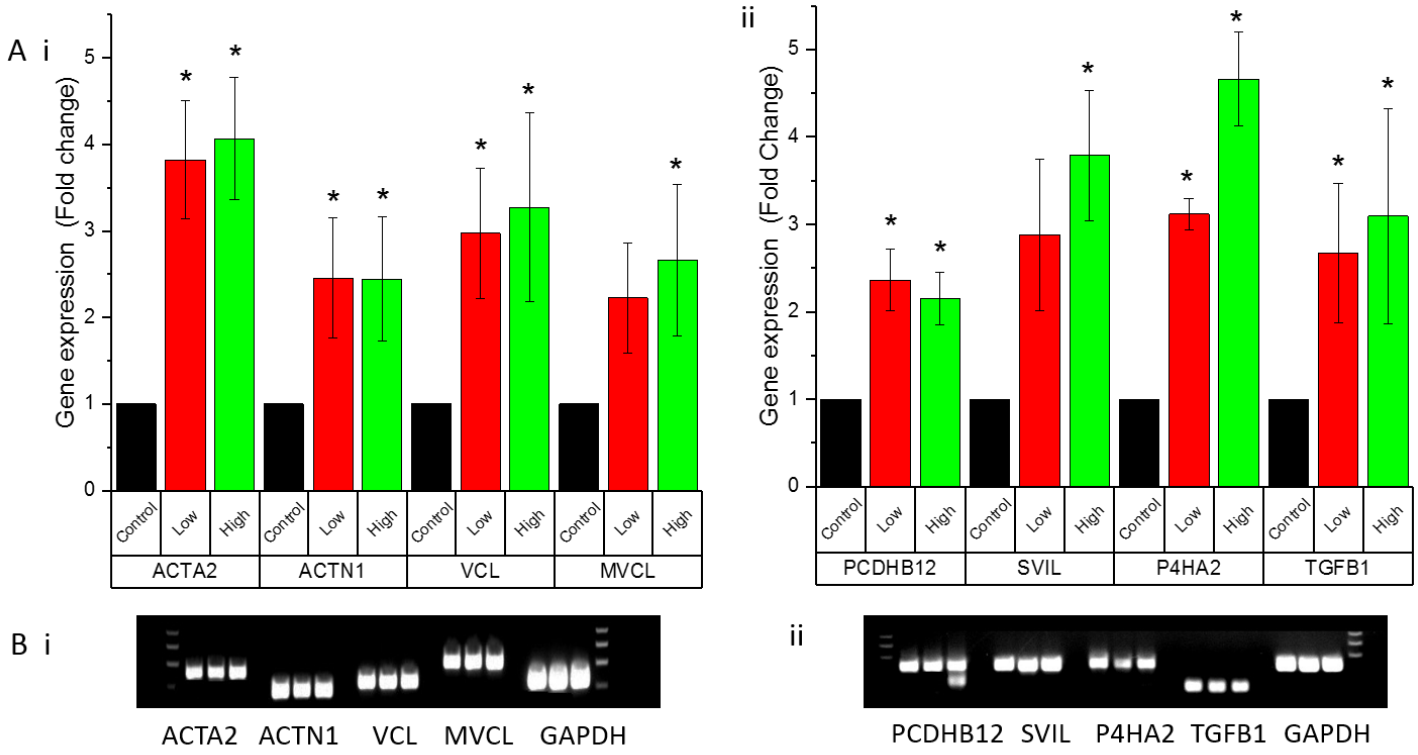

Figure 6.9 qPCR of genes involved in cell adhesion and the cytoskeleton showing the effect of MNP-PEI in cells. Treatment of MNP-PEI in low dose (1.5 μL) (green) and high dose (3.0 μL) (red) is compared to control (black) and expressed in fold changes. F tests and student's t-tests were performed using ΔCt values, n=3–4, $p<0.05$. (A) (i) Genes ACTA2, ACTN1, MVCL and VCL and (ii) P4HA2, PCDHB12, SVIL and TGFB1. (B) Gel electrophoresis of qPCR products indicating the purity of qPCR products with each band group showing control (left), low MNP-PEI (middle), and high MNP-PEI (right); n=3–4.

gene PCDHB12 high dose, which shows 2 bands.

6.4 Discussion

The present study investigates the underlying implications for cell processes resulting from the internalization of MNP-PEI with regard to cell adhesion and stress fibre formation.

The mechanism with which cells increase their attachment onto a matrix is by the formation of focal adhesions. Focal adhesions are the site where the cell is connected to the external microenvironment, where it acts as a link between the ECM and the cell cytoskeleton. Cells are connected to the ECM through the anchoring of integrins and adhesion-associated proteins such as vinculin and talin to actin fibres. Besides focal adhesion localization, vinculin are also present in adherens junctions to mediate cell-cell adhesions. A major function of vinculin is to bind and bundle F-actin for the transduction of external stimuli (Thompson et al., 2013).

In this study, a positive correlation was observed between the increase in vinculin expression and intensity of actin stress fibres. Soenen et al. presented findings that the effect of iron oxide MNP on vinculin and the cytoskeleton was dose dependent, and this effect was influenced by the interaction of the surface coating on iron oxide MNPs with the cell and consequently determines its uptake efficiency into cells (Soenen et al., 2011). This finding was in line with observations in the present study using PEI surface coating and iron oxide MNP core, where the increase in vinculin expression and cytoskeleton stiffening was related to the uptake concentration of MNP-PEI in cells.

Adherent cells, unlike cells in suspension, need to attach to a surface before it regains normal function and remain viable (Discher, 2005). The actin cytoskeleton functions in various cell processes such as cell spreading, migration, morphogenesis, cell division, and endocytosis (Ridley and Hall, 1992; Tojkander et al., 2012). The uptake of material from the extracellular environment into the cell requires plasma membrane deformation and invagination to form endocytic vesicles (Lamaze et al., 1997). Therefore, one possible reason for the increased F-actin tensioning and increase in ACTA gene expression is to facilitate capture of MNP-PEI by endocytosis, hence causing the formation of actin bundles with increasing MNP-PEI dosage.

The cytoskeleton is also involved in cell anchorage to the ECM by forming stress fibres with the help of focal adhesions. Stress fibres form by the polymerization of 10 to 30 actin fibres and myosin-II filaments by alpha-actinin (ACTN), which ACTN gene was found to be upregulated with MNP-PEI treatment in this study. Adhesion typically starts with formation of new focal adhesions at the ECM, concurrently the bundling of actin fibers into larger stress fibres. The ends of these stress fibres associate with focal adhesions at the plasma membrane (Ridley and Hall, 1992).

Cells react to different stimuli to increase adherence such as substrate stiffness, mechanotransduction or chemical stimuli. Cell adhesion is affected by the stiffness of the substrate, where stiffer substrates like glass induce stronger and less dynamic adhesion (Discher, 2005). Similarly, mechanotransduction is relatively well known for its effect on cell behaviour, and have been used to study potential regenerative medicine therapies. Mechanotransduction is the conversion of mechanical force on a cell into chemical signals, affecting various cell functions such as growth, differentiation and apoptosis.

Cell proliferation was observed to be affected by the presence of MNP-PEI. Micrographs of cells treated with MNP-PEI show lower cell density and increased cell size compared to the control groups (Figure 6.4, Figure 6.5 and Figure 6.6). This effect is evidence that MNP-PEI internalization interferes with actin-mediated regulatory processes as the actin cytoskeleton is involved in cell signalling and processes such as proliferation, migration and differentiation (Soenen et al., 2010). This effect has been noted in previous studies with different cell lines, where

iron oxide MNP and polystyrene particles reduce proliferation (Fröhlich et al., 2009; Hohnholt et al., 2011) by interfering with cell metabolism and signalling (Oliveira et al., 2016).

Cytotoxicity studies have shown that MNP induce the production of ROS causing oxidative stress to cells. Effects of oxidative stress are concentration dependent, from mitogenesis to cell cycle arrest and reduced proliferation, apoptosis, and even necrosis at high ROS concentrations (Davies, 1999). Uncoated magnetic iron oxide nanoparticles have been studied to induce ROS production (Wang et al., 2014), as well as uncoated silver NP, silica NP, titanium oxide NP, and zinc oxide NP (McCracken et al., 2015). The detection of ROS in cells due to NPs have been shown to inhibit or reduce cell proliferation. The excessive production of ROS by iron oxide MNPs also altered cell mechanics by an increase in actin stress fibres and changed cell morphology by cell elongation (Buyukhatipoglu and Clyne, 2010).

PEI has also been reported to induce oxidative stress in cells compared to chitosan and anionic polymers (Lojk et al., 2017; Regnström et al., 2006), however when complexed with another copolymer the production of ROS reduced (Lee et al., 2013). Besides a chemical reaction of cells from the transfection agent, a mechanical effect cannot be ruled out as the effect of an oscillating external magnet on MNP in cells creates a downward force and lateral movement on the cell surface. Zheng et.al demonstrated a negative effect of a mechanical force on the proliferation and migration of cells (Zheng et al., 2016). Cells also exhibit a larger surface area when treated with high concentrations of MNP-PEI.

One possibility for this phenomenon is the extension of the cells pseudopodia to explore suitable areas to move to, away from the foreign material causing cell stress (Miller et al., 2010). The presence of filopodia was observed in Figure 6.6, for MG-63 cells treated with 0.6 μL and 1.0 μL MNP-PEI, as well as in the previous chapter (Figure 5.9), along with bundles of actin stress fibres. Filopodia forms from the bundling of actin fibres and function in cell-cell adhesion and motility, as well as for probing the environment (Mattila and Lappalainen, 2008). Therefore cells treated with high doses of MNP-PEI show these protrusions in order to feel the MNP in their surroundings and move away from them.

MG-63 had noticeably stronger adhesion compared to HeLa cells. The effect of cell adhesion may be more pronounced in certain cell types. Osteosarcoma cells such as MG-63s are known to synthesize high amounts of various collagen types (Jukkola et al., 1993; Baumann and Hennet, 2016). The effect of collagen on improved cell adhesion have also been documented (Heino, 2007) for different collagen types, such as lining tissue culture plastic with collagen to promote adhesion of certain cells such as mesenchymal stem cells (MSC) (Somaiah et al., 2015). The upregulation of prolyl-4-hydroxylase (P4HA) induced by MNP-PEI treatment indicates increased collagen synthesis by cells and with the help of TGFBI, cells are able to anchor to extracellular collagen to strengthen cell adhesion to the extracellular matrix. Therefore MG-63 cells show more pronounced cell adhesion compared to HeLa cells when treated with MNP-PEI from the ability to lay out collagen in the extracellular matrix (ECM).

The stimulus that these cells are reacting to can either be chemical, though the interaction of PEI and tdMNP, or it can be mechanical cues. Mechanotrasduction has been widely reported to induce the formation of focal adhesions and cytoskeleton rearrangement. Focal adhesions can form when a force from inside or outside the cell is present, thus recruiting adhesion molecules to the site for focal adhesion formation (Galbraith et al., 2002). Mechanical stimuli are transmitted to cells through ion-channels or receptors located on the plasma membrane. The extracellular matrix (ECM) also receives mechanical forces and transmits them to the cell through receptors and the cytoskeleton (Alenghat and Ingber, 2002).

Previous studies report the manipulation of MNP using external magnetic fields to exert rotating-oscillating motions or a simple magnetic pull downwards with a static magnet (Golovin et al., 2015; Kenneth et al., 2005) and the magnetic manipulation was strong enough to cause cellular mechanotrasduction. In some cases, the development of focal adhesions to increase cell

adhesion is desirable, and mechanotransduction using MNP tethered to cells improved adhesion to the matrix as well as subsequent MSC differentiation (Wong et al., 2017).

In this study, mechanotransduction is a likely factor in the increase in cell adhesion. The oscillatory motion of MNP on the surface of cells from the magnefect nano and even the downward pull of MNP on cells from a static magnet may initiate mechanical cues for cells to recruit focal adhesion molecules. A cell surface receptor that responds to MNP magnetic pulling using a static magnet was also identified, and this was the N-type mechano-sensitive calcium ion channel (Tay and Di Carlo, 2017).

Although receptor-targeted magnetic mechanotransduction has applications in tissue engineering and regenerative medicine, not much is known about chemical driven focal adhesion signalling caused by internalized MNP. Cell interactions with a biomaterial is studied extensively in tissue engineering to create biomaterials which promote desirable cellular responses, such as stem cell differentiation or hydrogel integration within tissue. Some materials however cause undesirable side-effects in cells. Soenen et.al. studied the effect of iron oxide MNP and magnetoliposomes causing adverse cytological effects when internalized into cells and found similar effects described in this study, regarding reduced proliferation, increased focal adhesion complexes and a rearrangement of the actin cytoskeleton (Soenen et al., 2009, 2010).

Cells in the presence of MNP-PEI causes a reaction in the form of actin stress fibres and focal adhesions in a dose dependent manner. The two components of the transfection vector (MNP and PEI) were studied individually to determine the underlying cause of cell adhesion using the PicoGreen assay. MG-63 cells treated with either positively charged PEI polymer or negatively charged MNP expressed different intensities of cell adhesion in response to each component. The effect of PEI was stronger and more damaging to cells although PEI doses were lower than MNP doses in cells.

As described in Chapter 4, PEI elicits a cytotoxic effect on cells when incubated with cells for a long period or at high concentration which can cause cell death. At lower concentrations however, PEI may induce the formation of focal adhesions and stress fibres. The increased adhesion may be useful in some applications, where PEI is used as a surface coating agent to enhance cell adhesion onto substrates, and have demonstrated higher attachment of some cell lines compared to collagen and poly-lysine (Vancha et al., 2004). For gene therapy and drug delivery applications, however, changes in cell morphology and gene regulation is not a desirable effect and maintaining the native state of a cell is preferable.

6.5 Conclusion

This study demonstrates the increase in focal adhesion assembly and the formation of actin stress fibres in response to external chemical cues, in this case from tdMNP-PEI and PEI. Apart from the biological incompatibility of PEI, other possibilities causing the increased adhesive responses in cells could be from the additional PEI causing trypsin inhibition or the immobilization of trypsin onto PEI which reduces trypsin activity. The endosomal lysis caused by PEI in cells also causes leaking of the acidic pH of endolysosomes into the cell cytoplasm, causing an adverse reaction and toxicity to cells.

The genes affected by tdMNP-PEI were also determined, with relation to actin and focal adhesion regulation. The effect of mechanical forces and substrate stiffness has long been thought to be the main cause for the formation of stress fibres and focal adhesions (Burridge and Guilluy, 2016). This study provides an additional dimension to the mechanics of focal adhesion and stress fibre formation, where a similar cellular effect is observed arising from chemical cues from the external environment.

For cell therapy applications, changes in cell signalling and processes should be studied thoroughly in addition to cell viability and toxicity assays. Future work should study the long-term implications of stress fibres and focal adhesion formation on long-term physiological effects during nanomagnetic transfection.

Chapter 7

General Discussion

7.1 Summary of findings

The work presented in this thesis were exploratory studies to understand the different aspects of nanomagnetic transfection. The development of an MNP based transfection vector was discussed in Chapter 3, followed by the application of the synthesized tdMNP transfection vector using the oscillating magnefect-nano system. To understand the mechanism of nanomagnetic transfection, the magnetic behaviour and movement of MNPs in cells were researched. Finally, the biological/cellular response to MNP transfection was studied in terms of cell stress and cell adhesion.

In Chapter 1, the aims of this project had been established. The first aim was to design a PEI-coated MNP transfection vector. This was successfully achieved whereby an MNP suspension with a narrow size distribution was obtained and the PEI-coated MNPs were well characterized. Besides the development of the tdMNP transfection vector, the method using AC susceptometry to study changes in MNP behaviour with addition of coatings and particle-particle interaction was developed. ACS characterization is advantageous as it measures magnetic material in a sample and disregarding noise from non-magnetic moieties. This technique can be applied to MNPs for many applications in biomedicine and is a more precise and sensitive technique to DLS.

Aim 2 studied the parameters and optimization of nTMag and synthesized tdMNP-PEI. Although nTMag was able to achieve 50 – 60% transfection, cytotoxicity of this transfection vector was high and caused high cell death. The synthesized tdMNP-PEI had highest transfection of 20% after optimization but the treated cells were healthier. The parameters that affected nanomagnetic transfection were established, detailed in Chapter 4. To increase transfection rate of tdMNP-PEI, additional PEI can be added into the MNP suspension, at the cost of cell viability. However, the MNP suspension will have longer storage life and transfection function.

Once transfection functionality had been established, the mechanism of nanomagnetic transfection was elucidated in Chapter 5 for Aim 3. AC susceptometry was used to determine the proton-sponge effect for endosomal escape of MNP-PEI in cells by monitoring the changes in the Brownian relaxation of particles. The low transfection rate of MNP-PEI suggests that a either only small population of MNPs were able to escape from the endosome or there was aggregation of MNPs which were too large to detect using the ACS, therefore the Brownian signal on the ACS was too low to observe a change. Microscopy was also a complementary technique to ACS where mobility and morphology of MNP-PEI in the cell could be observed and correlated to ACS results. Confocal fluorescence images show localization of tagged-DNA in the nucleus of cells expressing GFP, however the localization of MNPs in the nucleus was not determined.

To study the movement of MNP-PEI and potential dissociation of PEI from MNPs in the cell, Raman spectroscopy was used for single cell analysis. It was established that the 780 nm laser was more suitable to study iron oxide particles due to a lower fluorescence signal. Also, SERS

is a powerful technique to improve spectral resolution of MNP spectra. Although preliminary information was obtained to carry out the study, the Raman spectrometer used was unable to identify MNPs as a heat map. Although the third aim was unsuccessful to elucidate the mechanism of MNP-based transfection, many useful information was obtained to carry out similar studies, and with suitable/more sensitive equipment better results can be obtained.

In Aim 4, I studied the effect of MNP-PEI on changes in cell regulation. Loading of MNP-PEI onto HeLa and MG-63 cells showed a dose dependent increased cell adhesion. Cells showed higher expression of vinculin and actin stress fibres after short-term MNP-PEI treatment. Genes involved with cell adhesion and actin fibre formation was also identified to be upregulated. PEI was determined to be the main component causing cell stress.

7.2 Discussion and future work

Initially, the commercial MNP transfection agent, nTMag was used to assess the efficiency of nanomagnetic transfection and cytotoxic effects compared to conventional chemical transfection methods. Although nTMag was a highly efficient transfection vector, besides the cost of the product, the lack of information available about the product limited the research in terms of experimental design and understanding the outcomes of experiments. The superparamagnetic properties of nTMag proved difficult when studying the MNPs using AC susceptometry, due to the frequency limit of the ACS which is unable to measure the presence of Néel peaks. The low nTMag concentration also limited the characterization methods to highly sensitive instruments which require little material such as the DLS and zeta potential measurements and limits experimental designs to ones which only require low volume of nTMag, such as transfection studies. Besides that, the commercial aspect of nTMag makes the material and its production method proprietary, therefore important information regarding the PEI coating type, the ratio of MNP to PEI, the size of the MNP, the type of interaction between the PEI and MNP, the MNP surface charge, and iron oxide type were unknown. nTMag was suitable for transfection experiments, however in studies involving the very nature of nanomagnetic transfection, a detailed understanding of the product being used was crucial.

To overcome the difficulty with using commercial MNPs, magnetite particles were synthesized using thermal decomposition. This is a controlled synthesis method to obtain MNPs with a small size distribution. Besides that, the oleic acid coating on MNP was bound by chemisorption, making this MNP type colloidally stable for a long period of time, compared to bare MNPs. With the flexibility of tailoring the MNP surface coating and the MNP suspension, different hypotheses were able to be tested and many aspects of the transfection vector could be understood.

The advantage of using blocked particles that display the Brownian relaxation mechanism over superparamagnetic MNPs is that using ACS measurements the particle hydrodynamic size can be calculated, therefore changes on the external MNP surface or MNP aggregation affects the physical rotation of the MNPs which can be monitored using ACS. Superparamagnetic particles, however, provide limited information about changes in the suspension with the ACS as the Néel relaxation time can only be used to determine the MNP core volume. The synthesized MNPs in this study had a higher proportion of Brownian relaxation behaviour and therefore the MNP suspension was suitable to study on the AC susceptometer, where the Brownian peak fell within the measurement range of the susceptometer. Based on the Brownian equation in Chapter 3, particle hydrodynamic size could be obtained based on the relaxation time of MNPs.

Many studies using MNPs for biological applications as well as companies selling MNPs use DLS to determine MNP hydrodynamic size. The first experimental chapter (Chapter 3) sought to provide a more accurate size measurement of MNP suspensions using ACS which can be employed in many studies involving MNPs for various applications. Furthermore, the saturation of coating on MNPs of a fixed mass could be observed using ACS as it only measures

magnetic material. When the peak position of Brownian relaxation is unchanged with the addition of coating material in an MNP suspension, this indicate no changes in the hydrodynamic size.

The AC susceptometer is a useful technique to observe changes to MNPs, from coating material to changes in the external environment. For example, in theory, MNPs with Brownian relaxation behaviour lose their mobility when trapped in endocytic vesicles in cells. If MNPs were able to escape from the endocytic pathway, their relaxation behaviour can be observed using the ACS. Therefore the loss and emergence of a Brownian peak when MNPs are in cells can provide information to their interaction within the cytoplasm. Another possiblity is the clustering of MNPs too large to be detected by the ACS.

Chapter 5 sought to study the method of MNP tracking and endosomal escape in cells, however the low ACS signal obtained was not enough to draw conclusive results. It would be interesting to obtain proof-of-concept for this hypothesis, therefore further work would include internalization of MNPs that bypass the endocytic pathway. Using this method, not only may transfection rates improve, the ACS signal may increase since the MNPs are not trapped in endocytic vesicles. Besides that, a more efficient MNP transfection vector should be employed to increase the population of MNPs able to escape from endocytic vesicles. One suggestion would be to increase the PEI content in the MNP suspension by adding excess PEI, which may induce more efficient proton-sponge effect.

The mechanism of nanomagnetic transfection is not clearly understood, however the results obtained in the study in Chapter 4 suggests that PEI covalently bound to MNPs do not facilitate transfection and free/unbound PEI contributes to transfection by traversing the nuclear membrane to deliver DNA. Covalently bound PEI onto MNPs (MNP cPEI) were studied for transfection ability (Cruz-Acuna et al., 2016), which was successful in transfecting 20% of cells. This study contradicted the results obtained in Section 4.5.5.1, whereby MNP cPEI were unable to transfect HeLa cells after undergoing magnetic separation to wash off excess PEI. The results obtained in Acunas paper suggests that the centrifugal filtration/solvent exchange is an inefficient method to remove unbound/free PEI and the transfection that was obtained was due to the excess PEI in the suspension, and not the MNP-PEI complex. To confirm that the MNP-PEI was indeed responsible for the transfection, evidence of MNP-PEI carrying DNA entering the nucleus should be included. Further studies should show the localization of MNP with covalently bound PEI in the nucleus of cells expressing GFP.

In the development of a suitable nanomagnetic transfection vector, the surface coating was the primary factor driving the transfection process, whereas the MNPs acted as a vehicle to speed-up the transfection process and to target the cells using external magnetic fields. With MNPs playing a very specific role in transfection, the surface of MNPs could be modified to incorporate or replace PEI with other gene delivery agents. Studies have been performed where MNPs were coated with streptavidin (Prow et al., 2006), cationic lipids (Govindarajan et al., 2013; Badieyan et al., 2017) and cationic polymers (Liu et al., 2016; Sohrabijam et al., 2017) for applications in gene delivery. However, comparisons between the coating types on MNPs that affect transfection efficiency have not been studied in these cases.

Other methods to improve nanomagnetic transfection is to incorporate targeting molecules, either to tether the MNP transfection complex to the plasma membrane or to deliver the DNA into the nucleus. Conjugation of cell penetrating peptides (CPPs) with MNPs is a fairly new approach and until recently there were only a few reports describing this method of MNP internalization. An interesting study conducted by Smith et al. (2010) combined 2 targeting approaches, which were biomolecule targeting and magnetic targeting. The group found that size of the MNPs influenced their magnetic internalization into the cell. Particles of 6 nm in size were found to be too small, thus had low magnetization at field strength of 350 mT. The force experienced by small particles was insufficient to pull them towards cells. It seemed that the TAT peptide played a larger role in improving internalization into the cell by cell membrane targeting. Another consequence of the small size of MNPs is the TAT peptide was able to

ferry the MNPs into the nucleus via the nuclear pore. Besides cell targeting, various nuclear localization sequences have been identified which are used in research for cargo delivery into the nucleus. One such DNA-based NLS is from the Simian vacuolating virus 40 (SV40), which has been used in gene delivery studies to improve transfection efficiency. Vernon et al. studied the combined effect of the SV40 NLS in the GFP reporter plasmid with commercial MNP tranfection agents to enhance nanomagnetic transfection in neuronal cells (Vernon et al., 2015). Therefore, more studies should be performed to incorporate cell and nuclear-targeting molecules with MNPs to improve gene delivery.

PEI has been shown in this study to have adverse effects on cells, from inducing cell death to cell stress and changes in gene regulation. The toxicity of PEI have also been reported extensively with PEI-based transfection (Hall et al., 2017). The incorporation of MNP in PEI transfection reduces PEI toxicity due to the lower dose of PEI required when bound to MNPs, where PEI transfection protocols require a PEI:DNA ratio of 4:1, whereas MNP-PEI based transfection require a 1:1 ratio to DNA. Apart from PEI dosage, the time of transfection is significantly reduced, from 6 hours to 30 minutes using the magnefect-nano oscillating system. Despite these improvements to conventional chemical transfection methods, PEI toxicity is still an important factor to be considered when improving the transfection rate of MNP-PEI based transfection. To overcome the toxic effects of PEI while maintaining transfection efficiency, many studies have looked at synthesizing PEI copolymers with polymers such as polyethylene glycol (PEG) and polylactic acid (PLA) (Sim et al., 2017; Lv et al., 2017). PEI block copolymers could be used in further studies to coat MNPs for transfection, thus increasing the transfection to cytotoxicity ratio.

7.3 Conclusion

The recent breakthrough in gene therapy technology has opened up new avenues in medicine and advances in human health. Since the discovery of the CRISPR in 1987 in Japan, the CRISPR/Cas9 genome editing machinery was first shown to work in eukaryotic cells in 2013 by researchers at The Broad Institute and Harvard University. Since the proof-of-concept was established there has been an exponential increase in publications relating to CRISPR/Cas9 and its accuracy and precision in gene editing. Despite the powerful gene editing tool at our disposal, the CRISPR/Cas9 complex is still limited to its gene delivery system. Viral vectors have undergone various clinical trials and although they are efficient gene delivery systems that produce high transduction rates, viral vectors are largely unsafe for clinical treatment due to their potential immunogenic and genotoxic properties (Naldini, 2015). Current non-viral vectors are inefficient as they have relatively low transfection rates to viral vectors and are cytotoxic.

Therefore, the need to develop a safe and efficient transfection vector for *in vitro* and *in vivo* delivery is crucial to push the boundaries of gene therapy in medicine. MNP-based transfection vectors may be a suitable candidate as they offer targeting capabilities with low dosage requirements. By surface modification of MNPs to improve their transfection rates using non-viral and viral molecules and multi-modal functionalities, the nanomagnetic transfection technique could be developed further for gene and cancer therapy applications.

Appendix

Results and discussion from Chapter 4: Shelf-life of transfection agents

PEI polymer only – Effect of pH on transfection

Protocols for PEI polymer-mediated transfection have shown that PEI has the highest transfection activity at pH 7 or below for improved transfection and long-term storage of PEI polyplexes. This study is to determine the best pH for PEI only transfection and treatment of PEI polymer before coating onto MNPs. Preparation and transfection procedures were performed according to Section4.4.2. The 5 PEI treatments were PEI at pH 10.5, pH 2, pH 7, PEI renutralized from pH 2 to 7, and aged PEI at pH 7 (more than 2 months).

DLS and zeta potential measurements (Figure 7.1 A left column) were performed on each sample to characterize their hydrodynamic size and surface charge. At pH 10.5 (Figure 7.1 A i) before pH changes are made, PEI are polydispersed over a range of 0 – 6000 mn hydrodynamic size and a zeta potential of +14.7 mV.

PEI acidified to pH 2 (Figure A ii) was also small at 14.5 nm. However PEI at neutral pH (Figure A iii) formed slightly larger polyplexes at 29 nm average with larger peak intensity formed at ∼1000 nm. When PEI was acidified to pH 2 and reneutralized to pH 7 (Fig. A iv), the hydrodynamic size was 15 nm, similar to PEI pH 2 with a size distribution similar to (Fig. A ii). Aged PEI of more than 2 months at neutral pH had a much larger size distribution of 277 nm.

Based on zeta potential measurements in Figure 7.1 A (right column), PEI polymers have a positively charged surface regardless of pH. PEI older than 2 months had the highest surface charge of +74 mV.

A dilute solution of PEI of branched 25 kDa has a pH of around 10. The zeta potential of the solution is still positive but low due to some amine groups having a neutral charge. At this pH, PEI may be close to its isoelectric point. By introducing HCl into the polymer solution, the zeta potential increased to above 20 mV for pH 7 and 2, possibly attributed to the H^+ ions in the acid solution donated to the neutral amine groups forming NH^+, NH^{2+} and NH^{3+} in the PEI complex. The highest zeta potential measurement was observed for aged PEI at pH 7, and the increased DLS size compared to the other solutions suggest the formation of large polyplexes which gives rise to a high charge density in the solution. This effect can also be seen for PEI pH 7. Therefore, an increase in positive charge of PEI could be attributed to either a solution with high H^+ content or the formation of polyplexes between PEI monomers.

PEI of different pH were then used for transfection of HeLa cells to study the effect of pH of PEI on the success of gene delivery, with nTMag as a positive control for transfection. Transfection of HeLa cells using PEI of different pH showed no difference in GFP expression between treatments. The transfection rate however, was low which could be due to lack of optimization procedures of PEI transfection. The ability of PEI to form complexes with DNA and transfect cells even at low charge density (at pH 10) was also observed by Hobel et al. (Höbel et al., 2008). Since PEI has a high positive charge density, acidification of the polymers creates more charged amine groups due to excess protons in the solution. Previous studies report a low

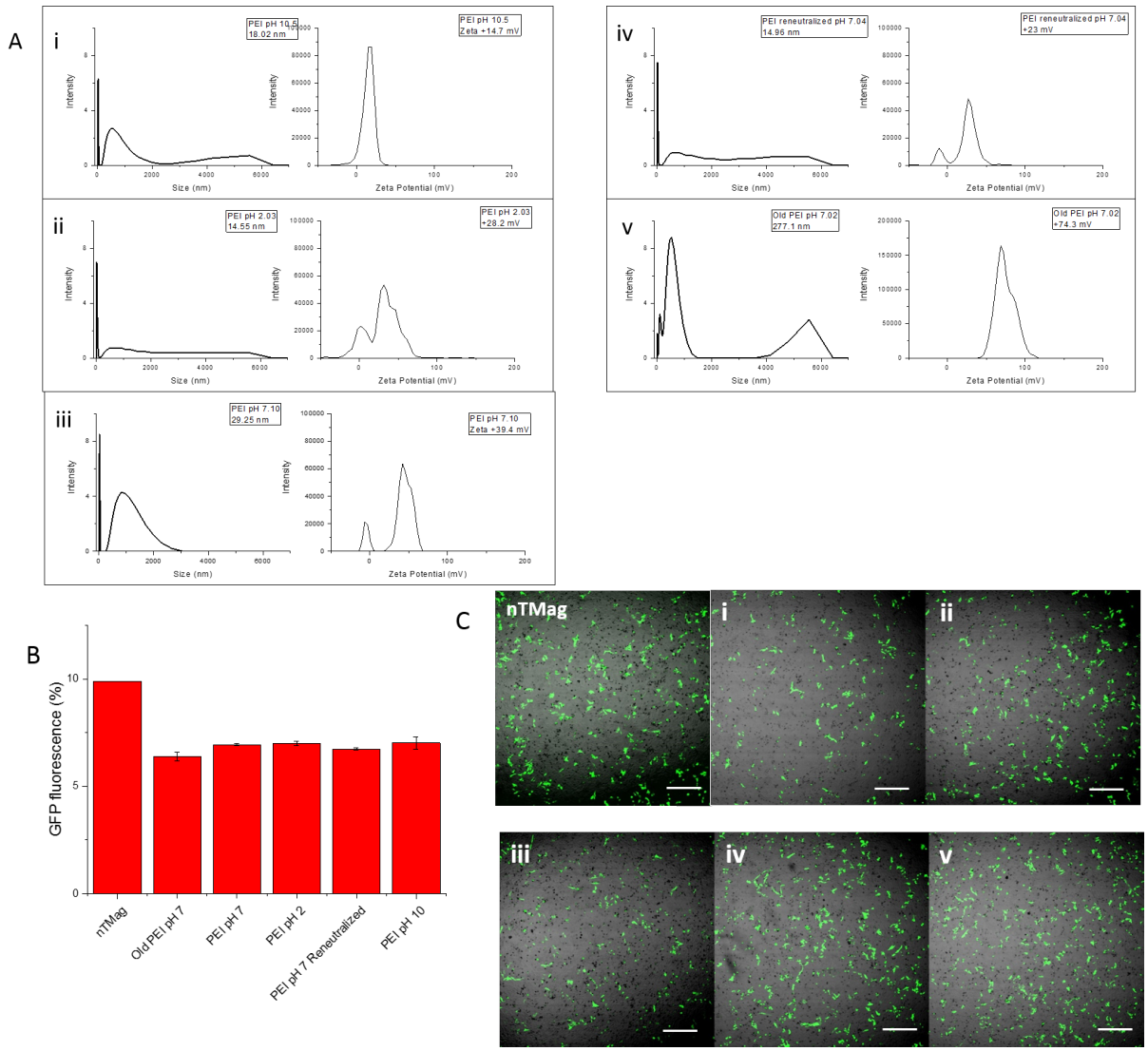

Figure 7.1 (A) DLS (left column) and zeta potential (right column) measurements of PEI polymers at (i) pH 2, (ii) pH 7, (iii) pH 10.5, (iv) acid-reneutralized pH 7, (v) aged PEI (>2 months) pH 7. (B) GFP expression of HeLa cells transfected with PEI polymers of different pH; n=2. (C) Overlay of fluorescence and brighfield images showing cells expressing GFP, scale bar=200um.

transfection rate when PEI was used at a pH below 5, suggesting low complexation rate with DNA or reduced buffering capacity for endosomal escape (Amin et al., 2013; Höbel et al., 2008). Endosomal escape requires amine groups to be unprotonated for the buffering effect to work. When the unprotonated amine groups are in the endosome, it attracts H^+ ions for protonation, which causes an influx of water into the endosome and results in vesicle rupture. This proton sponge effect was described in Chapter 1.4.

Based on literature for PEI mediated transfection, PEI acidified to pH 7 was suitable for high efficiency transfection with longer storage time (Fukumoto et al., 2010) Furthermore, this study relates to the effect of storage time and loss of colloidal stability of PEI coated tdMNPs, due to the formation of large polyplexes for aged PEI.

Aged and New tdMNP-PEI before and after dialysis

The ability of tdMNP-PEI to transfect decreases with time. The shelf life of tdMNP-PEI was determined before the sample became unstable and unusable. To study this, the transfection efficiency of tdMNP-PEI that had been prepared for more than a month was compared with freshly prepared tdMNP-PEI (less than a month). PEI only samples were transfected using the nanomagnetic transfection procedure.

Aged tdMNP-PEI (>1 month old) were compared before dialysis (-dialysis) and after dialysis (+dialysis) for transfection efficiency and ACS measurements. Figure 7.2 A shows the confocal images of transfected groups, where Column 1 is the nuclear count representing number of cells and Column 2 is the GFP expression of cells. nTMag showed the highest GFP expression (Column 2) however nuclear cell count was low (Column 1) whereas the other treatment groups had similar nuclear counts to control groups signifying low cytotoxicity. In Figure 7.2 B, nTMag had a high transfection rate of 50%, followed by significantly lower transfection of aged tdMNP-PEI before dialysis of ∼18% ($p<0.0001$). Aged tdMNP-PEI sample +dialysis however showed zero transfection, while aged and New PEI had no significant difference in transfection capacities with a low 2% transfection rate. Aged tdMNP-PEI -dialysis was able to retain its transfection properties and had significantly higher transfection rates compared to the sample +dialysis and PEI alone ($p<0.0001$).

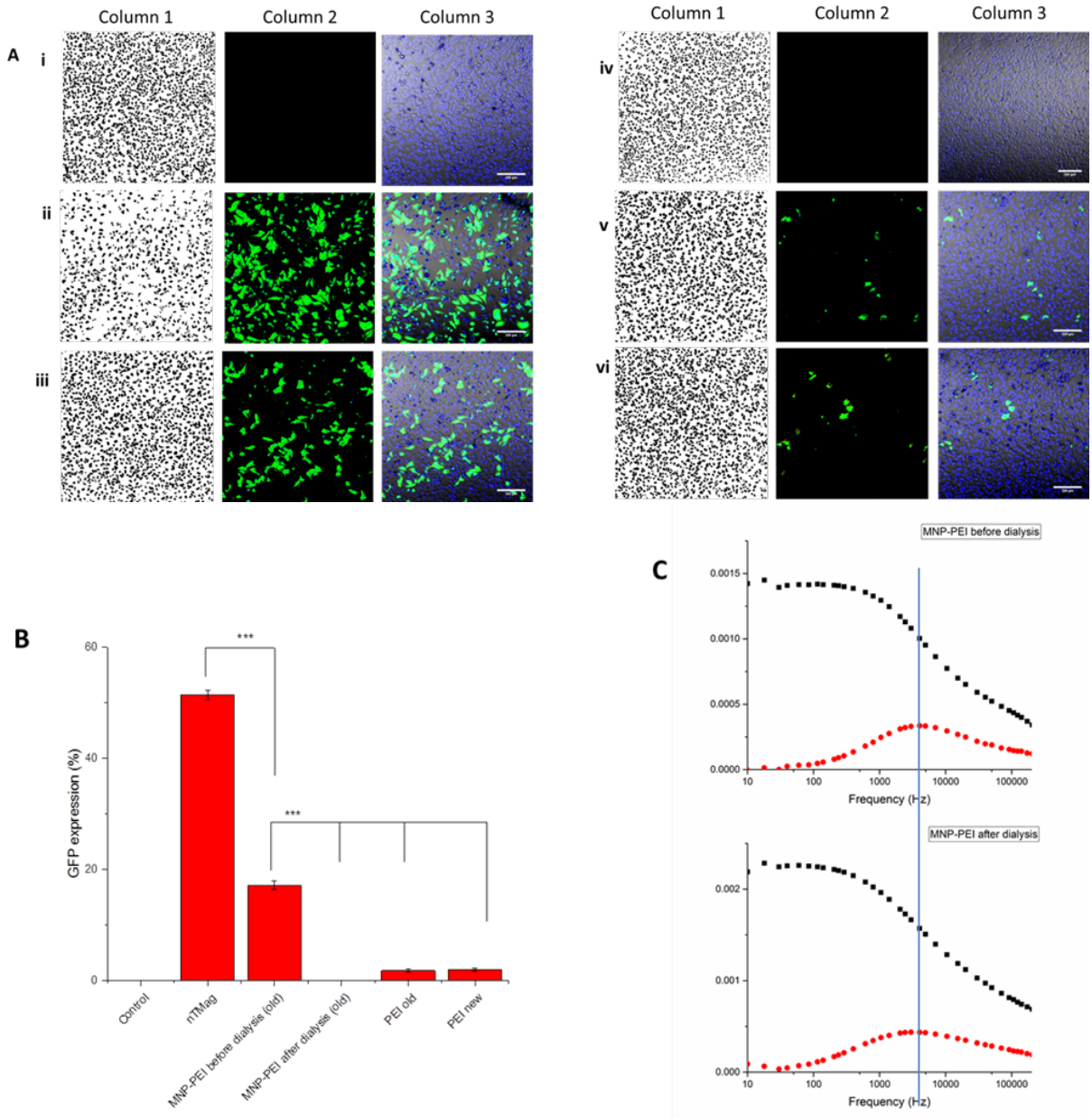

Figure 7.2 (A) Confocal microscope images of HeLa cells transfected with pGFP and different transfection complexes. Column 1 is nuclear count in an area of cells based on Hoescht staining, Column 2 is cells expressing GFP, and Column 3 is an overlay of brightfield, nuclear stain and GFP expression of cells. The treatment groups are (i) control, (ii) nTMag, (iii) aged tdMNP-PEI before dialysis, (iv) aged tdMNP-PEI after dialysis, (v) aged PEI, and (vi) new PEI —scale bar 200um. (B) GFP expression of treatment groups with t-test statistical analysis— n=3. (C) ACS measurements of aged tdMNP-PEI before and after dialysis.

To further understand the reason for loss of transfection in aged tdMNP-PEI +dialysis sample, ACS measurements were performed on the two magnetic samples (Figure 7.2 C). Aged tdMNP-PEI -dialysis had a slightly lower Brownian peak frequency (4300 Hz) compared to aged tdMNP-PEI +dialysis (3490 Hz). tdMNP-PEI +dialysis (bottom) also shows a broader peak at lower frequency.

Based on the results, nTMag had high transfection rates but were cytotoxic compared to tdMNP-PEI. Aged tdMNP-PEI +dialysis were had an increase in size compared to -dialysis indicating higher MNP clustering of +dialysis sample over time. This resulted in low/no transfection, whereas aged tdMNP-PEI without dialysis retained transfection efficiency.

The shelf life of tdMNP-PEI was further studied by comparing newly prepared tdMNP-PEI (<1 month old) to aged tdMNP-PEI before and after dialysis, as well as the effect of dialysis on nTMag. Figure 7.3 A is the confocal images of treatment groups. Transfection was successful in all the treated groups except for aged tdMNP-PEI +dialysis (Figure 7.3 Av). Both the nTMag groups (Figure 7.3 D ii and iii) had high GFP expression but also the lowest nuclear counts (Figure 7.3 A, Column 1 and 2), similar to Figure 7.2 A above.

ACS measurements were performed on all the MNP groups and nTMag (Figure 7.3 B). Column 1 represents nTMag -dialysis (top) and +dialysis (bottom). Similarly, Column 2 represents new tdMNP-PEI and Column 3 is aged tdMNP-PEI. New tdMNP-PEI (Figure B, Column 2) measured on the ACS shows a peak at 5020 Hz -dialysis and 4470 Hz +dialysis, with calculated hydrodynamic size of 50 nm and 52 nm respectively before and after dialysis. Aged tdMNP-PEI (Column 3) has Brownian peaks at lower frequencies compared to the new tdMNP-PEI, with 4230 Hz -dialysis and 2720 Hz +dialysis, corresponding to 53 nm and 61 nm hydrodynamic size respectively. There is a small increase in size between new and aged tdMNP-PEI -dialysis of 3 nm, but aged tdMNP-PEI +dialysis had a larger shift in the peak compared to new tdMNP-PEI +dialysis where aging induced an increase in size of 9 nm, indicating dialysis of tdMNP-PEI induces clustering of MNPs over time but without dialysis the clustering effect is reduced.

nTMag exhibits Néel relaxation where there is no loss of magnetization in the in-phase component of the ACS measurement. Therefore, the physical properties of nTMag cannot be obtained from ACS measurements alone. DLS measurements were performed on the nTMag samples (Figure 7.3 C) -dialysis and +dialysis. DLS of nTMag -dialysis shows two peaks, a small distribution at ∼130 nm and a larger population at ∼400 nm for all three DLS weighted measurements (volume, intensity and number). In the nTMag +dialysis however, the volume-, intensity-, and number- weighted measurements show different distributions. The number distribution is usually weighted towards smaller particles, which shows peaks at 50 nm, 220 nm, and a small peak at 400 nm. The volume distribution is inverse to number-weighted without the smallest peak at 50 nm and a large size population at 400 nm. Intensity-weighted calculation shows a lognormal size distribution with a peak at 240 nm tapering off at 700 nm. Dialysis influenced nTMag size, however the change in size or clustering was inconclusive based on DLS measurements alone.

Figure 7.3 D is the transfection efficiency of each group. The highest transfection was obtained with nTMag as a vector, with almost 40% transfection. Dialysis of nTMag did not have an effect on its transfection efficiency. New tdMNP-PEI +dialysis had the highest transfection of all the tdMNP-PEI groups with a 25% rate, which was significantly higher than its non-dialyzed counterpart of 20% ($p=0.048$). Aged tdMNP-PEI on the other hand, had a transfection of 17% in the non-dialyzed tdMNP-PEI but developed a loss in transfection activity once dialyzed and stored for more than a month ($p<0.0001$). Additionally, both the dialyzed and non-dialyzed new tdMNP-PEI had significantly higher transfection that the old samples ($p<0.00712$). Therefore the shelf life of tdMNP-PEI was determined to be one month for samples that underwent dialysis. To lengthen the shelf life, the dialysis procedure will have to be omitted or free PEI will have to be added into the suspension.

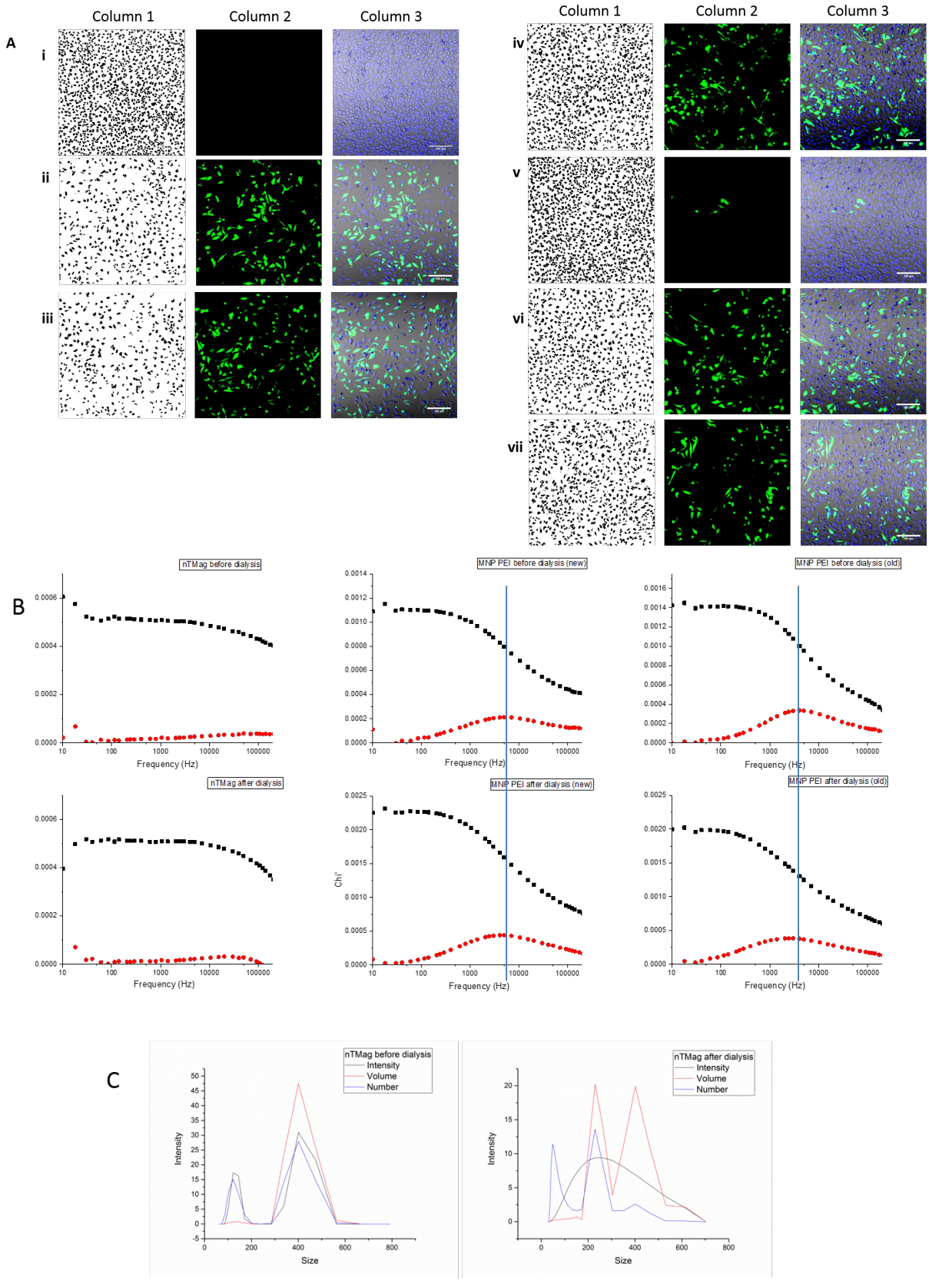

Figure 7.3 (Figure continued on the following page)

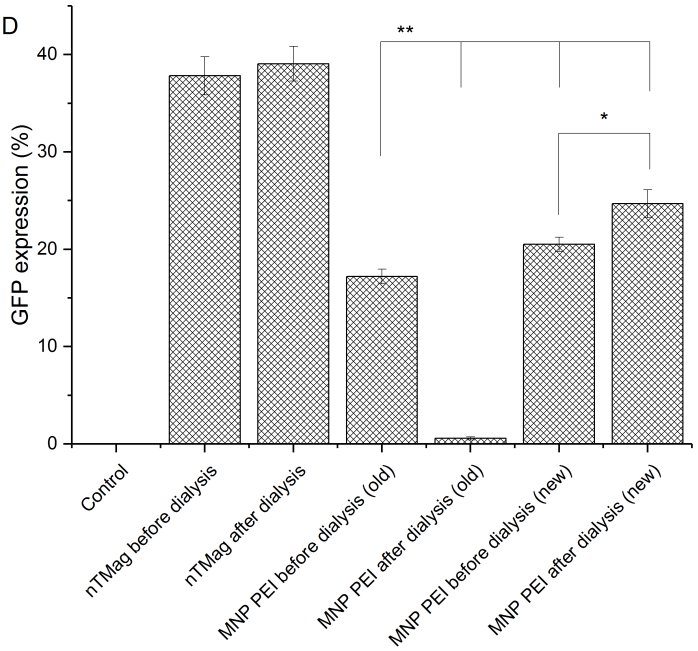

Transfection of HeLa cells with old (>1 month old) and new (<1 month old) tdMNP-PEI before and after dialysis. (A) Confocal microscope images of cells transfected with pGFP and tdMNP-PEI. Column 1 is nuclear count in an area of cells based on Hoescht staining, Column 2 is cells expressing GFP, and Column 3 is an overlay of brightfield, nuclear stain and GFP expression of cells. The treatment groups are (i) control, (ii) nTMag before dialysis, (iii) nTMag after dialysis, (iv) tdMNP-PEI before dialysis (old), (v) tdMNP-PEI after dialysis (old), (vi) tdMNP-PEI before dialysis (new), (vii) tdMNP-PEI after dialysis (new), scale bar 200um. (B) ACS measurements of nTMag before and after dialysis, as well as the tdMNP-PEI samples. (C) DLS measurements of nTMag before and after dialysis. (D) GFP expression of cells transfected with tdMNP-PEI groups and nTMag. Student's t-test shows significant increase in transfection with new tdMNP-PEI, n=3.

Over time, PEI has a tendency to complex with itself to form polyplexes, and in the dialyzed tdMNP-PEI sample the amount of PEI is just sufficient to coat each particle. Once PEI starts to detach from the surface of MNP and complex with each other, MNP becomes unstable and starts to clump and precipitate. The increase in size after a month suggests that PEI is slowly detaching from MNP and this creates aggregates of MNP in the suspension. With undialyzed MNP however, the excess free PEI in the suspension is sufficient to maintain the PEI coating on MNP, hence if PEI polyplexes form they are still able to wrap around MNP providing colloid stability.

Discussion: Shelf-life of transfection agents

Many chemical transfection agents have a short shelf life, and proper treatment and storage is required to prolong their activity. Fukumoto et al. reported that PEI at neutral pH stored at $-40\,^{\circ}\mathrm{C}$ or $-80\,^{\circ}\mathrm{C}$ are able to retain transfection activity for only one month (Fukumoto et al., 2010). Based on Figure 7.1 A, PEI measured using the DLS show that after more than a month, aged PEI had a large size distribution. Therefore, the loss of activity could stem from PEI forming polyplexes after a prolonged duration and this interferes with complex formation with DNA.

It was observed that dialyzed tdMNP-PEI that was prepared had gradually reduced in transfection capacity until the particles became unstable after 2–3 months. The particles were monitored to understand their physical characteristics that influenced the loss of transfection activity. When aged tdMNP-PEI were used for transfection, only the particles that were undialyzed were able to transfect cells whereas the particles that underwent dialysis were unable to transfect after more than a month since preparation. New MNP-PEI however showed that

dialyzed particles had better transfection than undialyzed ones.

Based on ACS measurements, a change in size was observed with time, where old tdMNP-PEI (dialyzed and undialyzed) increased in hydrodynamic size. Dialysis of tdMNP-PEI improves transfection efficiency compared to undialyzed suspensions possibly due to lower cytotoxic effect with the absence of excess free PEI. PEI exists in an equilibrium between bound and free states, therefore PEI that becomes unbound from MNPs may be replaced by free PEI in the suspension. In the dialyzed suspension, the lack of free PEI causes thinning of the PEI coating on MNPs over time which leads to MNP aggregation. Furthermore, the presence of free PEI in an MNP suspension improves transfection efficiency, as observed in Section 4.5.6.3.

To further understand the effect of dialysis on the transfection activity of particles, nTMag was dialyzed. Based on intensity-weighted DLS measurements, there was little change in nTMag size after dialysis. Transfection was also unaffected after nTMag dialysis, and both the samples were equally cytotoxic based on the low nuclear count in Figure 7.3 A. It is possible that dialysis did not work as there is a high amount of PEI in the suspension which had formed large polyplexes and are unable to pass through the 50 kDa MWCO of the dialysis tube. The high cytotoxicity of nTMag is also characteristic of large amount of PEI in the suspension.

Bibliography

Aires, A., Cabrera, D., Alonso-Pardo, L. C., Cortajarena, A. L., and Teran, F. J. (2017). Elucidation of the Physicochemical Properties Ruling the Colloidal Stability of Iron Oxide Nanoparticles under Physiological Conditions. *ChemNanoMat*, 3:183–189.

al Yacoub, N., Romanowska, M., Haritonova, N., and Foerster, J. (2007). Optimized production and concentration of lentiviral vectors containing large inserts. *J. Gene Med.*, 9:579–584.

Alenghat, F. J. and Ingber, D. E. (2002). Mechanotransduction: all signals point to cytoskeleton, matrix, and integrins. *Sci. STKE*, 2002(119):pe6.

American Chemical Society International Historic Chemical Landmarks (1998). The Raman Effect.

Amin, Z. R., Rahimizadeh, M., Eshghi, H., Dehshahri, A., and Ramezani, M. (2013). The effect of cationic charge density change on transfection efficiency of Polyethylenimine. *Iran. J. Basic Med. Sci.*, 16:150–156.

Anadolu, E. I. (2014). Mihaliccik Tremolite: An XRD, FTIR and Raman Spectroscopic Study. *11th Int. GeoRaman Conf.*, pages 15–16.

Ang, D., Nguyen, Q., Kayal, S., Preiser, P., Rawat, R., and Ramanujan, R. (2011). Insights into the mechanism of magnetic particle assisted gene delivery. *Acta Biomater.*, 7(3):1319–1326.

Aravindan, L., Bicknell, K. A., Brooks, G., Khutoryanskiy, V. V., and Williams, A. C. (2009). Effect of acyl chain length on transfection efficiency and toxicity of polyethylenimine. *Int. J. Pharm.*, 378:201–210.

Arruebo, M., Fernández-pacheco, R., Ibarra, M. R., and Santamaría, J. (2007). Magnetic nanoparticles for drug delivery. *nanotoday*, 2:22–32.

Arsianti, M., Lim, M., Marquis, C. P., and Amal, R. (2010). Assembly of polyethylenimine-based magnetic iron oxide vectors: insights into gene delivery. *Langmuir*, 26:7314–26.

Baber, O., Jang, M., Barber, D., and Powers, K. (2011). Amorphous silica coatings on magnetic nanoparticles enhance stability and reduce toxicity to in vitro BEAS-2B cells. *Inhal. Toxicol.*, 23:532–543.

Badieyan, Z. S., Pasewald, T., Mykhaylyk, O., Rudolph, C., and Plank, C. (2017). Biochemical and Biophysical Research Communications Ef fi cient ex vivo delivery of chemically modi fi ed messenger RNA using lipofection and magnetofection. *Biochem. Biophys. Res. Commun.*, 482:796–801.

Baumann, S. and Hennet, T. (2016). Collagen accumulation in osteosarcoma cells lacking GLT25D1 collagen galactosyltransferase. *J. Biol. Chem.*, 291:18514–18524.

Baynes, R. D., Skikne, B. S., and Cook, J. D. (1994). Circulating transferrin receptors and assessment of iron status. *J. Nutr. Biochem.*, 5:322–330.

Bean, C. P. and Livingston, J. D. (1959). Superparamagnetism. *J. Appl. Phys.*, 30:120.

Behr, J. (1997). The proton sponge: a trick to enter cells the viruses did not exploit. *Chim. Int. J. Chem.*, 2:34–36.

Benjaminsen, R. V., Mattebjerg, M. A., Henriksen, J. R., Moghimi, S. M., and Andresen, T. L. (2013). The Possible Proton Sponge Effect of Polyethylenimine (PEI) Does Not Include Change in Lysosomal pH. *Mol. Ther.*, 21:149–157.

Bertoli, F., Davies, G.-L., Monopoli, M. P., Moloney, M., Gun'ko, Y. K., Salvati, A., and Dawson, K. A. (2014). Magnetic Nanoparticles to Recover Cellular Organelles and Study the Time Resolved Nanoparticle-Cell Interactome throughout Uptake. *Small*, 10:3307–3315.

Beyerle, A., Irmler, M., Beckers, J., Kissel, T., Stoeger, T., and Mu, Z. (2010). Toxicity Pathway Focused Gene Expression Profiling of PEI-Based Polymers for Pulmonary Applications. *Mol. Pharm.*, 7:727–737.

Blakemore, R. (1975). Magnetotactic bacteria. *Science (80-.).*, 190:1–3.

Boholm, M. and Arvidsson, R. (2016). A Definition Framework for the Terms Nanomaterial and Nanoparticle. *Nanoethics*, 10:25–40.

Bouillot, S., Tillet, E., Carmona, G., Prandini, M. H., Gauchez, A. S., Hoffmann, P., Alfaidy, N., Cand, F., and Huber, P. (2011). Protocadherin-12 cleavage is a regulated process mediated by ADAM10 protein: Evidence of shedding up-regulation in pre-eclampsia. *J. Biol. Chem.*, 286:15195–15204.

Boussif, O., Lezoualc'h, F., Zanta, M. A., Mergny, M. D., Scherman, D., Demeneix, B., and Behr, J.-P. (1995). A versatile vector for gene and oligonucleotide transfer into cells in culture and in vivo: Polyethylenimine. *Proc. Natl. Acad. Sci. USA*, 92:7297–7301.

Boyd, A. R., Burke, G. A., and Meenan, B. J. (2010). Monitoring cellular behaviour using Raman spectroscopy for tissue engineering and regenerative medicine applications. *J Mater Sci Mater Med*, 21(8):2317–2324.

Brgles, M., Šantak, M., Halassy, B., Forcic, D., and Tomašić, J. (2012). Influence of charge ratio of liposome/DNA complexes on their size after extrusion and transfection efficiency. *Int. J. Nanomedicine*, 7:393–401.

Browne, W. R. and McGarvey, J. J. (2007). The Raman effect and its application to electronic spectroscopies in metal-centered species: Techniques and investigations in ground and excited states. *Coord. Chem. Rev.*, 251(3-4):454–473.

Burridge, K. and Guilluy, C. (2016). Focal adhesions , stress fi bers and mechanical tension. *Exp. Cell Res.*, 343(1):14–20.

Butler, H. J., Ashton, L., Bird, B., Cinque, G., Curtis, K., Dorney, J., Esmonde-white, K., Fullwood, N. J., Gardner, B., Martin-Hirsch, P. L., Walsh, M. J., Mcainsh, M. R., Stone, N., and Martin, F. L. (2016). Using Raman spectroscopy to characterise biological materials. *Nat. Protoc.*, 11(4):664–687.

Buyukhatipoglu, K. and Clyne, A. M. (2010). Superparamagnetic iron oxide nanoparticles change endothelial cell morphology and mechanics via reactive oxygen species formation. *J. Biomed. Mater. Res. - Part A*, 96(1):186–195.

Byrne, J. M., Coker, V. S., Cespedes, E., Wincott, P. L., Vaughan, D. J., Pattrick, R. A. D., Laan, G. V. D., Arenholz, E., Tuna, F., Bencsik, M., Lloyd, J. R., and Telling, N. D. (2014). Biosynthesis of Zinc Substituted Magnetite Nanoparticles with Enhanced Magnetic Properties. *Adv. Funct. Mater.*, 24:2518–2529.

Cai, L., Fisher, A. L., Huang, H., and Xie, Z. (2016). ScienceDirect CRISPR-mediated genome editing and human diseases. *Genes Dis.*, 3:244–251.

Calatayud, M. P., Sanz, B., Raffa, V., Riggio, C., Ibarra, M. R., and Goya, G. F. (2014). The effect of surface charge of functionalized Fe 3 O 4 nanoparticles on protein adsorption and cell uptake. *Biomaterials*, 35(24):6389–6399.

Campelj, S., Makovec, D., and Drofenik, M. (2008). Preparation and properties of water-based magnetic fluids. *J. Phys. Condens. Matter*, 20(20):204101.

Canton, I. and Battaglia, G. (2012). Nanomedicine themed issue. *Chem. Soc. R ev*, 41(7).

Carrey, J., Mehdaoui, B., and Respaud, M. (2011). Simple models for dynamic hysteresis loop calculations of magnetic single- domain nanoparticles: Application to magnetic hyperthermia optimization. *J. Appl. Phys*, 109:083921.

Cebrián, V., Martín-Saavedra, F., Yagüe, C., Arruebo, M., Santamaría, J., and Vilaboa, N. (2011). Size-dependent transfection efficiency of PEI-coated gold nanoparticles. *Acta Biomater.*, 7(10):3645–3655.

Céspedes, E., Byrne, J. M., Farrow, N., Moise, S., Coker, V. S., Bencsik, M., Lloyd, J. R., and Telling, N. D. (2014). Bacterially synthesized ferrite nanoparticles for magnetic hyperthermia applications. *Nanoscale*, 6(21):12958–12970.

Chabot, S., Orio, J., Schmeer, M., Schleef, M., Golzio, M., and Teissié, J. (2013). Minicircle DNA electrotransfer for efficient tissue-targeted gene delivery. *Gene Ther.*, 20:62–68.

Chatterjee, A., Xiao, H., Bollong, M., Ai, H.-W., and Schultz, P. G. (2013). Efficient viral delivery system for unnatural amino acid mutagenesis in mammalian cells. *Proc. Natl. Acad. Sci.*, 110:11803–11808.

Chen, C.-w., Syu, W.-j., Huang, T.-c., Lee, Y.-c., Hsiao, J.-k., Huang, K.-y., Yu, H.-p., Liao, M.-y., and Lai, P.-s. (2017). Encapsulation of Au / Fe 3 O 4 nanoparticles into a polymer nanoarchitecture with combined near. *J. Mater. Chem. B*, 5:5774–5782.

Chen, L., Mccrate, J. M., Lee, J. C.-M., and Li, H. (2011). The role of surface charge on the uptake and biocompatibility of hydroxyapatite nanoparticles with osteoblast cells. *Nanotechnology*, 22:105708.

Cheung, W., Kotzamanis, G., Abdulrazzak, H., Goussard, S., Kaname, T., Kotsinas, A., Gorgoulis, V. G., Grillot-Courvalin, C., and Huxley, C. (2012). Bacterial delivery of large intact genomic-DNA containing BACs into mammalian cells. *Bioeng. Bugs*, 3:86–92.

Chourpa, I., Douziech-Eyrolles, L., Ngaboni-Okassa, L., Fouquenet, J.-F., Cohen-Jonathan, S., Soucé, M., Marchais, H., and Dubois, P. (2005). Molecular composition of iron oxide nanoparticles, precursors for magnetic drug targeting, as characterized by confocal Raman microspectroscopy. *Analyst*, 130:1395–403.

Clark, K. L., Hughes, S. A., Bulsara, P., Coates, J., Moores, K., Parry, J., Carr, M., Mayer, R. J., Wilson, P., Gruenloh, C., Levin, D., Darton, J., Weber, W.-M., Sobczak, K., Gill, D. R., Hyde, S. C., Davies, L. A., Pringle, I. A., Sumner-Jones, S. G., Jadhav, V., Jamison, S., Strapps, W. R., Pickering, V., and Edbrooke, M. R. (2013). Pharmacological Characterization of a Novel ENaCα siRNA (GSK2225745) With Potential for the Treatment of Cystic Fibrosis. *Mol. Ther. Nucleic Acids*, 2:e65.

Coey, J. (2010). *Magnetism and magnetic materials*. Cambridge University Press.

Crick, F. (1958). On protein synthesis. *Symp. Soc. Exp. Biol.*

Cruz-Acuna, M., Maldonado-Camargo, L., Dobson, J., and Rinaldi, C. (2016). From oleic acid-capped iron oxide nanoparticles to polyethyleneimine-coated single-particle magnetofectins. *J. Nanoparticle Res.*, 18:268.

Davidson, B. L. and McCray, P. B. (2011). Current prospects for RNA interference-based therapies. *Nat. Rev. Genet.*, 12:329–40.

Davies, K. J. (1999). The broad spectrum of responses to oxidants in proliferating cells: a new paradigm for oxidative stress. *IUBMB Life*, 48:41–47.

de Sousa, M. E., Fernández van Raap, M. B., Rivas, P. C., Mendoza Zélis, P., Girardin, P., Pasquevich, G. A., Alessandrini, J. L., Muraca, D., and Sánchez, F. H. (2013). Stability and Relaxation Mechanisms of Citric Acid Coated Magnetite Nanoparticles for Magnetic Hyperthermia. *J. Phys. Chem. C*, 117:5436–5445.

Decuzzi, P., Causa, F., Ferrari, M., and Netti, P. A. (2006). The Effective Dispersion of Nanovectors Within the Tumor Microvasculature. *Ann. Biomed. Eng.*, 34:633–641.

Delaney, A. M., Adams, C. F., Fernandes, A. R., Al-Shakli, A. F., Sen, J., Carwardine, D., Granger, N., and Chari, D. M. (2017). A fusion of minicircle DNA and nanoparticle delivery technologies facilitates therapeutic genetic engineering of autologous canine olfactory mucosal cells. *Nanoscale*, 9:8560–8566.

Deng, Z. J., Morton, S. W., Ben-Akiva, E., Dreaden, E. C., Shopsowitz, K. E., and Hammond, P. T. (2013). Layer-by-layer nanoparticles for systemic codelivery of an anticancer drug and siRNA for potential triple-negative breast cancer treatment. *ACS Nano*, 7:9571–9584.

DePasquale, J. A. and Izzard, C. S. (1987). Evidence for an actin-containing cytoplasmic precursor of the focal contact and the timing of incorporation of vinculin at the focal contact. *J. Cell Biol.*, 105:2803–2809.

Dinari, M. and Ahmadizadegan, H. (2014). Synthesis, structural characterization and properties of novel functional poly(ether imide)/titania nanocomposite thin films. *Polymer (Guildf).*, 55:6252–6260.

Discher, D. E. (2005). Tissue Cells Feel and Respon to the Stiffness of Their Substrate. *Science (80-.).*, 310:1139–1143.

Dobson, J. (2006). Gene therapy progress and prospects: magnetic nanoparticle-based gene delivery. *Gene Ther.*, 13:283–7.

Dobson, J., Keramane, A., and Haj, A. J. E. (2002). Theory and Applications of a Magnetic Force Bioreactor. *Eur. Cells Mater.*, 4:42–44.

Doherty, G. J. and McMahon, H. T. (2009). Mechanisms of endocytosis. *Annu. Rev. Biochem.*, 78:857–902.

Du, T., Zhao, C., Rehman, F., Lai, L., Li, X., Sun, Y., Luo, S., and Jiang, H. (2017). Rapid and multimodal in vivo bioimaging of cancer cells through in situ biosynthesis of Zn & Fe nanoclusters. *Nano Res.*, 10:2626–2632.

Edge, D., Shortt, C. M., Gobbo, O. L., Teughels, S., Prina-mello, A., Volkov, Y., Maceneaney, P., Radomski, M. W., and Markos, F. (2016). Pharmacokinetics and bio-distribution of novel super paramagnetic iron oxide nanoparticles (SPIONs) in the anaesthetized pig. *Clin. Exp. Pharmacol. Physiol.*, 43:319–326.

El-sayed, A., Futaki, S., and Harashima, H. (2009). Delivery of Macromolecules Using Arginine-Rich Cell-Penetrating Peptides : Ways to Overcome Endosomal Entrapment. *AAPS J.*, 11:13–22.

Fargašová, A., Balzerová, A., Prucek, R., Sedláková, M. H., Bogdanova, K., Gallo, J., Kolar, M., Fargašová, A., Balzerová, A., Prucek, R., Sedláková, M. H., Ranc, V., and Zboil, R. (2017). Rapid Detection of Prosthetic Joint Infection Based on Magnetically Assisted Surface Enhanced Raman Spectroscopy (MA-SERS). *Anal. Biochem.*, 89:6598–6607.

Feng, Y., Ngu, H., Alford, S. K., Ward, M., Yin, F., and Longmore, G. D. (2013). Actinin1 and 4 tyrosine phosphorylation is critical for stress fiber establishment, maintenance and focal adhesion maturation. *Exp. Cell Res.*, 319:1124–1135.

Fernandes, R., Smyth, N. R., Muskens, O. L., Nitti, S., Heuer-Jungemann, A., Ardern-Jones, M. R., and Kanaras, A. G. (2015). Interactions of skin with gold nanoparticles of different surface charge, shape, and functionality. *Small*, 11:713–21.

Ferrari, A. C. and Basko, D. M. (2013). Raman spectroscopy as a versatile tool for studying the properties of graphene. *Nat Nanotechnol*, 8:235–246.

Feynman, R., Leighton, R., and Sands, M. (1963). *The Feynman Lectures on Physics*. Addison-Wesley.

Fire, A., Xu, S., Montgomery, M. K., Kostas, S. A., Driver, S. E., and Mello, C. C. (1998). Potent and specific genetic interference by double-stranded RNA in Caenorhabditis elegans. *Nature*, 391:806–811.

Fouriki, A. and Dobson, J. (2013). Nanomagnetic gene transfection for non-viral gene delivery in nih 3t3 mouse embryonic fibroblasts. *Materials (Basel).*, 6:255–264.

Fouriki, a., Farrow, N., Clements, M., and Dobson, J. (2010). Evaluation of the magnetic field requirements for nanomagnetic gene transfection. *Nano Rev.*, 1:1–5.

Fröhlich, E. (2012). The role of surface charge in cellular uptake and cytotoxicity of medical nanoparticles. *Int. J. Nanomedicine*, 7:5577–5591.

Fröhlich, E., Samberger, C., Kueznik, T., Absenger, M., Roblegg, E., Zimmer, A., and Pieber, T. R. (2009). Cytotoxicity of nanoparticles independent from oxidative stress. *J. Toxicol. Sci.*, 34:363–375.

Fu, G.-F., Pan, J.-C., Lin, N., Hu, H.-Y., Tang, W.-M., Xu, J.-S., Wang, X.-L., Xu, X.-Q., Qiu, T., Liu, X.-Y., Chen, G.-H., Mahapatra, T., Huan, X.-P., and Yang, H.-T. (2014). siRNA Against KIR3DL1 as a Potential Gene Therapeutic Agent in Controlling HIV-1 Infection. *Viral Immunol.*, 27:207–213.

Fukumoto, Y., Obata, Y., Ishibashi, K., Tamura, N., Kikuchi, I., Aoyama, K., Hattori, Y., Tsuda, K., Nakayama, Y., and Yamaguchi, N. (2010). Cost-effective gene transfection by DNA compaction at pH 4.0 using acidified, long shelf-life polyethylenimine. *Cytotechnology*, 62:73–82.

Furlani, E. P. and Xue, X. (2012). Field, force and transport analysis for magnetic particle-based gene delivery. *Microfluid. Nanofluidics*, 13:589–602.

Gabrielson, N. P. and Pack, D. W. (2009). Efficient polyethylenimine-mediated gene delivery proceeds via a caveolar pathway in HeLa cells. *J. Control. Release*, 136:54–61.

Galbraith, C. G., Yamada, K. M., and Sheetz, M. P. (2002). The relationship between force and focal complex development. *J. Cell Biol.*, 159:695–705.

Gianotti, A., Melani, R., Caci, E., Sondo, E., Ravazzolo, R., Galietta, L. J. V., and Zegarra-Moran, O. (2013). Epithelial Sodium Channel Silencing as a Strategy to Correct the Airway Surface Fluid Deficit in Cystic Fibrosis. *Am. J. Respir. Cell Mol. Biol.*, 49:445–452.

Gillard, M., Jia, Z., Hou, J. J. C., Song, M., Gray, P. P., Munro, T. P., and Monteiro, M. J. (2014). Intracellular Trafficking Pathways for Nuclear Delivery of Plasmid DNA Complexed with Highly Efficient Endosome Escape Polymers. *Biomacromolecules*, 15:3569–3576.

Godbey, W. T., Barry, M. a., Saggau, P., Wu, K. K., and Mikos, a. G. (2000). Poly(ethylenimine)-mediated transfection: a new paradigm for gene delivery. *J. Biomed. Mater. Res.*, 51:321–8.

Godbey, W. T., Wu, K. K., Hirasaki, G. J., and Mikos, A. G. (1999a). Improved packing of poly (ethylenimine)/ DNA complexes increases transfection efficiency. *Gene Ther.*, 6:1380–1388.

Godbey, W. T., Wu, K. K., and Mikos, a. G. (1999b). Tracking the intracellular path of poly(ethylenimine)/DNA complexes for gene delivery. *Proc. Natl. Acad. Sci. U. S. A.*, 96:5177–81.

Godbey, W. T., Wu, K. K., and Mikos, A. G. (2001). Poly(ethylenimine)-mediated gene delivery affects endothelial cell function and viability. *Biomaterials*, 22:471–480.

Goldmann, W. H., Guttenberg, Z., Tang, J. X., Kroy, K., Isenberg, G., and Ezzell, R. M. (1998). Analysis of the F-actin binding fragments of vinculin using stopped-flow and dynamic light-scattering measurements. *Eur. J. Biochem.*, 254:413–9.

Golovin, Y. I., Klyachko, N. L., Gribanovskii, S. L., Golovin, D. Y., Samodurov, A. A., Majouga, A. G., Sokolsky-Papkov, M., and Kabanov, A. V. (2015). Nanomechanical control of properties of biological membranes achieved by rodlike magnetic nanoparticles in a superlow-frequency magnetic field. *Tech. Phys. Lett.*, 41:455–457.

Govindarajan, S., Kitaura, K., Takafuji, M., and Ihara, H. (2013). Gene delivery into human cancer cells by cationic lipid-mediated magnetofection. *Int. J. Pharm.*, 446:87–99.

Gratton, S. E. A., Napier, M. E., Ropp, P. A., Tian, S., and DeSimone, J. M. (2008a). Microfabricated particles for engineered drug therapies: Elucidation into the mechanisms of cellular internalization of PRINT particles. *Pharm. Res.*, 25:2845–2852.

Gratton, S. E. a., Ropp, P. a., Pohlhaus, P. D., Luft, J. C., Madden, V. J., Napier, M. E., and DeSimone, J. M. (2008b). The effect of particle design on cellular internalization pathways. *Proc. Natl. Acad. Sci. U. S. A.*, 105:11613–11618.

Gupta, A. K. and Gupta, M. (2005). Synthesis and surface engineering of iron oxide nanoparticles for biomedical applications. *Biomaterials*, 26:3995–4021.

Halbleib, J. M. and Nelson, W. J. (2006). Cadherins in development: Cell adhesion, sorting, and tissue morphogenesis. *Genes Dev.*, 20:3199–3214.

Hall, A., Lächelt, U., Bartek, J., Wagner, E., and Moghimi, S. M. (2017). Polyplex Evolution : Understanding Biology , Optimizing Performance. *Mol. Ther.*, 25:1–15.

Heino, J. (2007). The collagen family members as cell adhesion proteins. *BioEssays*, 29:1001–1010.

Höbel, S., Prinz, R., Malek, A., Urban-Klein, B., Sitterberg, J., Bakowsky, U., Czubayko, F., and Aigner, A. (2008). Polyethylenimine PEI F25-LMW allows the long-term storage of frozen complexes as fully active reagents in siRNA-mediated gene targeting and DNA delivery. *Eur. J. Pharm. Biopharm.*, 70:29–41.

Hohnholt, M. C., Geppert, M., and Dringen, R. (2011). Treatment with iron oxide nanoparticles induces ferritin synthesis but not oxidative stress in oligodendroglial cells. *Acta Biomater.*, 7:3946–3954.

Holler, S., Mansley, E., Mazzeo, C., Donovan, M. J., Sobrero, M., and Miles, B. A. (2017). Raman Spectroscopy of Head and Neck Cancer : Separation of Malignant and Healthy Tissue Using Signatures Outside the Fingerprint Region. *Biosensors*, 7:E20.

Hoskins, C., Wang, L., Cheng, W. P., and Cuschieri, A. (2012). Dilemmas in the reliable estimation of the in-vitro cell viability in magnetic nanoparticle engineering : which tests and what protocols? *Nanoscale Res. Lett.*, 7:1–12.

Hsiao, S.-m., Peng, B.-y., Shun, Y., Liu, H.-t., Chen, C.-h., and Prof, H.-m. L. (2017). Microporous and Mesoporous Materials Preparation and characterization of multifunctional mesoporous silica nanoparticles for dual magnetic resonance and fluorescence imaging in targeted cancer therapy. *Microporous Mesoporous Mater.*, 250:210–220.

Hughes, C., Galea-Lauri, J., Farzaneh, F., and Darling, D. (2001). Streptavidin paramagnetic particles provide a choice of three affinity-based capture and magnetic concentration strategies for retroviral vectors. *Mol. Ther.*, 3:623–30.

Humphries, J. D., Wang, P., Streuli, C., Geiger, B., Humphries, M. J., and Ballestrem, C. (2007). Vinculin controls focal adhesion formation by direct interactions with talin and actin. *J. Cell Biol.*, 179:1043–1057.

Jain, T. K., Reddy, M. K., Morales, M. A., Leslie-pelecky, D. L., and Labhasetwar, V. (2008). Biodistribution , Clearance , and Biocompatibility of Iron Oxide Magnetic Nanoparticles in Rats. *Mol. Pharm.*, 5:316–327.

Jeong, B. U., Teng, X., Wang, Y., Yang, H., and Xia, Y. (2007). Superparamagnetic Colloids : Controlled Synthesis and Niche Applications. *Adv. Mater.*, 19:33–60.

Jiles, D. (1991). *Introduction to magnetism and magnetic materials*. Chapman and Hall.

Jinek, M. and Doudna, J. a. (2009). A three-dimensional view of the molecular machinery of RNA interference. *Nature*, 457(7228):405–12.

Josephson, L., Kircher, M. F., Mahmood, U., Tang, Y., and Weissleder, R. (2002). Near-Infrared Fluorescent Nanoparticles as Combined MR / Optical Imaging Probes. *Bioconjug. Chem.*, 13:554–560.

Jukkola, A., Risteli, L., Melkko, J., and Risteli, J. (1993). Procollagen Synthesis and Extracellular Matrix Deposition in MG- 63 Osteosarcoma Cells. *J.Bone Miner.Res.*, 8:651–657.

Jun, Y.-w., Seo, J.-w., and Cheon, J. (2008). Nanoscaling Laws of Magnetic Nanoparticles and Their Applicabilities in Biomedical Sciences. *Acc. Chem. Res.*, 41:179–189.

Kafil, V. and Omidi, Y. (2011). Cytotoxic Impacts of Linear and Branched Polyethylenimine Nanostructures in A431 Cells. *Bioimpacts*, 1:23–30.

Kamau, S. W., Hassa, P. O., Steitz, B., Petri-fink, A., Hofmann, H., Hofmann-amtenbrink, M., Rechenberg, B. V., and Hottiger, M. O. (2006). Enhancement of the efficiency of non-viral gene delivery by application of pulsed magnetic field. *Nucleic Acids Res.*, 34:e40.

Kang, B., Afifi, M. M., Austin, L. a., El-sayed, M. a., States, U., Science, M., Pathology, O., and St, C. (2013). Exploiting the Nanoparticle Plasmon Effect : Observing Drug Delivery Dynamics in Single Cells via Raman / Fluorescence Imaging Spectroscopy. *ACS Nano*, 7:7420–7427.

Kang, T., Li, F., Baik, S., Shao, W., Ling, D., and Hyeon, T. (2017). Surface design of magnetic nanoparticles for stimuli-responsive cancer imaging and therapy. *Biomaterials*, 136:98–114.

Kapilov-Buchman, Y., Lellouche, E., Michaeli, S., and Lellouche, J.-P. (2015). Unique Surface Modification of Silica Nanoparticles with Polyethylenimine (PEI) for siRNA Delivery Using Cerium Cation Coordination Chemistry. *Bioconjug. Chem.*, 26:880–889.

Karaagac, O., Kockar, H., Beyaz, S., and Tanrisever, T. (2010). A Simple Way to Synthesize Superparamagnetic Iron Oxide Nanoparticles in Air Atmosphere: Iron Ion Concentration Effect. *IEEE Trans. Magn.*, 46:3978–3983.

Karpov, A., Kozireva, S., Avotia, D., Chernobayeva, L., and Baryshev, M. (2014). Investigation of nanoparticle distribution formed by the rotation of the magnetic system. *J. Magn. Magn. Mater.*, 369:86–91.

Ke, C., Lan, Z., Hua, L., Ying, Z., Humina, X., Jia, S., Weizheng, T., Ping, Y., Lingying, C., and Meng, M. (2015). Iron metabolism in infants :influence of bovine lactoferrin from iron-fortified formula. *Nutrition*, 31:304–309.

Kenneth, D., Charles, S., Kevin, L., Guoda, L., Donald, G., and Matthew, J. (2005). Epithelial internalization of superparamagnetic nanoparticles and response to external magnetic field. *Biomaterials*, 26:2061–2072.

Khatau, S. B., Hale, C. M., Stewart-hutchinson, P. J., Patel, M. S., Stewart, C. L., Searson, P. C., Hodzic, D., and Wirtz, D. (2009). A perinuclear actin cap regulates nuclear shape. *Proc. Natl. Acad. Sci.*, 106:19017–19022.

Kiefer, W. (2007). Recent Advances in linear and nonlinear Raman spectroscopy I. *J. Raman Spectrosc.*, 38:1538–1553.

Kim, J.-E., Kim, S.-J., Jeong, H.-W., Lee, B.-H., Choi, J.-Y., Park, R.-W., Park, J. Y., and Kim, I.-S. (2003). RGD peptides released from beta ig-h3, a TGF-beta-induced cell-adhesive molecule, mediate apoptosis. *Oncogene*, 22:2045–53.

Kim, T. K. and Eberwine, J. H. (2010). Mammalian cell transfection: the present and the future. *Anal. Bioanal. Chem.*, 397(8):3173–8.

Kurtulus, I., Yilmaz, G., Ucuncu, M., Emrullahoglu, M., Becer, C. R., and Bulmus, V. (2014). A new proton sponge polymer synthesized by RAFT polymerization for intracellular delivery of biotherapeutics. *Polym. Chem.*, 5:1593–1604.

Lamaze, C., Fujimoto, L. M., Yin, H. L., and Schmid, S. L. (1997). The Actin Cytoskeleton Is Required for Receptor-mediated. *J. Biol. Chem.*, 272:20332–20335.

LaMer, V. and Dinegar, R. (1950). Theory, production and mechanism of formation of monodispersed hydrosols. *J. Am. Chem. Soc.*, 72:4847–4854.

Laner, A., Goussard, S., Ramalho, A. S., Schwarz, T., Amaral, M. D., Courvalin, P., Schindelhauer, D., and Grillot-Courvalin, C. (2005). Bacterial transfer of large functional genomic DNA into human cells. *Gene Ther.*, 12:1559–1572.

Langel, Ü. (2011). *Cell-penetrating peptides. Methods and protocols.* Humana Press.

Laurent, S., Forge, D., Port, M., Roch, A., Robic, C., Vander Elst, L., and Muller, R. N. (2008). Magnetic iron oxide nanoparticles: Synthesis, stabilization, vectorization, physicochemical characterizations and biological applications. *Chem. Rev.*, 108:2064–2110.

Le Clainche, C., Dwivedi, S. P., Didry, D., and Carlier, M. F. (2010). Vinculin is a dually regulated actin filament barbed end-capping and side-binding protein. *J. Biol. Chem.*, 285:23420–23432.

Leary, N. A. O., Wright, M. W., Brister, J. R., Ciufo, S., Haddad, D., Mcveigh, R., Rajput, B., Robbertse, B., Smith-white, B., Ako-adjei, D., Astashyn, A., Badretdin, A., Bao, Y., Blinkova, O., Brover, V., Chetvernin, V., Choi, J., Cox, E., Ermolaeva, O., Farrell, C. M., Goldfarb, T., Gupta, T., Haft, D., Hatcher, E., Hlavina, W., Joardar, S., Kodali, V. K., Li, W., Maglott, D., Masterson, P., Mcgarvey, M., Murphy, M. R., Neill, K. O., Pujar, S., Rangwala, S. H., Rausch, D., Riddick, L. D., Schoch, C., Shkeda, A., Storz, S. S., Sun, H., Thibaud-nissen, F., Tolstoy, I., Tully, R. E., Vatsan, R., Wallin, C., Webb, D., Wu, W., Landrum, M. J., Kimchi, A., Tatusova, T., Dicuccio, M., Kitts, P., Murphy, T. D., and Pruitt, K. D. (2016). Reference sequence (RefSeq) database at NCBI : current status, taxonomic expansion, and functional annotation. *Nucleic Acids Res.*, 44:733–745.

LeBaron, R. G., Bezverkov, K. I., Zimber, M. P., Pavelec, R., Skonier, J., and Purchio, A. F. (1995). Beta IG-H3, a novel secretory protein inducible by transforming growth factor-beta, is present in normal skin and promotes the adhesion and spreading of dermal fibroblasts in vitro.

Leclerc, L., Rima, W., Boudard, D., Pourchez, J., Forest, V., Bin, V., Mowat, P., Perriat, P., Tillement, O., Grosseau, P., Bernache-Assollant, D., and Cottier, M. (2012). Size of submicrometric and nanometric particles affect cellular uptake and biological activity of macrophages in vitro. *Inhal. Toxicol.*, 24:580–8.

Lee, J. M., Lee, E. H., Kim, I. S., and Kim, J. E. (2014). Tgfbi deficiency leads to a reduction in skeletal size and degradation of the bone matrix. *Calcif. Tissue Int.*, 96:56–64.

Lee, M. (2007). Apoptosis Induced by Polyethylenimine / DNA Complex in Polymer Mediated Gene Delivery. *Bull. Korean Chem. Soc*, 28:95–98.

Lee, M. S., Kim, N. W., Lee, K., Kim, H., and Jeong, J. H. (2013). Enhanced transfection by antioxidative polymeric gene carrier that reduces polyplex-mediated cellular oxidative stress. *Pharm. Res.*, 30:1642–1651.

Lerch, S., Dass, M., Musyanovych, A., Landfester, K., and Mailänder, V. (2013). Polymeric nanoparticles of different sizes overcome the cell membrane barrier. *Eur. J. Pharm. Biopharm.*, 84:265–274.

LeVine, H. (2006). *Genetic Engineering: A Reference Handbook*. ABC-CLIO.

Li, S.-D. and Huang, L. (2006). Gene therapy progress and prospects: non-viral gene therapy by systemic delivery. *Gene Ther.*, 13:1313–9.

Lim, J., Clements, M. A., and Dobson, J. (2012). Delivery of Short Interfering Ribonucleic Acid-Complexed Magnetic Nanoparticles in an Oscillating Field Occurs via Caveolae-Mediated Endocytosis. *PLoS One*, 7:e51350.

Lim, J., Yeap, S., Che, H., and Low, S. (2013). Characterization of magnetic nanoparticle by dynamic light scattering. *Nanoscale Res. Lett.*, 8:381.

Lin, Z.-b., Tian, J.-h., Xie, B.-g., Tang, Y.-a., Sun, J.-j., Chen, G.-n., Ren, B., Mao, B.-w., and Tian, Z.-q. (2009). Electrochemical and in Situ SERS Studies on the Adsorption of 2-Hydroxypyridine and Polyethyleneimine during Silver Electroplating. *J. Phys. Chem. C*, 113:9224–9229.

Litman, P., Amieva, M. R., and Furthmayr, H. (2000). Imaging of Dynamic Changes of the Actin Cytoskeleton in Microextensions of Live NIH3T3 Cells with a GFP Fusion of the F-Actin Binding Domain of Moesin. *BMC Cell Biol.*, 1:1.

Liu, W., Wang, H., Du, J., and Jing, C. (2017). Biosensors and Bioelectronics Raman microspectroscopy of nucleus and cytoplasm for human colon cancer diagnosis. *Biosens. Bioelectron.*, 97:70–74.

Liu, Y., Li, C. S., Feng, C. L., and Yu, A. H. (2016). Novel Disulfide-Containing Poly (b -amino ester) - Functionalised Magnetic Nanoparticles for Efficient Gene Delivery. *Aust. J. Chem.*, 69:349–356.

Lojk, J., Strojan, K., Mis, K., Bregar, B. V., Hafner Bratkovic, I., Bizjak, M., Pirkmajer, S., and Pavlin, M. (2017). Cell stress response to two different types of polymer coated cobalt ferrite nanoparticles. *Toxicol. Lett.*, 270:108–118.

Luo, D. and Saltzman, W. (2000). Synthetic DNA delivery systems. *Nat. Biotechnol.*, 18:33–37.

Lv, P., Zhou, C., Zhao, Y., Liao, X., and Yang, B. (2017). Modified-epsilon-polylysine-grafted-PEI-β-cyclodextrin Supramolecular Carrier for Gene Delivery. *Carbohydr. Polym.*, 168:103–111.

Magin-Lachmann, C., Kotzamanis, G., D'Aiuto, L., Cooke, H., Huxley, C., and Wagner, E. (2004). In vitro andin vivo delivery of intact BAC DNA comparison of different methods. *J. Gene Med.*, 6:195–209.

Mahmoudi, M., Hofmann, H., Rothen-Rutishauser, B., and Petri-Fink, A. (2012). Assessing the in vitro and in vivo toxicity of superparamagnetic iron oxide nanoparticles. *Chem. Rev.*, 112:2323–38.

Mahmoudi, M., Sant, S., Wang, B., Laurent, S., and Sen, T. (2011). Superparamagnetic iron oxide nanoparticles (SPIONs): development, surface modification and applications in chemotherapy. *Adv. Drug Deliv. Rev.*, 63:24–46.

Maldonado-Camargo, L., Torres-Díaz, I., Chiu-Lam, A., Hernández, M., and Rinaldi, C. (2016). Estimating the contribution of Brownian and Neel relaxation in a magnetic fluid through dynamic magnetic susceptibility measurements. *J. Magn. Magn. Mater.*, 412:223–233.

Markides, H., Rotherham, M., and El Haj, A. J. (2012). Biocompatibility and Toxicity of Magnetic Nanoparticles in Regenerative Medicine. *J. Nanomater.*, 2012:1–11.

Mattila, P. K. and Lappalainen, P. (2008). Filopodia: molecular architecture and cellular functions. *Nat. Rev. Mol. Cell Biol.*, 9:446–454.

Mayor, S. and Pagano, R. E. (2007). Pathways of clathrin-independent endocytosis. *Nat. Rev. Mol. Cell Biol.*, 8:603–612.

Mbeh, D. A., Mireles, L. K., Stanicki, D., Tabet, L., Maghni, K., Laurent, S., Sacher, E., and Yahia, L. (2015). Human Alveolar Epithelial Cell Responses to CoreShell Superparamagnetic Iron Oxide Nanoparticles (SPIONs). *Langmuir*, 31:3829–3839.

McBain, S. C., Griesenbach, U., Xenariou, S., Keramane, A., Batich, C. D., Alton, E. W. F. W., and Dobson, J. (2008a). Magnetic nanoparticles as gene delivery agents: enhanced transfection in the presence of oscillating magnet arrays. *Nanotechnology*, 19:405102.

McBain, S. C., Yiu, H. H. P., and Dobson, J. (2008b). Magnetic nanoparticles for gene and drug delivery. *Int. J. Nanomedicine*, 3:169–180.

McCracken, C., Zane, A., Knight, D. A., Hommel, E., Dutta, P. K., and Waldman, W. J. (2015). Oxidative stress-mediated inhibition of intestinal epithelial cell proliferation by silver nanoparticles. *Toxicol. Vitr.*, 29:1793–1808.

McMahon, H. T. H. and Boucrot, E. (2011). Molecular mechanism and physiological functions of clathrin-mediated endocytosis. *Nat. Rev. Mol. Cell Biol.*, 12:517–33.

Mehravi, B., Alizadeh, A. M., Khodayari, S., Khodayari, H., Ashtari, K., Mohseni, M., Anaraki, N. I., Dana, E. A., Safari, S., and Amanlou, M. (2017). Acute Toxicity Evaluation of Glycosylated Gd 3 + -Based Silica Nanoprobe. *Mol Imaging Biol*, 19:522–530.

Mehta, S. H., Webb, R. C., and Dorrance, A. M. (2004). Neuroprotection by tempol in a model of iron-induced oxidative stress in acute ischemic stroke. *Am J Physiol Regul Integr Comp Physiol*, 286:283–288.

Miller, I. S., Lynch, I., Dowling, D., Dawson, K. A., and Gallagher, W. M. (2010). Surface-induced cell signaling events control actin rearrangements and motility. *J. Biomed. Mater. Res. - Part A*, 93:493–504.

Mohseny, A. B., Machado, I., Cai, Y., Schaefer, K.-L., Serra, M., Hogendoorn, P. C. W., Llombart-Bosch, A., and Cleton-Jansen, A.-M. (2011). Functional characterization of osteosarcoma cell lines provides representative models to study the human disease. *Lab. Investig.*, 91:1195–1205.

Moreira, L. M., Silveira, L., Santos, F. V., Lyon, J. P., Rocha, R., Zângaro, R. A., Villaverde, A. B., and Pacheco, M. T. T. (2008). Raman spectroscopy: A powerful technique for biochemical analysis and diagnosis. *Spectroscopy*, 22:1–19.

Movasaghi, Z., Rehman, S., and Rehman, I. U. (2007). Raman Spectroscopy of Biological Tissues. *Appl. Spectrosc. Rev.*, 42:493–541.

Myllyharju, J. (2003). Prolyl 4-hydroxylases, the key enzymes of collagen biosynthesis. *Matrix Biol.*, 22:15–24.

Nabeshi, H., Yoshikawa, T., Arimori, A., Yoshida, T., Tochigi, S., Hirai, T., Akase, T., Nagano, K., Abe, Y., Kamada, H., Tsunoda, S.-i., and Itoh, N. (2011). Effect of surface properties of silica nanoparticles on their cytotoxicity and cellular distribution in murine macrophages. *Nanoscale Res. Lett.*, 6:1–6.

Naldini, L. (2015). Gene therapy returns to centre stage. *Nature*, 526:1–10.

Nishimura, Y., Mieda, H., Ishii, J., Ogino, C., Fujiwara, T., and Kondo, A. (2013). Targeting cancer cell-specific RNA interference by siRNA delivery using a complex carrier of affibody-displaying bio-nanocapsules and liposomes. *J. Nanobiotechnology*, 11:19–28.

Noothalapati, H., Iwasaki, K., and Yamamoto, T. (2017). Biological and Medical Applications of Multivariate Curve Resolution Assisted Raman Spectroscopy. *Anal. Sci.*, 33:15–22.

Okada, M., Smith, N. I., Palonpon, A. F., Endo, H., Kawata, S., Sodeoka, M., and Fujita, K. (2012). Label-free Raman observation of cytochrome c dynamics during apoptosis. *Proc. Natl. Acad. Sci. U. S. A.*, 109:28–32.

Oliveira, A. B. B., De Moraes, F. R., Candido, N. M., Sampaio, I., Paula, A. S., Miller, A. H., Rahal, P., Nery, J. G., and Calmon, M. F. (2016). Metabolic Effects of Cobalt Ferrite Nanoparticles on Cervical Carcinoma Cells and Nontumorigenic Keratinocytes. *J. Proteome Res.*, 15:4337–4348.

Pankhurst, Q. A., Connolly, J., Jones, S. K., and Dobson, J. (2003). Applications of magnetic nanoparticles in biomedicine. *J. Phys. D. Appl. Phys.*, 36:R167–R181.

Park, J., An, K., Hwang, Y., Park, J.-G., Noh, H.-J., Kim, J.-Y., Park, J.-H., Hwang, N.-M., and Hyeon, T. (2004). Ultra-large-scale syntheses of monodisperse nanocrystals. *Nat. Mater.*, 3:891–895.

Park, J., Hwang, M., Choi, B., Jeong, H., Kim, H. K., Hong, S., Park, J. H., Choi, Y., Park, J., Hwang, M., Choi, B., Jeong, H., Jung, J.-h., and Koo, H. (2017a). Exosome Classification by Pattern Analysis of Surface- enhanced Raman Spectroscopy Data for Lung Cancer Diagnosis. *Anal. Chem.*, 89:6695–6701.

Park, J. S., Park, W., Park, S.-j., Larson, A. C., Kim, D.-h., and Park, K.-h. (2017b). Multimodal Magnetic Nanoclusters for Gene Delivery, Directed Migration, and Tracking of Stem Cells. *Adv. Funct. Mater.*, 27:1700396.

Park, M. V. D. Z., Neigh, A. M., Vermeulen, J. P., de la Fonteyne, L. J. J., Verharen, H. W., Briedé, J. J., van Loveren, H., and de Jong, W. H. (2011). The effect of particle size on the cytotoxicity, inflammation, developmental toxicity and genotoxicity of silver nanoparticles. *Biomaterials*, 32:9810–9817.

Park, T. G., Jeong, J. H., and Kim, S. W. (2006). Current status of polymeric gene delivery systems. *Adv. Drug Deliv. Rev.*, 58:467–86.

Peer, D. and Lieberman, J. (2011). Special delivery: targeted therapy with small RNAs. *Gene Ther.*, 18:1127–1133.

Pellegrin, S. and Mellor, H. (2007). Actin stress fibres. *J. Cell Sci.*, 120:3491–3499.

Peng, H., Hu, J., Hu, C., Wu, T., and Tian, X. (2017). Microwave Absorbing Fe3O4@mTiO2 Nanoparticles as an Intelligent Drug Carrier for Microwave-Triggered Synergistic Cancer Therapy. *J. Nanosci. Nanotechnol.*, 17:5139–5146.

Pestonjamasp, K. N., Pope, R. K., Wulfkuhle, J. D., and Luna, E. J. (1997). Supervillin (p205): A novel membrane-associated, F-actin-binding protein in the villin/gelsolin superfamily. *J. Cell Biol.*, 139:1255–1269.

Pickard, M. and Chari, D. M. (2010a). Enhancement of magnetic nanoparticle-mediated gene transfer to astrocytes by magnetofection ': effects of static and oscillating fields. *Nanomedicine*, 5:217–232.

Pickard, M. R. and Chari, D. M. (2010b). Robust Uptake of Magnetic Nanoparticles (MNPs) by Central Nervous System (CNS) Microglia : Implications for Particle Uptake in Mixed Neural Cell Populations. *Int. J. Mol. Sci*, 11:967–981.

Plank, C., Zelphati, O., and Mykhaylyk, O. (2011). Magnetically enhanced nucleic acid delivery. Ten years of magnetofection-Progress and prospects. *Adv. Drug Deliv. Rev.*, 63:1300–1331.

Prow, T., Smith, J. N., Grebe, R., Salazar, J. H., Wang, N., Kotov, N., and Lutty, G. (2006). Construction , gene delivery , and expression of DNA tethered nanoparticles. *Mol. Vis.*, 12:606–615.

Raju, M., Srivastava, S., Nair, R. R., Raval, I. H., and Haldar, S. (2017). Biosensors and Bioelectronics Siderophore coated magnetic iron nanoparticles : Rational designing of water soluble nanobiosensor for visualizing Al3+ in live organism. *Biosens. Bioelectron.*, 97:338–344.

Ramimoghadam, D., Bagheri, S., and Abd Hamid, S. B. (2014). Stable monodisperse nanomagnetic colloidal suspensions: An overview. *Colloids Surfaces B Biointerfaces*, 133:388–411.

Raval, Y. S., Fellows, B. D., Murbach, J., Cordeau, Y., and Mefford, O. T. (2017). Multianchored Glycoconjugate-Functionalized Magnetic Nanoparticles : A Tool for Selective Killing of Targeted Bacteria via Alternating Magnetic Fields. *Adv. Funct. Mater.*, 27:1701473.

Reddy, L. H., Arias, J. L., Nicolas, J., and Couvreur, P. (2012). Magnetic nanoparticles: Design and characterization, toxicity and biocompatibility, pharmaceutical and biomedical applications. *Chem. Rev.*, 112:5818–5878.

Regnström, K., Ragnarsson, E. G. E., Fryknäs, M., Köping-Höggård, M., and Artursson, P. (2006). Gene expression profiles in mouse lung tissue after administration of two cationic polymers used for nonviral gene delivery. *Pharm. Res.*, 23:475–482.

Resnier, P., Montier, T., Mathieu, V., Benoit, J.-P., and Passirani, C. (2013). A review of the current status of siRNA nanomedicines in the treatment of cancer. *Biomaterials*, 34:6429–6443.

Ridley, A. J. and Hall, A. (1992). The small GTP-binding protein rho regulates the assembly of focal adhesions and actin stress fibers in response to growth factors. *Cell*, 70:389–399.

Robbins, P. D. and Ghivizzani, S. C. (1998). Viral vectors for gene therapy. *Pharmacol. Ther.*, 80:35–47.

Rodriguez-Lorenzo, L., Rothen-Rutishauser, B., Petri-Fink, A., and Balog, S. (2015). Nanoparticle Polydispersity Can Strongly Affect In Vitro Dose. *Part. Part. Syst. Charact.*, 32:321–333.

Sabuncu, A. C., Grubbs, J., Qian, S., Abdel-Fattah, T. M., Stacey, M. W., and Beskok, A. (2012). Probing nanoparticle interactions in cell culture media. *Colloids Surfaces B Biointerfaces*, 95:96–102.

Sancar, A., Lindsey-Boltz, L. a., Unsal-Kaçmaz, K., and Linn, S. (2004). Molecular mechanisms of mammalian DNA repair and the DNA damage checkpoints. *Annu. Rev. Biochem.*, 73:39–85.

Sanchez-Antequera, Y., Mykhaylyk, O., van Til, N. P., Cengizeroglu, A., de Jong, J. H., Huston, M. W., Anton, M., Johnston, I. C. D., Pojda, Z., Wagemaker, G., and Plank, C. (2011). Magselectofection: an integrated method of nanomagnetic separation and genetic modification of target cells. *Blood*, 117:e171–e181.

Sauer, A., de Bruin, K., Ruthardt, N., Mykhaylyk, O., Plank, C., and Bräuchle, C. (2009). Dynamics of magnetic lipoplexes studied by single particle tracking in living cells. *J. Control. Release*, 137:136–145.

Scherer, F., Anton, M., and Schillinger, U. (2002). Magnetofection: enhancing and targeting gene delivery by magnetic force in vitro and in vivo. *Gene Ther.*, 9:102–109.

Schladt, T. D., Graf, T., and Tremel, W. (2009). Synthesis and Characterization of Monodisperse Manganese Oxide NanoparticlesEvaluation of the Nucleation and Growth Mechanism. *Chem. Mater.*, 21:3183–3190.

Scholz, C. and Wagner, E. (2012). Therapeutic plasmid DNA versus siRNA delivery: Common and different tasks for synthetic carriers. *J. Control. Release*, 161:554–565.

Sensenig, R., Sapir, Y., MacDonald, C., Cohen, S., and Polyak, B. (2012). Magnetic nanoparticle-based approaches to locally target therapy and enhance tissue regeneration in vivo. *Nanomedicine*, 7:1425–1442.

Shah, B., Yin, P. T., Ghoshal, S., and Lee, K.-B. (2013). Multimodal Magnetic Core-Shell Nanoparticles for Effective Stem-Cell Differentiation and Imaging. *Angew. Chemie Int. Ed.*, 52:6190–6195.

Shang, L., Nienhaus, K., Jiang, X., Yang, L., Landfester, K., Mailander, V., Simmet, T., and Nienhaus, G. U. (2014). Nanoparticle interactions with live cells: Quantitative fluorescence microscopy of nanoparticle size effects. *Beilstein J. Nanotechnol.*, 5:2388–2397.

Shashni, B., Horiguchi, Y., Kurosu, K., and Furusho, H. (2017). Biomaterials Application of surface enhanced Raman spectroscopy as a diagnostic system for hypersialylated metastatic cancers. *Biomaterials*, 134:143–153.

Shaterabadi, Z., Nabiyouni, G., and Soleymani, M. (2017). High impact of in situ dextran coating on biocompatibility, stability and magnetic properties of iron oxide nanoparticles. *Mater. Sci. Eng. C*, 75:947–956.

Sim, T., Park, G., Min, H., Kang, S., Lim, C., Bae, S., Lee, E. S., and Youn, Y. S. (2017). Development of a gene carrier using a triblock co-polyelectrolyte with poly (ethylene imine) -poly (lactic acid) -poly (ethylene glycol). *J. Bioact. Compat. Polym.*, 32(3):280–292.

Sjöblom, B., Salmazo, A., and Djinović-Carugo, K. (2008). α-Actinin structure and regulation. *Cell. Mol. Life Sci.*, 65:2688–2701.

Small, J. V., Rottner, K., Kaverina, I., and Anderson, K. I. (1998). Assembling an actin cytoskeleton for cell attachment and movement. *Biochim. Biophys. Acta*, 1404:271–281.

Smith, C. A. M., Fuente, J. D. L., Pelaz, B., Furlani, E. P., Mullin, M., and Berry, C. C. (2010). The effect of static magnetic fields and tat peptides on cellular and nuclear uptake of magnetic nanoparticles. *Biomaterials*, 31:4392–4400.

Soenen, S. J. H., Himmelreich, U., Nuytten, N., and De Cuyper, M. (2011). Cytotoxic effects of iron oxide nanoparticles and implications for safety in cell labelling. *Biomaterials*, 32:195–205.

Soenen, S. J. H., Illyes, E., Vercauteren, D., Braeckmans, K., Majer, Z., Smedt, S. C. D., and Cuyper, M. D. (2009). Biomaterials The role of nanoparticle concentration-dependent induction of cellular stress in the internalization of non-toxic cationic magnetoliposomes. *Biomaterials*, 30:6803–6813.

Soenen, S. J. H., Nuytten, N., De Meyer, S. F., De Smedt, S. C., and De Cuyper, M. (2010). High intracellular iron oxide nanoparticle concentrations affect cellular cytoskeleton and focal adhesion kinase-mediated signaling. *Small*, 6:832–842.

Sohrabijam, Z., Saeidifar, M., and Zamanian, A. (2017). Colloids and Surfaces B : Biointerfaces Enhancement of magnetofection efficiency using chitosan coated superparamagnetic iron oxide nanoparticles and calf thymus DNA. *Colloids Surfaces B Biointerfaces*, 152:169–175.

Somaiah, C., Kumar, A., Mawrie, D., Sharma, A., Patil, S. D., Bhattacharyya, J., Swaminathan, R., and Jaganathan, B. G. (2015). Collagen promotes higher adhesion, survival and proliferation of mesenchymal stem cells. *PLoS One*, 10:1–15.

Sonawane, N. D., Szoka, F. C., and Verkman, A. S. (2003). Chloride Accumulation and Swelling in Endosomes Enhances DNA Transfer by Polyamine-DNA Polyplexes. *J. Biol. Chem.*, 278:44826–44831.

Soukup, D., Moise, S., Céspedes, E., Dobson, J., and Telling, N. D. (2015). In situ measurement of magnetization relaxation of internalized nanoparticles in live cells. *ACS Nano*, 9:231–40.

Stiles, P. L., Dieringer, J. A., Shah, N. C., and Duyne, R. P. V. (2008). Surface-Enhanced Raman Spectroscopy. *Annu. Rev. Anal. Chem.*, 1:601–626.

Subramanian, M., Lim, J., and Dobson, J. (2013). Enhanced nanomagnetic gene transfection of human prenatal cardiac progenitor cells and adult cardiomyocytes. *PLoS One*, 8:e69812.

Sun, C., Lee, J. S., and Zhang, M. (2008). Magnetic nanoparticles in MR imaging and drug delivery. *Adv. Drug Deliv. Rev.*, 60:1252–1265.

Takizawa, N., Ikebe, R., Ikebe, M., and Luna, E. J. (2007). Supervillin slows cell spreading by facilitating myosin II activation at the cell periphery. *J. Cell Sci.*, 120:3792–803.

Takizawa, N., Smith, T. C., Nebl, T., Crowley, J. L., Palmieri, S. J., Lifshitz, L. M., Ehrhardt, A. G., Hoffman, L. M., Beckerle, M. C., and Luna, E. J. (2006). Supervillin modulation of focal adhesions involving TRIP6/ZRP-1. *J. Cell Biol.*, 174:447–458.

Tay, A. and Di Carlo, D. (2017). Magnetic nanoparticle-based mechanical stimulation for restoration of mechano-sensitive ion channel equilibrium in neural networks. *Nano Lett.*, 17:886–892.

The UniProt Consortium (2017). UniProt : the universal protein knowledgebase. *Nucleic Acids Res.*, 45:158–169.

Thompson, P. M., Tolbert, C. E., and Campbell, S. L. (2013). Vinculin and metavinculin: Oligomerization and interactions with F-actin. *FEBS Lett.*, 587:1220–1229.

Thoss, F., Dietrich, F., Punkt, K., Illenberger, S., Rottner, K., Himmel, M., and Ziegler, W. H. (2013). Metavinculin: New insights into functional properties of a muscle adhesion protein. *Biochem. Biophys. Res. Commun.*, 430:7–13.

Tojkander, S., Gateva, G., and Lappalainen, P. (2012). Actin stress fibers - assembly, dynamics and biological roles. *J. Cell Sci.*, 125:1855–1864.

Trekker, J., Jans, K., Damm, H., Mertens, D., Nuytten, T., Vanacken, J., Moshchalkov, V., D'Haen, J., Stakenborg, T., Van Roy, W., Himmelreich, U., and Lagae, L. (2013). Synthesis of PEGylated magnetic nanoparticles with different core sizes. *IEEE Trans. Magn.*, 49:219–226.

University of Exeter (2017). Surface Enhanced Raman Spectroscopy.

Vancha, A. R., Govindaraju, S., Parsa, K. V. L., Jasti, M., González-García, M., and Ballestero, R. P. (2004). Use of polyethyleneimine polymer in cell culture as attachment factor and lipofection enhancer. *BMC Biotechnol.*, 4:23.

Vercauteren, D., Rejman, J., Martens, T. F., Demeester, J., De Smedt, S. C., and Braeckmans, K. (2012). On the cellular processing of non-viral nanomedicines for nucleic acid delivery: Mechanisms and methods. *J. Control. Release*, 161:566–581.

Verma, A. and Stellacci, F. (2010). Effect of Surface Properties on Nanoparticle-Cell Interactions. *Small*, 6:12–21.

Vernon, M. M., Dean, D. A., and Dobson, J. (2015). DNA Targeting Sequence Improves Magnetic Nanoparticle-Based Plasmid DNA Transfection Efficiency in Model Neurons. *Int. J. Mol. Sci.*, 16:19369–19386.

Villanueva, A., Canete, M., Roca, A. G., Calero, M., Veintemillas-verdaguer, S., Serna, C. J., Morales, M. d. P., and Miranda, R. (2009). The influence of surface functionalization on the enhanced internalization of magnetic nanoparticles in cancer cells. *Nanotechnology*, 20:115103–115112.

Votteler, M., Carvajal Berrio, D. a., Pudlas, M., Walles, H., and Schenke-Layland, K. (2012). Non-contact, label-free monitoring of cells and extracellular matrix using Raman spectroscopy. *J Vis Exp*, 63:1–7.

Wahadoszamen, M., Rahaman, A., Hoque, N. M. R., I Talukder, A., Abedin, K. M., and Haider, A. F. M. Y. (2015). Laser Raman spectroscopy with different excitation sources and extension to surface enhanced raman spectroscopy. *J. Spectrosc.*, 2015:1–8.

Walczyk, T. and von Blanckenburg, F. (2005). Deciphering the iron isotope message of the human body. *Int. J. Mass Spectrom.*, 242:117–134.

Wang, H., Yang, J., Li, Y., Sun, L., and Liu, W. (2013). Combining magnetic field/temperature dual stimuli to significantly enhance gene transfection of nonviral vectors. *J. Mater. Chem. B*, 1:43–51.

Wang, P., Chen, C., Zeng, K., Pan, W., and Song, T. (2014). Magnetic nanoparticles trigger cell proliferation arrest of neuro-2a cells and ROS-mediated endoplasmic reticulum stress response. *J. Nanoparticle Res.*, 16:2718–2731.

Wattiaux, R., Laurent, N., Wattiaux-De Coninck, S., and Jadot, M. (2000). Endosomes, lysosomes: their implication in gene transfer. *Adv. Drug Deliv. Rev.*, 41:201–208.

Weir, M. P., Gibson, J. F., and Peters, T. J. (1984). Haemosiderin and tissue damage. *Cell Biochem. Funct.*, 2:186–194.

Wheeler, L. A., Vrbanac, V., Trifonova, R., Brehm, M. A., Gilboa-Geffen, A., Tanno, S., Greiner, D. L., Luster, A. D., Tager, A. M., and Lieberman, J. (2013). Durable Knockdown and Protection From HIV Transmission in Humanized Mice Treated With Gel-formulated CD4 Aptamer-siRNA Chimeras. *Mol. Ther.*, 21:1378–1389.

Wong, S. H. D., Li, J., Yan, X., Wang, B., Li, R., Zhang, L., and Bian, L. (2017). Magnetically tuning tether mobility of integrin ligand regulates adhesion, spreading, and differentiation of stem cells. *Nano Lett.*, 17:1685–1695.

Wood, M. J. A., Gait, M. J., and Yin, H. (2010). RNA-targeted splice-correction therapy for neuromuscular disease. *Brain*, 133:957–972.

Wu, Z., Yang, H., and Colosi, P. (2010). Effect of Genome Size on AAV Vector Packaging. *Mol. Ther.*, 18:80–86.

Wulfkuhle, J. D., Donina, I. E., Stark, N. H., Pope, R. K., Pestonjamasp, K. N., Niswonger, M. L., and Luna, E. J. (1999). Domain analysis of supervillin, an F-actin bundling plasma membrane protein with functional nuclear localization signals. *J. Cell Sci.*, 112:2125–2136.

Xie, Q., Xinyong, G., Xianjin, C., and Yayu, W. (2013). PEI/DNA formation affects transient gene expression in suspension Chinese hamster ovary cells via a one-step transfection process. *Cytotechnology*, 65:263–271.

Xing, R., Liu, G., Zhu, J., Hou, Y., and Chen, X. (2014). Functional Magnetic Nanoparticles for Non-Viral Gene Delivery and MR Imaging. *Pharm. Res.*, 31:1377–1389.

Xu, C., Xie, J., Kohler, N., Walsh, E. G., and Chin, Y. E. (2008). Monodisperse Magnetite Nanoparticles Coupled with Nuclear Localization Signal Peptide for Cell-Nucleus Targeting. *Chem. Asian J.*, 3:548–552.

Xue, H.-Y., Zhang, X., Wang, Y., Xiaojie, L., Dai, W.-J., and Xu, Y. (2016). In vivo gene therapy potentials of CRISPR-Cas9. *Gene Ther.*, 23:557–559.

Yadav, A. K. and Singh, P. (2015). A review of the structures of oxide glasses by Raman spectroscopy. *RSC Adv.*, 5:67583–67609.

Yan, J., Berezhnoy, N. V., Korolev, N., Su, C. J., and Nordenskiöld, L. (2012). Structure and internal organization of overcharged cationic-lipid/peptide/ DNA self-assembly complexes. *Biochim. Biophys. Acta - Biomembr.*, 1818:1794–1800.

Yang, W. J., Lee, J. H., Hong, S. C., Lee, J., Lee, J., and Han, D.-W. (2013). Difference between Toxicities of Iron Oxide Magnetic Nanoparticles with Various Surface-Functional Groups against Human Normal Fibroblasts and Fibrosarcoma Cells. *Materials (Basel).*, 6:4689–4706.

Yin, W., Xiang, P., and Li, Q. (2005). Investigations of the effect of DNA size in transient transfection assay using dual luciferase system. *Anal. Biochem.*, 346:289–294.

Yonenaga, N., Kenjo, E., Asai, T., Tsuruta, A., Shimizu, K., Dewa, T., Nango, M., and Oku, N. (2012). RGD-based active targeting of novel polycation liposomes bearing siRNA for cancer treatment. *J. Control. Release*, 160:177–181.

Yu, S.-M., Laromaine, A., and Roig, A. (2014). Enhanced stability of superparamagnetic iron oxide nanoparticles in biological media using a pH adjusted-BSA adsorption protocol. *J. Nanoparticle Res.*, 16:2484.

Zeltner, M., Grass, R. N., Schaetz, A., Bubenhofer, S. B., Luechinger, N. A., and Stark, W. J. (2012). Stable dispersions of ferromagnetic carbon-coated metal nanoparticles: preparation via surface initiated atom transfer radical polymerization. *J. Mater. Chem.*, 22:12064.

Zemljic-Harpf, A., Manso, A. M., and Ross, R. S. (2009). Vinculin and talin: focus on the myocardium. *J. Investig. Med.*, 57:849–855.

Zhang, E., Kircher, M. F., Koch, M., Eliasson, L., Goldberg, S. N., and Renström, E. (2014a). Dynamic magnetic fields remote-control apoptosis via nanoparticle rotation. *ACS Nano*, 8:3192–3201.

Zhang, J., Ring, H. L., Hurley, K. R., Shao, Q., Carlson, C. S., Idiyatullin, D., Manuchehrabadi, N., Hoopes, P. J., Haynes, C. L., Bischof, J. C., and Garwood, M. (2017). Quantification and Biodistribution of Iron Oxide Nanoparticles in the Primary Clearance Organs of Mice Using T 1 Contrast for Heating. *Magn. Reson. Med.*, 78:702–712.

Zhang, L., Li, Y., Yu, J. C., Chen, Y. Y., and Chan, K. M. (2014b). Assembly of polyethylenimine-functionalized iron oxide nanoparticles as agents for DNA transfection with magnetofection technique. *J. Mater. Chem. B*, 2:7936–7944.

Zhang, X. D., Wu, D., Shen, X., Liu, P. X., Yang, N., Zhao, B., Zhang, H., Sun, Y. M., Zhang, L. A., and Fan, F. Y. (2011). Size-dependent in vivo toxicity of PEG-coated gold nanoparticles. *Int. J. Nanomedicine*, 6:2071–2081.

Zhao, X., Cui, H., Chen, W., Wang, Y., Cui, B., Sun, C., Meng, Z., and Liu, G. (2014). Morphology, structure and function characterization of PEI modified magnetic nanoparticles gene delivery system. *PLoS One*, 9:1–8.

Zheng, L., Chen, L., Chen, Y., Gui, J., Li, Q., Huang, Y., Liu, M., Jia, X., Song, W., Ji, J., Gong, X., Shi, R., and Fan, Y. (2016). The effects of fluid shear stress on proliferation and osteogenesis of human periodontal ligament cells. *J. Biomech.*, 49:572–579.